12-2020

Multiphysics Assessment of Accident Tolerant Fuel, Cladding, and Core Structural Material Concepts

Jacob Preston Gorton
jgorton@vols.utk.edu

To the Graduate Council:

I am submitting herewith a dissertation written by Jacob Preston Gorton entitled "Multiphysics Assessment of Accident Tolerant Fuel, Cladding, and Core Structural Material Concepts." I have examined the final electronic copy of this dissertation for form and content and recommend that it be accepted in partial fulfillment of the requirements for the degree of Doctor of Philosophy, with a major in Nuclear Engineering.

Nicholas R. Brown, Major Professor

We have read this dissertation and recommend its acceptance:

Jamie B. Coble, G. Ivan Maldonado, Benjamin S. Collins, Andrew T. Nelson

Accepted for the Council:

Dixie L. Thompson

Vice Provost and Dean of the Graduate School

(Original signatures are on file with official student records.)

Multiphysics Assessment of Accident Tolerant Fuel, Cladding, and Core Structural Material Concepts

A Dissertation Presented for the
Doctor of Philosophy
Degree
The University of Tennessee, Knoxville

Jacob Preston Gorton
December 2020

ACKNOWLEDGEMENTS

I would like to thank my advisor, Dr. Nicholas Brown, for his support and excellent mentorship throughout my years in graduate school. I also extend my gratitude to all of my other committee members, Dr. Jamie Coble, Dr. Ivan Maldonado, Dr. Ben Collins, and Dr. Andrew Nelson, for all of their time and feedback throughout the proposal and defense process. Further, I greatly appreciate the technical guidance and support Dr. Collins and Dr. Nelson provided while I was working on the studies in this dissertation. I also want to thank Dr. Aaron Graham, Dr. Bob Salko, Dr. Shane Stimpson, and Dr. Shane Henderson from the ORNL CASL team for helping me with VERA. Thank you to my collaborators on the works contained in this dissertation, including Mr. Soon Lee, Dr. Youho Lee, Dr. Aaron Wysocki, Dr. Danny Schappel, Dr. Gyan Singh, Dr. Yutai Katoh, and Dr. Brian Wirth. I want to thank my parents, Harvey and Robin, for their continuous support. Finally, I'd like to thank my domestic partner Haley for always supporting me, proofreading my papers, and watching me practice presentations.

Some of this work was supported by the U.S. Department of Energy (DOE) Nuclear Energy University Program (NEUP) award #17-12688 and the U.S. DOE Office of Nuclear Energy Advanced Fuels Campaign. Any opinions, findings, and conclusions presented in this dissertation are only those of the author and do not necessarily reflect the views of the funding agencies.

ABSTRACT

The severe accident at the Fukushima-Daiichi nuclear power plant in 2011 ignited a global research and development effort to replace traditionally-used materials in Light Water Reactors (LWRs) with Accident Tolerant Fuel (ATF) materials. These materials are intended to extend the coping time of nuclear power plants during severe accident scenarios, but must undergo thorough safety and performance evaluations before being implemented. Four ATF concepts are analyzed in this dissertation using state-of-the-art computer modeling tools: (1) iron-chromium-aluminum (FeCrAl) fuel rod cladding, (2) silicon carbide (SiC) fiber-reinforced, SiC matrix composite (SiC/SiC) boiling water reactor (BWR) channel boxes, (3) mixed thorium mononitride (ThN) and uranium mononitride (UN) fuel, (4) and UO_2 [uranium dioxide] with embedded high thermal conductivity Mo inserts. The goals and approaches used for each study differed, and portions of this dissertation focused on verifying the accuracy of advanced modeling tools. Although each ATF evaluation is distinct, the underlying theme is the enhancement of safety, efficiency, and economic competitiveness of nuclear power through the use of advanced modeling techniques applied to material characterization studies.

Results from the evaluations show the pros and cons of each ATF concept and highlight areas of needed modeling development. Comparisons of simulated and experimental critical heat flux (CHF) data for FeCrAl cladding and subsequent sensitivity analyses emphasized differences between real-world and simulated post-CHF phenomena. The Virtual Environment for Reactor Applications (VERA) multiphysics modeling suite was verified against other widely-used modeling tools for BWR application, and its advanced features were used to generate boundary conditions in SiC/SiC channel boxes used for deformation analyses. Several ThN-UN mixtures were analyzed using reactor physics and thermal hydraulic techniques and were shown to significantly increase the margin to fuel melt compared with UO_2 [uranium dioxide] in LWRs. Mo inserts for UO_2 [uranium dioxide] were optimized using sensitivity regression techniques and were also shown to significantly increase the margin to fuel melt compared with traditional UO_2 [uranium dioxide].

TABLE OF CONTENTS

LIST OF TABLES

LIST OF FIGURES

CHAPTER 1
INTRODUCTION

1.1 Accident Tolerant Fuels

On March 11, 2011, the Great East Japan Earthquake and ensuing tsunami caused a station blackout (SBO) accident at the Fukushima-Daiichi nuclear power plant. During the accident, all operating reactors were automatically shut down, and primary and backup generators that powered feedwater circulation pumps were disabled by the flooding. The loss of coolant circulation made decay heat removal impossible, and reactor core temperatures began to rise. Elevated core temperatures accelerated the oxidation reaction between water and Zircaloy, the typical fuel rod cladding material in Light Water Reactors (LWRs). Accumulation of hydrogen gas released from the oxidation reaction eventually exploded in three reactor units at the plant, and radioactive material was released into the environment. The events that transpired at Fukushima influenced the U.S Department of Energy Office of Nuclear Energy (DOE-NE) to prioritize research and development focused on Accident Tolerant Fuel (ATF) materials. The development of ATF technologies intended to extend the coping time during a Fukushima-like accident soon became an international effort [1].

Since then, the umbrella term "ATF" has been expanded to include not just fuel materials, but also fuel rod cladding and core structural material concepts that may enhance accident-tolerance. Candidates concepts must undergo thorough evaluation before being implemented in an operating nuclear reactor to ensure that the technology enhances safety and does not negatively impact reactor performance, operations, or economics. Four candidate ATF technologies are focused on in this dissertation: (1) iron-chromium-aluminum (FeCrAl) cladding, (2) silicon carbide (SiC) fiber-reinforced, SiC matrix composite (SiC/SiC) boiling water reactor (BWR) channel boxes, (3) mixtures of thorium mononitride (ThN) and uranium mononitride (UN) fuels (ThN-UN), and (4) UO_2 with embedded Mo inserts. The primary properties of these materials that qualify them as ATF concepts are enhanced oxidation resistance, which will reduce hydrogen gas

production during an accident scenario, and enhanced heat transfer capabilities, which will reduce the stored energy in the reactor core.

A primary objective of this dissertation is to evaluate these concepts using computational methods to characterize their performance from thermal hydraulic and reactor physics perspectives. Several of these analyses are supplemented with sensitivity and optimization techniques, with an overall aim to gain understanding of the reactor performance and safety characteristics of these ATF candidate materials. The second objective of this dissertation is to highlight areas of needed development in computational models and to verify the accuracy of novel model capabilities. Specifically, the accuracy of recently developed BWR modeling capabilities in the Virtual Environment for Reactor Applications (VERA) multiphysics modeling suite is verified using current regulator-grade tools.

1.2 The Role of Computer Modeling in ATF Assessments

The United States Nuclear Regulatory Commission (NRC) has outlined a process for licensing ATF materials, which requires a holistic understanding of a material's response to steady-state, transient, and accident conditions [2]. The technical basis for licensing an ATF material requires a series of tests that include unirradiated and irradiated materials testing, in-reactor experiments using lead test assemblies (LTA), transient irradiation testing, and characterization of materials outside the realm of fuel performance, such as fission product release, core melt progression, core relocation, and mechanical and chemical interactions. All of these experiments are used to compile data to provide a licensing basis for an ATF material and also to inform and calibrate computational models of nuclear designs.

Performing the full suite of required tests for any ATF concept is a process that even the most aggressive timelines foresee taking at least a decade or more [1], [2], [3]. This process also requires multiple large-scale experiments that are costly to conduct. However, the testing process can be made more efficient and economical through the use of computer modeling evaluations. Advanced computer models can be used to screen ATF concepts for their feasibility as a reactor material so that only the most promising

candidates move to the experimental stage. For the concepts that do progress to the experimental stage, computer models can be used to highlight areas of testing need and inform experimental designs. Accurate modeling tools that are validated and verified using experimental databases are used for regulatory purposes and can determine reactor response to design basis accidents (DBAs) and beyond design basis accidents (BDBAs). These accident scenarios are difficult and costly to replicate experimentally, which underscores the important role that computer modeling plays in the progression of a novel material concept to real-world application. Overall, computational modeling is a vital step in the screening and licensing of ATF materials, and is the essence of this dissertation.

1.3 Goals and Hypotheses

At a high level, the purpose of this dissertation is to evaluate ATF material concepts and advanced computational modeling capabilities that will enhance the safety, efficiency, and economic competitiveness of nuclear power. Distinct studies were carried out for each of the four aforementioned ATF concepts that each have different goals and approaches, but all support this single, overarching purpose. Additionally, portions of this work were dedicated to verifying the accuracy of novel modeling capabilities, which also supports the underlying theme of this dissertation. The goals of these distinct studies were designed to fill knowledge gaps for each of the ATF concepts.

FeCrAl cladding is considered an ATF concept because of its excellent resistance to oxidation in steam environments relative to Zircaloy [4], [5]. Additional understanding on the potential accident response of FeCrAl cladding from a thermal hydraulics standpoint is still needed, especially in regards to its behavior related to the critical heat flux (CHF). CHF is a pertinent parameter in determining the thermal response of a system to a high-temperature accident scenario and is directly related to the thermal safety margin of LWRs. The FeCrAl cladding study aims to enhance understanding of the impact that uncertainties in FeCrAl material properties, heat transfer coefficients, and CHF enhancement during transient heating events have on the CHF value and post-CHF cladding temperatures during accident scenarios using sensitivity analysis methods and

computer models. This study also compared results from small-scale CHF experiments [6] and computer models of the experiment to highlight differences between simulated results and observed behavior after CHF is reached.

SiC/SiC composite is also being considered as a potential material for BWR channel boxes due to its excellent oxidation resistance [7]. The temperature and neutron flux gradients experienced in BWR fuel assemblies may lead to irradiation swelling and deformation of a SiC/SiC channel box, which could then interfere with control blade insertion or other operational maneuvers. The purpose of the SiC/SiC channel box study is to calculate high-fidelity temperature and fast neutron flux distributions in the channel box for several control blade configurations that could then be used as boundary conditions in deformation and stress models. An advanced modeling tool that could calculate these boundary conditions using multiphysics methods with fine spatial fidelity was desired for this study. The Consortium for Advanced Simulation of LWRs (CASL) multiphysics modeling suite, VERA, met these qualifications. However, the BWR modeling capability in VERA was a recent development that had not yet been validated or verified. Comparisons between VERA results and those calculated using regulatory-grade tools for fuel assembly designs from the Peach Bottom reactor [8] were made to verify the accuracy of VERA's BWR modeling capability.

Admixture of ThN and UN fuels is a novel concept that is primarily intended to increase heat transfer capabilities of nuclear fuel in reactors. Although ThN-UN fuels have favorable heat transfer characteristics, its feasibility as an LWR fuel material was unknown. The purpose of the ThN-UN study is to compare the reactor performance and safety characteristics of this fuel form to that of traditional UO_2. Several mixtures of ThN, UN, and ^{235}U enrichment were determined that gave the same cycle length as UO_2 in a pressurized water reactor (PWR), and then reactivity temperature coefficients (RTCs), control worth, and thermal performance of each mixture was determined as a function of burnup.

Studies focused on the addition of Mo into UO_2, either in the form of insert structures or granule mixtures, to increase thermal conductivity have previously been conducted [9], [10], [11], [12]. However, the studies in the literature focused on the

measured thermal conductivity of the UO_2-Mo designs and the temperature reduction in single fuel pellet models, leaving several areas of research need for this concept. First, no attention has been given to the neutronic impact of replacing fuel material with a non-fissile insert. Second, the benefit of this concept to reducing fuel temperatures has only been quantified in a single fuel pellet model that was focused primarily on the heat transfer mechanism. Reactor-scale models are needed that account for neutronic and thermal hydraulic feedback mechanisms to better quantify the performance of this concept. Lastly, there is no systematic procedure in place that can be used to optimize the shape or structure of the insert design. The purpose of the UO_2-Mo study in this dissertation is to address all of these research needs using multiphysics, sensitivity, and optimization methods.

Based on the scope of these ATF evaluations, the following hypotheses are proposed:

1. The CHF and peak cladding temperature (PCT) of FeCrAl cladding are sensitive to heat transfer coefficients, material properties, and transient-induced CHF enhancement.
2. VERA is capable of accurately predicting BWR performance and is valid to use for novel, complex problems, such as ATF evaluations.
3. Temperature and fast neutron flux gradients in a SiC/SiC channel box will lead to deformation and control blade interference.
4. ThN-UN fuels provide an enhanced thermal safety margin due to the high thermal conductivity of nitride-based fuel.
5. A Mo insert design for UO_2 fuel pellets can be optimized to improve thermal safety margin of LWRs while having minimal impact on neutronic performance.

The contributions of this work include an increased knowledge base of fuel, cladding, and structural ATF concepts, demonstration of differences between experimental data and simulated results, validation of a U.S. Department of Energy (DOE) computational tool for BWR application, and novel use of that tool for ATF research. The work presented in this dissertation is informative for future experiments and studies, demonstrates the feasibility of a number of ATF concepts, and validates an

advanced multiphysics modeling tool for BWR application, all of which are vital steps in the NRC's project plan for licensing ATF materials. Of the four concepts considered, the NRC considers FeCrAl cladding to be a near-term concept, meaning it may be deployed as soon as the early to mid 2020s, while any SiC/SiC cladding or structural concept is considered a longer-term concept [2]. Both ThN-UN fuels and fuels with Mo inserts are at an infancy stage in which preliminary feasibility studies and initial materials evaluations are being performed. The breadth of ATF concepts considered, covering fuel, cladding, and structural concepts, varying in development from early formulation to near-term deployment and the use of state-of-the art modeling tools suggest that the studies presented in this dissertation will be relevant and impactful for years to come.

1.4 Dissertation Contributions and Outline

The work in this dissertation contributes new knowledge to a variety of ATF-related initiatives. CHAPTER 2 of this dissertation reviews literature relevant to the history, purpose, and requirements of ATF technologies and lists a number of the most developed ATF concepts and their properties. Some background on all of the computational modeling tools used in this dissertation is given, along with some review on other tools widely used in the nuclear industry. The ATF evaluations presented are all distinctly different and offer a wide viewpoint on the types of computational studies needed to advance ATF technologies. There are four ATF evaluations at the heart of this dissertation that have been previously published in first-author, peer-reviewed journal publications [13], [14], [15], [16]. Novel contributions to the literature from this dissertation are summarized as follows:

1. Development of flow boiling models for assessing CHF characteristics of new cladding materials during accident scenarios in two widely-used thermal hydraulic analysis tools [13]. These models are based on an experimental flow boiling apparatus constructed at the University of New Mexico (UNM) [6], and were used for code-to-experiment comparisons of measured CHF data for FeCrAl cladding. This work was performed in direct collaboration with UNM, in which they provided experimental data and guidance on the experiment design.

2. Execution of a sensitivity analysis focused on heat transfer coefficients, material properties, and transient CHF enhancement to determine the relationship between these parameters and CHF and PCT [13]. This sensitivity study used one of the models based on the UNM flow boiling apparatus and varied each input parameters based on measurement uncertainty, uncertainty in correlations, and the observed enhancement of CHF during a heating transient. Nearly 18,000 model runs were conducted in this study to elucidate the impact of each input parameter.
3. Investigation into the differences between how CHF and post-CHF effects are modeled and the observed phenomena [13]. Specifically, comparisons between simulated results and the UNM experimental data showed large differences in the rate of heat transfer decline after the CHF is reached, causing the computer models to be highly conservative in PCT predictions.
4. The initial assessment of VERA's coupled neutronics-to-thermal-hydraulics BWR analysis capability using other widely-used modeling tools [14]. BWR modeling is under development for VERA and has not yet been validated or verified. BWR fuel assembly models were developed in both VERA and regulatory-grade modeling tools to make comparisons between results and provide a preliminary appraisal of VERA's BWR modeling capability. These comparisons were performed with guidance from BWR modeling experts at the Oak Ridge National Laboratory (ORNL).
5. Determination of 3-D fast neutron flux and temperature distributions in SiC/SiC channel boxes for a number of control blade configurations using single and multi-fuel-assembly models in VERA. Work involving single-assembly models has been published in a co-author journal article, in which these fast flux and temperature distributions were used as boundary conditions for a finite-element channel box deformation study [17]. These distributions were also calculated in a mini-core model as an initial demonstration of VERA's advanced modeling features and applicability to ATF research [16].
6. Identification of several ThN and UN mixtures that are capable of matching conventional UO_2 cycle length in a PWR [15]. This required the development of simple PWR pin-cell models in multiple computational tools for verification purposes

and parametric studies of ThN content, UN content, and ^{235}U enrichments to find acceptable combinations. Additionally, this process was carried out using natural nitrogen, which is almost entirely ^{14}N, and then repeated for 100%-enriched ^{15}N. Accurate thorium modeling was performed with guidance from a VERA developer.

7. Calculation of reactor safety and thermal performance parameters for ThN-UN fuels and comparison to UO_2 performance [15]. RTCs, soluble boron coefficient (SBC), and control rod worth were calculated using reactor physics tools as a function of burnup for each of the identified ThN-UN mixtures. Homologous temperature, the ratio of fuel temperature to its melting point, was calculated using VERA's multiphysics methods.
8. Design and execution of a sensitivity analysis method to study the impact of insert geometry on the neutronic and heat transfer performance of UO_2 with Mo inserts [16]. The goals of the study precluded the use of traditional one-at-a-time sampling methods, and instead called for the adaptation of a more unique method. The Monte Carlo particle transport code Serpent [18] was utilized for the neutronics study, and the finite element code BISON [19] was used for the heat transfer study. This study was performed in collaboration with ORNL, and an ORNL researcher executed all BISON simulations. However, I designed the sensitivity study and programmed a Python script that automatically generated thousands of BISON geometry files from a template provided by the ORNL researcher.
9. Development of a thermal conductivity calibration scheme to match fuel temperature results from VERA's thermal hydraulics modeling tool to higher-fidelity temperature profiles predicted by BISON for UO_2 with Mo inserts [16]. This was required to make the leap from single fuel pellet models in BISON, which is capable of explicitly modeling the 3-D insert geometry, to a reactor analysis tool, which has to homogenize this composite fuel form into a single material.
10. Comparison of reactor safety-related parameters and thermal hydraulic performance of UO_2 with Mo inserts to conventional UO_2 in a PWR [16]. These comparisons used VERA PWR models to calculate RTCs, SBC, and control rod worth. Also, VERA

and the calibrated thermal conductivity relationships were used to determine homologous temperature of these fuels in comparison with UO_2.

More in-depth descriptions of each of these studies are given in CHAPTER 3 through CHAPTER 6. Specifically, the thermal hydraulic evaluation of FeCrAl cladding, which includes the first three contributions listed above, is given in CHAPTER 3. Verification of VERA's BWR modeling capability through comparisons with current state-of-the-art modeling tools is presented in CHAPTER 4. Also included in CHAPTER 4 is the calculation of temperature and fast neutron flux boundary conditions in SiC/SiC channel boxes for various reactor and control blade configurations.

ThN-UN fuel compositions that can match the UO_2 cycle length in a PWR were determined in CHAPTER 5, as are calculations of RTCs, SBC, control worth, and thermal performance of those fuel compositions as a function of burnup. In CHAPTER 6, the reader can find the study of Mo inserts for UO_2. The chapter includes sensitivity and optimization studies focused on the neutronic and heat transfer performance of the fuel design. As was done in the ThN-UN study, RTCs, SBC, control worth, and thermal performance were determined. In both chapters, comparisons were made between the performance and safety characteristics of these novel fuel types and UO_2. Lastly, CHAPTER 7 summarizes the findings and contributions of this work and concludes the dissertation.

CHAPTER 2
LITERATURE REVIEW

2.1 Motivation for ATF Technology Development

2.1.1 Historical Perspective

Following Admiral Hyman Rickover's decision to use LWR technology with zirconium-based alloy (or Zircaloy) cladding and UO_2 fuel in the U.S. Navy's first nuclear submarine, the U.S.S. *Nautilus*, LWRs have become the most common type of power-producing nuclear reactor in the world [20], [21]. Since that decision was made in the years shortly after World War II, relatively few changes to LWR materials technology have been made. Several operational and safety upgrades were implemented after the Three Mile Island accident in 1979, but LWR technology that uses the Zircaloy/UO_2 cladding and fuel system remains the dominant form of nuclear power [1]. However, the events that transpired at the Fukushima-Daiichi nuclear power plant in 2011 have inspired a global research and development effort to replace traditional LWR materials with ATF materials to enhance safety.

The tsunami that struck Japan as a result of a magnitude 9.0 earthquake caused an SBO at the Daiichi nuclear power plant, which cut power to the pumps that circulate coolant through three of the reactors at the site. Reactors at the Daiichi site automatically shut down by design when then earthquake was detected, but decay heat produced in the core required that coolant still be pumped through the system. Backup generators for the coolant pumps turned on, but failed shortly after as a result of the tsunami and flooding, leaving the coolant water stationary in the reactor cores. The stationary water quickly reached excessive temperatures, which led to boiling and an increased the rate of the oxidation reaction between Zircaloy and water. Flammable hydrogen gas is a byproduct of the oxidation reaction, which is given by Equation (1), and the build-up of hydrogen eventually led to several explosions that compromised the reactor containment building, thus allowing the radioactive material to escape to the environment [22].

$$Zr + 2H_2O \rightarrow ZrO_2 + 2H_2 \quad (1)$$

Contaminated coolant water was also released into the ocean during the accident containment process since it was unable to be pumped through the system [23]. The events that transpired at Fukushima led to increased research in ATF technologies, which includes nuclear fuel, fuel rod cladding, and core structural materials that could potentially replace the typical Zircaloy/UO_2 system used in current LWRs.

2.1.2 Review of ATF Technology Requirements and Desirable Traits

The major consequence from a nuclear accident is the release of fission products from inside the reactor core to the environment that results in adverse effects on public health, the environment, and the economy [23]. The NRC lists three hazard barriers in current LWRs intended to prevent the release of fission products to the environment: the metallic fuel rod cladding (typically Zircaloy), the reactor pressure vessel and water pipes, and the concrete containment building [24]. The UO_2 fuel pellets typically used in LWRs may also be considered a hazard barrier to fission product release due to their porous structure that retains fission gas [23]. The primary objectives for an ATF material are to extend the coping time during a BDBA, such as the one that occurred at Fukushima, and to prevent the release of fission products into the environment.

A set of required and desired attributes of an ATF candidate have been discussed in several publications [1], [3], [25]. In addition to extending the coping time during an accident, ATF materials must also meet economic and reactor performance criteria, otherwise commercial reactor vendors will not be willing to invest in them. For this reason, ATF technologies are expected to meet a “do no harm” criteria in which they perform at least as well as the Zircaloy/UO_2 system in terms of reactor operations and performance [3], [26], [27].

Characteristics of an ATF technology that will increase coping time during a severe accident and maintain fission product retention are significantly reduced oxidation and corrosion rates in high-pressure steam environments, reduced probability of mechanical failure from pellet-cladding interactions (PCIs) or other mechanisms, and increased ability to transfer heat from the fuel pellet to the coolant. It is desirable for an

ATF cladding material to be ~100 times more oxidation resistant than Zircaloy in reactor environments up to at least 1200°C [1], [28]. There are two reasons for finding a material with increased oxidation resistance: to reduce the build-up of hydrogen in the reactor vessel and to reduce the amount of heat that needs to be removed by the emergency core cooling system (ECCS) during a severe accident [29]. The oxidation reaction between water and Zircaloy is exothermic, meaning it releases heat as it occurs and adds to the decay heat produced by nuclear fuel during a reactor trip. At approximately 1200°C, the reaction becomes self-catalytic in steam environments and the rate at which heat is released increases [30]. It is understood that even at much slower reaction rates, no material can fully prevent oxidation and the build-up of hydrogen, but rather only provide extra time for containing an accident before hydrogen levels and core temperatures become dangerous.

PCIs can increase the likelihood of fuel rod cladding failure and therefore the release of fission products. Therefore, it is desirable for an ATF cladding candidate to be more likely than Zircaloy to either withstand PCIs or avoid them altogether. PCIs caused by chemical reactions, referred to pellet-cladding or fuel-cladding chemical interactions (PCCI or FCCI), between the fuel and cladding or fission products and the cladding often lead to stress corrosion cracking. A common FCCI in LWRs is the reaction between iodine and zirconium. The formation of ZrI_4 from the reaction removes zirconium atoms from the cladding in a process known as pitting. This reaction weakens the cladding and increases the likelihood of failure from stress corrosion cracking [31]. PCIs occurring from physical interaction between the pellet and cladding are referred to as pellet-cladding mechanical interactions (PCMIs) and occur due to the different thermal expansion rates of the fuel pellet and cladding, and the swelling of the fuel pellet over time. PCMIs can lead to breaching of the fuel rod cladding and the release of fission products into the reactor coolant [32]. The most limiting PCMI case occurs during a reactivity-initiated accident (RIA), which is discussed in more detail in Section 2.3.2.

UO_2 was originally selected as the fuel for LWRs because of its high melting temperature, stability under irradiation, and relatively high U density [33]. However, UO_2 is also known to have a low thermal conductivity [34], which leads to higher fuel

centerline temperatures and stored energy in the fuel. Enhanced thermal conductivity compared with UO_2 is a desirable characteristic of an ATF because it increases heat transfer from the fuel through the cladding and to the coolant. High thermal conductivity also contributes to shallower temperature gradients across the fuel pellet radius. These characteristics can improve the performance and safety of LWRs by reducing stored energy in the fuel, reducing fission gas release [9], [10], [35], and enhancing short-term accident tolerance [35]. Lower fuel temperatures may also reduce the likelihood of PCIs [9], [10], [32] and makes power uprates possible in LWRs [10].

There are several characteristics and metrics of the Zircaloy/UO_2 system that an ATF material must match in order to have a minimal impact on the performance of an LWR under normal operational conditions. For example, ATF materials should have similar reactivity coefficients and cycle lengths as the Zircaloy/UO_2 system. ATF materials need to be backwards compatible with current LWR designs so that they can be implemented in the current reactor fleet [3], [26]. Furthermore, ATF materials should have a minimal impact on the nuclear fuel cycle [27]. By mitigating the impact to performance and operations of a nuclear reactor while also enhancing safety, any implemented ATF technology will be a significant upgrade to current LWR technology.

2.2 Current Concepts

Of the ATF technologies considered in this dissertation, several of them have been heavily studied, while others are more unique. FeCrAl alloys, along with SiC/SiC, and coated Zircaloy, are among the most common fuel rod cladding concepts [29]. SiC/SiC is also considered as a potential channel box material in BWRs [36] [17]. UN, U_3Si_2, and fully ceramic microencapsulated (FCM) fuels are highly researched fuel concepts due to their greater thermal conductivity compared to UO_2 [9]. Two unique fuel concepts discussed in this dissertation are the mixture of ThN and UN, and the inclusion of non-fissile inserts in UO_2. The motivation of studying these concepts is that UN readily degrades in water, so mixing with another constituent may mitigate this issue [37], and the inclusion of non-fissile inserts with high thermal conductivity in UO_2 may enhance heat transfer capabilities.

2.2.1 FeCrAl Cladding

FeCrAl has been the subject of extensive material properties, reactor performance, and safety characteristics evaluations [4], [5], [26], [38], [39], [40]. Optimized FeCrAl alloys exhibit excellent oxidation resistance at temperatures up to at least 1475°C [4], [5], have superior mechanical properties at elevated temperatures relative to Zircaloy [4], and resist thermal and irradiation creep [38]. The oxidation characteristics of FeCrAl are attributed to the formation of chromium oxide and alumina oxide layers on the steam-exposed surface of the FeCrAl cladding, which then protects against further oxidation. The formation of the chromium and alumina oxide layers are dependent on the amount of chromium and aluminum present in the alloy, and it has been found that the most protective layers form when the chromium content is above 20% (weight percent) and the aluminum content is approximately 5% [30], [41]. However, too much chromium can lead to increased radiation embrittlement [42], [43], so alloys are being studied with chromium content in the range of 10-22% chromium and 4-6% aluminum [44].

A PCMI burst test using FeCrAl and Zircaloy claddings was performed at ORNL which showed that FeCrAl had approximately 10% greater burst strength compared with Zircaloy under loss of coolant accident (LOCA) conditions when the cladding had the same thickness [45]. However, the neutron absorption cross section of FeCrAl alloys is larger than that of Zircaloy, which causes a neutron penalty and would require a thinner cladding to be used to meet the cycle length of the Zircaloy/UO_2 system [26], [39], [40], [46]. The use of a thinner cladding may offset the increase in burst strength demonstrated in the PCMI test [45]. The effect of PCCI in FeCrAl is not yet well understood [30], [41].

It is also necessary to understand the thermal hydraulic response of FeCrAl to normal operating and DBA conditions. An investigation into pool boiling CHF for FeCrAl alloys conducted at UNM found surface characteristics such as wettability and roughness played a role in pool boiling CHF [47]. It was also found that the CHF of FeCrAl increased after the material had formed an oxidization layer when placed in PWR water conditions for one year. This increase in CHF is attributed to the decrease of contact angle, and therefore the increase in wettability, of the material surface.

To determine if this pool boiling effect also occurred in flow boiling, a low-pressure flow loop was developed at UNM for CHF testing [6]. The same test specimens were used for multiple experiments so that the impact of an evolving surface structure on CHF in flow boiling could be determined. After 10 steady-state experiments, the average contact angle of FeCrAl decreased from the as-received contact angle of 69.43º to 53.64º. The surface roughness also decreased after the steady-state experiments. Based on the relationship between surface morphology and CHF found in the UNM pool boiling experiments [47], it may be expected that the decrease in contact angle occurring after multiple flow boiling experiments would lead to an increase in CHF. However, there was no appreciable change in the steady-state CHF between each trial in the flow loop. After an additional six transient experiments on the same FeCrAl specimen, the contact angle was an average of 59.12º. Despite the contact angle changing throughout the tests, no significant change in CHF occurred between each transient experiment with the average CHF being 3371 kW/m^2 with a standard deviation of 109 kW/m^2 (3.23%).

The lack of appreciable change in flow boiling CHF due to increased surface wettability served as the technical basis for the hypothesis that heat transfer coefficients and material thermal properties, including thermal conductivity, k, and volumetric heat capacity, ρC_p, thermal effusivity, e, and thermal diffusivity, α, may have a significant impact on CHF in flow boiling conditions. Further, the FeCrAl CHF values observed in the flow boiling experiments were found to be 22% greater than the Zircaloy-4 CHF values during steady state tests under the same conditions [6]. This observation gave further reason to examine the influence of material properties on CHF.

2.2.2 SiC/SiC Cladding and Structural Material Concepts

Like FeCrAl, SiC/SiC composites are being considered as a cladding material due to its high oxidation resistance up to at least 1200°C (and potentially as high as 1700°C) [7], as well as its acceptable strength, low neutron absorption cross section, and resistance to irradiation creep [48]. As a cladding material, however, SiC/SiC has been found to present a number of challenges: SiC/SiC swells volumetrically under neutron irradiation and deforms significantly [49], [50], SiC/SiC is more brittle than Zircaloy and may be

more likely to fail during a PCMI [50], the thermal conductivity of SiC/SiC decreases when it is irradiated, and there is not currently a suitable manufacturing method for sealing SiC/SiC fuel rods after the fuel has been loaded [51].

Due to the challenges faced when using SiC/SiC as a cladding material, it has been proposed to use SiC/SiC as a channel box material in BWRs. Channel boxes surround each fuel assembly in a BWR to provide structural support and contain the flow of steam inside each fuel assembly. They make up approximately 40% of the Zircaloy in a BWR core [48], so replacing the channel box material with SiC/SiC may provide significant benefit in terms of reducing hydrogen production in the case of an accident. Over the course of the fuel cycle, the high-dose environment of a nuclear reactor leads to radiation degradation phenomena in the core materials [52]. Examples of radiation degradation phenomena are void swelling, irradiation creep, volumetric swelling, and radiation embrittlement, all of which are the result of the accumulation of point defects from fast neutrons [52], [53]. A primary challenge associated with the SiC/SiC channel box material concept is the effect of volumetric swelling under irradiation, which may lead to significant deformation in non-uniform neutron flux environments [36], [17]. A deformed channel box may come in contact with the cruciform control blades used in BWRs, which are inserted between fuel assemblies, and impact operational or safety performance.

The channel box that encloses each BWR fuel assembly provides structural support, forms paths for cruciform control blades to be inserted between assemblies, and maintains cooling in the active fuel regions of the core by preventing void drift to the bypass region between assemblies [54]. Boiling of coolant in the core, axially and radially heterogeneous fuel loading patterns, and control blade insertion all contribute to nonuniform fast neutron flux gradients in the entire fuel assembly, including in the channel box. The fast flux gradients contribute to channel box deformation because different parts of the channel box will grow or swell at different rates, causing the channel to bow. When Zircaloy is used as the channel box material, pressure differential between the inside and outside of the channel box can cause irradiation creep and bulging of the channel box [54]. This is not expected to be an issue for SiC-based channel boxes

because the material is resistant to irradiation to creep [48]. It is worth noting the distinction between irradiation growth and irradiation swelling: irradiation growth is an anisotropic process that conserves volume, while irradiation swelling is an isotropic process that does not conserve volume. Zircaloy is more susceptible to irradiation growth, while SiC/SiC is resistant to anisotropic growth but is susceptible to isotropic swelling. Regardless of the mechanism, nonuniform growth or swelling rates in the channel box lead to distortion.

There are two major implications that may result from channel box deformation. First, channel box bowing can alter inter-assembly gap widths, which directly affects neutron moderation and pin power distributions. A computational analysis of a Westinghouse SVEA-96+ BWR fuel assembly showed that the change in gap sizes resulting from a 9-mm channel bow led to a maximum change in the fission reaction rate of 16% and a maximum change in the ^{238}U parasitic capture rate of 6% [53]. While a 9-mm bow is considered an upper-bounding case, this phenomenon may have an impact on thermal safety margins, such as the critical power ratio (CPR).

The second major consequence resulting from channel box bowing is interference with control blades. It is estimated that the clearance between a channel box and control blade is between 2.4 and 3.3 mm, and potentially even less based on the tolerances of the channel box and control blade wings [55]. Interaction between the channel box and control blade can prevent the insertion of the control blade or may cause channel box failure, both of which have adverse effects on reactor safety. The main strategy for avoiding control blade interference is fuel assembly shuffling in such a manner that a fuel assembly which has been exposed to a flux gradient in one direction is exposed to a flux gradient in the opposite direction [53]. If interference is unable to be avoided, fully inserting the control blade at the first indication of interference and shutting down the control cell for the remainder of the cycle may be necessary, as was done at the LaSalle Units 1 and 2 in 2007 and 2008 [56]. The effect of neutron flux gradients in the channel box on deformation and the associated operational and safety ramifications serve as the motivation behind the study of SiC/SiC channel boxes using multiphysics methods in this dissertation.

2.2.3 Thorium-based Fuel Concepts

The use of thorium in a thermal reactor presents several unique advantages and challenges compared to a traditional uranium-based fuel cycle. Thorium is approximately three times more abundant than uranium in Earth's crust [57], [58]. U-233, produced from the absorption of a neutron by a ^{232}Th nucleus and subsequent β-decays, yields a greater reproduction factor, η, than ^{235}U or ^{239}Pu at thermal energies. This leads to better fuel cycle performance in terms of conversion ratio, and it opens the possibility of breeding or breakeven fuel cycles in a thermal reactor [57], [58], [59]. From a nonproliferation standpoint, the addition of thorium in an LWR leads to less plutonium production. The strong gamma emission from ^{232}U makes ^{233}U extraction a difficult process and therefore may improve proliferation resistance [57], [60]. Additionally, thorium-fueled reactors could be used to reduce the plutonium stockpile since thorium systems initially require a neutron source to convert thorium into ^{233}U [59], [60].

Another benefit that most directly relates to the interests of the ATF program is that thorium-based fuels have a higher thermal conductivity than uranium-based fuels [57]. It has been shown that the thermal conductivity of ThO_2 is several times greater than that of UO_2 at low temperatures, but it approaches approximately the same value at elevated temperatures (>1,200°C) [61], [62], thus limiting its potential as an ATF material. Further, transmutation of thorium to protactinium and uranium will degrade thermal conductivity during reactor operation [62], [63], [64], [65]. The thermal conductivity of ThN has also been shown to be greater than that of UN, and both ThN and UN have greater thermal conductivity than UO_2 [63]. Although the thermal conductivity of ThN decreases as temperature increases, it remains an order of magnitude greater than the thermal conductivity of UO_2 up to at least 1,500°C. Additionally, the thermal conductivity of UN increases with increasing temperature. If it is assumed that the thermal conductivity of a mixture is the volume-weighted average of the constituent thermal conductivities, then mixing the two fuels will lead to a thermal conductivity that is still an order of magnitude greater than that of UO_2 over the temperature range of interest for LWRs and up to at least 1,500°C.

Higher thermal conductivity of the fuel pellets leads to a larger thermal safety margin in terms of the homologous temperature, which is the ratio of the maximum temperature in the fuel (i.e., the fuel centerline temperature) to the melting point of the fuel using the Kelvin scale. The melting or disassociation point (temperature where solid mononitride transforms to liquid metal and gaseous nitrogen) of ThN and UN depends on the nitrogen overpressure, but is approximately 2,800–2,850°C when approximately atmospheric nitrogen pressure is available [66], [67], [68]. These temperatures are comparable to that of UO_2, which also melts at approximately 2,850°C [69]. Better thermal conductivity in nitride-based fuel forms may potentially reduce fission product release since the smaller temperature gradient in the fuel leads to smaller thermal stresses and a decreased likelihood of fuel pellet cracking [70].

A thorium-based fuel form also presents several challenges, the primary one being that thorium itself is not a fissile material and needs an external neutron source to convert thorium into the fissile ^{233}U. Uranium can act as the external neutron source, but the ^{235}U enrichment must be greater than the typical 5 wt% ^{235}U limit [60]. However, high assay, low-enriched uranium (HALEU) with enrichments greater than 5 but less than 20 wt% $^{235}U/U$ may be used, although this will increase fuel cycle costs [60]. Production of ^{233}U from the β-decay of ^{233}Pa, which is produced in the transmutation chain of ^{232}Th and has a half-life of 27 days, can cause an increase in reactivity after a reactor has been shut down. Furthermore, the ^{232}U gamma that makes thorium fuels proliferation resistant also makes fuel refabrication difficult. Despite these challenges, thorium fuels have been used in high-temperature gas-cooled reactors (HTGRs) and water reactors, and concepts exist for their use in molten salt reactors (MSRs).

BIstructural- and TRIstructural-ISOtropic (BISO and TRISO) fuels using UO_2/ThO_2 fuel particles coated in pyrolytic carbon and silicon carbide layers have been used in the prototype HTGRs Peach Bottom 1 in the United States, AVR in Germany, and Dragon in the United Kingdom. After successful experiments in these reactors, thorium fuels were used in the Fort Saint Vrain and Thorium High Temperature Reactor (THTR) experimental reactors in the United States and Germany, respectively [59], [71]. The successful Molten Salt Reactor Experiment (MSRE) at ORNL led to the

development of the Molten Salt Breeder Reactor (MSBR) project, which utilized a thorium fuel cycle [72]. More recently, fast-spectrum, thorium-fueled MSR concepts are being revisited [73].

Mixed UO_2/ThO_2 fuels were used in the Elk River and Indian Point LWRs [59], and the Shippingport reactor made use of the seed-blanket concept [74] to demonstrate breeding in an LWR. The seed-blanket concept, also known as the Radkowsy Thorium Fuel (RTF) concept [75], uses fissile seed regions to initially fuel the reactor and to supply neutrons to the blanket region of thorium, which is transmuted into ^{233}U for continued operation. LWRs with reduced moderation have been proposed, including heavy water PWRs and tight-pitch BWRs, both of which have a smaller moderator-to-fuel ratio and larger conversion ratio than typical LWRs, and they primarily operate in an intermediate energy spectrum (1 eV to 100 keV). Pressurized heavy water reactors (PHWRs) have been built in India, and several thorium-containing fuel bundles have been loaded into the Kakrapar Atomic Power Station [76]. An advanced heavy water reactor is currently under development in India [77], and several other nations, including Turkey [78] and Canada [79], have taken interest in and have performed computational studies on thorium fuels in heavy water reactors. Evaluations of these concepts show that break-even or breeding can be achieved in these systems when seed-blanket concepts and reduced moderator-to-fuel ratios are used [80], [81].

2.2.4 Non-fissile Inserts in UO_2

A variety of UO_2-based composite fuels have been developed with the primary intention to increase heat transfer capabilities. Zhou and Zhou [9] have compiled a comprehensive review of composite fuels containing UO_2 and a non-fissile phase. Several examples non-fissile phases that have been studied in the past include BeO, SiC, carbon-based phases, Cr, and Mo. The driving motivation behind the use of these phases is increasing the thermal conductivity of the fuel in an LWR, the benefits of which were stated in Section 2.1.2. To summarize, higher thermal conductivity leads to lower operating temperature, reduced energy storage, and shallower temperature gradients in the fuel. These characteristics enhance short-term accident tolerance and fission product

release, while also lowering the probability of PCIs. However, replacing fuel volume with a non-fissile material induces a neutronic penalty that likely must be compensated for with increased ^{235}U enrichment.

Though a number of potential high-thermal conductivity phases have been investigated, the study in this dissertation focuses on metallic Mo insert structures with the objective to quantify the impact of Mo inserts on PWR performance. Mo is focused on because of its excellent thermal conductivity [82] [83], thermochemical compatibility with UO_2 [83], and resistance to swelling or other degradation under irradiation [84]. Also, Mo has a melting point of 2,623°C [11], which is comparable with the melting point of fresh UO_2 at 2,850°C [69]. Several studies have focused on the fabrication, thermal conductivity, and potential improvement in LWR heat transfer performance of UO_2 that contains Mo, either as a structural insert or in a mixed form. Kim et al. [11] fabricated UO_2-Mo pellets by sintering mixtures of UO_2 granules and Mo powder and then demonstrated the ability to create a continuous channel of Mo microcells that had a higher thermal conductivity than pure UO_2. Finkeldei et al. [12] fabricated pellets of UO_2 and Mo that did not contain a continuous network of Mo within the UO_2, but instead featured a dispersed network and still found increased thermal conductivity compared to pure UO_2. Buckley, et al. [83] also developed UO_2-Mo fuel pellets by using spark plasma sintering to radially disperse Mo throughout the pellet. Both studies developed UO_2-Mo fuel pellets with 5 and 10% Mo by volume and measured similar thermal conductivities to each other. Medvedev and Mariani [10] used the BISON code [19] to evaluate the thermal performance of Mo insert designs. In that study, a design that used alternating 50-µm thick Mo disks and 0.95-mm thick UO_2 disks reduced the maximum fuel temperature by 995°C compared with regular UO_2 at a set linear heating rate of 500 W/cm.

Although its material properties and previous studies in the literature justify its use as an insert material from a heat transfer standpoint, less attention has been given to the effect of Mo inserts from a neutronic standpoint. Replacing fuel meat with a non-fissile material will reduce achievable cycle length, and Mo has a large neutron capture cross section in the resonance region, as shown by Brown et al [26]. There is currently a

gap in the understanding of how these inserts would impact neutronic performance and safety characteristics. Further, the use of advanced additive manufacturing techniques opens the doorway for a wide range of potential inserts to be fabricated. There is currently little understanding on how to optimize the geometry of the insert to maximize heat transfer and neutronic performance. The study of UO_2 with Mo inserts in CHAPTER 6 aims to fill both of these knowledge gaps.

2.3 Review of Accident and Safety-Related Concepts

Several accident and safety-related concepts that are pertinent to the ATF concepts studies in this dissertation are detailed in this section. Specifically, RTCs and the RIA, a type of DBA, are discussed. CHF, a potential repercussion of an RIA, is also discussed. RTC calculations are carried out for both the ThN-UN and UO_2-Mo fuel forms in CHAPTER 5 and CHAPTER 6, whereas RIAs and CHF are focused on in the analysis of FeCrAl cladding in CHAPTER 3.

2.3.1 Reactivity Temperature Coefficients

RTCs are the basis for the mechanism of thermal feedback in which changes in reactor conditions have an impact on the reactivity, and therefore the overall power level, of the reactor. They are an important measure related to the safety of nuclear reactors [85]. Temperature feedback is the first-order feedback mechanism in a nuclear reactor [86], and temperature coefficients of reactivity are typically characterized for the fuel and moderator in an LWR. Signified by α_T, RTCs describe the change in reactivity per change in temperature. This is shown in Equation (2) for a generic material *j*, which could denote fuel, moderator, or another core component. RTCs are typically required to be negative so that an increase in temperature leads to a decrease in reactor power, giving the reactor inherent stability. If the reactivity coefficient were positive, an increase in temperature would lead to an increase in power, which would further increase the temperature and lead to an unstable reactor.

$$\alpha_{T,j} = \frac{\partial \rho}{\partial T_j} \tag{2}$$

In nuclear fuel, the temperature feedback is dominated by the nuclear Doppler effect, in which the width of cross section resonances in heavy nuclei broadens as temperature increases [85]. The Doppler effect is quantified using the Doppler coefficient, also known as the fuel temperature coefficient (FTC). This phenomenon increases the likelihood of resonance absorption and thus leads to a decrease in reactivity.

In LWRs, the moderator temperature coefficient (MTC) takes into account changes in reactivity due to temperature changes and density changes, since the density of water is strongly dependent on its temperature. For water reactors, the change in moderator density is the primary contributor to the MTC because as the density of the water decreases, moderating ability is lost. The decrease in moderation leads to increased resonance absorption and neutron leakage rates. MTCs are typically negative in LWRs, although they become less negative with the addition of a chemical shim, such as soluble boron, because the expansion of the water with an increase in temperature also expels some of the chemical shim. The addition of too much chemical shim can make the MTC positive in an LWR.

Other reactivity-related values of interest often calculated for LWRs are the soluble boron coefficient (SBC) and control rod worth. The SBC, which is only relevant for PWRs, is the ratio of the change of reactivity to the change in boron concentration, often in units of ppm, in the coolant. The SBC is always negative because an increase in boron concentration reduces the thermal utilization factor and decreases reactivity. Control rod worth is equivalent to the change in the multiplication factor when the control rod goes from fully withdrawn to fully inserted.

Control rod worths are useful for calculating the shutdown margin of a reactor, which is defined to be the degree of subcriticality of the core when all control elements are fully inserted. Two caveats to that definition are used for licensing reactors: the shutdown margin must be calculated at ambient conditions, which is the most reactive core state, and with the highest-worth rod in the fully withdrawn position [86]. This definition provides an extra margin of safety when licensing reactors for operation.

2.3.2 Reactivity-Initiated Accidents and Critical Heat Flux

RIAs are a postulated accident scenario in an LWR that primarily takes the form of a control rod ejection in a PWR or a control blade drop in a BWR. The rapid ejection of a control rod inserts a large amount of positive reactivity in the core, which causes a power excursion. The power excursion is turned around by the thermal feedback effect, resulting in a wave-shaped power pulse that drastically increases core temperatures. RIAs can be broken down into low-temperature and high-temperature phases [87]. A depiction of the event in a PWR is provided in Figure 1 [88].

During the low-temperature phase, there is rapid energy deposition into the fuel pellets but on a timescale small enough that heat has not yet transferred to the cladding. Retention of heat in the fuel pellet causes rapid thermal expansion, and the pellet contacts the cladding inner wall. This is the phase that causes PCMI because the fuel pellet expands on a millisecond time scale and contacts the cladding [46]. The contact between the fuel pellet and cladding induces stress in the cladding, which can deform or even burst if the cladding is embrittled [87].

Brown et al. [46] studied RIAs in a PWR that used FeCrAl cladding with a decreased thickness and increased fuel pellet diameter compared with the typical values for Zircaloy and UO_2. It was shown that the pulse width of the RIA power response is narrower, the peak power is greater, and the energy deposition is similar compared with the UO_2-Zircaloy system. The total fuel pellet expansion is similar for the two cases because expansion is a function of energy deposition, but the rate at which fuel expands is greater for the FeCrAl cladding case because this is a function of pulse width and peak power. A higher rate of fuel expansion can lead to a higher strain rate within the cladding, which potentially increases the likelihood of a PCMI failure.

During the high-temperature phase of RIA, high cladding temperature caused by the CHF being exceeded is the dominant cladding failure mechanism [89]. Bubble crowding CHF, also referred to as departure from nucleate boiling (DNB), is the heat flux at which a vapor blanket forms between the liquid flow and the heated surface, and dryout CHF is the point at which the vapor void fraction of two-phase flow becomes so large that the heated surface is no longer in contact with any liquid. In either case, the

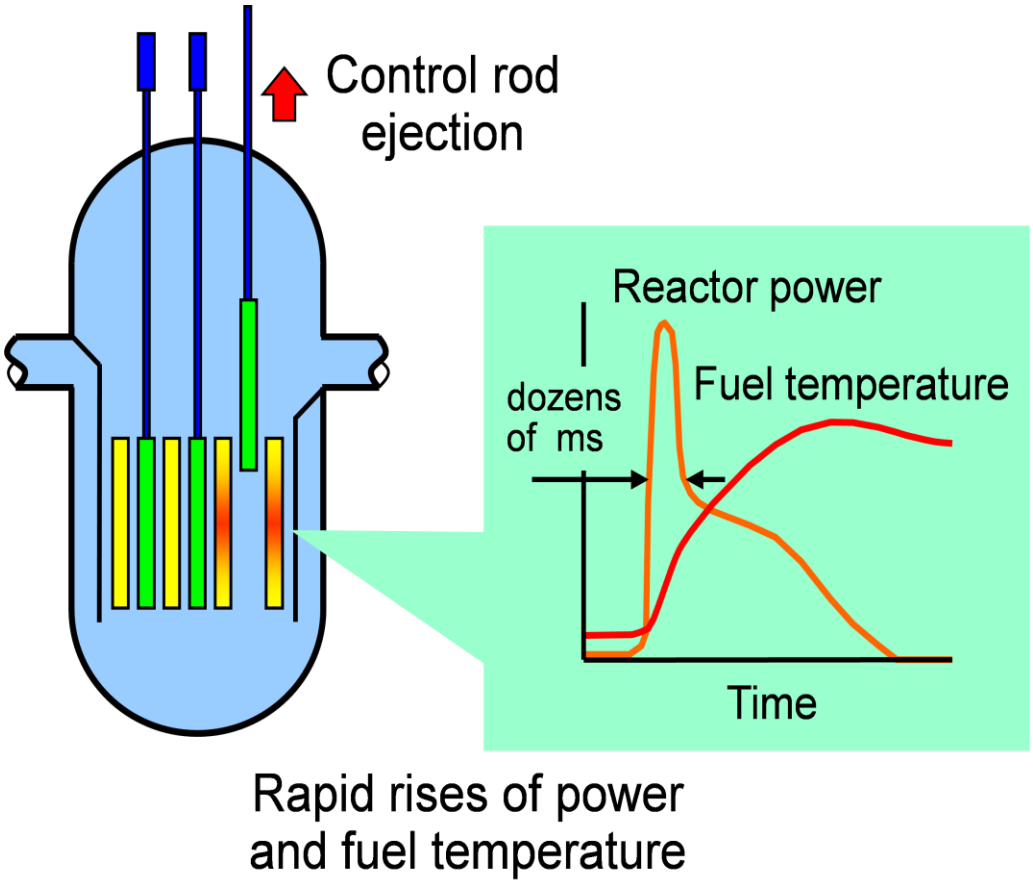

Figure 1: Depiction of a control rod ejection and RIA in a PWR (reproduced from [88])

heat flux from the heated surface to the coolant is drastically reduced due to the poorer heat transfer capabilities of single-phase vapor. The CHF mechanism associated with the rapid increase in heat flux caused by an RIA in a PWR is DNB [90]. Equilibrium quality of the coolant is quickly increased due to the heat flux ramp and forms the vapor blanket that causes a dramatic reduction in heat flux. DNB is directly related to the thermal safety margin of a PWR through the DNB ratio (DNBR). The DNBR is the ratio of the predicted CHF to the actual heat flux in a fuel rod, as given by Equation (3).

$$DNBR = \frac{q''_{CHF}}{q''_{actual}} \tag{3}$$

This ratio is required to be above 1.0, as a DNBR below 1.0 indicates that the CHF has been exceeded and a temperature excursion is expected that could lead to cladding failure.

One of the most widely used methods to predict CHF is the Groeneveld look-up table [91]. CHF is predicted from the look-up table using the local absolute pressure, mass flux, and equilibrium quality of the system. The tables were developed using an internal flow apparatus with stainless steel tubes, and the results were normalized to provide CHF values for tubes with an 8-mm inner diameter. Eight correction factors can be used to modify predicted CHF values based on geometry and various flow conditions. The experiments conducted at UNM [6] were designed to be geometrically representative of the Groeneveld experiments.

Despite the existence of the look-up table and other CHF prediction methods, it continues to be difficult to accurately project the CHF and post-CHF temperatures during transient events, which has warranted continued experimental work on the subject. Hohl et al. performed steady-state and transient pool boiling experiments and showed that the CHF was greater in the heating portion of transient experiments than in steady-state experiments, and the CHF increased as the heating rate increased [92]. Those same experiments showed that the CHF during transient cooling also varied with the cooling rate, and a faster cooling rate led to a lower CHF. Multiple steady-state pool boiling experiments have shown that the CHF under given conditions is the same for heating and

cooling processes [92], [93]. A large number of data have been produced that show a hysteresis in the transient boiling curve between heating and cooling processes [94].

The differences between steady-state and transient CHF have been demonstrated in experiments based on the RIA event. The PATRICIA Experimental Program at the CEA in Grenoble, France performed steady-state and transient CHF experiments by simulating an RIA using a single fuel rod and boundary conditions representative of a PWR at hot zero power (HZP) [95]. The PATRICIA test facility is able to apply a half sinewave power curve using the Joule effect with a Full Width at Half Maximum (FWHM) pulse width of 30 ms, which is within the typical range of HZP RIA pulse widths in PWRs of 25 to 65 ms [96]. The transient PATRICIA experiments produce a cladding heating rate between 2,200 K/s and 4,900 K/s to the single rod assembly. The cladding heating rate in a superprompt PWR RIA can vary, but is typically at least 1000 K/s [97], [98]. Between 201 J/g of cladding and 331 J/g of cladding was injected in each PWR-relevant transient. It was shown that CHF measured during the RIA-like transients was greater than that measured during steady-state experiments by as much as a factor of 2, although the initial conditions were different between the steady-state experiment and some of the transient experiments. The transient runs that had similar boundary conditions to the steady-state experiments had a CHF that was repeatedly 35.5% to 41.9% greater than the steady-state CHF. A similar effect was observed in the UNM experiments, where the transient CHF was 23% greater than the steady-state CHF for FeCrAl [6].

It has been postulated that greater CHF occurs during the heating phase of transients because there is a larger temperature gradient near the heater surface that promotes turbulent convective heat transfer [93]. Witte and Lienhard [94] believe the hysteresis exists because in a heating process, the boiling regime moves from nucleate to film, so the transition regime shows more properties of nucleate boiling and therefore allows better heat transfer. During cooling, the boiling regime moves from film to nucleate, so the transition regime shows more properties of film boiling, and therefore has worse heat transfer. Although there are several theories as to why the enhancement of

CHF during a heating transient occurs, there is no correlation in existence that can quantify this phenomenon.

2.4 Computational Modeling: Review of the State-of-the-Art

Numerous computer modeling tools exist for a wide variety of nuclear applications ranging from radiological protection to severe accident modeling. In this section, the focus will be on the current state-of-the-art in thermal hydraulics, reactor physics, and multiphysics modeling that is used for regulatory licensing purposes. Comparisons are made between tools used by the NRC and the next generation of modeling tools that employ high-fidelity multiphysics methods to increase the accuracy of reactor analyses. The advancement of computer modeling methods is vital to the nuclear industry because more accurate predictions will enhance the safety, efficiency, and economic competitiveness of nuclear power.

2.4.1 Computational Reactor Physics

The 3-D Boltzmann Transport Equation, given by Equation (4) for a fission reactor, describes the movement of neutrons through a system.

$$\frac{1}{v}\frac{\partial\psi(\vec{r},E,\hat{\Omega},t)}{\partial t}+\hat{\Omega}\cdot\vec{\nabla}\psi(\vec{r},E,\hat{\Omega},t)+\Sigma_t\psi(\vec{r},E,\hat{\Omega},t)$$
$$=\int_{4\pi}d\hat{\Omega}\int_0^\infty dE'\Sigma_s(E'\to E,\hat{\Omega}'\to\hat{\Omega})\psi(\vec{r},E,\hat{\Omega},t) \quad (4)$$
$$+\frac{\chi(E)}{4\pi k}\int_{4\pi}d\hat{\Omega}\int_0^\infty dE'\nu(E')\Sigma_f(E')\,\psi(\vec{r},E,\hat{\Omega},t)$$

The first term on the left-hand side of Equation (4) denotes the time rate of change of the angular flux (ψ), which is a function of the phase space defined by position ($\vec{r}$), energy (E), angular direction ($\hat{\Omega}$), and time (t), multiplied by the inverse neutron velocity $\left({}^{1}/_{v}\right)$. The next two terms on the left-hand side of Equation (4) describe neutron losses from the system due to leakage and nuclear reactions, respectively. The nuclear reactions include neutron absorption and neutron scattering out of the phase space of interest, the probability of which is denoted by the macroscopic total cross section (Σ_t). Neutrons coming into the system are described by the two terms on the right-hand side of Equation

(4). The first term on the right-hand side of the equation describes neutrons that are being scattered into the phase space of interest and takes into account the macroscopic scattering cross section (Σ_s). The final term describes the production of neutrons in the system from fission reactions, where $\chi(E)$ is the fission neutron energy probability density function, ν is the number of neutrons produced per fission, k is the neutron multiplication factor, and Σ_f is the macroscopic fission cross section.

Several approximations to the 3-D Boltzmann transport equation have been made to reduce complexity and make the equation more readily solvable. The primary approximation is the diffusion equation, in which isotropic fission and scattering sources are assumed, the angular dependence of the neutron flux is assumed to be negligible, and Fick's Law is used. In the context of reactor physics, Fick's Law states that the current of neutrons, $\vec{J}$, will diffuse through the system based on the negative gradient of neutron flux times the diffusion coefficient, *D*. The diffusion equation is often solved with a multi-group approach, where a "group" refers to each interval in a discretized energy mesh. The steady-state multi-group diffusion equation is given by Equation (5).

$$-\vec{\nabla} \cdot D_g \vec{\nabla} \phi_g + \Sigma_{R,g} \phi_g = \sum_{g'=1}^{g-1} \Sigma_{s,g'g} \phi_{g'} + \frac{1}{k} \chi_g \sum_{g'=1}^{G} \nu_{g'} \Sigma_{f,g'} \phi_{g'} \qquad (5)$$

In Equation (5), the subscript g indicates a group number, where *G* is the total number of groups. Traditionally, group 1 indicates the highest energy group, and the energy decreases as the group number increases. Σ_R indicates the removal cross section, which is the probability of neutron removal from the system through absorption or scattering. The two terms on the right-hand side of Equation (5) describe scattering into the group of interest and neutrons produced by fission into the group of interest, respectively.

Acquiring solutions to the Boltzmann transport or diffusion equations typically requires the use of computational numerical methods, which can be broken down into stochastic or deterministic methods. Monte Carlo is a widely-used stochastic solution method where probability density functions are used to track neutrons and the various possible nuclear reactions. Results from Monte Carlo calculations have an associated

uncertainty, which can be reduced by simulating additional neutron histories and the implementation of variance reduction techniques. The advantages of Monte Carlo are that no approximations need to be made for the problem geometry or the energy dependence of nuclear cross sections. However, the number of neutron histories that must be simulated in order to achieve acceptable uncertainties for complex systems often results in substantial computational cost.

The large cost of Monte Carlo calculations has led to deterministic methods being the preferred numerical method for large-scale reactor physics calculations [99]. Although deterministic methods are able to save on computational cost, they require that the space, energy, and angular domains be discretized into a mesh, which introduces discretization error. There is a trade-off between fine meshes, which reduce discretization error, and coarser meshes, which reduce computational cost. Even when solving the diffusion equation, in which the angular dependence has been integrated out, fine spatial mesh and energy group structures that incur significant computational cost may be required to obtain accurate solutions. This is a challenge especially for full-core calculations in which hundreds of fuel assemblies containing thousands of fuel rods are modeled. The length scale varies from under a cm for a single fuel rod diameter to ~15-20 cm for the side of a fuel assembly to several meters for the diameter of the core. This challenge is further exacerbated by the influence of other physical phenomena, such as thermal hydraulics and mechanics, which have motivated the coupling of multiple modeling tools together that will iteratively pass information back and forth to obtain a single solution. The following sections describe the various procedures that have been developed to address the challenge of accurate computer modeling across various physical scales and phenomena.

2.4.2 The Current Paradigm

Current regulatory practice is to use a two-step approach to perform full-core modeling [100]. The first step is to model single fuel rods, also known as pin-cells, and fuel assemblies using a lattice physics code and 1-D or 2-D transport methods. A fine spatial mesh and up to a few hundred energy groups are used to accurately predict the

neutron flux, reaction rates, and macroscopic cross sections in these relatively small models with infinite boundary conditions. These values are spatially averaged over each material, which includes the fuel, cladding, and moderator in a pin-cell model and may include control blades, channel boxes, or other core structural materials in a fuel assembly model. Then, these cross sections are homogenized, or collapsed, to a few-group structure using Equation (6).

$$\langle \Sigma_g \rangle = \frac{\int_{E_g}^{E_{g-1}} \Sigma(E)\tilde{\phi}(E)\, dE}{\int_{E_g}^{E_{g-1}} \tilde{\phi}(E)\, dE} \tag{6}$$

In Equation (6), $\Sigma(E)$ represents a generic macroscopic cross section and $\langle \Sigma_g \rangle$ represents the group-collapsed cross section to be used in full-core calculations. Equation (6) preserves the total reaction rates in the system by using a weighting function to average the cross section over a range of energies. $\tilde{\phi}(E)$ is used as the weighting function, and is the neutron flux calculated from the lattice physics calculations in the pin-cell and fuel assembly models. The use of the neutron flux from lattice physics calculations as a weighting function for collapsing cross sections is a good estimate of the flux in a larger system due to the regularity of LWRs in which fuel rods are arranged in square lattices and assemblies are loaded in a repetitive pattern.

Oftentimes, more than 200 energy groups are used for lattice physics calculations, and the resulting cross sections are collapsed down to two energy groups. Lattice physics calculations are typically performed for a variety of potential reactor conditions and configurations. These different conditions, known as branches, account for a range of fuel and moderator temperatures, as well as different control rod/blade configurations. Boron concentration is also considered for PWRs, and the void fraction of the two-phase flow is also considered for BWRs. Additionally, lattice physics depletion calculations may be performed to account for changes in cross sections as a function of burnup. All of the resulting collapsed cross sections are organized into a table or other computer-readable format to be used by a diffusion code for full-core calculations. For regulatory activities, the NRC uses the Standardized Computer Analyses for Licensing Evaluation (SCALE) code system [101] developed at ORNL for lattice physics calculations and generating

cross sections. The primary reactor kinetics tool used by the NRC is the Purdue Advanced Reactor Core Simulator (PARCS) [102], which is 3-D nodal diffusion code.

Following the traditional procedure for core analysis, the SCALE framework is used to generate cross sections from highly-discretized pin-cell and assembly models at numerous reactor configurations. SCALE is a framework that employs a number of codes, including the Transport Rigor Implemented with Time-Dependent Operation for Neutronic depletion (TRITON) control module, which can automatically execute a series of codes to perform lattice physics calculations. At the heart of TRITON is the Monte Carlo code KENO and the discrete ordinates code NEWT (New ESC-Based Weighting Transport, where ESC is Extended Step Characteristic), both of which can be used to perform lattice physics calculations and generate few-group cross sections. In addition to KENO and NEWT, the SCALE package also contains the Oak Ridge Isotope Generation (ORIGEN) code, which can be used with the lattice physics codes to perform depletion calculations. The general modeling process is to use TRITON to perform lattice physics calculations using highly-detailed but relatively simple models of fuel assembly lattices and a fine energy mesh structure containing 238 groups. Few-group cross sections (often just two-group) are collapsed from the resulting macroscopic cross sections for a variety of reactor conditions as a function of burnup. The few-group cross sections are then reorganized into a format that is readable by the nodal diffusion code, which for PARCS is the Purdue Macroscopic XS (cross section) Set (PMAXS) format [103].

PARCS reads the PMAXS file to perform diffusion calculations in 3-D. PARCS is able to solve the time-dependent neutron diffusion equation using few-group cross sections, making it a useful tool for analyzing accidents, such as RIAs. To increase the accuracy of reactor physics calculations, PARCS has been coupled to a variety of thermal hydraulics analysis tools in order to account for thermal feedback. The TRAC/RELAP Advanced Computational Engine (TRACE) [104] is a best-estimate reactor systems code with 1-D and 3-D modeling capabilities and is the primary thermal hydraulics code used by the NRC. TRACE is the culmination of development efforts to combine modeling features from the NRC legacy codes TRAC-P, TRAC-B, RAMONA, and the NRC version of the Reactor Excursion and Leak Analysis program (RELAP5) and is used to

analyze large and small break LOCAs and other reactor transients in LWRs. TRACE is able to be directly coupled to PARCS to provide thermal hydraulic feedback to update cross section data.

Another thermal hydraulics tool used by the NRC is PATHS [105], which is specifically used for coupling with PARCS to perform full-core, steady-state depletion calculations for BWRs. PATHS uses several simplifying assumptions, including the use of three differential equations for two-phase flow and an algebraic void-quality equation, in contrast to the six-differential-equation set used by TRACE for the void drift model. PATHS is also capable of simultaneously solving the velocity and pressure field equations [106]. These assumptions and capabilities result in fast run times compared to TRACE, which is useful in full-core analysis of BWRs because each of the more than 700 fuel assemblies in a typical BWR core must be modeled separately for accurate results.

This algorithm for performing full-core calculations typically results in solutions that provide one radial node per fuel assembly. For example, a model of the Edwin I. Hatch Unit 1 reactor was developed by Yarsky et al. [107]. Each of the reactor's 560 fuel assemblies were modeled using one radial node and 24 axial nodes. This nodalization scheme results in the calculated parameters, such as fuel temperature, cladding temperature, and coolant properties, being radially averaged over the array of fuel rods in each fuel assembly. In other words, modeling tools currently used for licensing purposes produce outputs on a fuel assembly scale and do not provide information for individual fuel rods. Although this method has relatively low computational cost, full-core calculations are often conservative and are unable to capture localized phenomena that may have reactor performance or safety implications [108].

2.4.3 Advanced Computational Methods

The continuous advancement of computational capabilities has led to the development of modeling tools that improve upon the current methods used for regulatory purposes in the nuclear industry. The heterogeneous nature of nuclear systems has demanded that modeling tools have high-fidelity multiphysics capabilities that can

capture localized phenomena on the fuel rod scale, rather than on the fuel assembly scale. Examples of local phenomena that may impact reactor performance and safety are grid-to-rod fretting, PCIs, DNB, and the impact of Chalk River Unidentified Deposits (CRUD), including CRUD-induced power shifts (CIPS), and CRUD-induced localized corrosion (CILC) [52]. Further, it has become desirable for these capabilities to be contained within a single framework or environment [109]. Two examples of these multiphysics packages developed by the DOE are the Multiphysics Object Oriented Simulation Environment (MOOSE) framework [110], and CASL VERA. Both MOOSE and VERA have subsidiary codes that have been integrated into the Nuclear Energy Advanced Modeling and Simulation (NEAMS) [111].

The MOOSE framework includes over 30 modules for modeling a wide variety of nuclear and non-nuclear systems. Some of the more commonly used tools within MOOSE are BISON, MARMOT, and Rattlesnake. BISON is a finite elements code that couples heat transfer, fuel mechanics, and species diffusion equations and is primarily used for fuel performance analysis [110], [19]. MARMOT is also a finite elements code but is used to predict microstructure evolution phenomena, such as void formation, grain boundary migration, and thermal conductivity evolution [112]. The code is often coupled to BISON, and an example of this was performed by Gaston et al. [113], who used BISON to predict fuel temperatures and fission rates in a PWR and passed that information to MARMOT, which would then determine the change in thermal conductivity as a function of burnup. The main radiation transport tool within the MOOSE framework is Rattlesnake [114] and is often used with BISON and RELAP-7 [115], the next generation thermal hydraulics system safety analysis code in the RELAP series, in a coupling scheme referred to as MAMMOTH [116].

VERA contains a number of subsidiary codes to perform coupled neutronics, thermal hydraulics, fuel performance, and chemistry analyses [117], [118]. The driving tool in VERA is MPACT, a full-core neutronics code that uses a 2-D/1-D Method of Characteristics (MOC) algorithm [119] [100]. This algorithm uses a 2-D approximation to the 3-D Boltzmann transport equation in the radial direction and a 1-D approximation in the axial direction. These approximations are suitable because heterogeneity in LWRs

occurs primarily in the radial direction. MOC is used to solve the partial differential equations in the 2-D/1-D transport approximations. Cross section libraries ranging from about 50 to 252 energy groups have been developed and optimized for MPACT [120], allowing MPACT to perform its own lattice physics calculations. A coarse-mesh finite-difference (CMFD) acceleration scheme [119] is used to spatially average the flux and cross sections from the finer MOC calculations over each fuel rod. CMFD accelerates the convergence of the problem and provides stability, but still provides solutions on a pin-resolved scale. This methodology provides higher-order and higher-fidelity solutions compared to the two-step method currently used in the nuclear community, although laboratory or industry-scale computer clusters are needed for full-core calculations.

The primary thermal hydraulics tool in VERA is CTF [121], a sub-channel tool that derives from the Coolant Boiling in Rod Arrays – Two Fluid (COBRA-TF) line of codes that were originally developed at the Pacific Northwest National Laboratory and later at Pennsylvania State University, North Carolina State University, and ORNL. CTF considers three separate fluid fields (liquid film, liquid droplets, and vapor) that each have their own set of conservation equations and is capable of modeling crossflow between coolant channels due to pressure differences, turbulent mixing, and void drift. CTF calculates temperature distributions in each fuel rod and sub-channel, which is the coolant flow path between each fuel rod. Coupling between MPACT and CTF is often performed in VERA so that temperatures and densities calculated by CTF are used to update the cross section data used by MPACT to calculate flux and power distributions. Several components of the SCALE system are used in VERA, most specifically the isotopic depletion capabilities of ORIGEN. VERA leverages the MOOSE framework for fuel performance modeling and uses a version of the BISON, while the CRUD chemistry code MAMBA [122] is used to determine the change in thermal resistances due to CRUD build-up, which can lead to CIPS and CILC in nuclear reactors.

The high-fidelity multiphysics methods employed by environments like MOOSE and VERA are on the forefront of computational nuclear modeling and provide numerous benefits over the previous generation of nuclear modeling codes by capturing the various physical phenomena at play. The development of these systems is vital to improving the

safety, efficiency, and economic competitiveness of nuclear power since they are more accurate and better able to predict localized phenomena that may have operational or safety-related consequences [118]. The evaluation of ATF candidates further motivates the use of these novel computational tools, since their advanced features allow them to solve complex problems that the legacy tools cannot.

The multiphysics capabilities of VERA are leveraged for several of the ATF studies in this dissertation. VERA has previously been validated for PWR analysis [123], [124], and is used to study the reactor performance and safety characteristics of ThN-UN and UO_2-Mo fuel concepts in PWRs in CHAPTER 5 and CHAPTER 6, respectively. However, application of VERA to BWR analysis is under development, and this capability has not yet been fully validated against experimental data [125]. An initial assessment of VERA's capability to perform BWR analysis is provided in CHAPTER 4. This assessment is performed by comparing results from models of fuel assemblies from the Peach Bottom Unit 2 reactor developed in VERA and PARCS/PATHS for a select set of progression problems. This set of progression problems is a novel contribution to the literature.

CHAPTER 3
THERMAL HYDRAULIC EVALUATION OF FECRAL CLADDING

3.1 Background

FeCrAl alloys are considered an ATF candidate for the reasons highlighted in Section 2.2.1: they exhibit excellent oxidation resistance and superior mechanical strength in comparison to Zircaloy at elevated temperatures [4], [5]. Pool and flow boiling experiments conducted at UNM have shown that FeCrAl may also have enhanced CHF properties compared with Zircaloy [6], [47]. This is a favorable characteristic that may increase the thermal safety margin in an LWR during normal operating and accident conditions. This work provides an early thermal hydraulic evaluation of FeCrAl cladding by comparing data from flow boiling CHF experiments conducted at UNM to results from computer models of those experiments developed in the DOE version of RELAP5-3D [126] and the CASL version of CTF. There are three main objectives of this work:

1. To compare best-estimate predictions from widely-used system and sub-channel analysis codes to a simple, well-understood CHF test for an ATF material where test repeatability has been demonstrated.
2. To enhance understanding of the sensitivity of these models to the shape of the boiling curve and the thermophysical properties of the test section.
3. To demonstrate an approach to optimize CHF and post-CHF model predictions in these system and sub-channel analysis codes while highlighting differences between how CHF is modeled and what occurs in reality using a single test. It is noted that the best application of this approach would be to apply it to a large dataset consisting of a significant number of tests.

Objectives 2 and 3 both consider three key figures of merit (FoMs) for the model predictions: (1) maximum heat flux (MHF, which is the same as critical heat flux in the system and subchannel analysis codes), (2) integral heat flux (an analog to the energy deposition), and (3) the peak test section temperature (an analog to peak temperature of the cladding in a reactor).

The flow boiling test loop at UNM was used to perform transient and steady-state tests on various materials, including FeCrAl [6]. The purpose of the test loop is to determine the CHF and post-CHF response of different materials under a variety of conditions. This work focuses on the experimental results from tests using power transients representative of those that occur during an RIA applied to test sections made of Inconel 600, Stainless Steel 316 (SS316), and Fe-13Cr-6Al (13% Cr and 6% Al content by weight) and compares them to models of the experiment built in RELAP5-3D and CTF. The power transients performed in the experiment are RIA-like because of their half sinewave shape and pulse width [26], [46]. The approximately 1-second pulse width used in the experiment is longer than the typical superprompt RIA pulse width of 25 to 65 ms and is more similar to the pulse width of a subprompt RIA in a PWR at hot full power (HFP), which can range from 0.4 to 4.5 seconds [96]. The wider pulse width of the power transients performed at UNM leads to a cladding heating rate of 685 K/s, which is below the expected cladding heating rate for a superprompt RIA at HZP of 1000 K/s or more [97], [98].

Because the UNM experiments showed no appreciable change in flow boiling CHF due to increased surface wettability, it is hypothesized that heat transfer coefficients and material thermal properties, including thermal conductivity, k, and volumetric heat capacity, ρC_p, thermal effusivity, e, and thermal diffusivity, α, may have a greater impact on CHF in flow boiling conditions. The work in this chapter describes two sensitivity studies in which the impact of heat transfer coefficients and material thermal properties on CHF and peak test section temperature, which is analogous to the PCT in a nuclear reactor, were determined. FeCrAl was the only material considered in the sensitivity studies. Sensitivity analysis can be a useful step in understanding complex phenomena, such as CHF, and can reduce costs by informing experimental designs and reducing conservatism in new fuel and cladding designs [127], [128]. Liu et al. [89] performed a sensitivity study using a RELAP5-3D model of the Three Mile Island Unit 2 reactor in which multipliers on heat transfer coefficients and the predicted CHF were varied from 0.7 to 1.3 during an RIA transient. They found that the PCT was sensitive to the film boiling heat transfer coefficient and CHF multipliers. The sensitivity of CHF to the

multipliers was not investigated, and the study did not include material heat transfer properties. Chen et al. [129] also showed that PCT was sensitive to the film boiling and CHF multipliers using a one-eighth PWR core model in COBRA-EN, but additionally showed a dependence of PCT upon the nucleate boiling heat transfer coefficient multiplier. Several fuel pellet and cladding material combinations were investigated by Chen et al. [129], and it was shown that PCT and the fuel centerline temperature was sensitive to the materials, and therefore the material properties, used.

Using the uncertainty quantification tool Risk Analysis and Virtual Environment (RAVEN) [130] coupled to the RELAP5-3D model of the UNM test facility, two sensitivity studies were conducted. The first study varied heat transfer coefficient and CHF multipliers, and the second study varied thermal conductivity and volumetric heat capacity to determine the sensitivity of CHF and PCT to these parameters, as well as to thermal effusivity and thermal diffusivity, which are calculated using the sampled k and ρC_p values. The parameter space for each input was chosen based upon experimental data, uncertainties of material properties, and error values within certain heat transfer correlations.

3.2 Experiment and Computer Model Descriptions

3.2.1 Experiment Setup

An in-depth description of the UNM flow boiling apparatus is given by Lee, et al. [6]. The test facility, shown in Figure 2, consists of a tank for steam separation, chiller and cooler condensing system, pump, heater, a section to install a 50.8-cm test specimen, as well as various instrumentation to measure coolant temperature, pressure, and mass flow. Water flows internally throughout the system with an uncertainty in flow velocity of ± 2% and inlet temperature uncertainty of ± 0.2 °C [6]. The test sections were thermally insulated on the outside surface. A DC power supply was used to apply voltage through copper terminals to the heated length of the test specimens, which were located 25.4 cm up the specimens' lengths to ensure flow was fully developed before being heated. In the transient experiments, a K-type thermocouple was used to measure the temperature of the

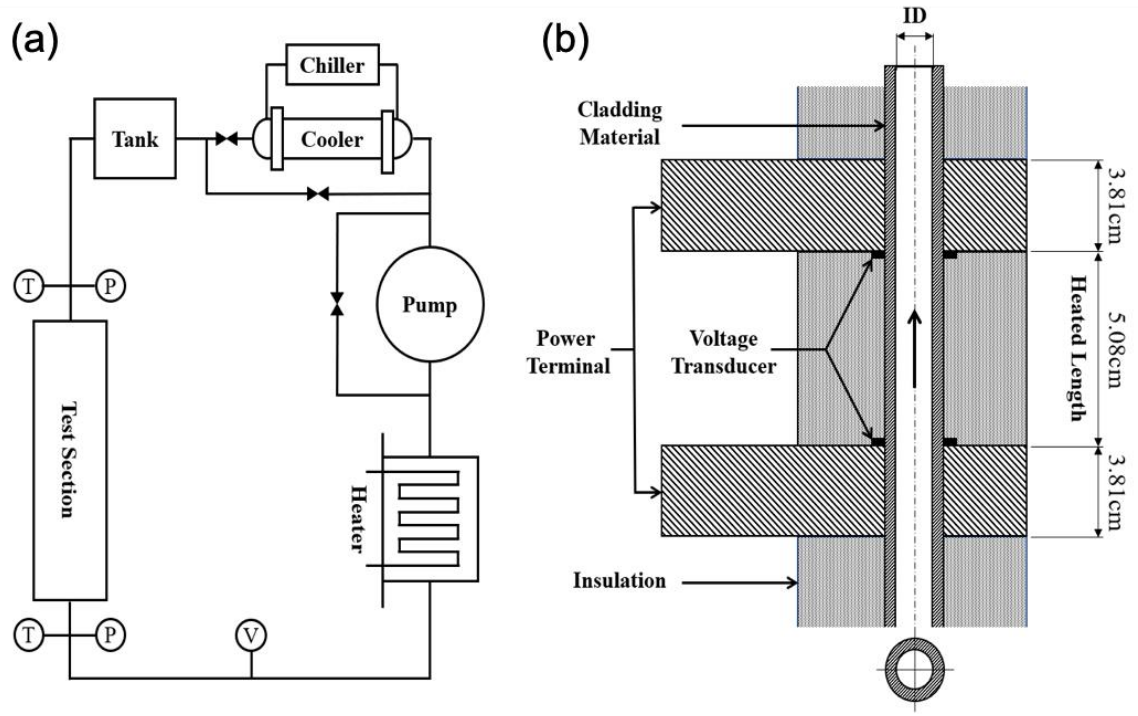

Figure 2: (a) UNM Flow boiling loop schematic (b) cross-sectional view of the test section [6]

tubes' outer surfaces and was located at the axial center of the heated lengths. In the steady-state experiments, the thermocouple was located near the top of the heated length. The thermocouples were attached to the test sections using ~3-mm thick high-temperature silica tape. To prevent electrical interference between the current and voltage applied to the test specimen and the thermocouple, the outer surface of each specimen was coated with a less than 0.5-mm thick layer of silicon. Thermocouple wires were ungrounded, unsheathed, and 0.05 mm in diameter, so thermal lag and the fin effect were assumed to be negligible. A 50 Hz response rate was used to prevent response error from thermal mass. Uncertainty of the temperature measurements under constant flow and zero power is ± 0.1ºC, and is expected to remain small at the temperatures at which DNB was recorded.

Heat flux through the tubes and the tube inner surface temperature was calculated using the measured surface temperature, measured voltage drop across the heated length, and measured current through the copper terminals to solve the transient conduction equation with an implicit finite difference method. CHF was determined in the experiments by finding the point at which the outside surface temperature rate of change with respect to time dramatically increased, indicating the formation of a vapor layer and the start of the post-CHF temperature excursion.

Specific experiments were conducted to quantify the impact of the thermocouple location on the potential uncertainty in CHF prediction. Measurements were performed with transient power pulses using 5 different thermocouples arranged axially at 5 mm intervals from the top to the center of the test section. The experiment results indicated less than 3.3% difference between values at different test section locations [6]. In addition, multiple measurements of CHF were made with multiple samples to ensure the repeatability of the experiments. For FeCrAl, 10 measurements were made with one sample and 3 measurements were made with an independent sample. The average of the measurements was 2,736 $\mathrm{kW/m^2}$ with a standard deviation of 213 $\mathrm{kW/m^2}$, approximately 8%. The transient experiments analyzed in this paper used Inconel 600, SS316, and FeCrAl alloy as the test section materials. Table 1 lists the experimental parameters for each material.

Table 1: Experimental parameters for all materials

	Inconel 600	SS316	FeCrAl
Inner Diameter (cm)	0.8509	0.8763	0.8763
Outer Diameter (cm)	0.9525	0.9525	0.9525
Total Length (cm)	50.8	50.8	50.8
Entrance Length (cm)	25.4	25.4	25.4
Heated Length (cm)	5.08	10.16	5.08
Peak Power (kW)	2.5	8.8	8.1
Pressure (absolute, kPa)	84	84	84
Mass Flux (kg/m^2-s)	300	300	300
Inlet Equilibrium Quality	-0.0089	-0.0827	-0.0089
Inlet Coolant Temperature (°C)	90	50	90
Degree of Subcooling (°C)	4.8	44.8	4.8

3.2.2 CTF and RELAP5-3D Model Descriptions

The RELAP5-3D model is comprised of a time-dependent inlet volume connected to a vertical pipe using a time-dependent junction, which is then connected to a sink time--dependent volume using a single junction. A heat structure is attached to the pipe to provide the power transient. A nodalization diagram of the RELAP5 model is shown in Figure 3. The tube dimensions listed in Table 1 were replicated in the models. Only the heated lengths of the test sections were modeled in RELAP5-3D because the heat transfer packages within the codes always assume fully developed, steady flow [126]. CTF does not assume fully developed flow, so the full 50.8 cm of the test sections were modeled as a tube with a single, internal sub-channel. The test sections were thermally insulated on the outer surface in both RELAP5-3D and CTF. Mesh and time sensitivity studies were performed in both computational tools to ensure the models were stable. Models with up to 100 axial nodes were tested, and it was found that 50 axial nodes were sufficient for model stability in both RELAP5 and CTF. The heat structure in RELAP5 also had 50 nodes. In RELAP5-3D, a minimum timestep of $1x10^{-8}$ seconds was used, and in CTF, a minimum timestep of $1x10^{-6}$ seconds was found to be sufficient. Both RELAP and CTF automatically ensure that the maximum timestep used is below the Courant limit, and in practice, neither code used a timestep larger than $5x10^{-5}$ seconds for any model. UNM provided the transient power pulse data, which was applied to the appropriate nodes in each model. The pressure, mass flux, and temperature of the coolant listed in Table 1 were used as boundary conditions in the models. The Groeneveld look-up table was used as the CHF prediction method in all models, and all results presented are from the axial center of the heated length to match the experiment.

3.3 Results

3.3.1 UNM Experimental Results

The heat flux and surface temperature results from the experiments conducted at UNM are shown in Figure 4 for Inconel, SS316, and FeCrAl. Input power converted to MW/m^2 is also shown in Figure 4. CHF was reached in all cases, which is indicated by

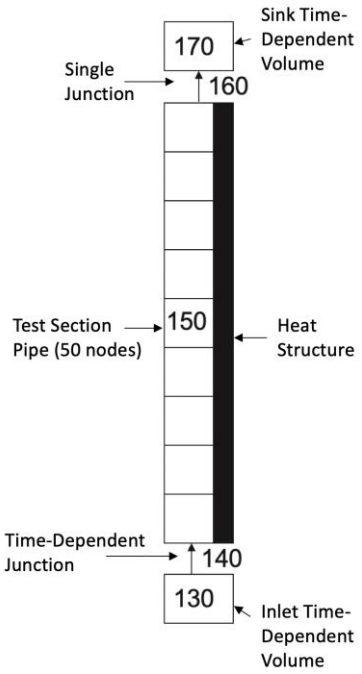

Figure 3: Nodalization diagram of RELAP5-3D model

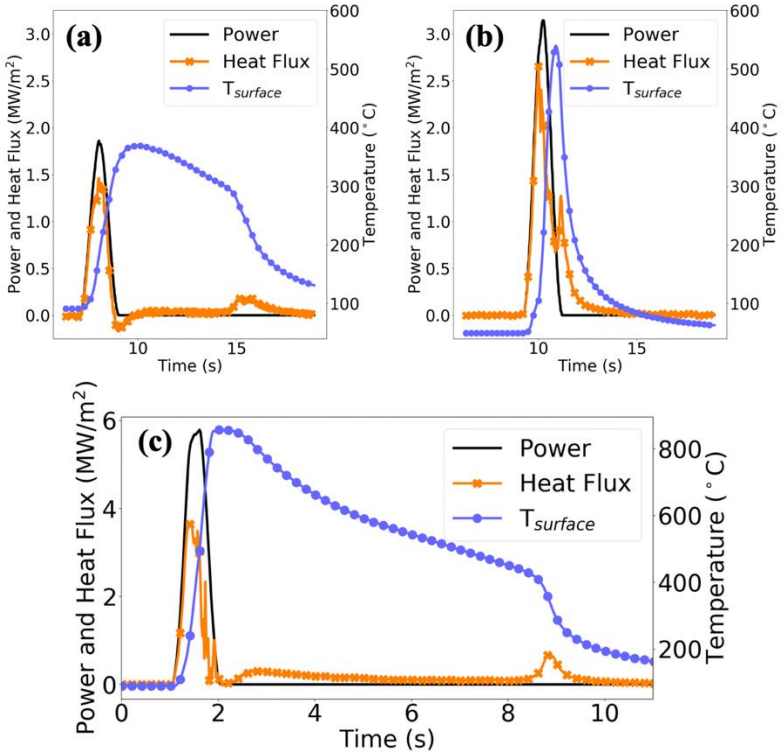

Figure 4: Experimental results for (a) Inconel, (b) SS316 and (c) FeCrAl

the peak of the heat flux curves being lower than the peak of the applied power curves, as well as by the rewetting heat flux spikes after the transient. The occurrence of DNB leads to the sharp reduction in heat flux and the overshoot in tube surface temperature for all three materials. The slightly negative heat flux in Figure 4(a) after the test was complete is due to axial conduction of heat out of the test section. In all cases, rewetting occurs when liquid water recontacts the heated surface after CHF is reached and causes the heat flux to rise again. This phenomenon allows for the tube surface temperatures to approach the initial temperature after the power transient has ended. The greater degree of subcooling in the SS316 case caused the tube temperature to return to the initial temperature much faster than in the Inconel and FeCrAl cases. Based on the test section geometries, material densities, and integral of the power curves, the energy deposition in each sample per gram of cladding is 100.7 J/g, 240.6 J/g, and 270.6 J/g for Inconel, SS316, and FeCrAl, respectively. The energy deposition in the SS316 and FeCrAl samples is within the range of energy deposition achieved in the PATRICIA PWR transient experiments of 201 to 331 J/g of cladding [95].

3.3.2 Code-to-Experiment Comparisons

Figure 5 shows the heat flux predicted by RELAP5-3D and CTF compared to the heat flux calculated in the experiments for Inconel, SS316, and FeCrAl. Results from both codes show that CHF was exceeded in all three cases. In the Inconel 600 case, RELAP5-3D and CTF overpredicted the CHF point relative to the experiment. Rewetting occurred in the CTF model before any post-CHF effects were observed, but CTF output files confirm that CHF was reached and post-CHF heat transfer regimes were briefly entered. CHF was underpredicted by the simulations in the SS316 case, and even more so in the FeCrAl case. In these cases, only RELAP5-3D shows rewetting behavior that is somewhat representative of the experimental rewetting behavior. The tube outer surface temperatures measured in the experiment and predicted by CTF and RELAP5-3D are shown in Figure 6 for all three materials. Because CHF was overpredicted by the codes in the Inconel 600 case, the tube temperature was underpredicted relative to the experimental measurements. The underprediction of CHF in the SS316 and FeCrAl cases

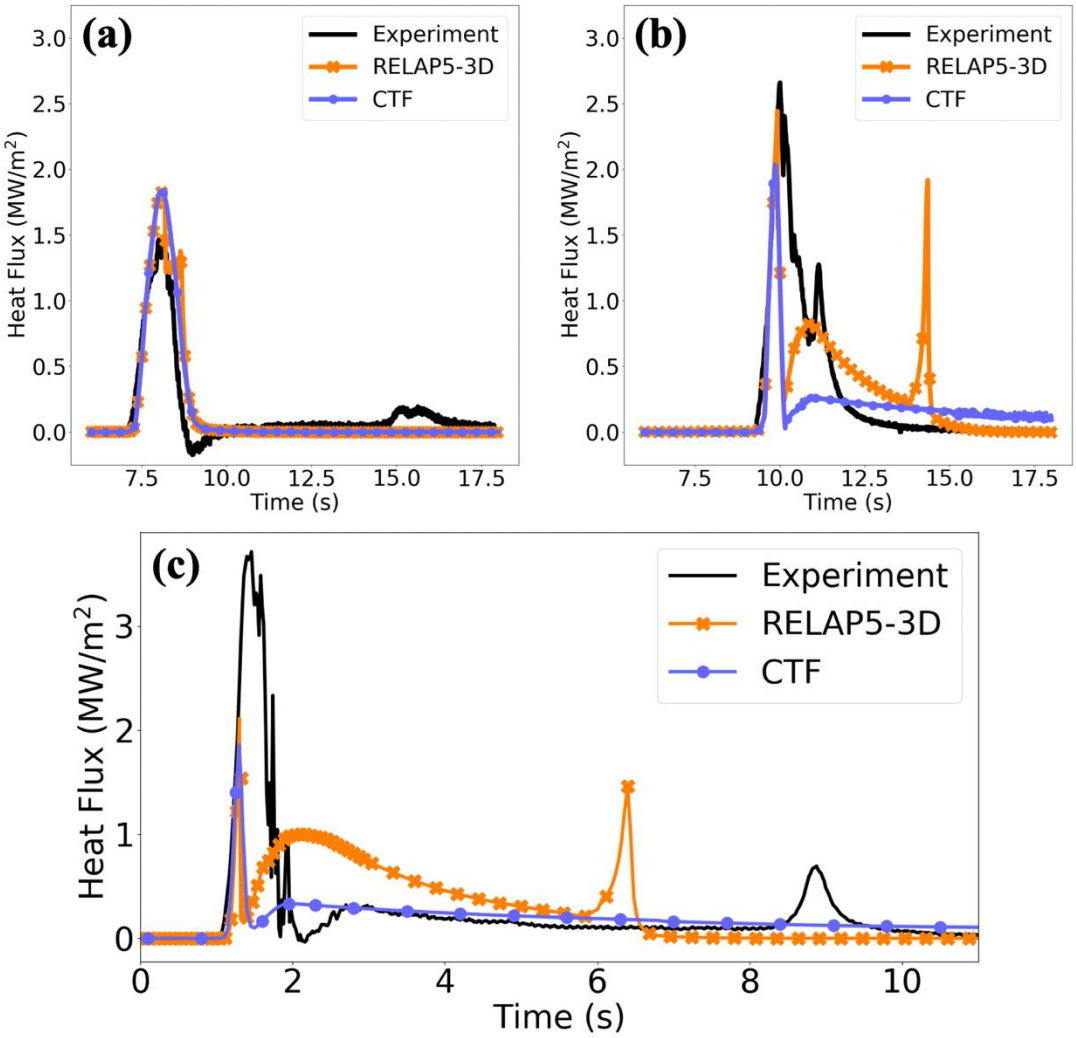

Figure 5: Comparison of experimental and simulated heat flux for (a) Inconel, (b) SS316 and (c) FeCrAl

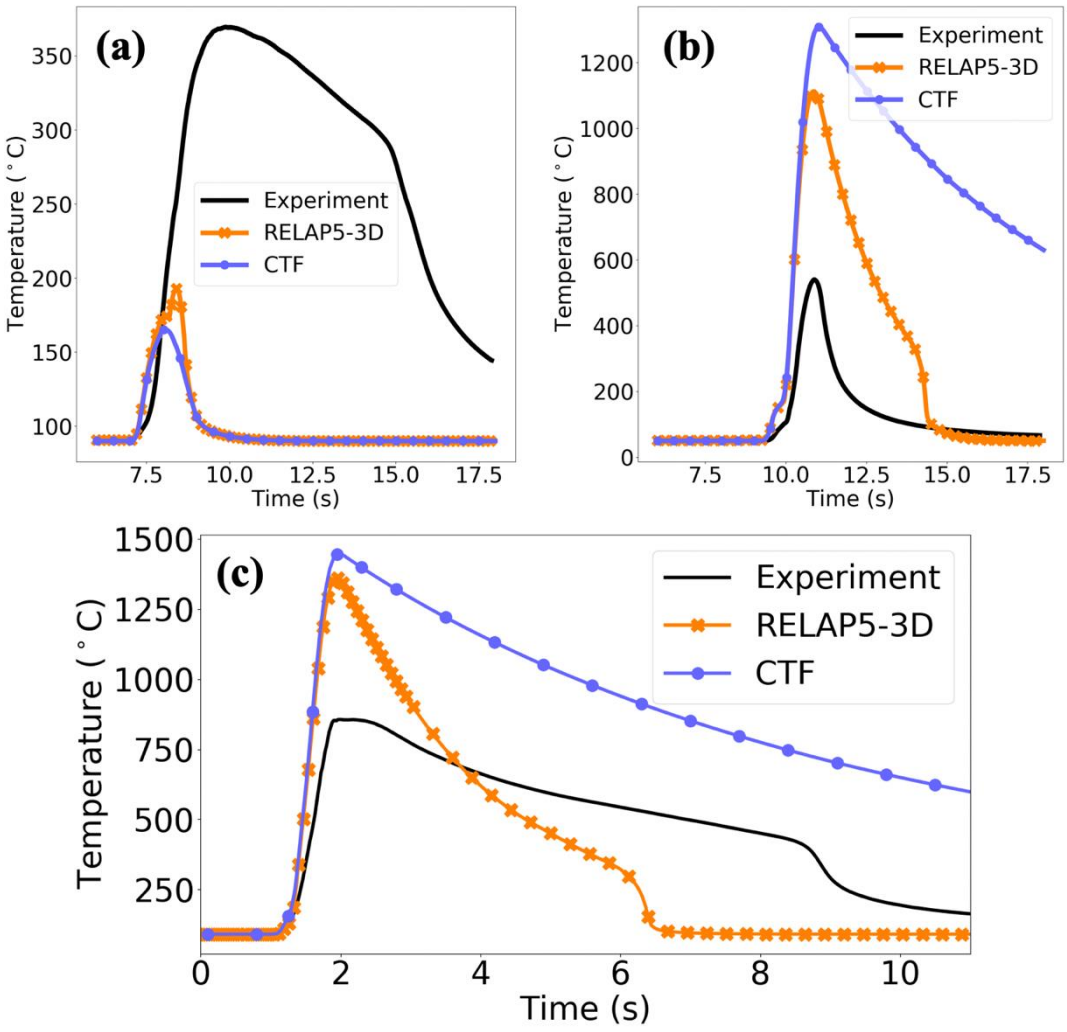

Figure 6: Comparison of experimental and simulated tube outer surface temperatures for (a) Inconel, (b) SS316 and (c) FeCrAl

led to an overshoot in tube surface temperature predictions. In the FeCrAl case, the temperatures calculated by RELAP5-3D and CTF approach the melting point of most FeCrAl alloys, which is approximately 1500°C [131].

Table 2 quantifies the percent error of the simulated predictions relative to the experimental values using the MHF and PCT as the two FoMs. Relative error calculations are performed with temperatures converted to Kelvin. Note that the MHF and the CHF were not necessarily equivalent in the experimental results, but typically were in the simulated results. Further discussion on the separation of MHF and CHF is provided in Section 3.5 of this chapter. In the Inconel case, the codes overpredicted the MHF by approximately 25%, leading to an underprediction of PCT by 27.5% to 31.8%. RELAP5-3D and CTF underpredicted the MHF in the SS316 case by 8.16% and 20.0%, respectively, causing both codes to overpredict the PCT by 70% to nearly 100%. The MHF was underpredicted by the codes by approximately 50% in the FeCrAl case, causing an approximately 45% to 52% overprediction in the PCT.

As were shown in Figure 5 and Figure 6, CTF and RELAP5-3D predicted different CHF and temperatures than the experiments and also predicting CHF and temperatures different from each other. It is worth noting that the differences in cladding temperature predictions between CTF and RELAP5 for an RIA-like event are not uncommon, as demonstrated by predictions of cladding temperature for the nuclear safety research reactor (NSRR) VA-1 experiment using a variety of computer modeling tools [132]. Figure 7 shows the CHF predictions within each code as a function of time. Note that RELAP defaults to a CHF of 0.0 when no power source is applied. Despite both codes using the 2006 Groeneveld look-up table, the predictions made by RELAP5-3D and CTF are clearly different from each other.

Because the Groeneveld look-up table is a function of absolute pressure, mass flux, and equilibrium quality, differences in CHF predictions by RELAP5-3D and CTF may be explained by differences in calculations for these hydrodynamic parameters. Figure 8 shows the simulated predictions for these hydrodynamic parameters for the FeCrAl case only. Also included in Figure 8 are the predictions for vapor void fraction, which, while not used in the look-up table, is a relevant parameter to CHF and typically

Table 2: Relative error between the RELAP5 and CTF results to the experimental values

	MHF (MW/m^2)	MHF Error (%)	PCT (°C)	PCT Error (%)
		Inconel		
Experiment	1.463	-	369.5	-
RELAP5-3D	1.798	22.9	192.8	-27.5
CTF	1.828	25.0	165.2	-31.8
		SS316		
Experiment	2.659	-	539.8	-
RELAP5-3D	2.442	-8.16	1111.7	70.3
CTF	2.128	-20.0	1336.6	98.0
		FeCrAl		
Experiment	3.713	-	856.2	-
RELAP5-3D	2.110	-43.2	1360.9	44.7
CTF	1.857	-50.0	1447.3	52.3

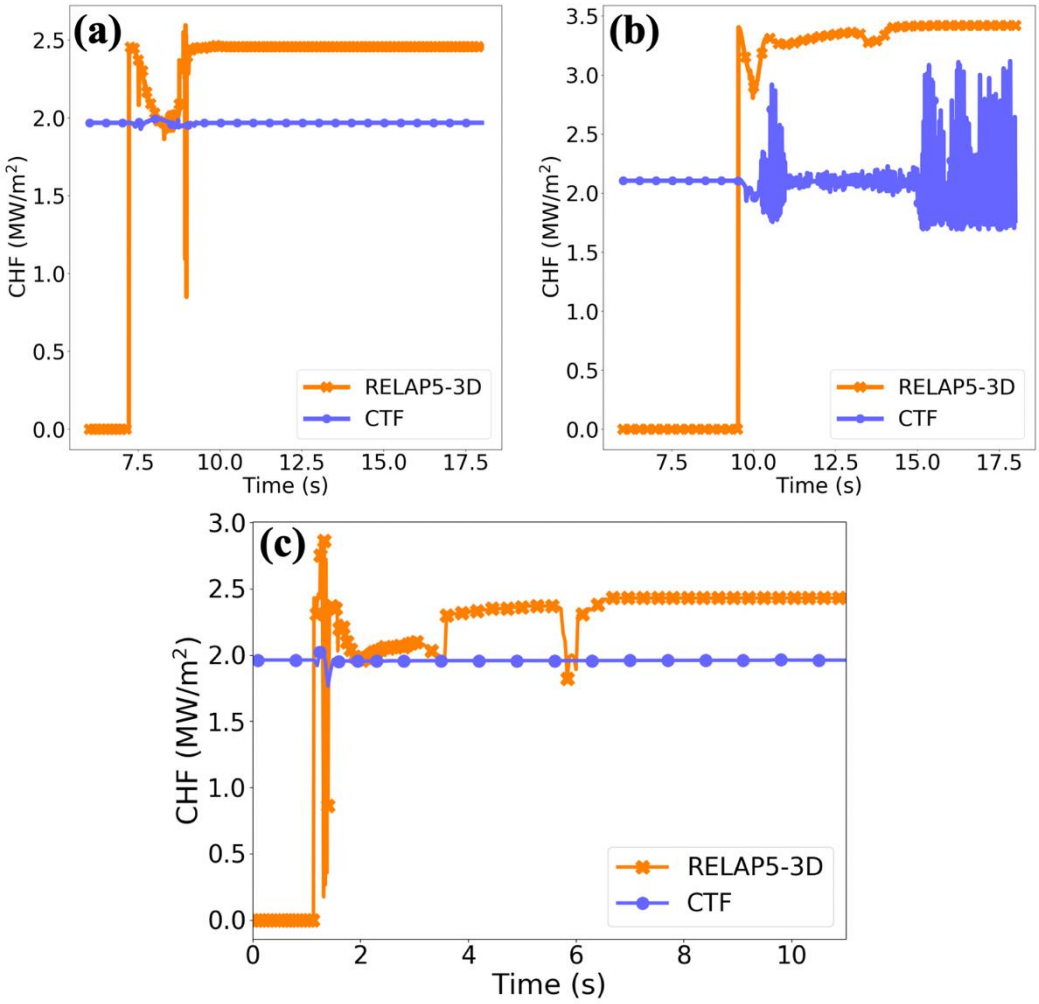

Figure 7: CHF predictions by RELAP5-3D and CTF using the Groeneveld look-up table for (a) Inconel, (b) SS316 and (c) FeCrAl

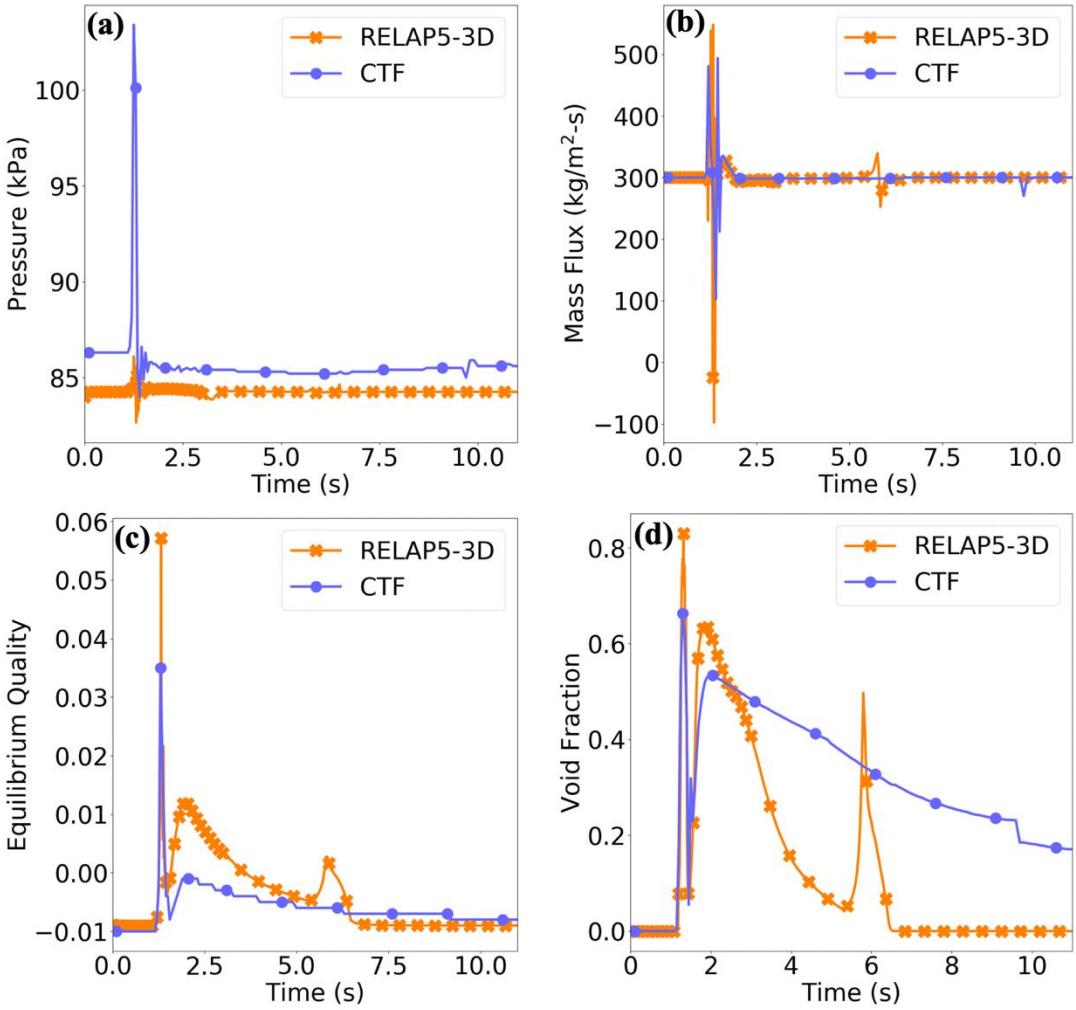

Figure 8: RELAP5-3D and CTF predictions for (a) pressure, (b) mass flux, (c) equilibrium quality and (d) vapor void fraction for the FeCrAl case

follows a similar trend as equilibrium quality. The hydrodynamic predictions between the two codes differ significantly from each other, which would then lead to differences in CHF prediction using the Groeneveld look-up table. CTF predicts a much larger spike in pressure during the power transient, while RELAP5-3D shows larger oscillations in mass flux and even shows the flow rate going negative. This is because the two infinite volumes in the model maintain the initial conditions throughout the transient, so the conservation of mass and momentum leads to large oscillations in mass flux.

Another source of error is that the lowest pressure in the Groeneveld look-up table is 100 kPa absolute, and RELAP5-3D and CTF extrapolate differently to predict CHF at 84 kPa. The 2006 look-up table is 15 pressure values by 21 mass flux values by 23 equilibrium quality values; CTF duplicates the outer boundaries of the table to create a 17-by-23-by-25 matrix of values so that any parameter outside of the table limits are always extrapolated as constant values. RELAP5-3D uses a correction factor based on the ratio of water properties at the pressure of interest to water properties at 100 kPa, and then multiplies this correction factor by the CHF predicted at 100 kPa.

3.4 Sensitivity and Uncertainty Analysis of FeCrAl Heat Transfer Coefficients and Material Properties

Two sensitivity studies were performed using the RELAP5-3D FeCrAl model and RAVEN to elucidate the predicted impact of heat transfer coefficients and material thermal properties on CHF and PCT. The motivation behind the sensitivity studies is to determine if uncertainties in heat transfer correlations and material thermophysical properties can help explain the discrepancies between the experimental data and computer model predictions, as well as the differences in CHF for different materials. Both sensitivity studies also show the impact of the CHF multiplier, which is a linear multiplier that is applied to the CHF value predicted using the Groeneveld look-up tables. While the impact of a CHF multiplier may seem obvious, it is included in these studies as a means to reflect the enhancement of CHF that occurs during transient heating processes. The magnitude of the CHF enhancement is dependent on the heating rate used, although no correlation exists to predict the CHF enhancement caused by a given heating

rate. Two sensitivity studies were performed because a separate effects relationship between the input parameters and FoMs, CHF and PCT, was desired. Uniformly-distributed, discrete parameters were used in both sensitivity studies to ensure the parameter space of interest was covered while also not assuming any prior knowledge of how each parameter is distributed. This is an initial study that is intended to be informative, and the results presented here could be used to inform future parametric studies. Note that the CHF and MHF are always equivalent in the RELAP5-3D FeCrAl models.

3.4.1 Sensitivity Case 1: Heat Transfer Coefficient and the CHF Multiplier

RELAP5-3D heat structure input allows for the use of multipliers on heat transfer coefficients and CHF predicted by their respective correlations. In the base model, it was found that the flow regimes entered during the transient are laminar forced convection, turbulent forced convection, nucleate boiling, transition boiling, and film boiling. RAVEN was used to vary multipliers on the heat transfer coefficients for these flow regimes, as well as the CHF value predicted by the Groeneveld look-up table.

The multiplier values over which the sensitivity study was performed were chosen in several ways. Laminar and turbulent forced convection regimes were only entered before and after the power transient, and it was not expected that these would have much impact on CHF. Therefore, the multipliers were arbitrarily varied from 0.7 to 1.3 to confirm this expectation. It was shown in the UNM experiments that the nucleate boiling heat transfer coefficient for FeCrAl could be as much as double the value for Zircaloy [6], so the nucleate boiling heat transfer coefficient multiplier was varied from 1.0 to 2.0 to determine if this effect could have an impact on CHF. The film boiling heat transfer coefficient measured in the experiment was approximately 1/3 of the value predicted in the RELAP5-3D base model, so the film boiling heat transfer coefficient multiplier was varied from 0.3 to 1.0. The Chen-Sundaram-Ozkaynak correlation [133] is used to predict the transition boiling heat transfer coefficient, and, while the average deviation of the correlation from experimental data is 16%, some data points vary from experimental data by much more than this. For this reason, the transition boiling heat transfer coefficient

multiplier was varied from 1.0 to 2.0. The CHF multiplier was ranged from 1.0 to 2.0, which was the maximum CHF enhancement observed over the steady state value in the RIA transient experiments by Bessiron [95]. Regardless of the range of values tested, the goal of the study was to determine the overall dependence of CHF and PCT on these heat transfer coefficients.

In total, 13,608 combinations of heat transfer coefficients and CHF multipliers were tested. Figure 9 shows CHF as a function of each multiplier. All 13,608 data points are shown in each subplot of Figure 9, and a linear fit to the data is also plotted to show how CHF depends on each multiplier. As shown in the figure, CHF somewhat depends on the transition boiling heat transfer coefficient and strongly depends on the CHF multiplier. The impact of the transition boiling heat transfer coefficient multiplier is a result of CHF and the transition boiling regime being reached elsewhere in the tube before it is reached at the center node (recall that all presented results are from the center node of the test section). The combination of enhanced transition boiling heat transfer and CHF being reached elsewhere before the center node leads to enhanced heat transfer throughout the entire tube relative to the base model. The enhanced heat transfer delays DNB at the center node and increases the CHF. Figure 10 shows the sensitivity of PCT to each of the heat transfer coefficient and CHF multipliers.

The PCT decreased as the transition and film boiling heat transition coefficient and CHF multiplier were increased. This occurs because transition and film boiling are the flow regimes that occur post-CHF, so increased heat transfer during this period would decrease the maximum temperature reached. Increasing the CHF multiplier would also lead to a decrease in PCT because more heat is transferred out of the tube before the CHF is reached, so the post-CHF temperature excursion is less severe.

3.4.2 Sensitivity Case 2: FeCrAl Thermophysical Properties

For this case, several thermophysical properties of FeCrAl were varied, including volumetric heat capacity and thermal conductivity, within the uncertainty ranges of those properties. The sensitivity of CHF to thermal effusivity and thermal diffusivity was also determined since they are functions of volumetric heat capacity and thermal conductivity.

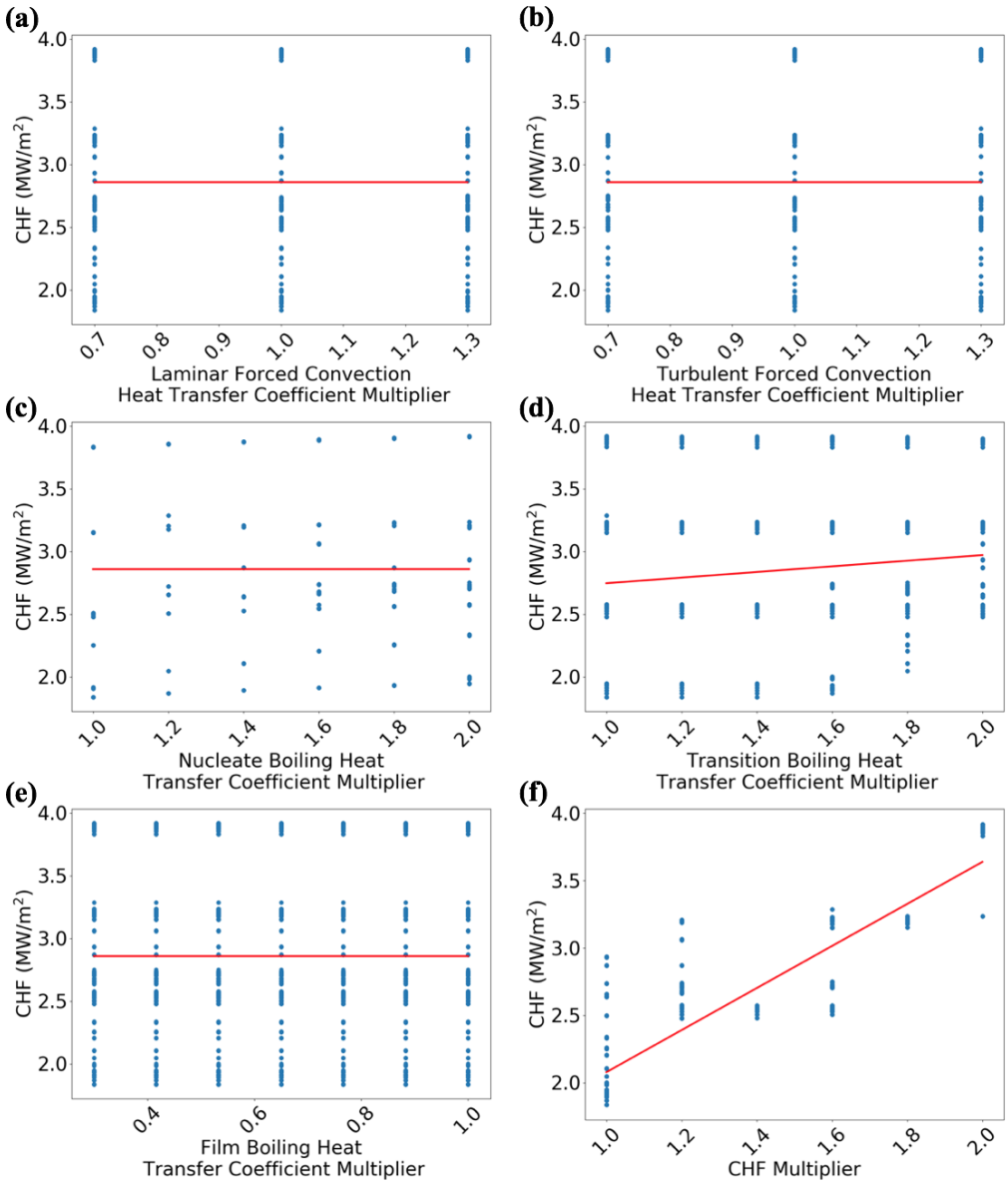

Figure 9: Sensitivity of CHF to heat transfer coefficient and CHF multipliers

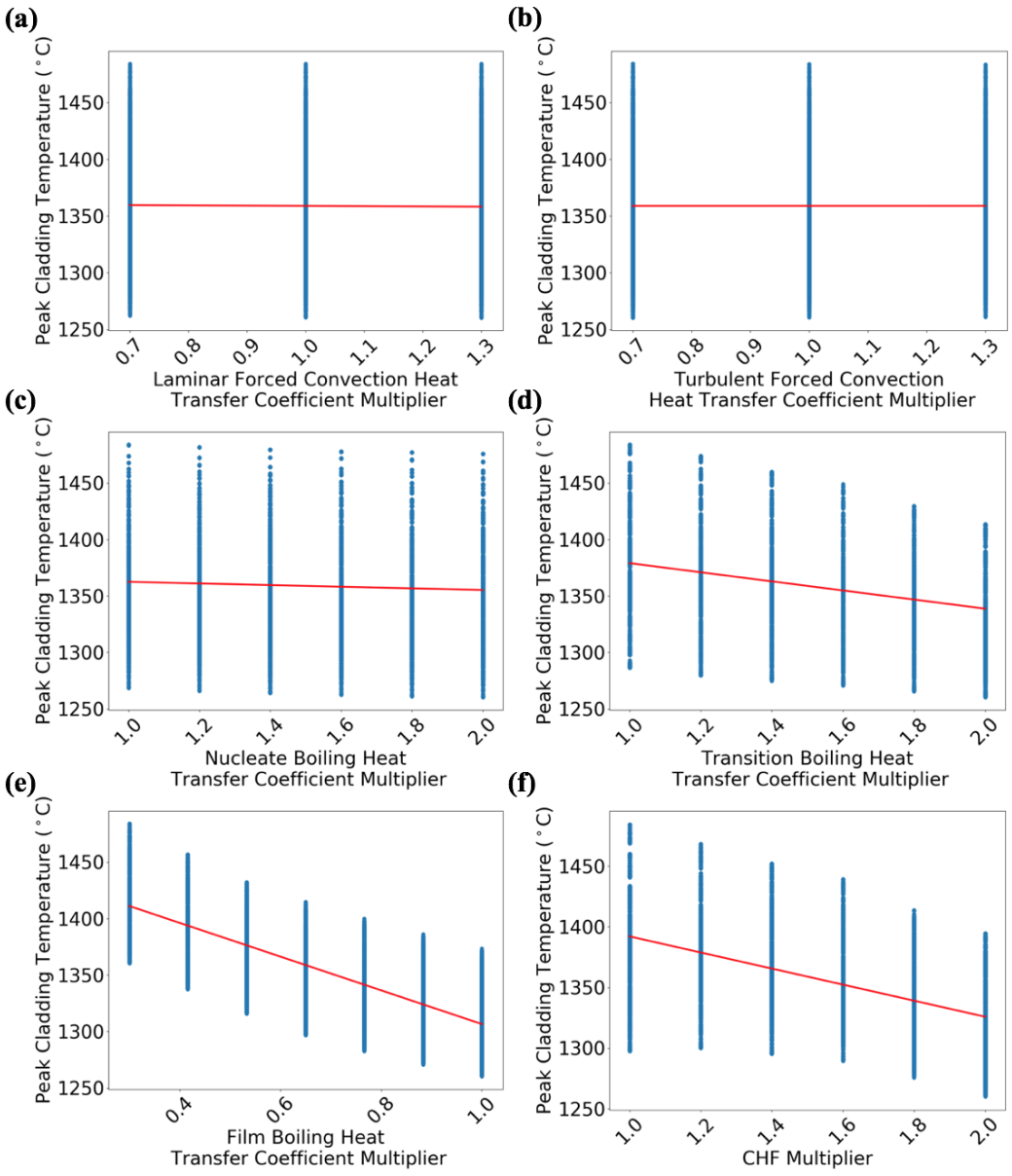

Figure 10: Sensitivity of PCT to heat transfer coefficient and CHF multipliers

Variation of the CHF multiplier is again included to reflect the enhancement in CHF caused by a transient heating process and to ensure that the experimental CHF is reached. A total of 4,275 combinations were explored to help understand the sensitivities. In this case, a main effects technique was used in which the impact of a single input is shown by averaging the output across all other input variables [134].

The thermal conductivity and specific heat capacity of FeCrAl were obtained from a handbook on FeCrAl properties published by ORNL [5]. The theoretical density limits of Fe-13Cr-6Al using Equations (7) and (8), where x_i is the weight percentage of each component in an alloy and ρ_i is the density of each component in an alloy, are 6.98 g/cm^3 and 7.47 g/cm^3, respectively.

$$\rho = \frac{1}{\sum x_i/\rho_i} \tag{7}$$

$$\rho = \sum x_i \rho_i \tag{8}$$

These theoretical density values were used as the limits of the density in the sensitivity study, with the average of the two limits being 7.225 g/cm^3. Kanthal reports the density of several FeCrAl alloys with similar chemical compositions to Fe-13Cr-6Al to be approximately 7.20 to 7.30 g/cm^3 [135], confirming these limits. Thermal conductivity and specific heat capacity limits were based on the uncertainties of measurements reported in the FeCrAl handbook [5]. The sensitivity study limits on volumetric heat capacity, which is the product of density and specific heat capacity, is then the product of the lower and upper limits of these two parameters.

Thermal effusivity, e, and thermal diffusivity, α, are calculated from thermal conductivity and volumetric heat capacity, as shown in Equations (9) and (10). Thermal conductivity, density, and specific heat capacity are sampled in this study, and thermal effusivity and diffusivity are calculated at each sampled combination of k, ρ, and C_p.

$$e = \sqrt{k\rho C_p} \tag{9}$$

$$\alpha = \frac{k}{\rho C_p} \tag{10}$$

Figure 11 shows CHF as functions of the CHF multiplier, thermal conductivity, volumetric heat capacity, thermal effusivity, and thermal diffusivity, respectively, and shows that CHF is sensitive to all of the tested parameters and increases with each of them except for the volumetric heat capacity. The sensitivity of PCT is shown in Figure 12. From the figure, PCT decreases as the volumetric heat capacity increases, which also causes a decrease in PCT as thermal effusivity increases, but an increase in PCT as thermal diffusivity increases. An increase in the CHF multiplier also led to a decrease in PCT, while varying thermal conductivity appeared to have little impact on PCT.

3.4.3 Best Match Parameters

Using the results from the sensitivity studies, the RELAP5-3D simulations using FeCrAl alloy that best matched the experimental results were able to be determined using three FoMs. The MHF and PCT were again used as FoMs, as was the total integral heat flux deposited into the tube. The integral heat flux was used as an analog to represent the total energy deposited in the test section. A RELAP5 run that had the minimum relative error from the experiment was determined for each FoM. Additionally, a run was identified that had the minimum root-mean-square error (RMSE) for all three FoMs in order to find the input parameters that gave the best overall match to the experimental results. Several extra criteria were used in determining the best overall match to the experiment:

1. The relative MHF error could not exceed 3.5%, which is within the repeatability range of the experimental MHF obtained by UNM [6].
2. The magnitude of the rewetting heat flux spike occurring after the power transient could not exceed the heat flux during the power transient, which would not be consistent with physical expectations.
3. PCT could not exceed 1500°C, which is the approximate melting temperature of FeCrAl [131]. Temperatures above 1500°C are physically incorrect since the test section did not melt in any of the 13 FeCrAl tests that were conducted at UNM.

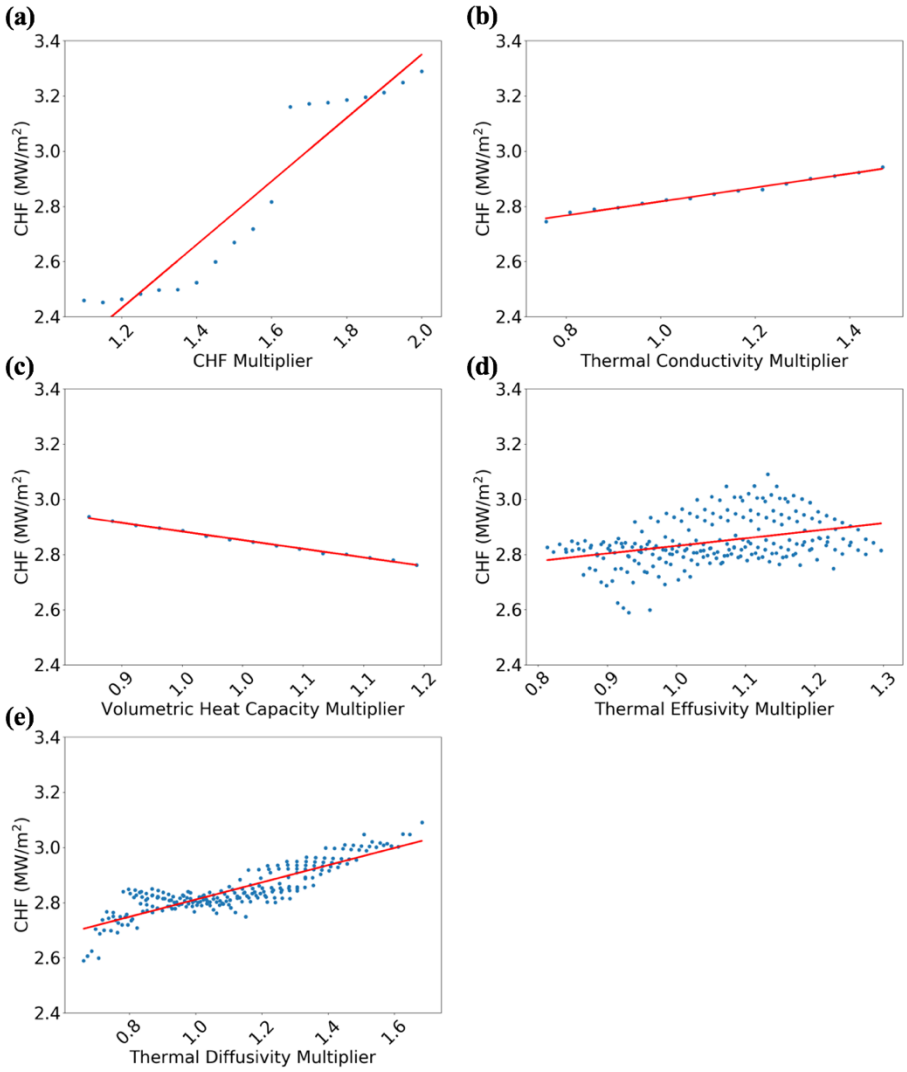

Figure 11: Sensitivity of CHF to (a) the CHF, (b) thermal conductivity, (c) volumetric heat capacity, (d) thermal effusivity and (e) thermal diffusivity multipliers

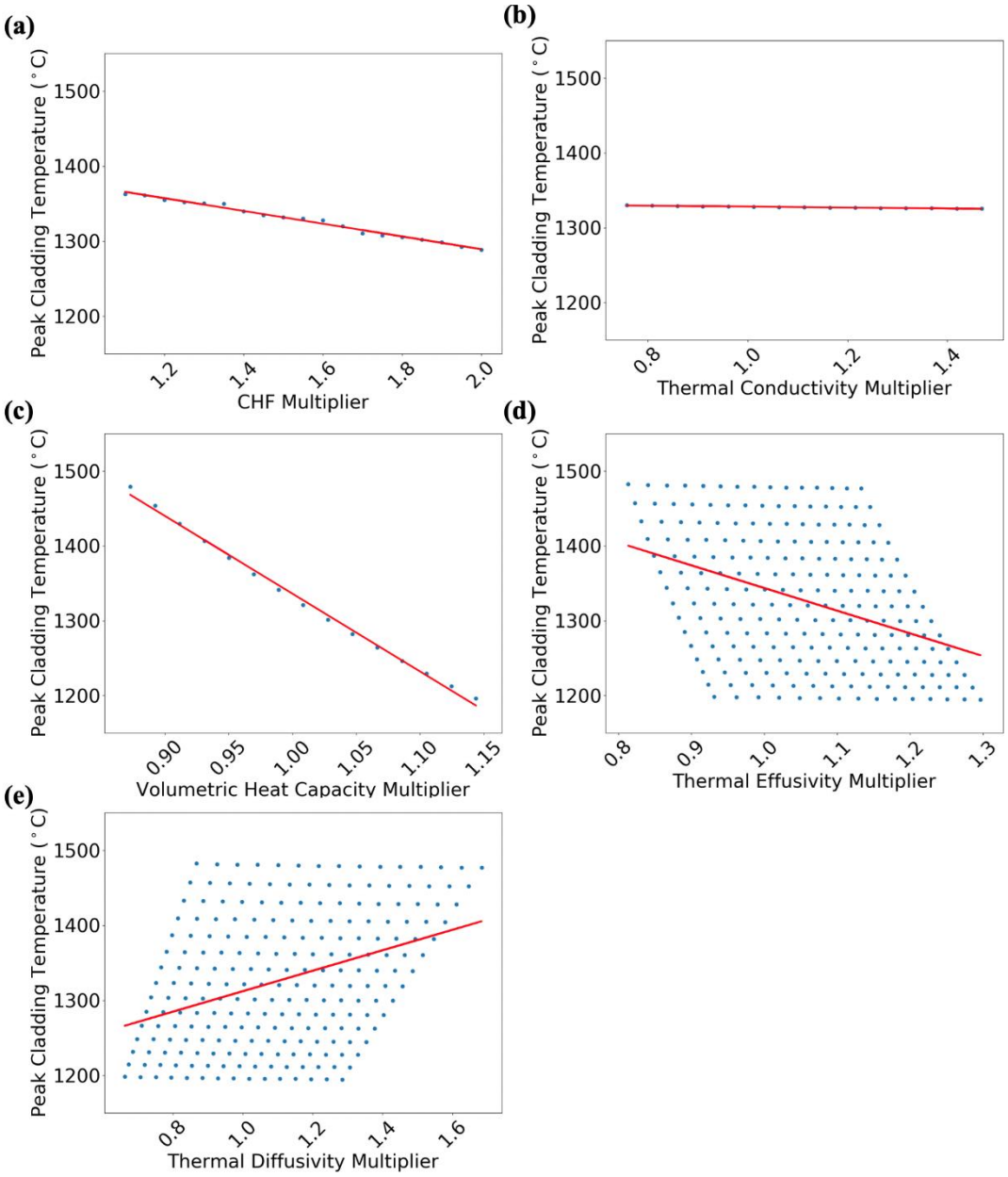

Figure 12: Sensitivity of PCT to (a) the CHF, (b) thermal conductivity, (c) volumetric heat capacity, (d) thermal effusivity and (e) thermal diffusivity multipliers

The best match plots based on the Sensitivity Case 1 parameters for heat flux and surface temperature are shown in Figure 13 and Figure 14, respectively. Figure 13 includes a subplot that is zoomed in around the power transient. The run with the minimum RMSE predicted the PCT nearly as well as the run with the minimum PCT error, so the lines overlap in Figure 14. Because CHF/MHF (the two are equivalent in the RELAP5-3D simulations for the FeCrAl case) is relatively insensitive to the heat transfer coefficient multipliers, the CHF multiplier is the key parameter in matching the experiment. Table 3 lists the parameters used in run #756, which provided the best overall match to the experiment by having the minimum RMSE. Table 4 lists the relative error of each FoM from run #756 to the experimental values, as well as its RMSE. The PCT relative error is calculated with the temperatures in Kelvin. Compared to the base model results previously presented in Table 2, the PCT error decreased from 44.7% to 36.52% and the MHF error improved from -43.2% to 3.22%. It is important to note that the uncertainty in the measured CHF value is about 8%, so this relative error in MHF is within the uncertainty of the measurement itself.

Figure 15 and Figure 16 show comparisons of the experimental results to the best match cases from Sensitivity Case 2 for heat flux and surface temperature, respectively. Again, the minimum RMSE run predicted PCT almost as well as the run with the minimum PCT error, so the lines overlap. In this case, run #4155 was the best overall match to the experiment based on minimum RMSE. Table 5 lists the thermophysical parameters used in run #4155, and Table 6 lists the error values relative to the experiment. As shown by Table 5, the CHF multiplier is still the major factor in matching the experimental MHF. The MHF error of 1.24% is better than both the base model error of -43.2% and the Sensitivity Case 1 error of 3.22%. Variation of thermal conductivity and volumetric heat capacity and their derived quantities brought the relative error of the PCT down from 44.7% in the base model to 27.02%. The MHF and RMSE values are smaller than in Sensitivity Case 1 involving heat transfer coefficient multipliers, which reiterates the stronger dependence of PCT upon the thermal properties that was shown in Figure 12.

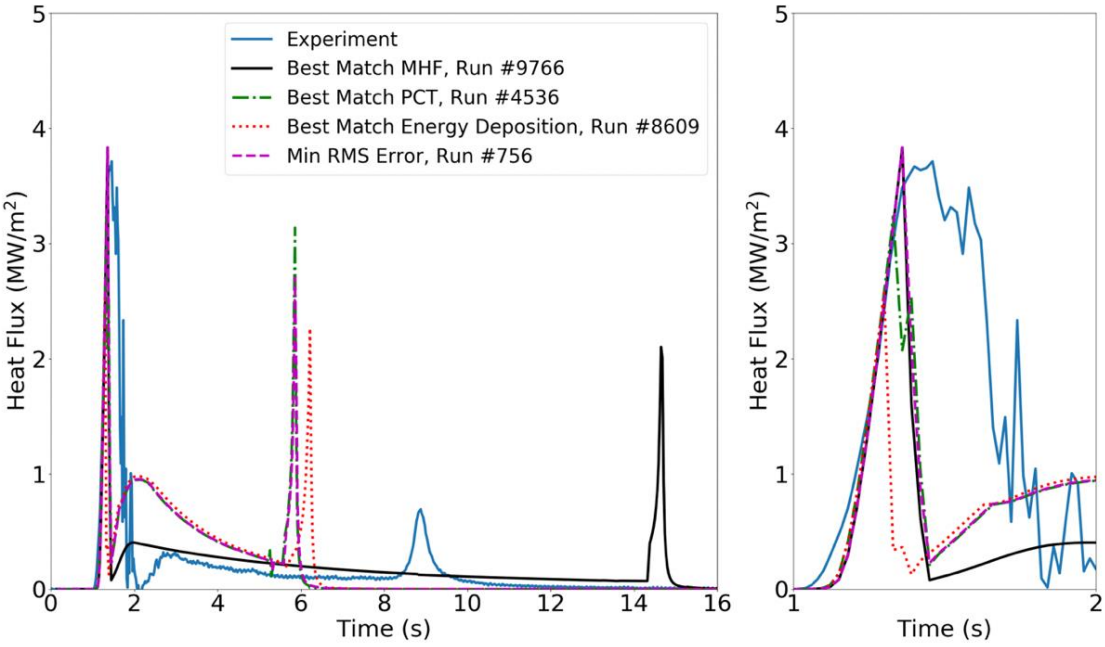

Figure 13: Comparison of experimental heat flux to the best matches for each FoM from Sensitivity Case 1

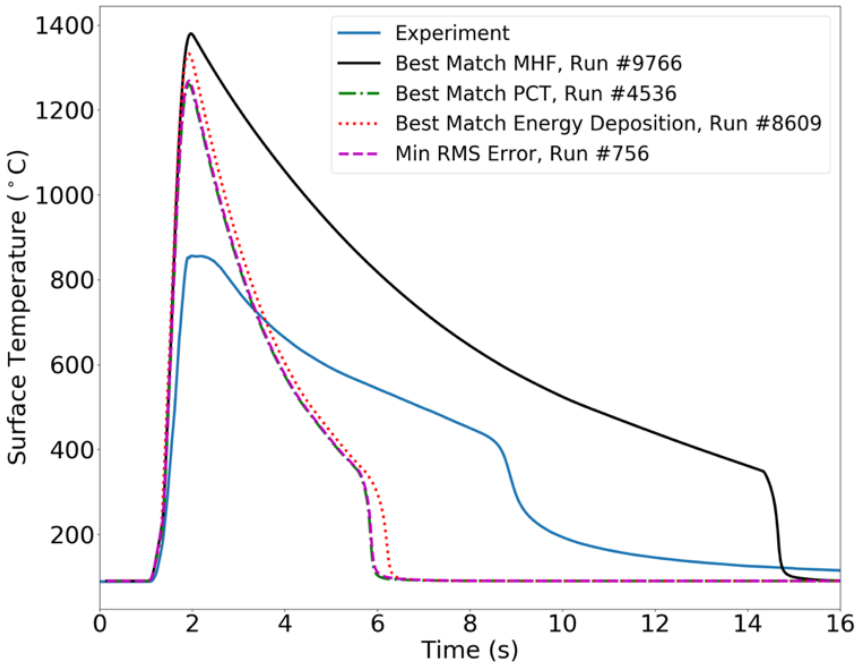

Figure 14: Comparison of experimental surface temperature to the best matches for each FoM from Sensitivity Case 1

Table 3: Parameters used in the Best Match Combined run from Sensitivity Case 1

Parameter	Value
$h_{laminar}$ multiplier	1.3
$h_{turbulent}$ multiplier	0.7
$h_{nucleate}$ multiplier	1.0
$h_{transition}$ multiplier	2.0
h_{film} multiplier	1.0
CHF multiplier	2.0

Table 4: Relative error of the Best Match Combined run from Sensitivity Case 1

FoM	Relative Error (%)
MHF	3.22
PCT	36.52
Integral Heat Flux	2.52
RMSE	36.74

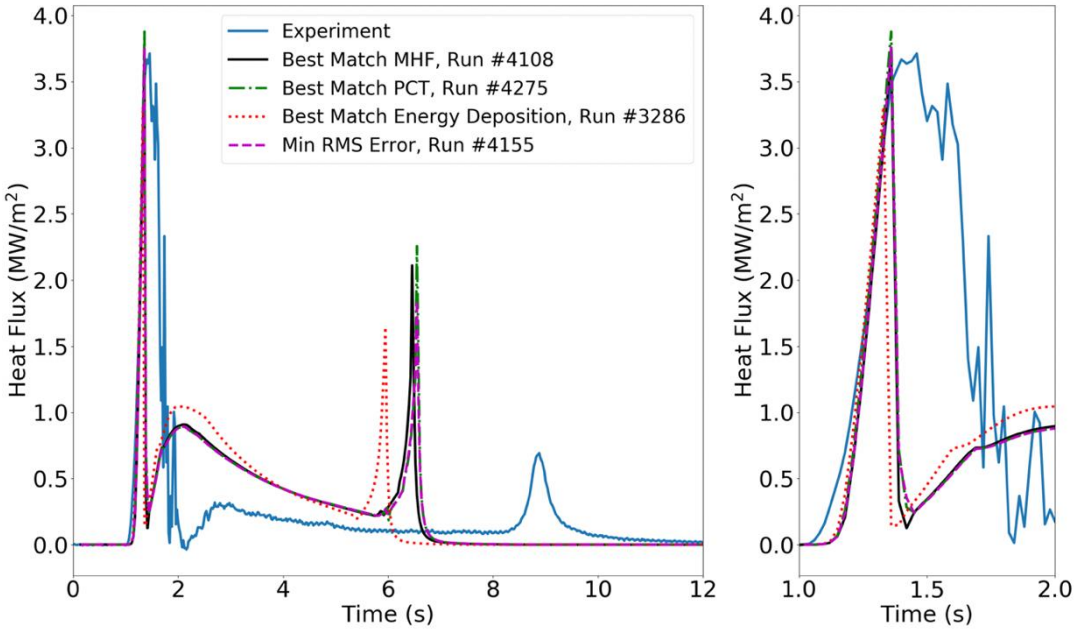

Figure 15: Comparison of experimental heat flux to the best matches for each FoM from Sensitivity Case 2

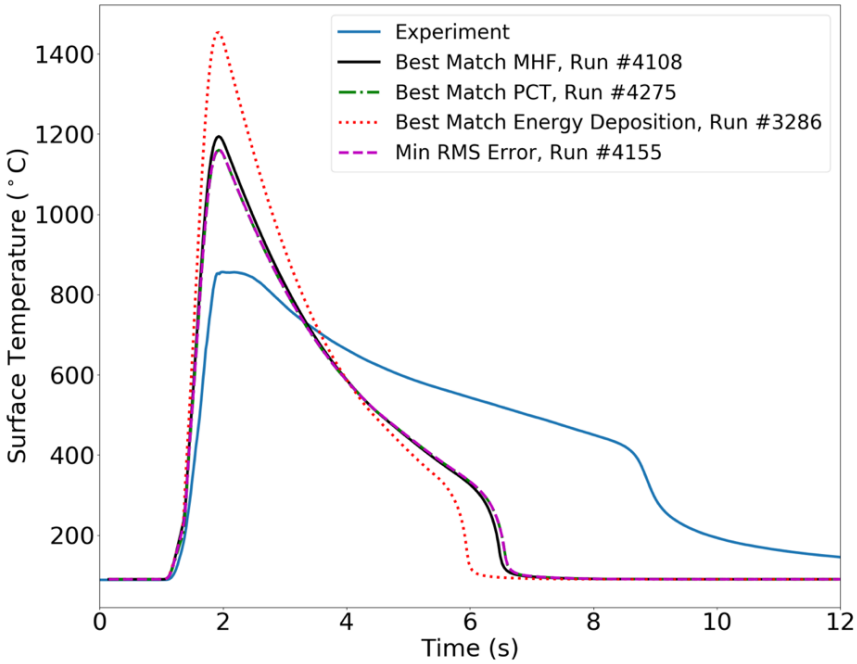

Figure 16: Comparison of experimental surface temperature to the best matches for each FoM from Sensitivity Case 2

Table 5: Parameters used in the Best Match Combined run from Sensitivity Case 2

Parameter	Value
k multiplier	1.06
ρC_p multiplier	1.14
e multiplier	1.10
α multiplier	0.93
CHF multiplier	2.0

Table 6: Relative error of the Best Match Combined run from Sensitivity Case 2

FoM	Relative Error (%)
MHF	1.24
PCT	27.02
Integral Heat Flux	1.70
RMSE	27.10

3.5 Discussion

The two sensitivity studies presented in this chapter show that CHF is not very sensitive to heat transfer coefficients but is much more dependent on the CHF multiplier and thermal properties. Based on these dependencies, a close match to the experimental results could be obtained in terms of MHF and integral of the heat flux (analog to energy deposition). The RELAP5-3D simulation from Sensitivity Case 2 that best matched the experiment in terms of minimum RMSE was still conservative when predicting the PCT, although the time required for the tube temperature to return to the initial value was smaller in the RELAP5-3D results than in the experiments. The main reason for the conservative PCT predictions is the width of the heat flux pulses in the experiment compared to the simulations. In the experiments, the heat flux pulse width was always wider than in the simulations, which means more heat is transferred out of the tube and into the coolant during the power transient. The narrow heat flux pulse width and large drop in heat flux due to the CHF being reached in the computer models means that more energy is going to be stored in the tube, leading to a greater PCT.

The broader heat flux pulse width measured in the experiments is caused by the much greater rate of change in the post-CHF heat flux predicted by RELAP5-3D. In the UNM experiments, it was shown that after CHF was reached, the reduction in heat flux is significant but occurs relatively slowly. By classical definition, the CHF is both the maximum heat flux possible under given conditions and the heat flux at which DNB occurs. In the experiment using FeCrAl, it was found that these two points were not necessarily the same. The occurrence of DNB was determined by finding the point at which the rate of change of the inner surface temperature of the tube rapidly increased, which indicates the formation of a vapor blanket and the start of the post-CHF temperature excursion. After the occurrence of DNB, which is regarded as the CHF point, there is a 1-second period where the heat flux slightly increased to the MHF before drastically decreasing.

When the CHF is reached in the computer models, heat flux instantaneously drops, and at a much faster rate than measured in the experiment. This effect is clearly shown in Figure 17, which shows the heat flux and tube inner surface temperature around

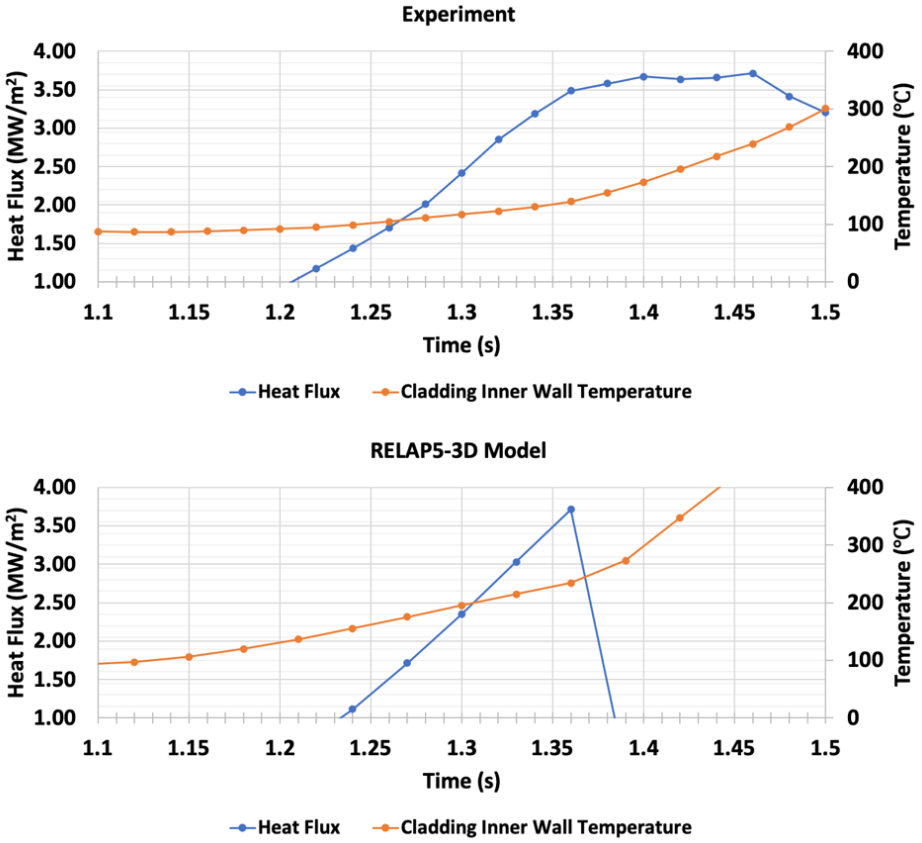

Figure 17: Comparison of heat flux and inner surface temperature between the experiment and RELAP5-3D best match model around the CHF/MHF point

the CHF and MHF points from the UNM FeCrAl experiment and a model from Sensitivity Case 2. Figure 18 shows the time rate of change of the heat flux (dq''/dt) and cladding inner surface temperature (dT/dt) around the time of CHF and MHF being reached in the FeCrAl experiment. Figure 18 shows that there is a noticeable increase in dT/dt and decrease in dq''/dt at both the CHF and MHF points identified in Figure 17. This phenomenon was only observed in the FeCrAl experiment, not in the Inconel or SS316 experiments. CHF and MHF were equivalent to each other in the Inconel and SS316 experiments.

Figure 19 shows the heat flux, cladding inner surface temperature, dq''/dt, and dT/dt around the CHF for Inconel and SS316. There is no evidence in any of these subplots that there is a reduction in heat flux due to DNB occurring before the maximum measured heat flux. It is worth noting that in the FeCrAl experiment, the MHF is approximately 6.5% greater than the CHF, which is within the uncertainty of the experimental temperature measurement and heat flux calculation. It could also be postulated that an unstable vapor layer formed at the CHF point identified in the FeCrAl experiment, which then reflooded and reformed with stability at the MHF.

After CHF occurred, the heat flux through the Inconel test section began to decline but did not drastically drop until approximately 0.2-0.25 seconds after the CHF was reached. From the Inconel time derivative subplot shown in Figure 19, it is shown that the change in heat flux and cladding temperature over time remains relatively constant in the tenths of seconds before and after CHF is reached. In the SS316 experiment, heat flux also declined after CHF was reached, but shows a jump in heat flux starting at 10.1 seconds. This suggests reflooding occurred, even if only temporarily, and is further evidence that unstable vapor layers are forming and rewetting before a stable layer is developed. Regardless of the cause of the discrepancy between CHF and MHF found in the FeCrAl experimental data, a key takeaway from Figure 17 through Figure 19, along with the computational results previously presented in Figure 5, is that after CHF is reached, the computational tools predict a much faster rate of change in heat flux than is experienced in reality. From this takeaway and the best match results presented in Section 3.4.3, it can be concluded that even if the computational tools were to predict the

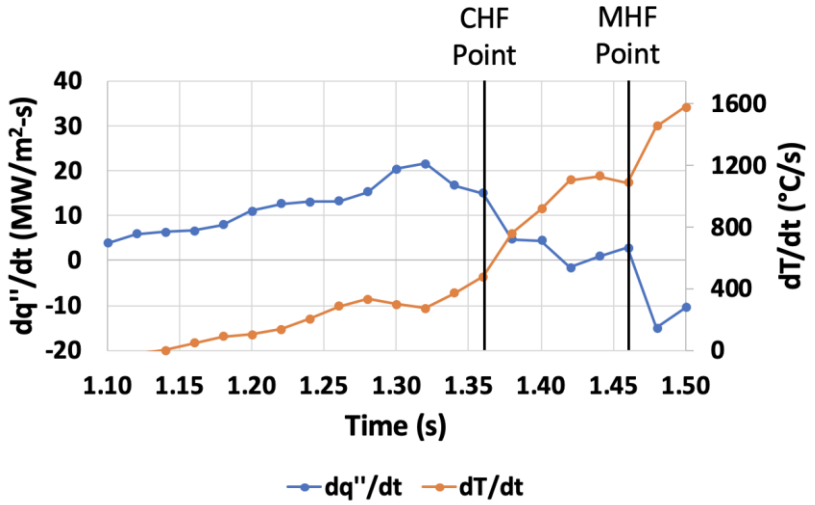

Figure 18: Time rate of change of heat flux and cladding inner surface temperature around the CHF and MHF from the FeCrAl experiment

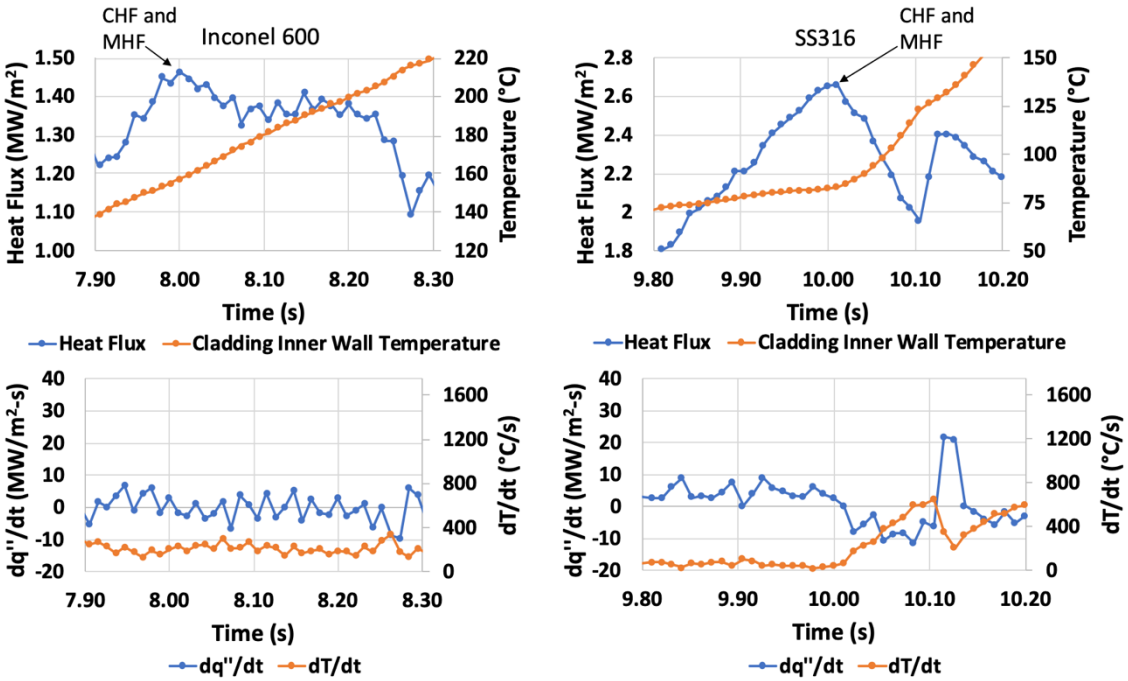

Figure 19: Heat flux and temperature around the CHF (top) and time rate of change of heat flux and temperature around the CHF (bottom) for Inconel 600 (left) and SS316 (right)

correct CHF, they will overpredict the PCT due to the faster rate of heat flux decline.

The observations on the differences between experimental and simulated CHF and post-CHF behavior is a novel contribution of this work. Additionally, the sensitivity studies that elucidate on the effects of FeCrAl cladding material properties and predicted heat transfer coefficients are a new contribution to the literature. This work highlights several areas of experimental and computational development need. There is currently no correlation in existence that can predict the enhancement of CHF during a heating transient, or the rate of heat transfer decline after CHF has been reached. This study is a preliminary heat transfer evaluation that is useful for informing future work, and its primary contribution is pointing out the areas of research need in order to increase the accuracy of nuclear reactor safety analysis.

CHAPTER 4
ASSESSMENT OF CASL VERA FOR BWR ANALYSIS AND APPLICATION TO SIC/SIC CHANNEL BOX

4.1 Background

CASL has been developing VERA to improve the accuracy of LWR modeling through the coupling of subsidiary computational tools that employ multiphysics techniques and a high-fidelity discretization structure [118]. VERA has previously been validated for PWR analysis [123], [124]. However, application of VERA to BWR analysis is under development, and this capability has not yet been fully validated against experimental data or benchmarked against other modeling tools [125]. This study was motivated by the need identified in the literature to perform very high-fidelity coupled assessments of ATF materials in BWRs [36].

This study has two objectives, the first of which is to provide an initial assessment of VERA's capability to perform BWR analysis by comparing results calculated for models based on the Peach Bottom Unit 2 reactor to those calculated by other widely-used modeling tools for a select set of progression problems. This set of progression problems is a novel contribution to the literature. The second objective of this study is to use VERA to evaluate modern BWR fuel assemblies with SiC/SiC composite channel boxes, which is a potential ATF core structural material concept for reasons identified in Section 2.2.2. The importance of this work is grounded in the need for increased accuracy in modeling predictions that can improve the economic competitiveness of nuclear power, as well as the need for advanced modeling tools that can solve complex and novel problems. An example of such a problem is the unique contribution demonstrated in this paper to determine high fidelity neutron flux and temperature boundary conditions for stress and deformation analysis of SiC/SiC channel boxes in BWRs.

Motivation for the assessment of VERA lies in the foundational objectives of CASL, which was established to improve the economic competitiveness of nuclear power by addressing key challenges facing the nuclear industry. This can be achieved through

the integration of subsidiary nuclear modeling tools into VERA [136]. Several example approaches for increasing the competitiveness of nuclear energy include uprating nominal reactor power, achieving higher burnup and fuel cycle lengths, and extending the lifetime of nuclear power plants. However, each of these approaches may increase the likelihood and/or severity of operational occurrences, such as grid-to-rod fretting, PCI, DNB, CIPS, and CILC [52]. Any of these phenomena may increase the probability of cladding or fuel failure during normal operation and accident scenarios, which has operational and safety related consequences. Current modeling tools used in industry and for reactor licensing purposes either lack the multiphysics integration or the spatial fidelity required to fully capture the localized effects caused by these phenomena, which can result in large uncertainties and overly conservative safety margin estimates. This drives the need for tools like VERA, which, compared to current regulatory-grade modeling tools, uses higher-order neutron transport and thermal hydraulic solution methods and a higher-fidelity spatial discretization scheme. These advanced modeling features suggest that VERA could be integrated into the nuclear industry to improve the accuracy of reactor performance predictions and reduce costs [136], [108].

Multiphysics simulators like VERA must undergo an extensive validation and verification (V&V) procedure to ensure safety margin estimates for nuclear reactors are produced with a high level of confidence. This procedure includes V&V exercises first for each of the single-physics tools, followed by additional exercises for the multiphysics coupling of those tools. V&V is supplemented by uncertainty quantification to define the confidence bounds of predicted safety margins [137]. VERA has undergone this procedure for PWR applications, with the final demonstration being a simulation of 20 years of the Watts Bar Nuclear Power Station Unit 1 operating history [123], [138].

This V&V process is yet to be performed for VERA's application to BWR analysis, although the primary VERA codes leveraged in the current study, MPACT and CTF, have undergone single-physics assessments. Kochunas, et al., [139] compared eigenvalue predictions from MPACT for Peach Bottom fuel assemblies to the KENO Monte Carlo code from the SCALE framework [140], and demonstrated MPACT's ability to model 3-D BWR control cells and a 2-D BWR full core problem. Porter and

Avramova [141] compared CTF pressure drop and void fraction predictions to data contained in the Japanese Nuclear Power Engineering Corporation (NUPEC) BWR database, and also summarized other BWR-relevant validation exercises performed using the COBRA-TF line of codes from which CTF originates. Parametric studies were performed by Avramova, et al., [142] and Gorton, et al., [143] that showed single and two-phase turbulent mixing coefficients and interfacial drag coefficients significantly contribute to uncertainties in void fraction distributions. The current study is the first to assess VERA's capability to perform multiphysics evaluations of BWR fuel assemblies and is an integral part of the broader V&V process that VERA must go through to be applied with confidence for BWR applications.

The code-to-code comparisons in this study are made for steady-state BWR performance parameters and two-group nuclear cross sections for BWR fuel lattices. A set of code-to-code progression problems was developed with increasing complexity to perform the comparisons, analogous to past efforts in the literature for PWRs. The modeling tools used for the comparisons are the U.S. NRC's reactor kinetics code PARCS/PATHS and the Monte Carlo particle transport code, Serpent [18]. VERA's primary subsidiary tools that are employed in the comparisons and in the evaluation of SiC/SiC channel boxes are MPACT and CTF. The few-group nuclear cross section data used in PARCS in this study are provided by MPACT, which has its own cross section libraries.

PARCS/PATHS was chosen as the computational tool to compare VERA against because it is considered state-of-the-art for coupled regulatory analysis in the United States and is the NRC's primary tool for BWR depletion analysis [106], [107]. It is worth noting that PARCS has been coupled to other regulatory thermal hydraulic solvers, including RELAP5 [144] and TRACE [145]. However, PATHS offers faster simulation times compared to these other thermal hydraulic solvers, and a comparative study by Wysocki, et al., [106] showed that PATHS is able to predict steady-state BWR performance similarly to both TRACE and SIMULATE-3, a nodal diffusion code with thermal hydraulic feedback that is commonly used in industry for BWR analysis [146].

Serpent was chosen as the neutronics tool for the two-group cross section

comparisons against MPACT because it is a continuous-energy Monte Carlo code that has been employed in a wide range of nuclear applications. Validated continuous-energy Monte Carlo tools are known to be more accurate than deterministic solvers because no approximations are made in cross section energy dependence and exact geometries can be modeled without introducing discretization error. Still, deterministic solvers are typically preferred for large scale multiphysics applications due to reduced computational burden and faster runtimes compared to Monte Carlo methods [99], hence the selection of a deterministic code in VERA. In this context, Serpent is used to verify the two-group cross sections generated by MPACT using infinite 2-D fuel lattice models, an exercise that has been carried out with Serpent for a number of deterministic codes with LWR applications [147], [148], [149].

While the code-to-code comparisons use historical Peach Bottom BWR fuel assembly designs with typical Zircaloy-4 channel boxes, a section of this chapter is dedicated to a high-fidelity, multiphysics evaluation of modern BWR fuel assembly designs equipped with accident tolerant SiC/SiC channel boxes. This type of analysis can only be performed with a tool like VERA and would be impossible to carry out with the same level of output resolution using current regulatory tools. This portion of the study not only demonstrates the advanced capabilities of VERA, but also furthers ATF research and development efforts.

4.2 BWR Model Descriptions and Study Organization

This section details the BWR models developed for this work and the general organization of the study. Section 4.2.1 details the Peach Bottom fuel assembly models that were used for the code-to-code comparisons between MPACT and Serpent for two-group cross sections and between VERA and PARCS/PATHS for steady-state reactor performance parameters. Section 4.2.2 describes a sixteen-assembly mini-core model developed in VERA that comprises of modern BWR fuel assembly designs with SiC/SiC channel boxes. Analysis of the mini-core model with VERA is intended to highlight the tool's advanced modeling capabilities and potential utilization of VERA for ATF research and in the broader nuclear industry. Lastly, Section 4.2.3 summarizes the

organization of this study and reiterates the role that each computational tool plays in this analysis.

4.2.1 Peach Bottom Fuel Assembly Model Descriptions

The BWR fuel assembly designs used for the code-to-code comparison part of this study are based on the six types of fuel assemblies used in cycles 1 and 2 of the Peach Bottom Unit 2 reactor [8]. Assembly types 1 through 3 contain 7×7 fuel pin lattices, and types 4 through 6 contain 8×8 fuel pin lattices. Types 1 through 5 have a heated length of 365.76 cm, while type 6 is a lead test assembly (LTA) design with a heated length of 381.00 cm and contains natural uranium blankets at the top and bottom of the assembly. Of the six assemblies, type 1 is the simplest and contains a single fuel loading pattern for the entire assembly and contains no gadolinia. The other five fuel assemblies have four or five gadolinia-containing rods, and assembly types 2, 3, and 6 have axially-varying fuel loading patterns. Grid spacers are not considered for this analysis, and none of the Peach Bottom BWR fuel assemblies have part-length rods. Zircaloy-4 is used as the channel box material for all Peach Bottom fuel assembly models. Additional geometric parameters of the fuel assembly designs are given in Table 7, which were used in the VERA, Serpent, and PARCS/PATHS models. Each fuel assembly model used for the VERA-to-PARCS/PATHS comparison had identical boundary conditions, which are listed in Table 8. The assembly power of 4.31 MW and coolant mass flow rate of 16.904 kg/s were calculated by dividing the total rated core power and flow rate by the 764 assemblies in the Peach Bottom 2 core.

For the VERA-to-PARCS/PATHS comparisons, reflective boundary conditions were used on the radial sides of the assemblies, while axial leakage was allowed on the top and bottom of the models. Seventy-three axial nodes were used in each assembly model in both computational tools. On the fuel pin level, 8 azimuthal angles and 8 radial regions were used for modeling fuel rods in MPACT. Eight fuel rings were used in CTF's conduction model in each rod, while 10 rings were used in PATHS's homogenized fuel conduction model. By default, PARCS/PATHS provides radially averaged outputs at each axial node while VERA provides results on a pin- and sub-channel-resolved scale.

Table 7: Peach Bottom fuel assembly geometry [8]

Assembly Type	Pin Lattice Design	Fuel Pellet Radius (cm)	Pellet-Cladding Gap Thickness (cm)	Cladding Thickness (cm)	Number of Water Rods
1	7×7	0.61849	0.01524	0.08128	0
2	7×7	0.60579	0.01524	0.09398	0
3	7×7	0.60579	0.01524	0.09398	0
4	8×8	0.52832	0.01143	0.08636	1
5	8×8	0.52832	0.01143	0.08636	1
6	8×8	0.52070	0.01143	0.08128	2

Table 8: Peach Bottom fuel assembly boundary conditions

Parameter	Value
Power (MW)	4.31
Coolant Mass Flow Rate (kg/s)	16.904
Outlet Pressure (Bar)	71.36
Coolant Inlet Temperature (°C)	274.85

This means that PARCS/PATHS can provide centerline, average, and surface fuel temperatures, averaged power profiles, and average coolant properties, while VERA provides radial fuel pellet temperatures in each rod, axial power distributions for each rod, and coolant properties in each sub-channel. Due to the finer mesh used in the VERA models, additional computational resources were used to run the models. All VERA and PARCS/PATHS models were ran on ORNL computing clusters, where VERA used 64 cores over two computing nodes, while PARCS/PATHS used a single core.

To ensure a direct comparison, the CTF models were designed to use the default temperature-dependent polynomials used for UO_2 and Zircaloy-2 thermal conductivities in PATHS. A constant pellet-cladding gap heat transfer coefficient of 5700 W/m^2-K was used in both CTF and PATHS, as was the Churchill wall friction correlation [150]. The Lellouche-Zolotar model [151] was used in PATHS for subcooled boiling, while the Chen model [152] was used in CTF. Neither PARCS/PATHS nor the version of VERA used for this analysis currently has the capability to explicitly model the bypass region that exists between BWR fuel assemblies, meaning that the models were considered to be adiabatic. Bypass flow modeling is currently under development by CASL.

4.2.2 Description of Modern BWR Fuel Assembly and Mini-Core Models

The neutronic and thermal-hydraulic capabilities in VERA were used to obtain fast neutron flux and temperature profiles in BWR fuel assemblies. The BWR models created in VERA are based on a modern 10×10 fuel pin lattice design. The geometry of the BWR fuel assembly models used for this study is based on the geometric data detailed in the thesis by Ferroni [153], as are the power, pressure, and coolant mass flow rate. Seven axial zones were used in the computer models, each of which contains a unique fuel loading pattern [49]. Reflective boundary conditions are used, making the models used in this study representative of assemblies near the center of the reactor core.

Thermal properties of irradiated SiC-SiC [49] were implemented in the CTF input decks for the channel box. The channel box was modeled as heat slabs were to the sub-channels along the periphery of the assembly in CTF. A 47-group neutron cross-section library was used in MPACT. In a previous channel box study using Serpent (which uses a

continuous cross-section library), a 0.1 MeV cutoff was used for tallying fast neutron flux [36]. This cutoff is not available in the 47-group library, while the nearest fast neutron cutoff energies available in the current analysis are 0.067 MeV and 0.183 MeV. Single fuel assembly models with a SiC-SiC channel box were modeled using both cutoffs to show the impact on fast flux tallies.

VERA is capable of modeling the cruciform control blades used in BWR cores. This study provides fast neutron flux and temperature distributions in cladding and the channel box for three cases: the control blade fully withdrawn, the control blade halfway inserted, and the control blade fully inserted. The control blade design implemented in the models is on the design used in the LaSalle Unit 1 reactor [154]. Figure 20 shows a 2-D cross-sectional view of the single BWR assembly model used for this study and includes the control blade. Different colored fuel pins within the figure indicate different levels of ^{235}U enrichment. For demonstration purposes, the same power is used for all the three cases of control blade position in the fuel assembly.

For the accident-tolerant SiC/SiC channel box analysis, a mini-core model was developed in VERA that consisted of sixteen identical BWR fuel assemblies. Each assembly contains a 10×10 fuel pin lattice, two large water rods, seven distinct axial fuel regions with varying fuel enrichments and gadolinia content [155], and seven grid spacers. Modern 10×10 BWR fuel assemblies often feature part-length rods, however, this modeling feature is still under development in VERA. As a workaround, part-length rods were modeled as full-length rods that have extremely low fuel density and ^{235}U enrichment (both values on the order of 10^{-6}) in the regions where the part-length rods would have disappeared. The neutronic impact of this workaround is negligible, but it will have some impact on thermal hydraulic calculations in CTF. Seventy-five axial nodes were used in the mini-core model, and 5 conduction rings were used in the CTF fuel model to shorten run times. Eight azimuthal angles and 8 radial regions were again used in MPACT for modeling the fuel rods.

The mini-core is arranged into a 4×4 array of fuel assemblies with a cruciform control blade modeled in the center of the core. As was the case for the single fuel assembly models, the control blade design is based on that from the LaSalle Unit 1

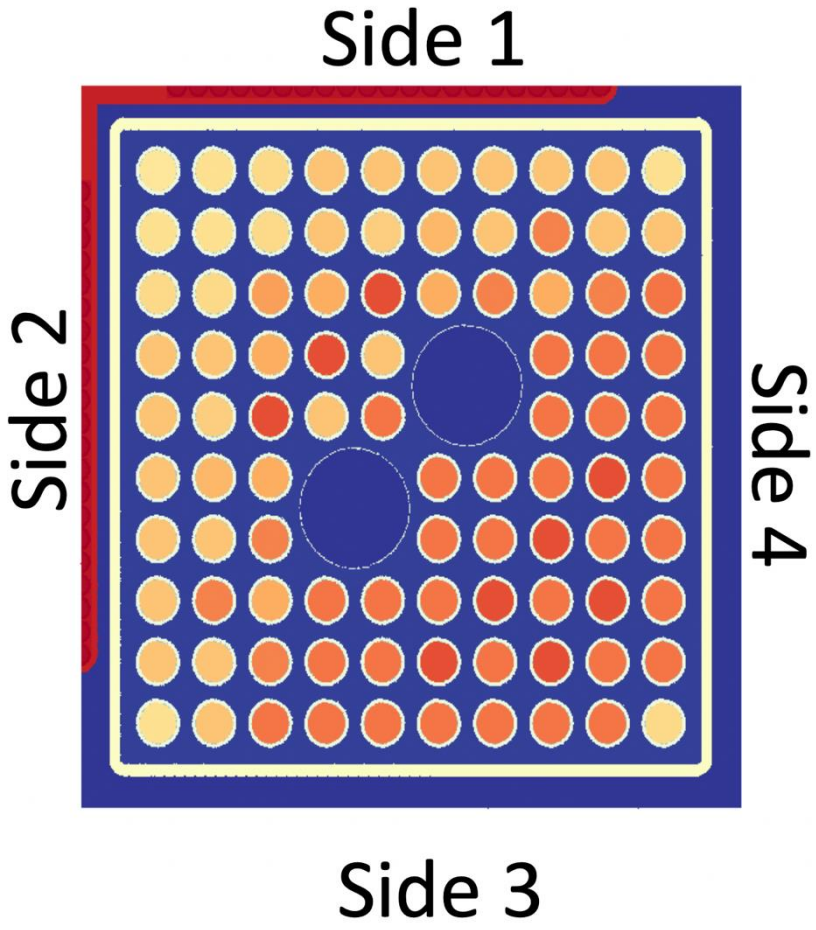

Figure 20: Cross section of the single fuel assembly model with the control blade (shown in red on sides 1 and 2) fully inserted

reactor [154]. Typical UO_2 fuel and Zircaloy-2 cladding were used, along with the default thermal properties for these materials in CTF, while SiC/SiC was used as the channel box material. Because the thermal conductivity of SiC/SiC degrades under irradiation, the thermal properties of preirradiated SiC/SiC were used [49] in CTF. The dynamic pellet-cladding gap conductance model in CTF was turned on for this analysis, and heat transfer from the channel box to the coolant in the bypass region was not modeled. Although the bypass region was not explicitly modeled, VERA automatically adjusts the flow rate in each fuel assembly so that the same axial pressure drop is experienced across all assemblies in the mini-core. Due to the symmetry of the model, results are presented from a single control cell (cluster of four fuel assemblies), which is shown in Figure 21, where "Asm" is short for "assembly." Note that these analyses of modern fuel assemblies are the only portion of this study that utilize SiC/SiC channel boxes.

4.2.3 Summary of Modeling Tools and Study Organization

This study can be broken down into three primary segments:

1. Two-group cross section comparisons between MPACT and Serpent for BWR fuel lattices
2. Comparison of steady-state performance parameter predictions between VERA and PARCS/PATHS for legacy BWR fuel assemblies
3. Analysis of modern BWR fuel assemblies with SiC/SiC channel boxes using VERA

The two-group cross section comparison is a neutronics-only study and is presented in Section 4.3. The purpose of this comparison is to show how well MPACT can generate few-group cross sections to be used in nodal diffusion codes compared to a widely-used, continuous-energy Monte Carlo code. Comparisons of steady-state BWR performance parameter calculations are made between VERA and PARCS/PATHS in Section 4.4.1. These comparisons assess VERA's ability to model BWR fuel assemblies relative to a regulatory-grade tool. The high-fidelity outputs provided by VERA are post-processed to match the output fidelity of PARCS/PATHS in order to make direct comparisons between the two modeling tools. To better illustrate VERA's modeling features, an analysis of modern BWR fuel assemblies with SiC/SiC channel boxes is

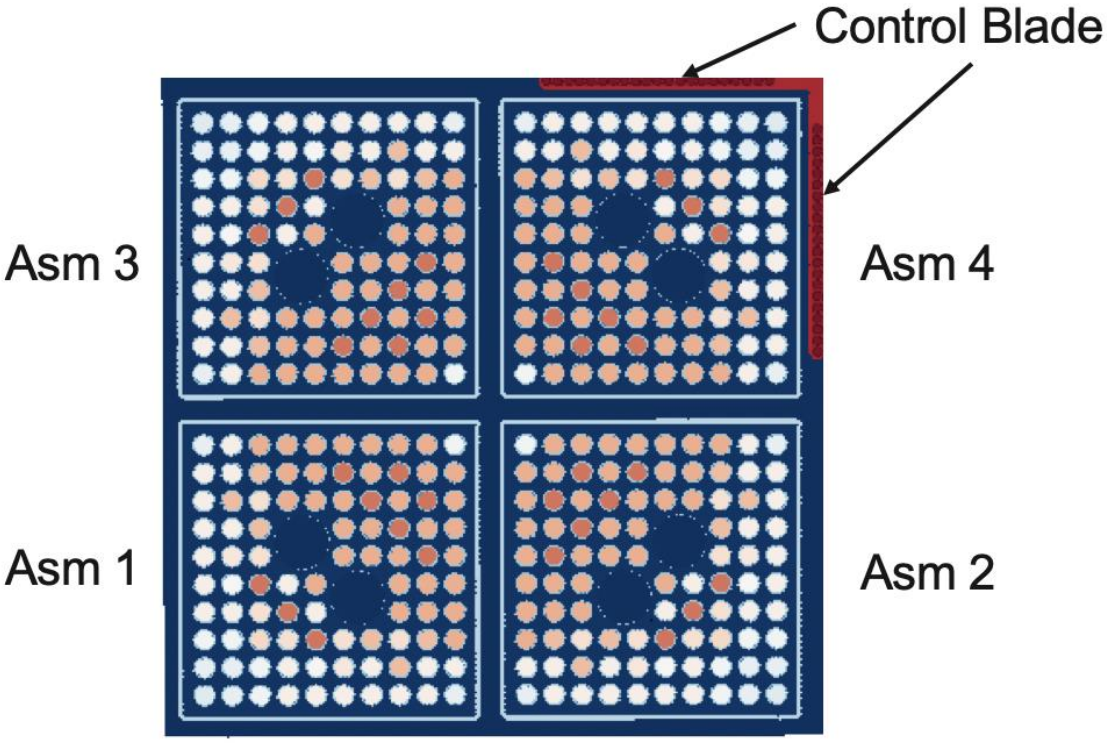

Figure 21: BWR Control Cell

presented in Section 4.5. The purpose of this analysis is to present a unique study that can only be performed with a tool like VERA with high-fidelity and high-order modeling capabilities while also providing an evaluation of an accident tolerant material that is useful in and of itself. This demonstration that VERA can carry out an analysis of a novel problem that currently-used regulatory tools are unable to perform incentivizes its use in the broader nuclear industry. Figure 22 provides a graphical summary of the three primary components of this paper. Note that historical Peach Bottom fuel assembly designs are used for the code-to-code comparisons, meaning that Zircaloy-4 is used as the channel box material, while modern BWR fuel assembly designs with SiC/SiC channel boxes are used for the fast neutron flux and temperature calculations with VERA.

4.3 Few-Group Cross Section Comparisons

Three fuel loading patterns from the six fuel assembly types were modeled as infinite 2-D lattices in MPACT and Serpent to verify MPACT's ability to generate few-group macroscopic cross sections from a lattice physics calculation using a finer energy group structure. Fuel loading patterns from assembly types 1, 3, and 5 were used for this comparison, and were chosen because these lattices cover a range of design complexity. The loading patterns from assembly types 1 and 5 are the only loading patterns used in these assemblies, while the loading pattern from type 3 only extends a portion of the assembly length and is referred to as lattice type D by Larsen [8]. Each MPACT calculation utilized a 51-group cross section library, and a fuel temperature of 900 K, coolant temperature of 548 K, and a void fraction of 40% were used as boundary conditions for all lattice calculations in both Serpent and MPACT. These comparisons are made for fresh fuel only.

Table 9 shows a comparison of k_∞ and Figure 23 shows comparisons of macroscopic cross sections pertinent to two-group diffusion calculations calculated by Serpent and MPACT for the three lattices examined. The differences in k_∞ in Table 9 are given in units of percent millirho (pcm), where 1 pcm is equal to $1\times10^{-5}\ \Delta k$. A transport-corrected, zeroth-order Legendre polynomial expansion for scattering (the TCP_0 approximation) was used to obtain the results in Figure 23. Scattering in Group 1 is

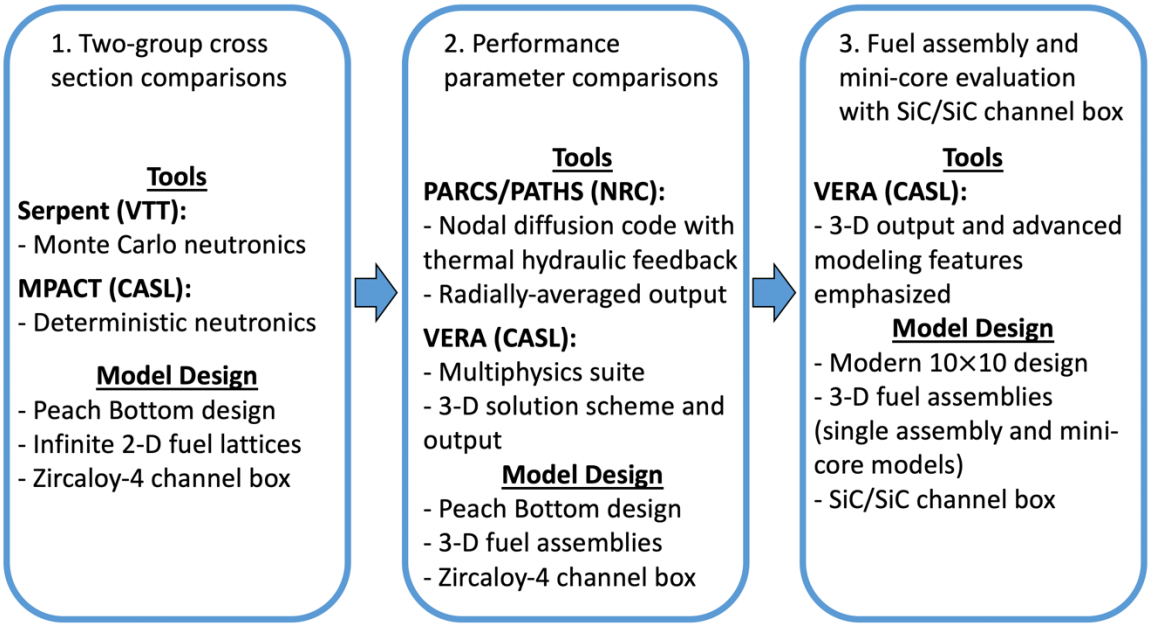

Figure 22: Organization of the current study and summary of modeling tools used

Table 9: Comparison of infinite multiplication factor between Serpent and MPACT

Lattice Designation	k_∞ from MPACT	k_∞ from Serpent	Absolute Difference (pcm)	Uncertainty (pcm)
Type 1	1.04502	1.04786	284	33
Type 3	1.06067	1.06039	38	36
Type 5	1.08141	1.08445	304	31

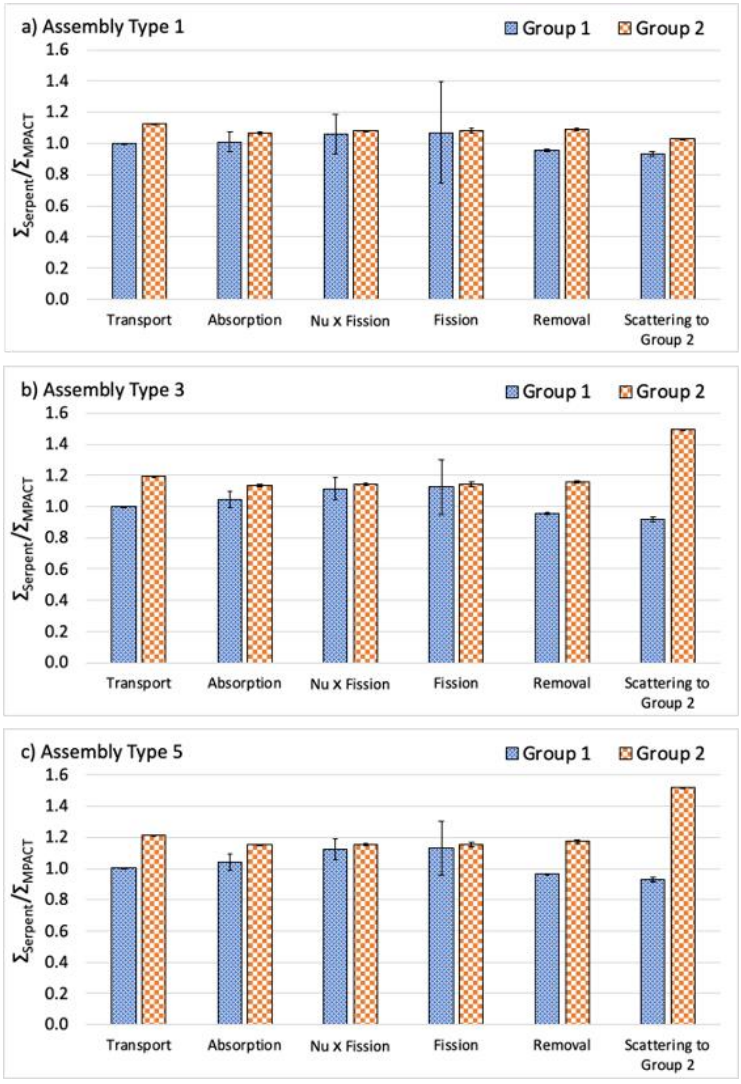

Figure 23: Comparison of cross sections from Serpent and MPACT for assembly types a) 1, b) 3, and c) 5

excluded from the figure and is discussed separately. Results are presented as a ratio of the Serpent-predicted value to the MPACT-predicted value, so values close to 1.0 indicate better agreement. Because Serpent is a Monte Carlo code, the statistical uncertainty in the cross section predictions is propagated into the ratios.

The Group 1 scattering cross sections include within group scattering $\left(\Sigma_{s,1\to1}\right)$ and upscattering from Group 2 $\left(\Sigma_{s,2\to1}\right)$. For $\Sigma_{s,1\to1}$, the Serpent-to-MPACT ratios are 1.036, 1.966, and 1.962 for assembly types 1, 3, and 5, respectively, and have negligible uncertainties. In a two-group energy structure, MPACT assumes there is no upscatter, while Serpent calculated $\Sigma_{s,2\to1}$ cross sections of 6.879×10^{-4} 1/cm, 1.049×10^{-3} 1/cm, and 1.107×10^{-3} 1/cm for types 1, 3, and 5, respectively. The calculated uncertainty for each of these values is more than 100%, meaning that MPACT's assumption of no upscatter falls within the range of possible values predicted by Serpent.

When the statistical uncertainty in the Serpent calculations are taken into account, most of the Group 1 cross sections match within a few percent. In Group 2, Serpent consistently predicted macroscopic cross sections that were approximately 10-20% greater than those predicted by MPACT. In terms of the multiplication factor, the tools matched within about 304 pcm or less. Some of the differences may be accounted for by the use of different cross section library versions, since MPACT used an Evaluated Nuclear Data File Version B (ENDF/B)-VII.1 library [156] while Serpent used an ENDF/B-VII.0 library [157]. The largest discrepancy occurs for the within group scattering cross sections, $\Sigma_{s,1\to1}$ and $\Sigma_{s,2\to2}$, specifically in the cases where gadolinia is present. For assembly types 3 and 5, Serpent predicted a nearly 100% larger Group 1 self-scattering cross section and approximately 50% greater Group 2 self-scattering cross section. To address the differences in scattering cross section predictions, two additional higher-order P_2 approximation for scattering. In one case, the same 51-group cross section library was used, and in the other case, a 252-group cross section library was used. Figure 24 shows the Serpent-to-MPACT ratio for the various cross sections using a 51-group library and the P_2 approximation in MPACT.

From Figure 24, it is shown that most of the Serpent-to-MPACT ratios did not

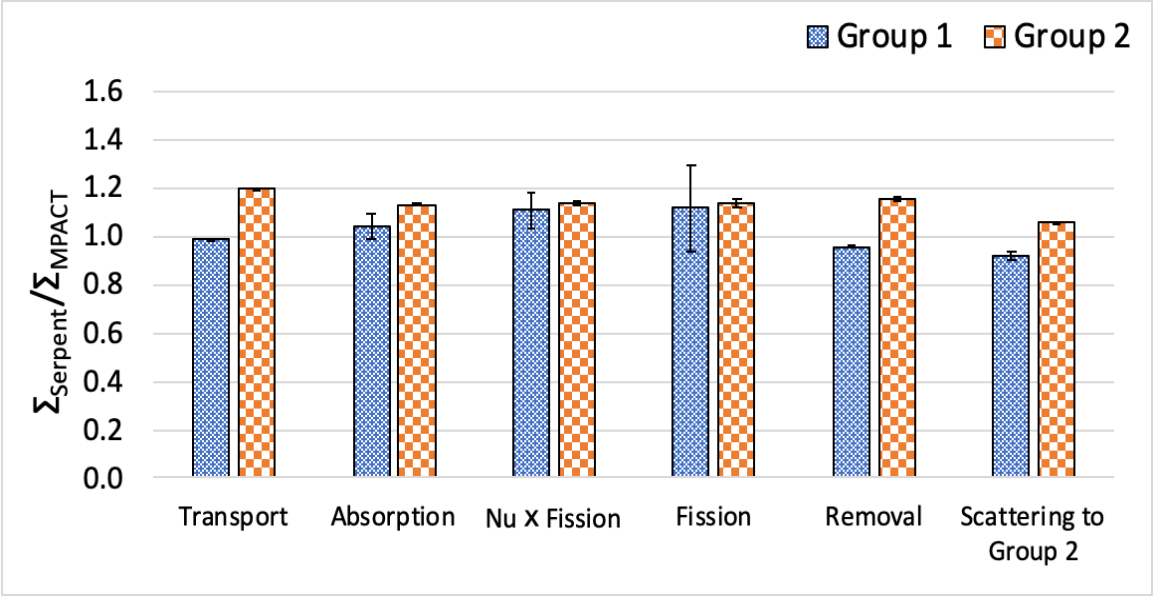

Figure 24: Comparison of cross sections calculated by Serpent and MPACT for Assembly Type 3 using the P2 scattering approximation

change significantly, but the Group 2 self-scattering cross section ratio dropped from 1.495 to 1.061. Additionally, the Group 1 self-scattering cross section ratio decreased from 1.966 to 1.039, showing significantly better agreement between the codes. For k_∞, however, the difference between the Serpent and MPACT predictions increased from 28 ± 36 pcm to 163 ± 36 pcm. The final MPACT case, which used the P_2 approximation and a 252-group cross section library, showed marginal improvement over the case using P_2 and 51-group library in terms of cross section agreement, but the difference between Serpent and MPACT decreased to just 1 ± 36 pcm. These cross section differences may lead to somewhat harder spectrum predictions in MPACT since each of the predicted thermal cross sections were less than those predicted by Serpent, and the lower transport cross section in MPACT will decrease axial streaming.

4.4 VERA to PARCS/PATHS Comparisons

4.4.1 Code-to-code Comparison of BWR Analysis

Comparisons of a number of neutronic and thermal hydraulic parameters were made between VERA and PARCS/PATHS for the six Peach Bottom BWR fuel assemblies described in Section 4.2.1. To perform these comparisons, PARCS/PATHS requires two-group cross sections and other diffusion parameters generated by a reactor physics code for a given reference state and a number of branch cases with different thermal hydraulic parameters. For this study, MPACT was used in standalone mode to generate these parameters, which include two-group cross sections, the diffusion coefficient, and assembly discontinuity factors. The MPACT models used a 252-group cross section library, the TCP_0 approximation for scattering, and reflective boundary conditions on the radial sides of the assemblies but vacuum conditions on the top and bottom. The reference state used a coolant temperature of 548 K, a fuel temperature of 900 K, and a void fraction of 40%. Six coolant density branches were calculated with void fractions of 0%, 10%, 30%, 50%, 70%, and 90%, and three fuel temperature branches were calculated off of the reference state and each density branch using fuel temperatures of 500 K, 1500 K, and 2500 K. Additionally, two coolant temperature branches were calculated at void fractions of 40% and 70% using a coolant temperature

of 561 K and fuel temperature of 900 K. This branch structure more than encapsulates the recommendation by the NRC for BWR analysis using PARCS/PATHS [158].

For each fuel assembly type, k_{eff}, relative power profile, void fraction, outlet equilibrium quality, average fuel temperature, and coolant pressure drop are compared. Because PARCS/PATHS uses a single radial node per fuel assembly, the pin-resolved results from VERA had to be radially averaged to match the fidelity of PARCS/PATHS. For fuel pin parameters, such as relative power and fuel temperature, the values were simply averaged at each axial level. Sub-channel area was used as a weighting factor when averaging void fraction and pressure because the corner and side subchannels have different areas than inner sub-channels, while sub-channel coolant mass flow rate was used to weight the quality. Figures shown in this section are only for assembly types 1 and 2 since the single fuel loading pattern of type 1 and the gadolinia content and axially-varying fuel loading pattern of type 2 make these assemblies representative of all six assembly types. A table is used to quantify the differences between the two modeling tools for all six assembly types.

Figure 25 shows the comparison of relative power and k_{eff} between VERA and PARCS/PATHS for assembly types 1 and 2. Comparisons for void fraction, coolant pressure, and average fuel temperature for the two assemblies are shown in Figure 26 through Figure 28, respectively. Figure 26 also lists the outlet equilibrium quality predicted by PATHS and CTF, and Figure 27 also lists the total pressure drop. Qualitatively, PARCS/PATHS predicted a greater peak relative power and greater peak fuel temperature for both fuel assemblies. The exit void fraction was slightly greater in PARCS/PATHS for both cases, although the void fraction predicted by VERA was greater at lower axial regions. The same outlet equilibrium quality was predicted by both modeling tools, and VERA predicted a greater pressure drop for the two assemblies shown. Table 10 is shown below to better quantify the differences between the two tools for all six assembly types. The differences in k_{eff} are presented as absolute differences in units of pcm while all other differences are all relative to the values predicted by PARCS/PATHS. It should also be noted that the computing time of the VERA models on 64 cores required runtimes from approximately 32 to 78 minutes, while the

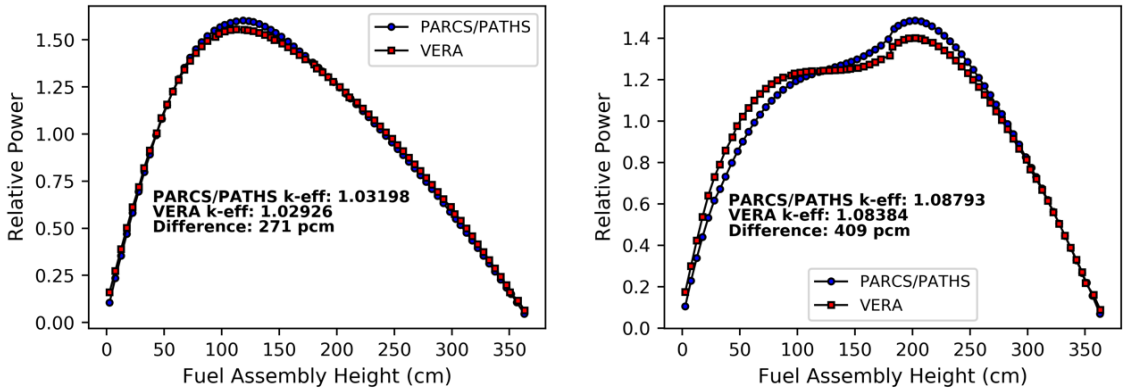

Figure 25: Comparison of relative power and k_{eff} for assembly types 1 (left) and 2 (right)

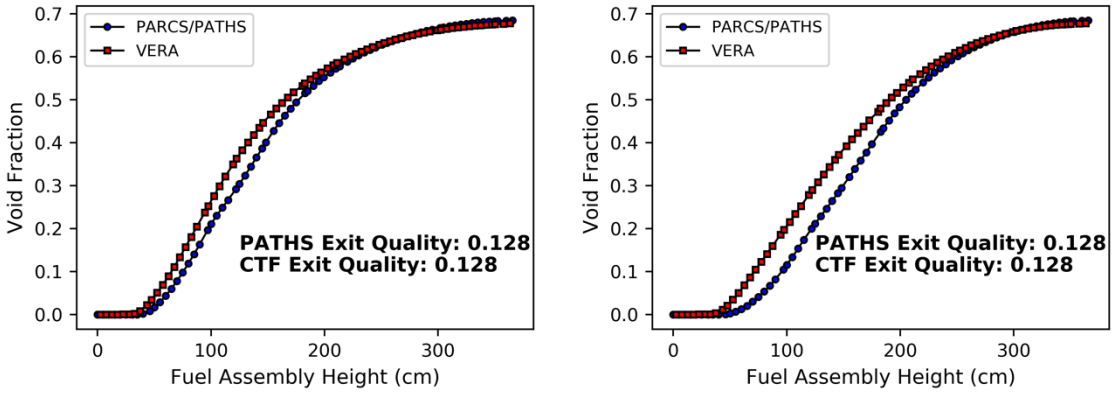

Figure 26: Comparison of void fraction and outlet equilibrium quality for assembly types 1 (left) and 2 (right)

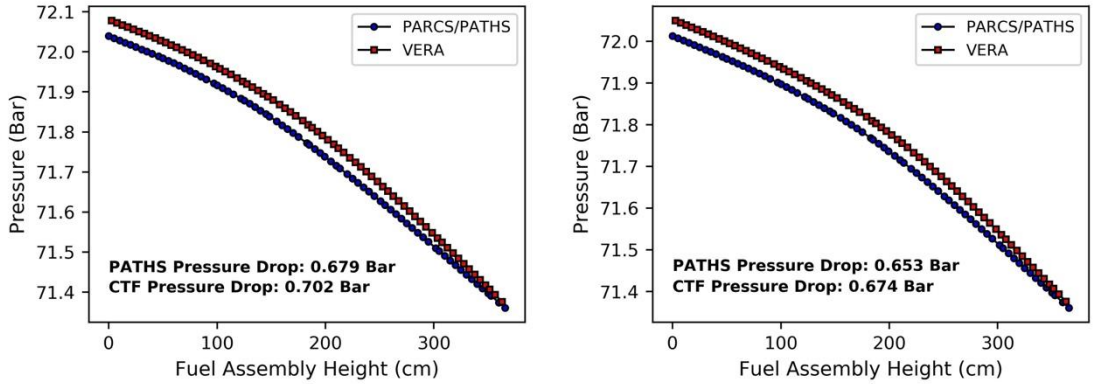

Figure 27: Comparison of coolant pressure drop for assembly types 1 (left) and 2 (right)

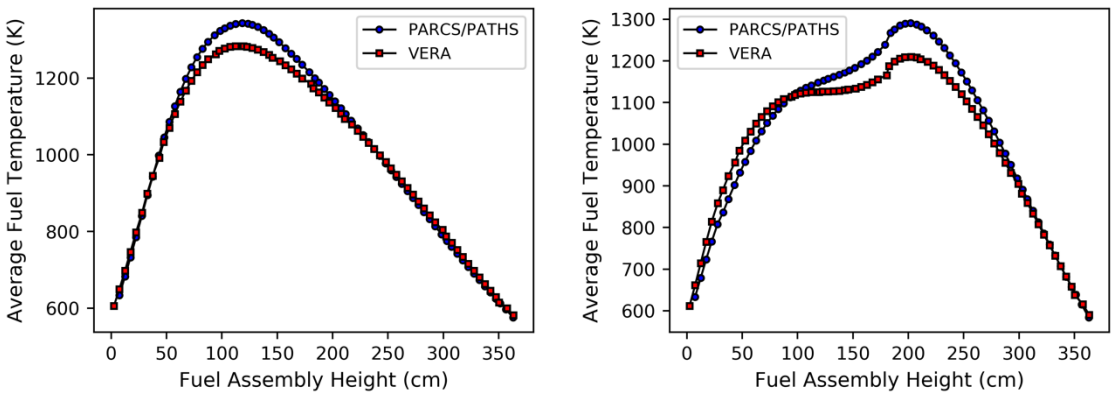

Figure 28: Comparison of average fuel temperature for assembly types 1 (left) and 2 (right)

Table 10: Comparison of key parameter predictions between PARCS/PATHS and VERA

Assembly Type	Δk (pcm)	Relative difference in maximum fuel temperature (%)	Relative difference in exit void fraction (%)	Relative difference in pressure drop (%)
1	271	4.44	0.98	-3.41
2	409	6.24	0.95	-3.27
3	153	17.80	1.13	1.35
4	235	6.65	1.28	-4.37
5	197	7.26	1.28	-4.36
6	282	6.44	1.11	1.14

PARCS/PATHS models run in approximately 1 second. However, PARCS requires few-group cross sections that are generated using a separate lattice physics code and converted into the PARCS format, while VERA has its own cross section data libraries.

From Table 10, it is shown that a greater multiplication factor was predicted by PARCS/PATHS for all six assembly types, and the differences are within several hundred pcm. In terms of axial power profiles, the RMSE across all six fuel assemblies and all axial locations between the two modeling tools is 10.36%. PARCS/PATHS also predicted a greater peak fuel temperature for all six assembly types. For most of the assemblies, the agreement in peak fuel temperature was from 4% to 7%, however, the tools differed by nearly 18% for assembly type 3. In terms of void fraction, PARCS/PATHS predicted a greater exit void in all cases by about 1.3% or less, but, as is shown in Figure 26, VERA predicted greater void at lower axial regions in the fuel assemblies for all six cases. VERA predicted a greater total pressure drop in four out of the six cases, and relative differences of 1.14% to 4.37% were demonstrated for all assembly types.

4.4.2 Discussion on VERA-to-PARCS/PATHS Comparisons

Further discussion on the code-to-code comparisons made in Section 4.4.1 is provided here to provide additional understanding on the differences between the predictions from the two modeling tools. Some differences between results from VERA and PARCS/PATHS may be expected based on the different methodologies used each in of the codes. Recall that PARCS uses the diffusion approximation with few-group cross sections, while MPACT uses MOC to solve a 2-D radial, 1-D axial approximation to the 3-D Boltzmann transport equation and a much finer energy group structure. CTF solves conservation equations for each of the three fluid fields (liquid film, liquid droplets, and vapor) modeled in the code, while PATHS uses the drift flux model. Also, both PARCS and PATHS homogenize fuel assemblies into a single radial node, while MPACT and CTF use a higher-fidelity spatial mesh. Comparisons of detailed transport and homogenized diffusion solutions for BWRs performed by Tada et al. [159] showed differences between the two solution methods in k_{∞} predictions of as much as 2,200

pcm. Although assembly discontinuity factors, which were used in this analysis, have been shown to significantly reduce the discrepancy [160], some differences between PARCS/PATHS and VERA predictions are expected to occur due to different spatial meshes, energy group structures, and solution methodologies.

Discrepancies similar to those presented in this paper between PARCS/PATHS and VERA have been shown before between other commonly used modeling tools and experimental and reactor data. Comparisons of thermal hydraulic results for a BWR fuel assembly were made by Wysocki et al. [106] using PATHS, TRACE, and SIMULATE. The results from that study showed that PATHS predicted the lowest void fraction in the lower axial regions of the assembly but predicted the greatest exit void fraction out of the three modeling tools. Validation work for CTF has shown that compared to measured data from several two-phase flow experimental facilities, CTF often overpredicts two-phase pressure drop and void fraction in the bubbly and slug flow regimes [161], [141]. The study by Wysocki et al. [106] also presented a comparison of axial power profiles from a BWR core that were measured using a traveling in-core probe (TIP) and calculated using PARCS/PATHS that showed a 9.9% RMSE across all TIP measurement locations, which is similar to the RMSE for relative power predicted between VERA and PARCS/PATHS of 10.36%. Yarsky et al. [107] also compared PARCS/PATHS power profiles to TIP data from Edwin Hatch Unit 1, Cycle 2 and found that compared to the measured data, PARCS/PATHS always predicted a greater peak power as well as a lower relative power at the top and bottom nodes of the model. Each of these observations are consistent with those made in the present study.

The observed differences in relative power and void fraction between the codes and measured data will have cascading effects on other key parameters and on each other. Relative power directly impacts fuel temperature and void fraction, which then impacts pressure drop and relative power due to increased neutron absorption. To understand the first-order cause of the discrepancies between VERA and PARCS/PATHS, standalone neutronics and thermal hydraulics calculations were performed for assembly type 1. Figure 29 shows a comparison of relative power and k_{eff} predicted by MPACT and PARCS for assembly type 1 at a void fraction of 40%, while Figure 30 through Figure 32

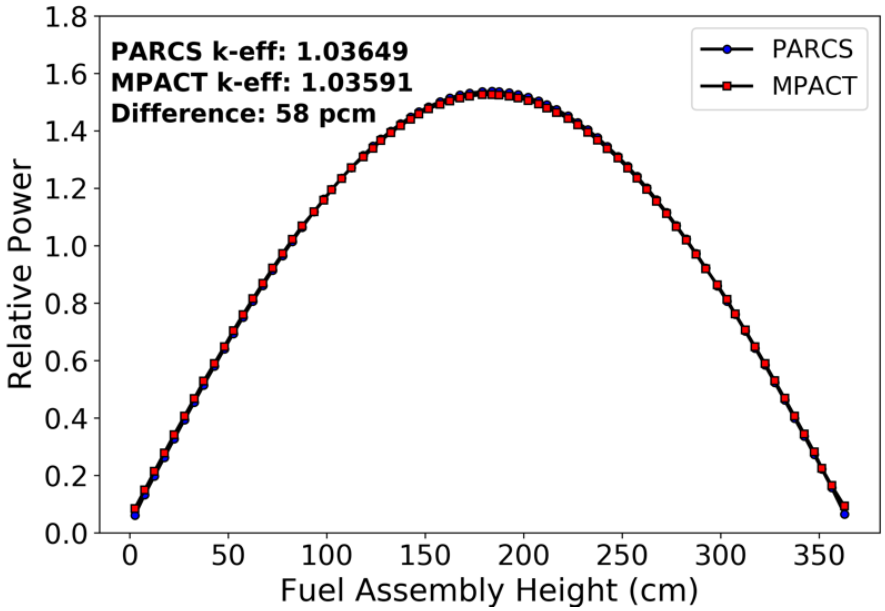

Figure 29: Comparison of relative power and k_{eff} predictions from MPACT and PARCS for assembly type 1

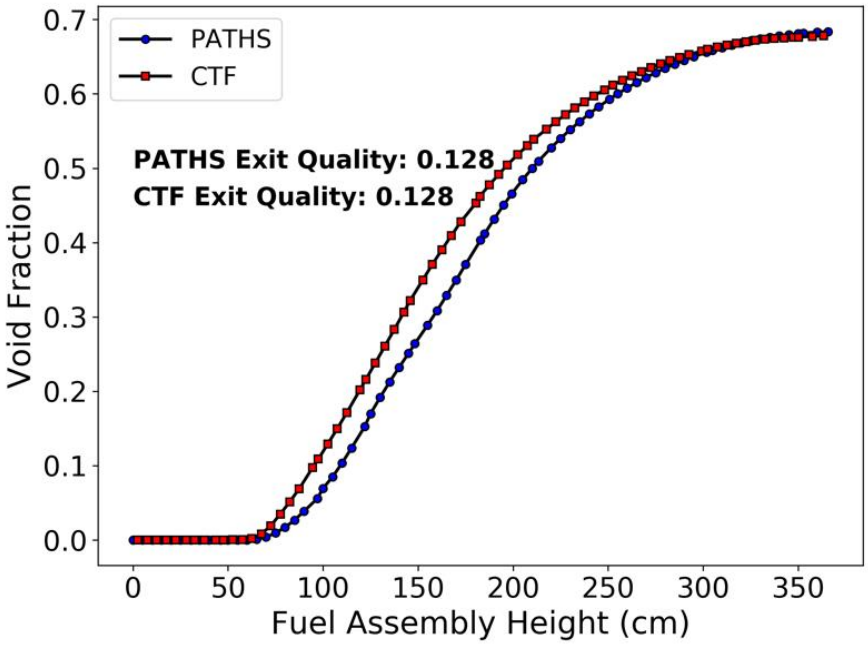

Figure 30: Comparison of void fraction and outlet equilibrium quality predicted by CTF and PATHS for assembly type 1

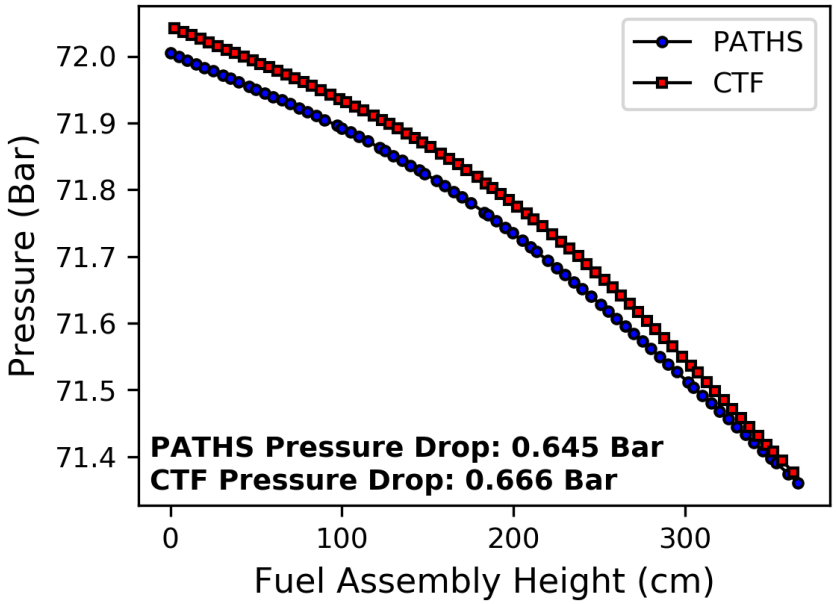

Figure 31: Comparison of pressure drop predicted by CTF and PATHS for assembly type 1

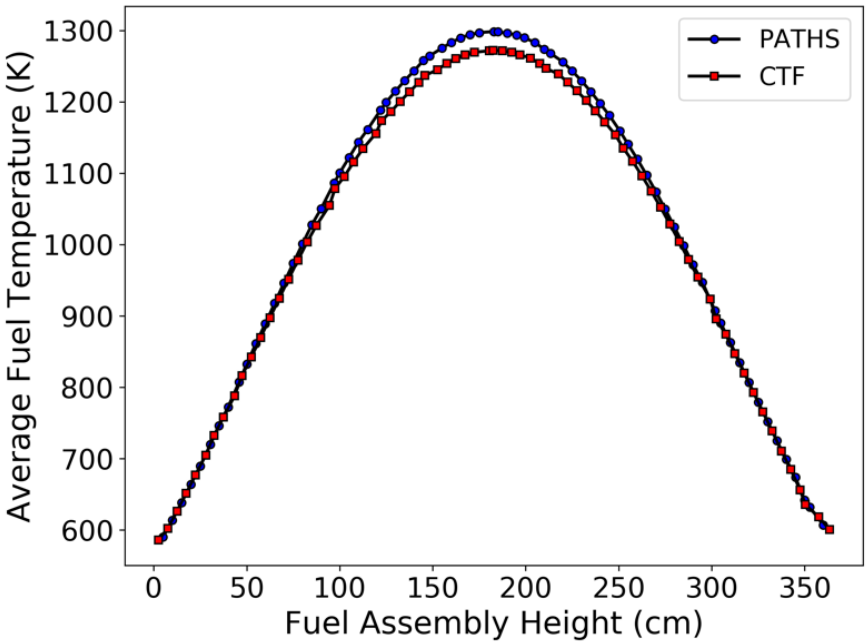

Figure 32: Comparison of average fuel temperature predicted by CTF and PATHS for assembly type 1

show comparisons of void fraction, pressure, and average fuel temperature, respectively, calculated by CTF and PATHS using the power profile calculated by the MPACT model.

For this particular set of boundary conditions, the difference in k_{eff} predictions is 58 pcm and the RMSE in relative power across all axial nodes is 0.92%, while the RMSE for the coupled analysis of assembly type 1 shown in Figure 25 was 2.60%. The relative difference in peak fuel temperatures predicted in the standalone CTF and PATHS models is 2.02%, less than half of the relative error found in the coupled analysis for assembly type 1. CTF and PATHS each predicted a smaller pressure drop in standalone mode compared to the coupled values, although the relative difference in pressure drop is -3.35%, similar to the -3.41% difference observed in the coupled case. In terms of void fraction, the predictions from CTF and PATHS are essentially identical to those from the coupled analyses using VERA and PARCS/PATHS. Contributing factors to the discrepancies between the modeling tools are the use of different subcooled boiling correlations, different solution methodologies, and different spatial resolution. Void fraction discrepancies likely cause the differences in pressure drop because of the use of two-phase friction multipliers used in both CTF and PATHS. The improved agreement for relative power, k_{eff}, and fuel temperature with little change in pressure drop and void fraction predictions suggest that void fraction discrepancies are the primary cause of other discrepancies found in the coupled cases.

Another potential source of the discrepancies between the VERA and PARCS/PATHS results is the CASL mission and philosophy from which VERA was designed. CASL was established to improve the economic competitiveness of nuclear energy by more accurately predicting nuclear reactor performance [136]. Historically speaking, conservative and best-estimate approaches have been employed in nuclear reactor modeling and simulation, which can predict safety margins that are overly cautious and thereby induce additional costs [108]. While some conservatism is removed through the use of coupled methodology, like that of PARCS/PATHS, some accuracy is still lost due to the lack of spatial fidelity. VERA was developed with high-fidelity spatial resolution with the intention to reduce reactor operational costs by further increasing accuracy of LWR assessments and capturing highly-localized phenomena, which could

potentially result in stronger negative feedback from local void and fuel temperature. It is possible that some of the discrepancies between VERA and PARCS/PATHS, which showed that VERA always predicted lower relative power and peak fuel temperatures, may be the result of reduced conservatism from higher-order multiphysics solution methods and finer spatial resolution.

4.5 SiC/SiC Channel Box Analysis using VERA

4.5.1 Evaluation of SiC/SiC Channel Box

Figure 33 through Figure 35 show the 3-D spatial distribution of the fast neutron flux in a BWR channel box for the fully withdrawn control blade, the partially inserted control blade and the fully inserted control blade positioning, respectively. The distributions using the 0.067 MeV and 0.183 MeV neutron energy cutoffs are both shown, as is the percent difference between using these two different energy cutoff values. The difference in fast flux between the two cutoffs is spatially dependent and ranges from approximately 4% to 17%, depending on the control blade position. All four sides of the channel box are shown for a clear visualization of the radial heterogeneity in the flux distributions. The side numbers correspond to those that were shown in Figure 20. Figure 36 through Figure 38 show the temperature distributions in the channel box for the fully withdrawn, partially inserted, and fully inserted control blade positions, respectively.

Figure 33 through Figure 38 show that there is significant axial variation in the fast flux and temperature, regardless of the control blade position. The axial gradient is most pronounced when the control blade is partially inserted, since this position causes a top-heavy power shape in the fuel assembly. The radial gradient in fast flux and temperature becomes most pronounced when the control blade is fully inserted because the power is most depressed along the two sides of the assembly adjacent to the control blade wings. Linearly interpolating between the maximum flux values calculated using the two different neutron energy cutoffs (1.804×10^{14} neutrons/cm^2-s for the 0.067 MeV cutoff and 1.502×10^{14} neutrons/cm^2-s for the 0.183 MeV cutoff) gives an estimate of the flux at a 0.1 MeV neutron energy cutoff of 1.644×10^{14} neutrons/cm^2-s. This value is

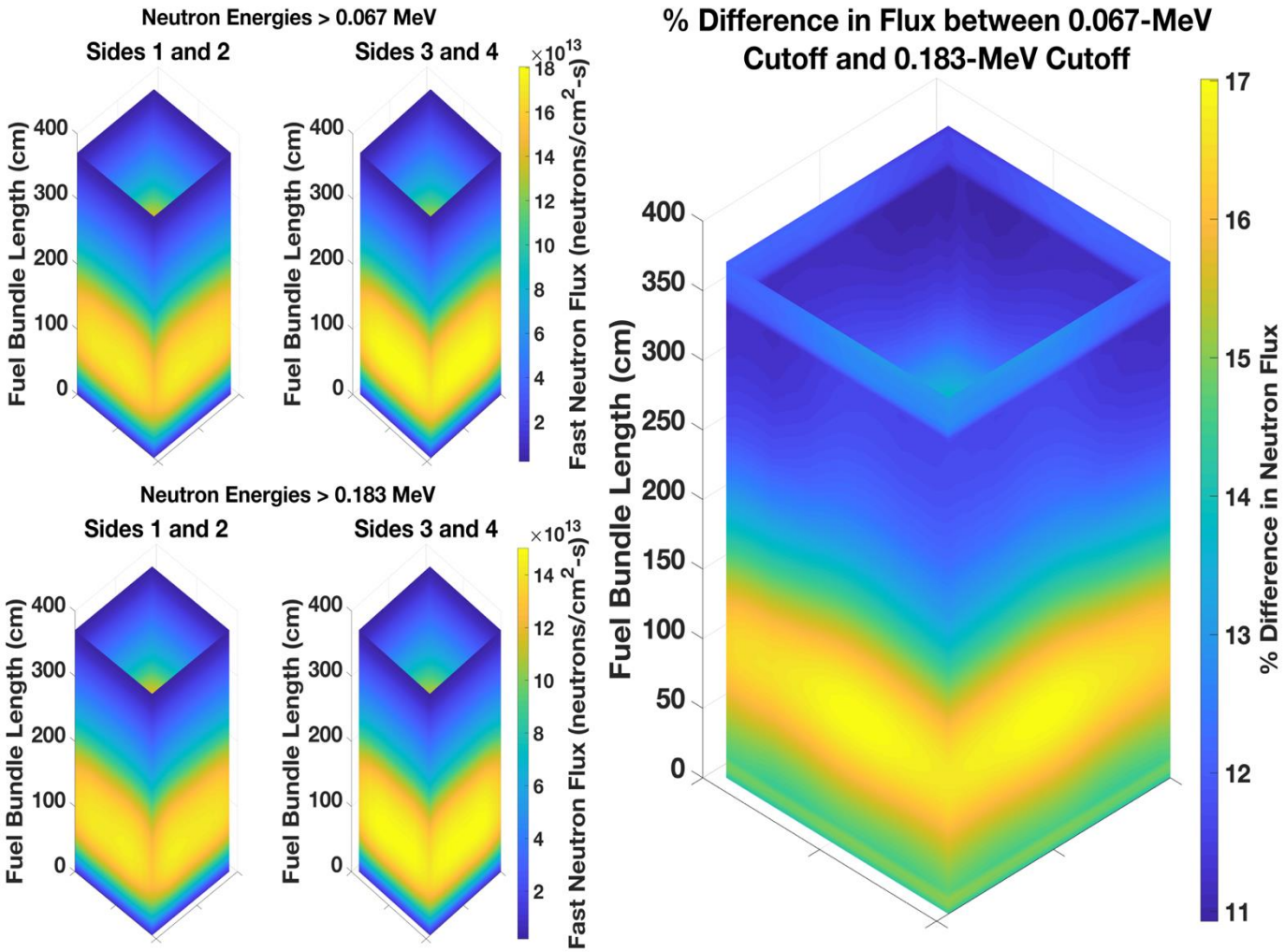

Figure 33: Fast neutron flux distribution in a SiC-SiC channel box using a 0.067 MeV cutoff (top), 0.183 MeV cutoff (bottom), and the percent difference in flux between the two cutoffs (right) with the control blade fully withdrawn

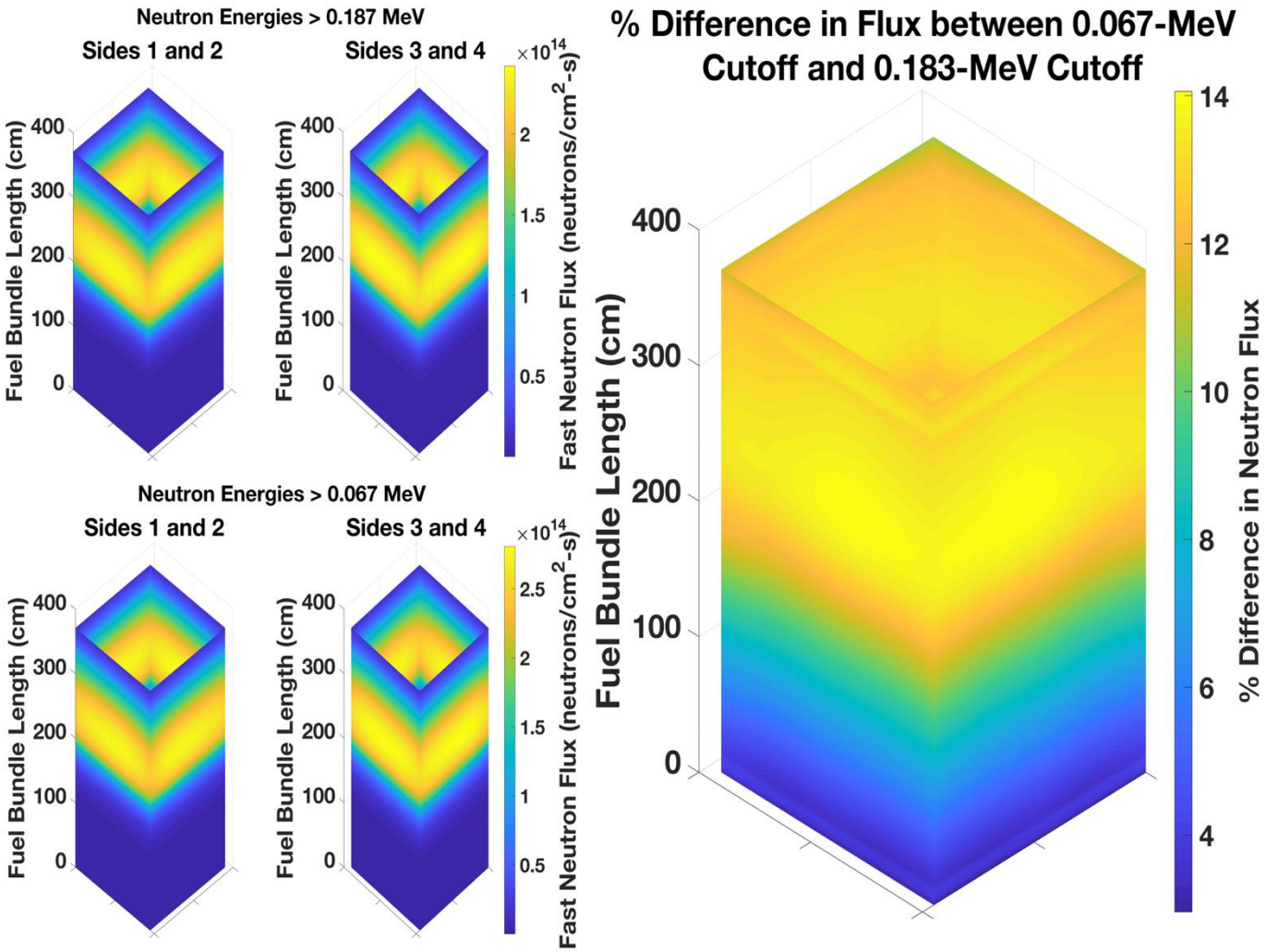

Figure 34: Fast neutron flux distribution in a SiC-SiC channel box using a 0.067 MeV cutoff (top), 0.183 MeV cutoff (bottom), and the percent difference in flux between the two cutoffs (right) with the control blade halfway inserted

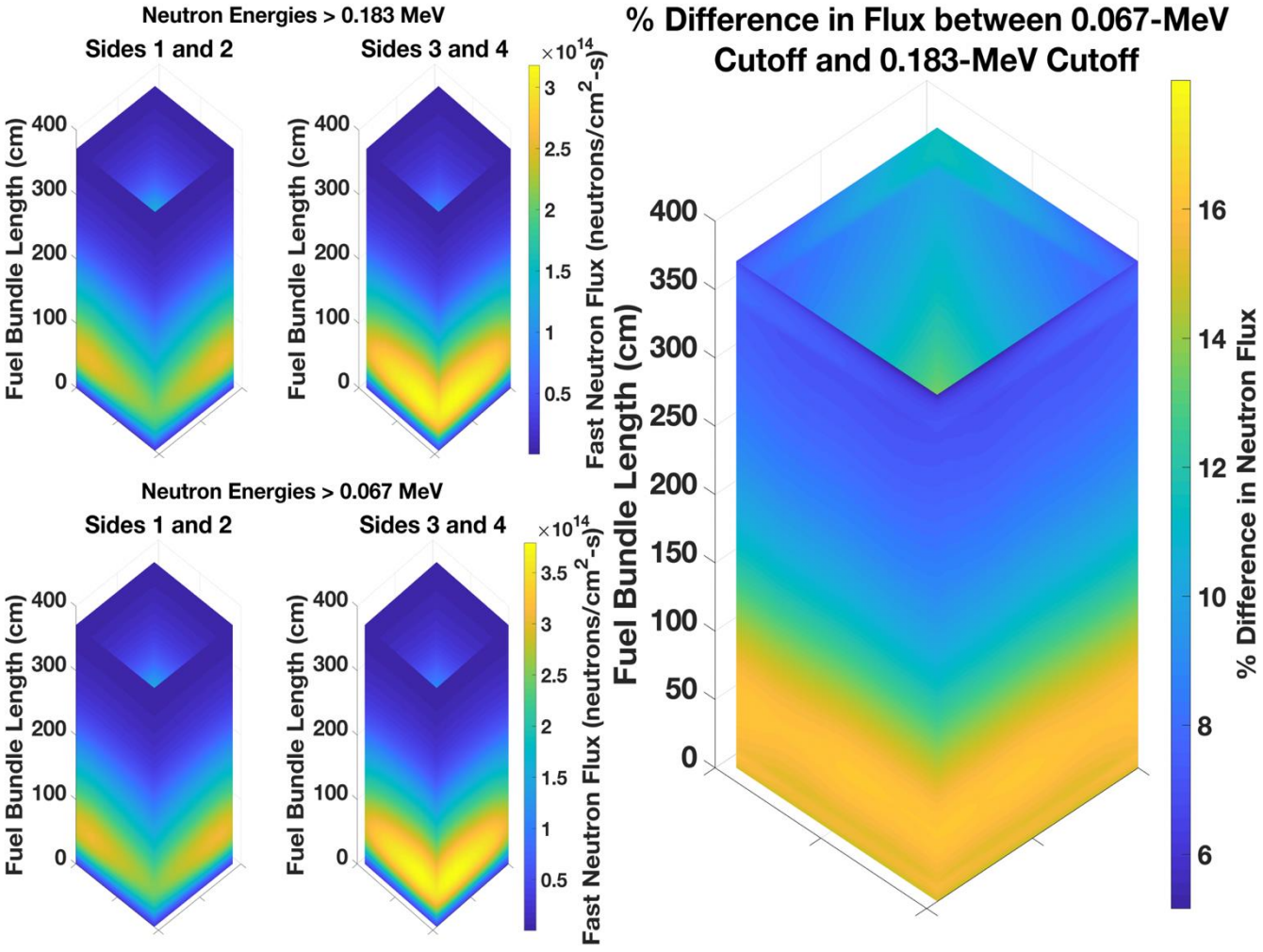

Figure 35: Fast neutron flux distribution in a SiC-SiC channel box using a 0.067 MeV cutoff (top), 0.183 MeV cutoff (bottom), and the percent difference in flux between the two cutoffs (right) with the control blade fully inserted

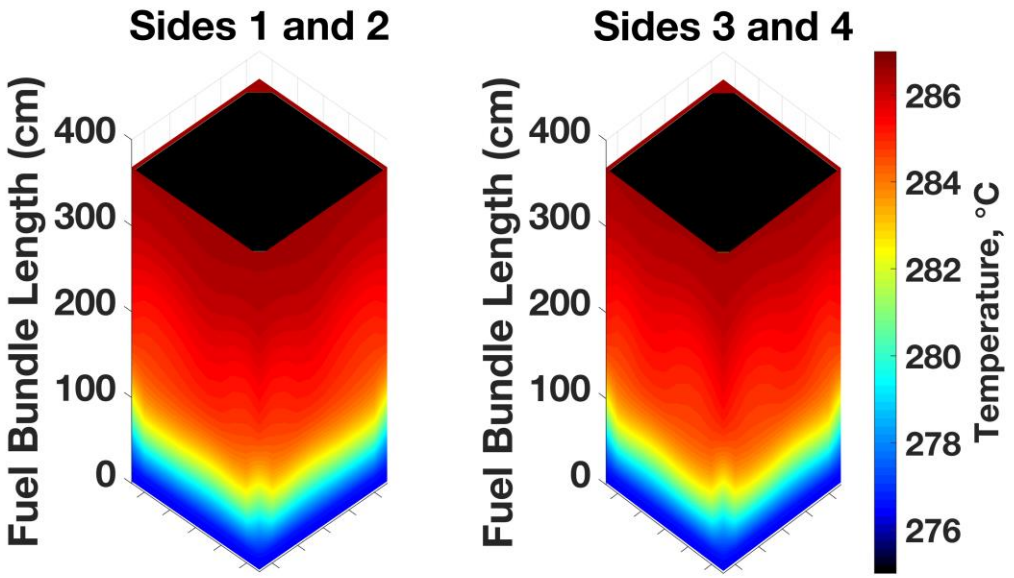

Figure 36: Temperature distribution in the channel box for the case with control blade fully withdrawn

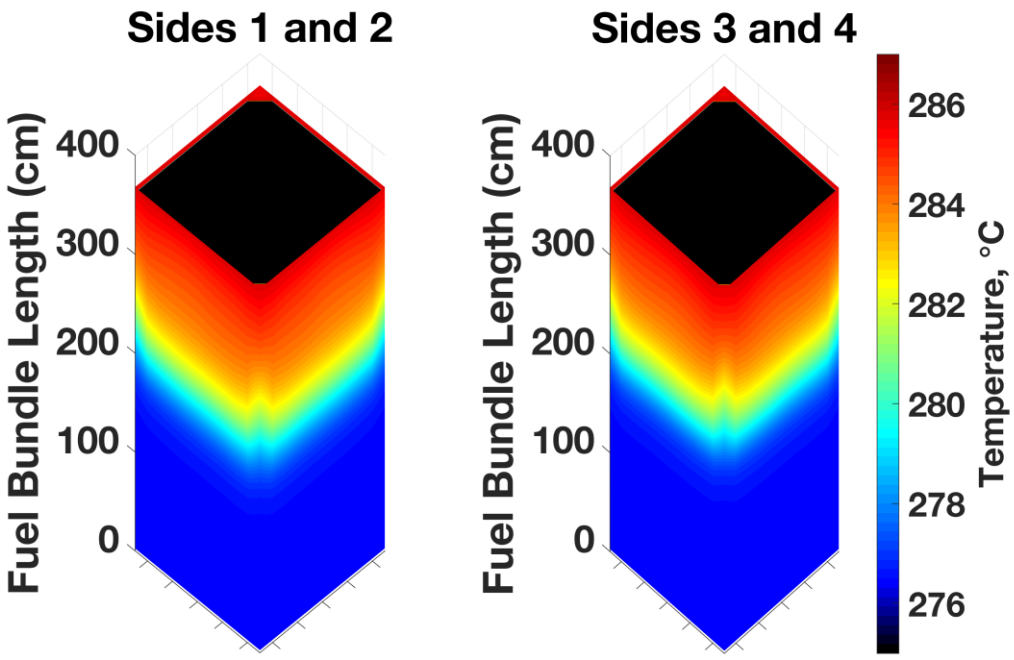

Figure 37: Temperature distribution in the channel box for the case with control blade halfway inserted

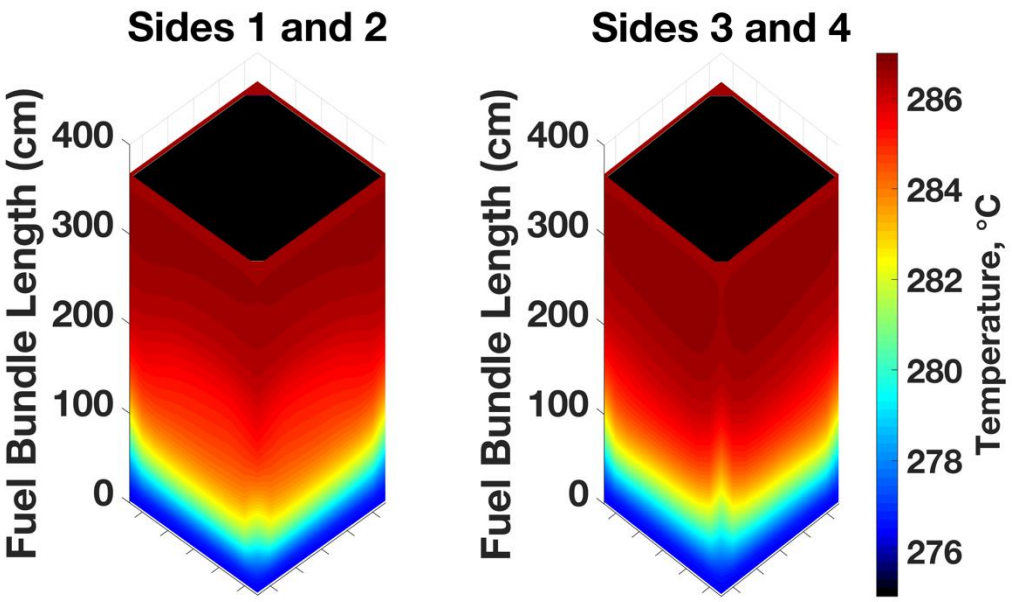

Figure 38: Temperature distribution in the channel box for the case with control blade fully inserted.

approximately 25% less than the peak fast flux calculated in previous work using CTF and Serpent [36]. The difference in peak flux values is caused by using a 3-D method with pin-resolved thermal hydraulic feedback in this study versus a 2-D method using interpolation and averaged thermal hydraulic parameters in the previous study.

The sixteen-assembly mini-core model which contains the control cell previously shown in Figure 21 was ran with SiC/SiC channel boxes surrounding each fuel assembly. Only the case with a fully inserted control blade using 0.067 MeV as the fast neutron cutoff energy has been considered. Fast neutron flux in the channel boxes ranges from 8.34×10^{11} to 4.24×10^{14} neutrons/cm^2-s with an average value of 1.81×10^{14} neutrons/cm^2-s. Figure 39 shows the relative difference of the fast neutron flux from the average value in the SiC/SiC channel boxes. The assembly number designations correspond to those in Figure 21 with Assembly 4 (prominent on the right-hand side of the figure) being closest to the control blade location and Assembly 1 (prominent on the left-hand side of the figure) being the farthest from the control blade The flux gradient ranges from an approximately -99% to 135% difference from the average value, and the figure highlights the significant axial and radial gradient in fast flux that contributes to channel box deformation. Three-dimensional distributions of temperature in the SiC/SiC channel boxes are shown in Figure 40 with the control blade fully inserted.

Figure 39 and Figure 40 show the expected behavior caused by the control blade: the fast flux and temperature are lowest on right-hand side of the figures, which depict the two faces of Assembly 4 nearest the blade. Gradients in the fast neutron flux are the first order cause of channel box deformation, so these results indicate that the Assembly 4 channel box may undergo the most deformation since it has the greatest radial fast flux gradient. Additionally, temperature gradients are the cause of residual deformation once irradiation swelling occurs in the entire channel box, so Assembly 4 may also have the largest degree of post-saturation deformation. However, further analyses are required to confirm these hypotheses.

The purpose of calculating these fast neutron flux and temperature distributions is to use them as boundary conditions in other computational assessments of SiC/SiC channel boxes. One such assessment is the deformation of SiC/SiC channel boxes, which

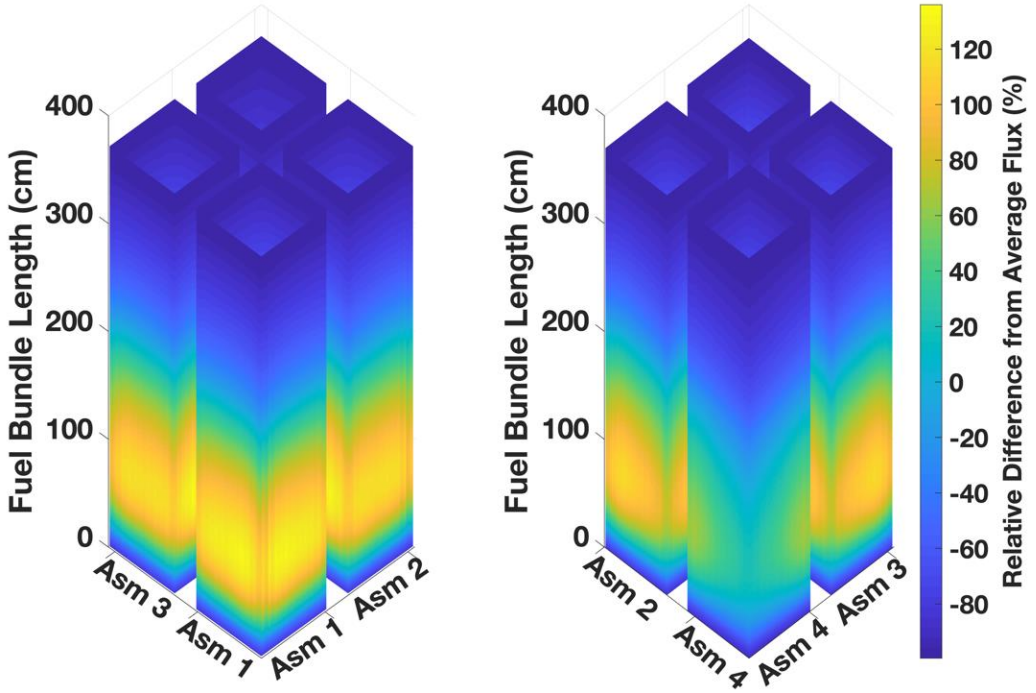

Figure 39: Fast flux distribution in a control cell with a fully inserted control blade

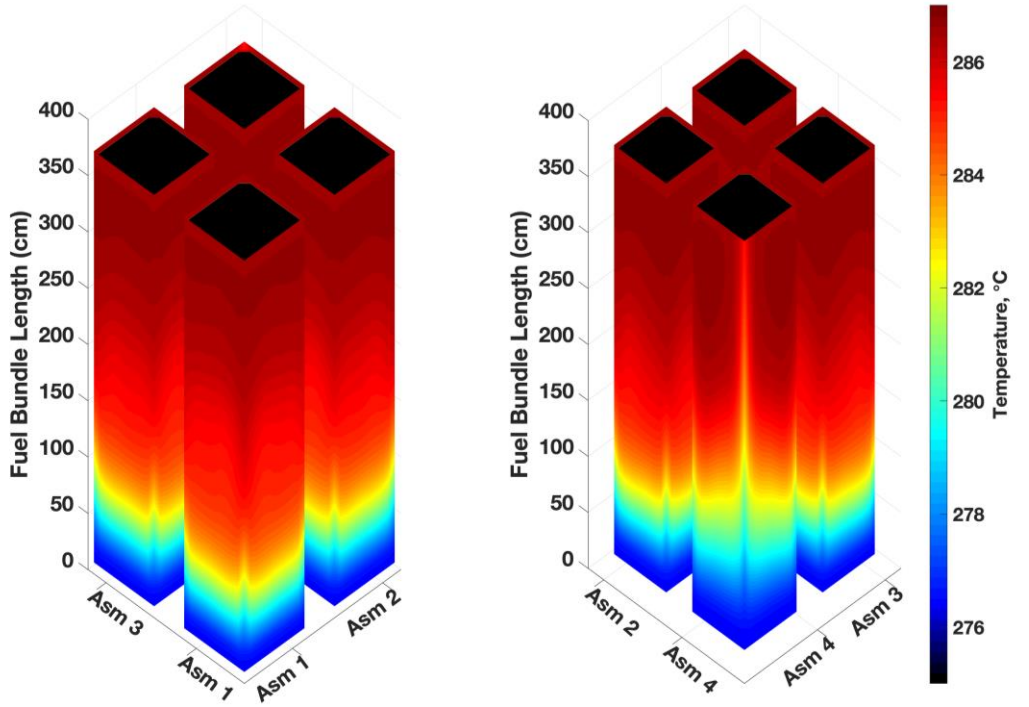

Figure 40: Temperature distribution in a control cell with a fully inserted control blade

is caused by irradiation swelling and is a strong function of fast neutron flux gradients. The fast flux and temperature distributions shown in Figure 33 through Figure 38 were used as boundary conditions in an Abuqus finite difference model developed by Singh et al. [17] that utilized fast flux dependent correlations to calculate channel box deformation over time. Figure 41 shows the total lateral displacement calculated by Singh et al. [17] as a function of time for each control blade configuration and fast flux energy cutoff.

At a high level, this analysis highlights the advanced modeling features available in VERA while also assessing a potential ATF concept. Although a specific case study is presented here, these results pave the way for a number of future studies that take into account other spatial and temporal effects such as control blade history, fuel assembly location within the core, and core shuffling. A primary contribution of this study is an initial assessment of an advanced multiphysics modeling tool through comparisons to currently used regulatory analysis and Monte Carlo tools. The comparisons were favorable and add confidence to the use of VERA for BWR applications. Following the assessments, VERA was used to generate temperature and fast neutron flux boundary conditions in SiC/SiC channel boxes in both single and multiple fuel assmebly models for a variety of control blade configurations. The generation of these boundary conditions using a high-fidelity multiphysics tool is an additional key contribution of this work.

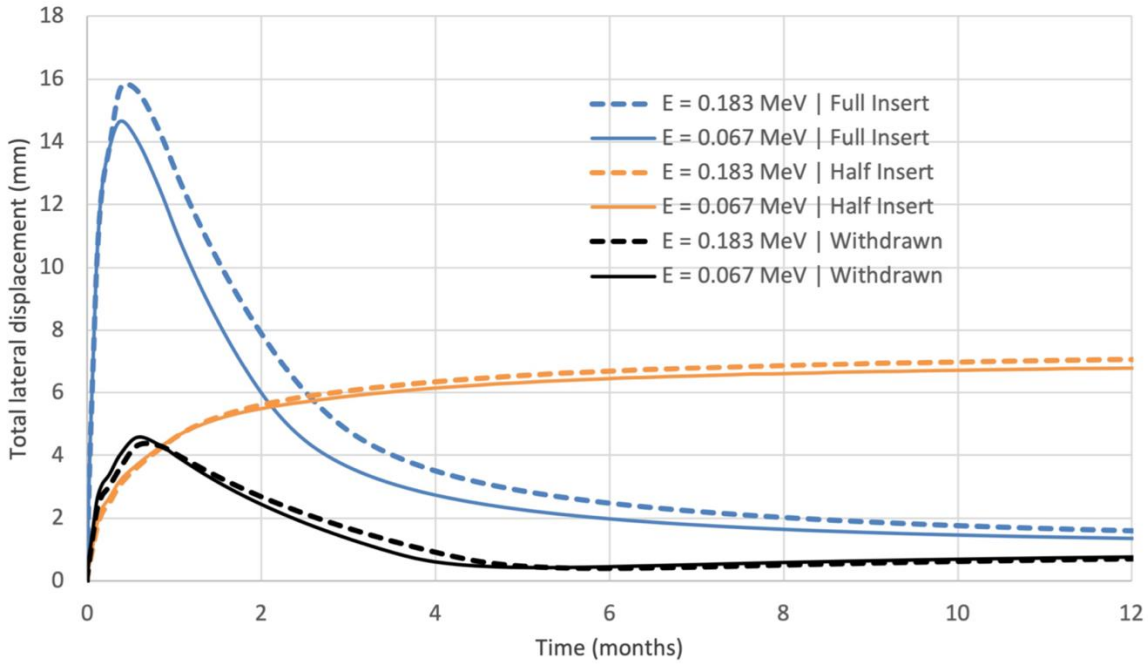

Figure 41: Total lateral displacement of SiC/SiC channel box as a function of time and control blade configuration [17]

CHAPTER 5
REACTOR PERFORMANCE AND SAFETY CHARACTERISTICS OF THN-UN FUEL CONCEPTS IN A PWR

5.1 Motivation for ThN-UN

Among the ATF candidates considered in research and development efforts are composite fuels with UN as one phase. UN fuel provides several advantages over UO_2, most notably a significantly higher thermal conductivity and higher uranium density. UN, though, is known to chemically react and deteriorate in water, and has been shown to do so under water pressure and temperature representative of LWR operating conditions [66], [67], [162], [163]. To combat the reactivity of UN with water, research efforts have investigated the benefits of mixing UN with other fuel forms, such as UO_2 [164], [165] and another ATF candidate, U_3Si_2, driven by the hypothesis that UO_2 or U_3Si_2 may shield UN from degradation in water [26], [166], [163]. However, later experiments at the Los Alamos National Laboratory showed that U_3Si_2 may pulverize and wash out when exposed to PWR coolant chemistry within 30 days at 300°C and can be severely degraded after 1 hour of coolant exposure at 350°C [162], [167].

Another potential composite phase that may shield UN from reacting with water is ThN. The potential benefits and challenges of a thorium-based fuel form were highlighted in Section 2.2.3. To reiterate, the primary benefits of ThN are its thermal conductivity that is greater than both UO_2 and UN and its high melting point. The high thermal conductivity and melting point of both ThN and UN should lead to lower homologous temperatures in a reactor, thus increasing the thermal margin to fuel melt. Further, high thermal conductivity leads to reduced thermal stresses, energy storage, and fission product release in the fuel. Each of these characteristics are beneficial from a reactor performance and safety standpoint [9], [10], [32], [35]. However, thorium is not fissile or fissionable and must transmute to ^{233}U to become fissile. The uranium in UN can provide the neutron source to cause the transmutation, but the introduction of thorium into the fuel will require the use of HALEU that has ^{235}U enrichment between 5 and 20%.

This chapter presents a preliminary analysis of homogenously mixed ThN-UN fuels in a typical PWR pin-cell model. MPACT was used to determine ThN-UN mixture ratios and corresponding ^{235}U enrichments needed to match the cycle length of conventional UO_2 fuel. For verification purposes, these cycle length calculations were compared with results from the Monte Carlo code Serpent. FTC, MTC, SBC, and control rod worth were all determined using MPACT. Further, a comparison of cycle length and reactivity coefficients for ThN-UN fuels that used natural nitrogen, which is almost 100% ^{14}N, and 100% enriched ^{15}N was made. Finally, a thermal hydraulic performance comparison between the ThN-UN mixtures and the UO_2 baseline was made that focused on homologous temperature. This comparison was made using the coupled neutronics and thermal hydraulics capabilities of MPACT and CTF within CASL VERA.

5.2 ThN-UN Fuel Composition for UO_2 Cycle Length Matching

5.2.1 Pin-cell Model Descriptions

Two-dimensional PWR pin-cell models were developed in MPACT to determine the combinations of ThN-UN and ^{235}U enrichments needed to match the cycle length of a pin-cell with 4.90 wt% enriched UO_2 using a 252-group ENDF/B-VII.1 nuclear cross section library [156]. The pin-cell models include a fuel pellet, helium-filled pellet-cladding gap, Zircaloy-4 cladding, and coolant. Table 11 lists the dimensions of the pin-cell model, which are based on the Westinghouse AP1000 design [168].

The P_2 approximation was used for scattering, and all models treated the ^{232}Th and ^{238}U resonances explicitly rather than lumping them together. MPACT was chosen as the primary tool for this analysis due to its speed as a deterministic code, its LWR-focused development, and its ease of coupling to the thermal hydraulic sub-channel code CTF within CASL's VERA. Reflective boundary conditions were applied on all sides of the model. After running the models, the burnup, cycle length, and infinite multiplication factors were adjusted by assuming a three-batch fuel management scheme and 3% neutron leakage, both of which are typical values for large PWRs [169], [170]. A fuel temperature of 900 K was used, and all other temperatures in the model were set to the AP1000 inlet temperature of 552.6 K (535.0°F). The same power density in W/cm^3

Table 11: Dimensions of PWR pin-cell model

Parameter	Value (cm)
Fuel pellet radius	0.4096
Pellet-cladding gap thickness	0.0084
Cladding thickness	0.057
Height	1.0
Pin pitch	1.26

was used in all models and is also equal to that of the AP1000. All ^{235}U enrichments are given in units of wt% ^{235}U /U, while ThN and UN weight fractions are relative to the weight of the entire fuel mixture.

5.2.2 UO_2 Cycle Length Matching and Comparison to Serpent Results

The ^{235}U enrichment required to meet the UO_2 cycle length was determined for a 100% UN case, a 20% (by weight) ThN-80% UN mixture, and a 40% ThN-60% UN mixture. Additionally, a mixture with maximized thorium content was determined by setting the ^{235}U enrichment to 19.90% and adjusting the ThN and UN weight fractions (which also changes the density of the mixture) until the UO_2 fuel cycle was met. Fuel cycle lengths were calculated using the linear reactivity model [169]. The UO_2 cycle length was calculated to be 472 effective full power days (EFPDs), and the nitride-based fuel compositions were accepted if their cycle lengths matched this target value within 3%. The density of UN and ThN can be found in a forthcoming paper by Parker et al. [63], where theoretical densities of 95% and 92% were used for UN and ThN, respectively. Equation (8), previously given in Section 3.4.2 and repeated here for convenience, was used to calculate the density of the mixtures, where x_i and ρ_i refer to the weight fraction and density of each constituent in the mixture, respectively.

$$\rho = \sum x_i \rho_i \tag{8}$$

The nitride-based fuel compositions found to match the UO_2 cycle length are listed in Table 12, which also lists the three-batch discharge burnup of the fuels, all of which are lower than the calculated UO_2 discharge burnup of 56.06 GWd/t. Discharge burnup is lower for the UN and ThN-UN fuels because of their greater heavy metal loading (due to increased density) and increased absorption from ^{232}Th, ^{238}U, and ^{14}N. Note that an increase in the neutron leakage above 3% would cause a larger reduction in the discharge burnup for the ThN-UN and UN fuel forms than for UO_2 and would therefore increase the ^{235}U enrichment needed in the ThN-UN and UN fuels to match the UO_2 cycle length.

These mixtures were determined using natural nitrogen, which is more than 99% ^{14}N. UN fuels have been considered which are enriched to 90% ^{15}N or more because of

Table 12: ThN-UN mixtures that approximately match the UO_2 cycle length

Thorium Content (wt%)	UN content (wt%)	^{235}U Enrichment (wt% $^{235}U/U$)	Cycle Length (EFPD)	Discharge Burnup (GWd/t)
20.0	80.0	7.80	471	41.81
40.0	60.0	11.10	472	43.68
66.0	34.0	19.90	469	45.99
0	100	5.20	470	38.04

its smaller absorption cross section in the thermal region compared to ^{14}N [163], [171], but doing so increases production costs, and natural nitrogen is the current default in the VERA modeling suite. N-15 enrichment is also preferable because of the (n,p) reaction that occurs in ^{14}N, which produces the radioactive ^{14}C and poses a disposal issue. Brown, Todosow, and Cuadra [26] consider the neutronic penalty caused by using natural nitrogen rather than ^{15}N enrichment. Section 5.3.2 of this article recalculates the ^{235}U enrichments needed to match the UO_2 cycle length for 20% ThN-80% UN, 40% ThN-60% UN, and UN cases, as well as the maximum possible weight fraction of ThN for a ^{235}U enrichment of 19.90% using 100% enriched ^{15}N.

Because MPACT is a deterministic code optimized for LWR analysis and traditional UO_2 fuel, the predictions of k_{eff} as a function of burnup for the ThN-UN mixtures are compared to predictions by the Monte Carlo code Serpent for verification. Figure 42 shows a comparison of the three-batch multiplication factor throughout the cycle as predicted by MPACT and Serpent, as well as the absolute difference between the two codes in pcm for UO_2, UN, and all ThN-UN mixtures. A neutron leakage of 3% is assumed in Figure 42. At beginning of cycle (BOC), the difference in k_{eff} between the two codes is 100–500 pcm for all cases. Brown et al. (2014) [163] show that differences in k_{eff} calculated by Serpent and TRITON for UN fuels of varying densities at BOC were between 290 and 327 pcm when a 238-group cross section library was used in TRITON. Serpent predicted a greater k_{eff} at BOC but a smaller k_{eff} at end of cycle (EOC) for all cases. Note that the Serpent continuous energy library is based on the ENDF/B-VII.0 data library [157], whereas the MPACT models used ENDF/B-VII.1 data, which may explain some of the differences between predictions from the two codes. The behavior trends between the two codes were consistent across each enrichment and fuel type considered.

A comparison of the ^{232}Th and ^{233}U mass throughout the cycle calculated by MPACT and Serpent is shown in Figure 43. The relative difference in mass calculations between MPACT and Serpent is less than 1.2% for ^{233}U and less than approximately 0.03% for ^{232}Th across all burnup steps.

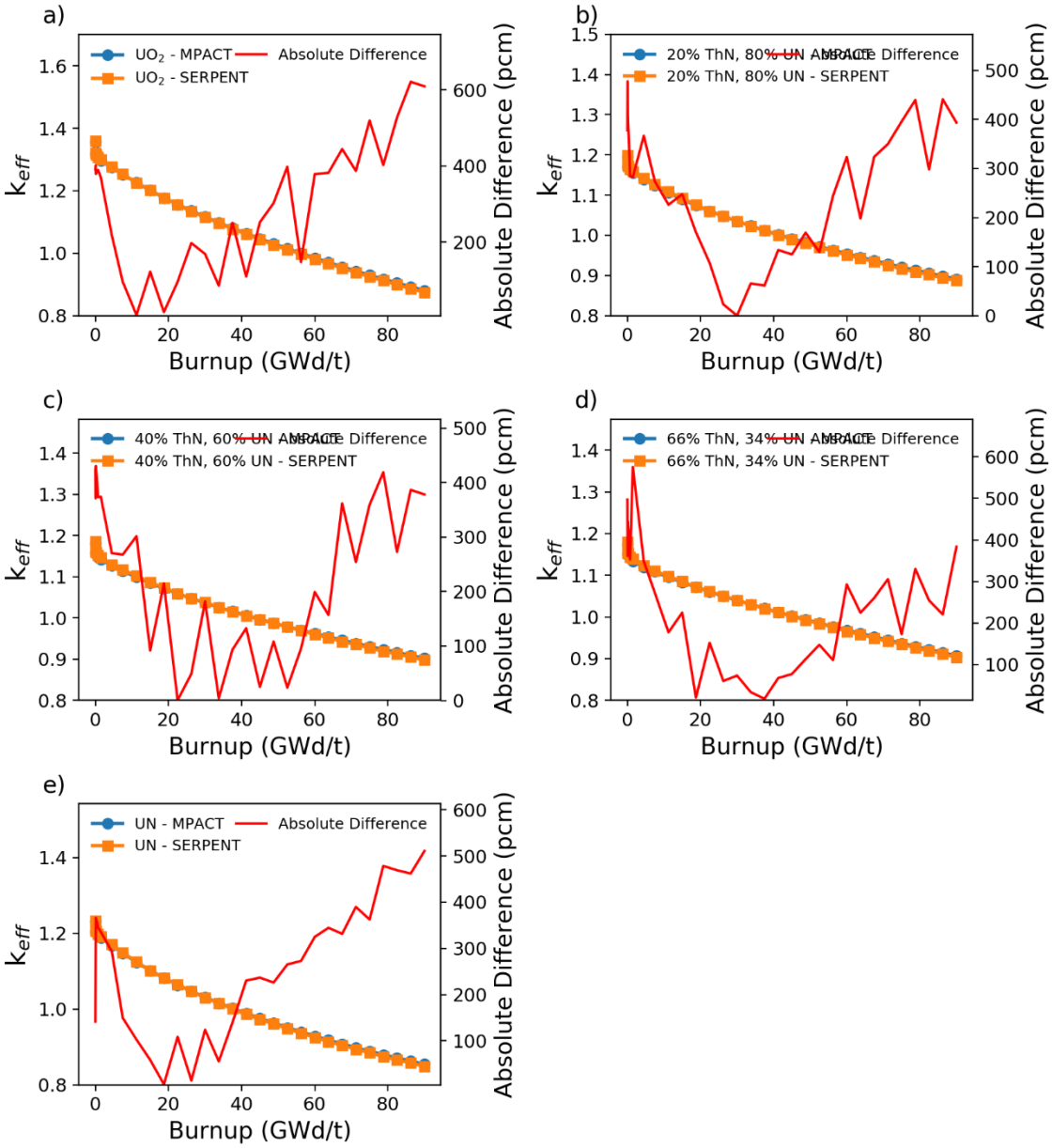

Figure 42: Comparison of k_{eff} calculated by MPACT and Serpent for a) UO_2, b) 20% ThN-80% UN, c) 40% ThN-60% UN, d) 66% ThN-34% UN, and e) UN

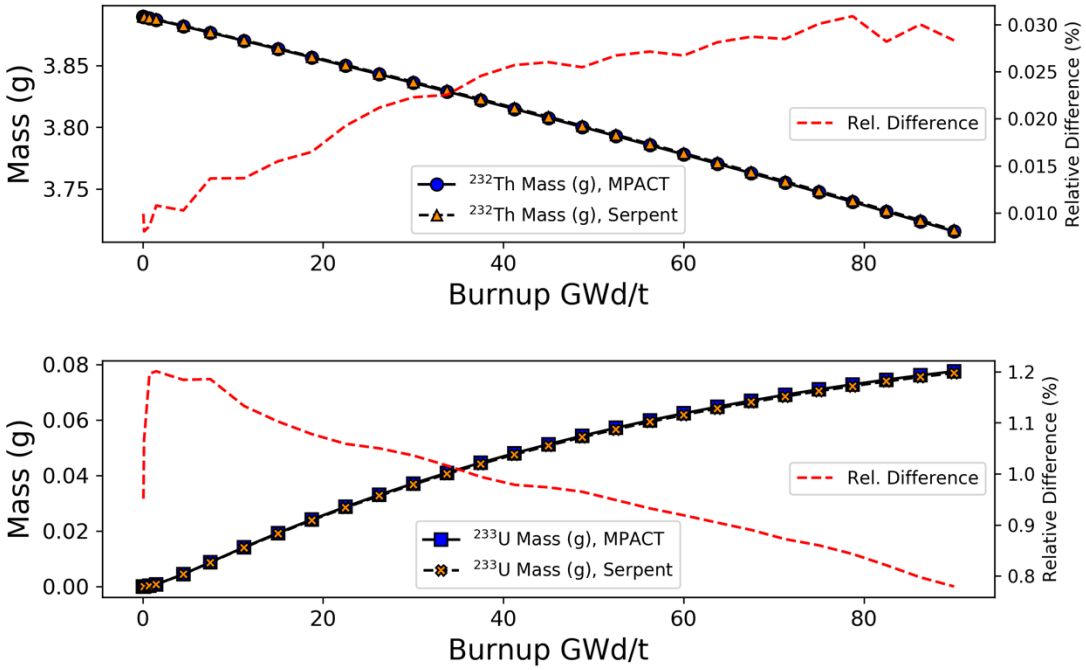

Figure 43: Comparison of ^{232}Th and ^{233}U mass as a function of burnup in the 66% ThN, 34% UN mixture

5.3 Fuel Performance of ThN-UN

5.3.1 Flux Spectra Characterization and Reactivity Coefficients

Normalized neutron flux spectra at BOC calculated using MPACT are shown in Figure 44 for the thermal and intermediate energy regimes and in Figure 45 for the fast energy regime. All spectra are typical of a thermal LWR, but UN has a harder spectrum than UO_2 due to the greater amount of ^{238}U, and the ThN-UN fuels have an even harder spectrum than UN because of the presence of thorium. However, the neutron spectrum is softer for the ThN-UN mixed fuels at EOC compared to UN due to the build-up of ^{233}U throughout the cycle. This is shown in Figure 46 where the BOC and EOC thermal and intermediate flux spectra are shown on the left axis for UO_2, UN, and 66% ThN-34% UN. The EOC to BOC spectral ratios for the same three fuel types are plotted on the right axis of Figure 46 and show that 66% ThN-34% UN has the greatest EOC/BOC spectral ratio for neutron energies below approximately 1 eV. UN has the lowest EOC/BOC spectral ratio, meaning it hardened the most throughout the cycle.

MPACT was used to calculate the FTC, MTC, SBC, and control rod worth, for each of the ThN-UN mixtures listed in Table 12. These calculations were performed as a function of burnup and compared to the UO_2 reactivity coefficients. The FTC is shown in Figure 47, and the MTC is shown in Figure 48. Fuel temperatures of 800 K and 900 K were used to calculate the FTC, and moderator temperatures of 550 K and 585 K were used to calculate the MTC. The corresponding density of water at 550 K and 585 K were also included in the branch cases, so both spectral and density effects were captured. Figure 49 shows the impact of boron concentration on the MTC for the UO_2 and 66% ThN-34% UN cases using soluble boron concentrations of 0, 500, and 1,000 ppm. The SBC is shown in Figure 50 and was calculated using boron concentrations of 0 and 1,000 ppm at each burnup step. The pin-cell model described in Section 5.2.1 was used to calculate the FTC, MTC, and SBC. To calculate the control rod worth shown in Figure 51, a 2-D quarter-symmetry 17 × 17 fuel assembly model with silver-indium-cadmium (Ag-In-Cd) control rods was used.

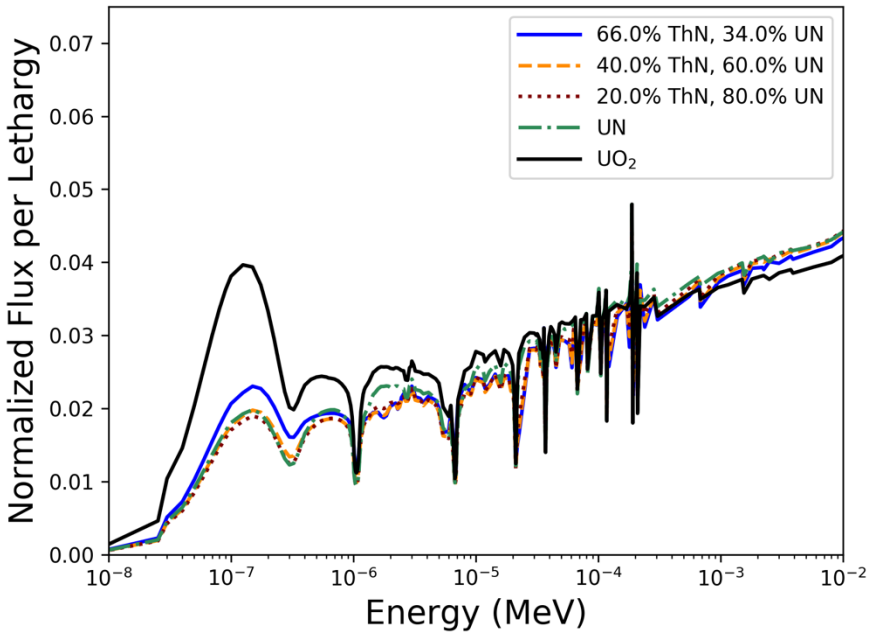

Figure 44: Thermal and intermediate neutron flux spectra at BOC for UO_2, UN, and ThN-UN mixtures

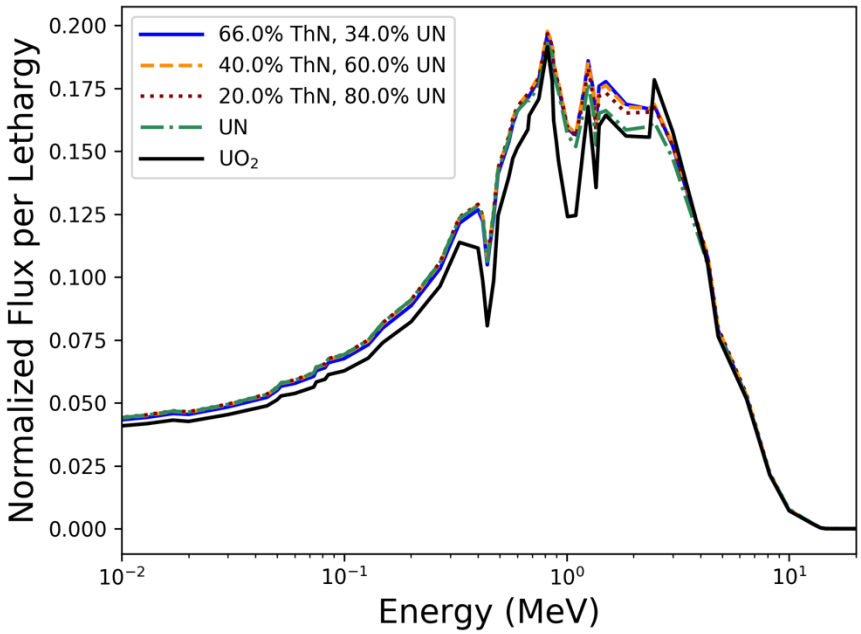

Figure 45: Fast neutron flux spectra at BOC for UO_2, UN, and ThN-UN mixtures

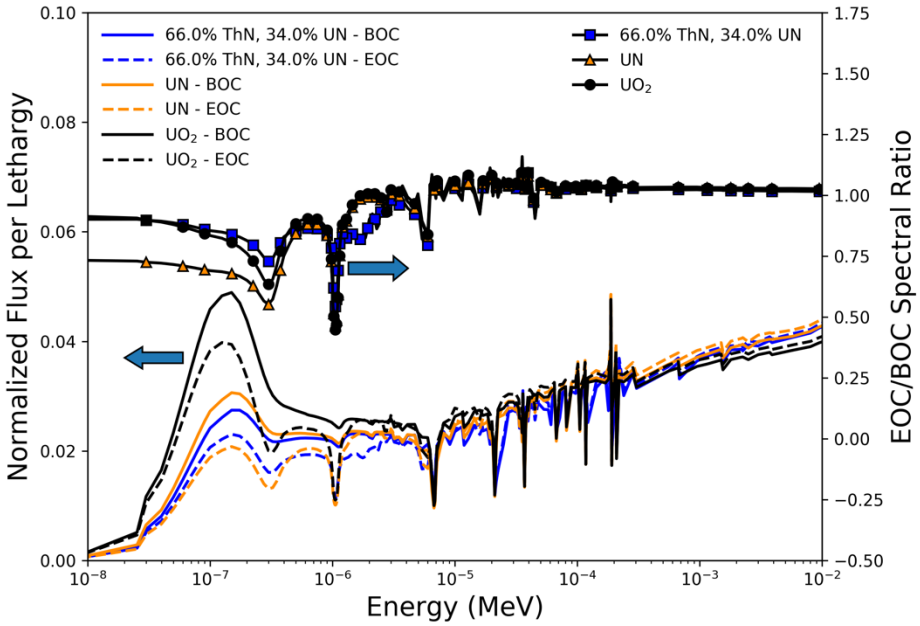

Figure 46: Comparison of BOC and EOC thermal and intermediate flux spectra for UO_2, UN, and 66% ThN-34% UN

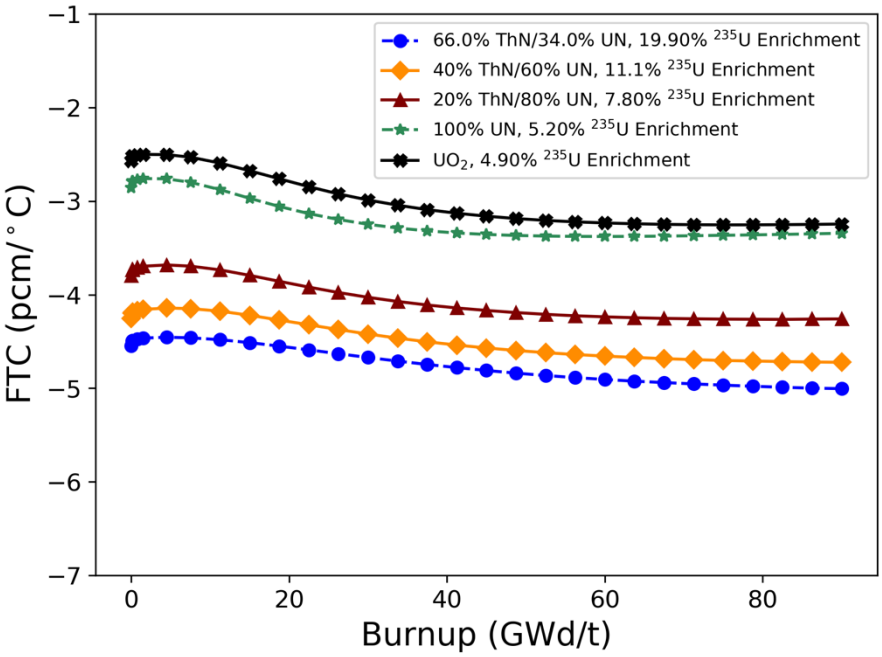

Figure 47: FTC of UO_2, UN, and ThN-UN fuels as a function of burnup

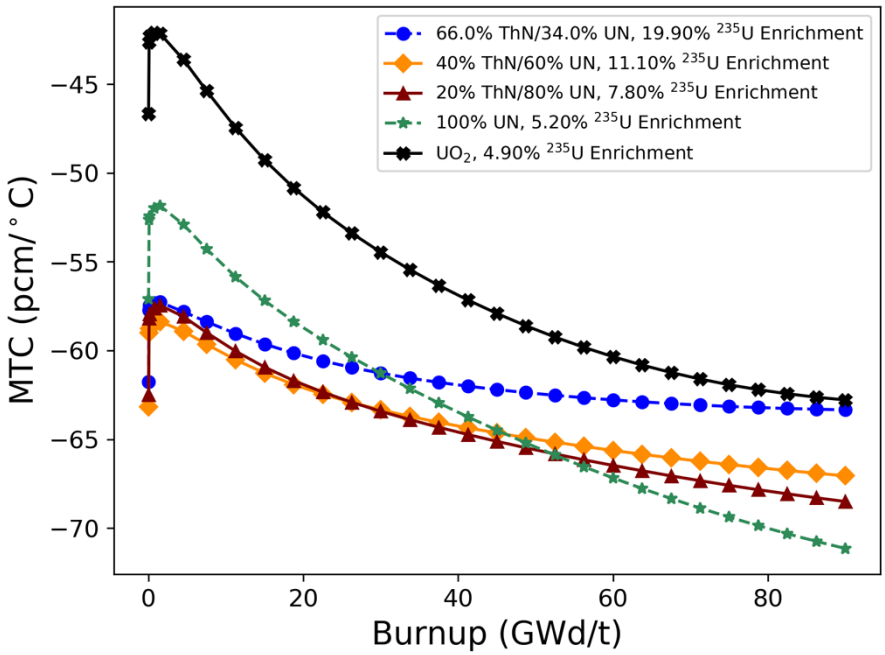

Figure 48: Moderator temperature coefficient of UO_2, UN, and ThN-UN fuels as a function of burnup

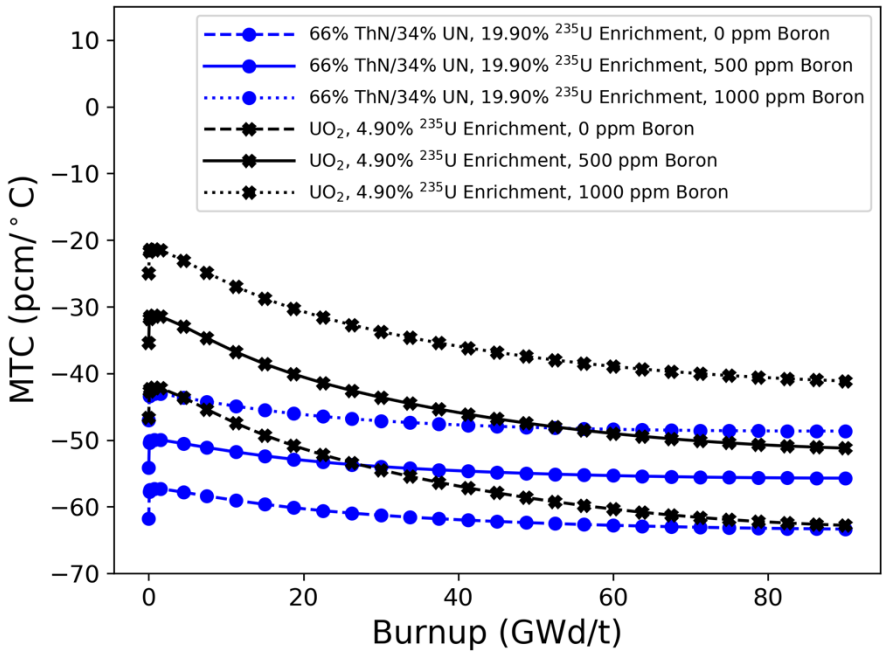

Figure 49: Impact of boron on moderator temperature coefficient for UO_2 and 66% ThN-34% UN

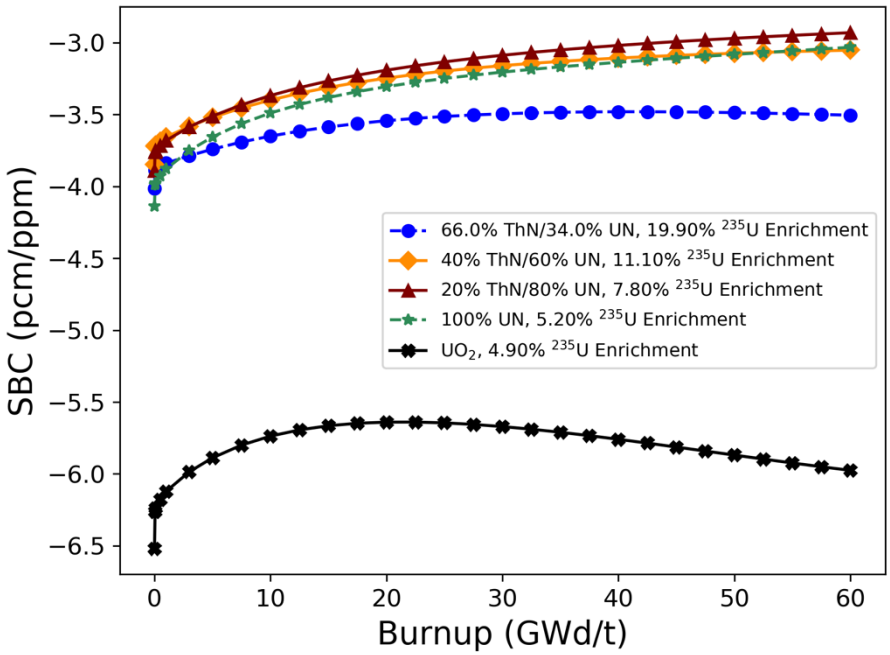

Figure 50: Soluble boron coefficient of UO_2, UN, and ThN-UN fuels as a function of burnup

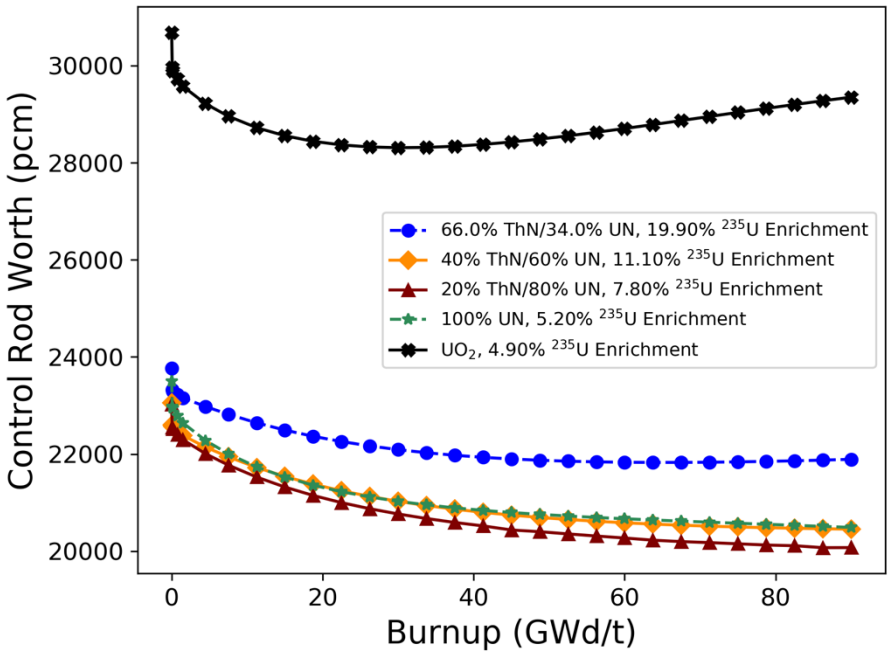

Figure 51: Control rod worth of UO_2, UN, and ThN-UN fuels as a function of burnup

Greater fuel density, increased parasitic absorption, reaction yields (e.g. ^{233}U production), and evolution of the isotopics with burnup are all factors in explaining why the reactivity coefficients and control worth for the nitride fuel forms differ from UO_2. Each of these fuels has a negative FTC for the entire cycle, which is a desirable safety feature. The FTC is similar in magnitude for each of the fuel types but is more negative for the nitride-based fuels than for UO_2 because of the greater sensitivity of the reproductive factor, η, due to increased fuel density and increased resonance absorption from ^{238}U and ^{232}Th. Increased heavy metal loading in the UN and ThN-UN cases reduces the moderator-to-fuel ratio and enhances under-moderation. This is the primary cause of the more negative MTC for the nitride cases compared to the UO_2 case. Production of ^{233}U throughout the cycle and differences in BOC and EOC cross sections cause the ThN-UN mixtures to have a less negative MTC at EOC compared to UN. For example, at BOC, the 66% ThN-34% UN case has the largest thermal capture cross section and UN has the smallest out of the nitride-based fuels, but the opposite is true at EOC.

Increased absorption causes the nitride-based fuels to have lower control rod worth and SBC than UO_2. U-233 production and cross section evolution dictate the change in control worth with burnup for each nitride fuel. Additionally, each fuel type considered has a different equilibrium ^{135}Xe concentration, which impacts the amount of parasitic absorption in the fuel and therefore impacts the reactivity coefficients and control worth. To further illustrate these points, the BOC and EOC two-group macroscopic capture cross sections (Σ_c) for each fuel type are shown in Table 13, and the mass of ^{135}Xe in each pin-cell model as a function of burnup is shown in Figure 52. Table 14 lists the ranges of reactivity coefficients for each fuel type found in this study and compares them to the limits specified in the AP1000 Design Control Document (DCD) [168]. Note that the AP1000 DCD limits take into account a range of fuel and moderator temperatures across varying operating conditions, whereas only 900 K and 800 K were used as fuel temperatures and 550 K and 585 K were used as moderator temperatures in this study. The MTCs listed from this study are at 0 boron concentration.

Table 13: Two-group macroscopic capture cross sections for each fuel form at BOC and EOC

Fuel	Fast Energy Σ_c (cm^{-1})		Thermal Energy Σ_c (cm^{-1})	
	BOC	EOC	BOC	EOC
UO_2	0.0223	0.0306	0.0837	0.1936
UN	0.0310	0.0389	0.1476	0.3348
20% ThN – 80% UN	0.0325	0.0396	0.1587	0.3228
40% ThN – 60% UN	0.0322	0.0389	0.1684	0.3073
66% ThN – 34% UN	0.0306	0.0366	0.1755	0.2735

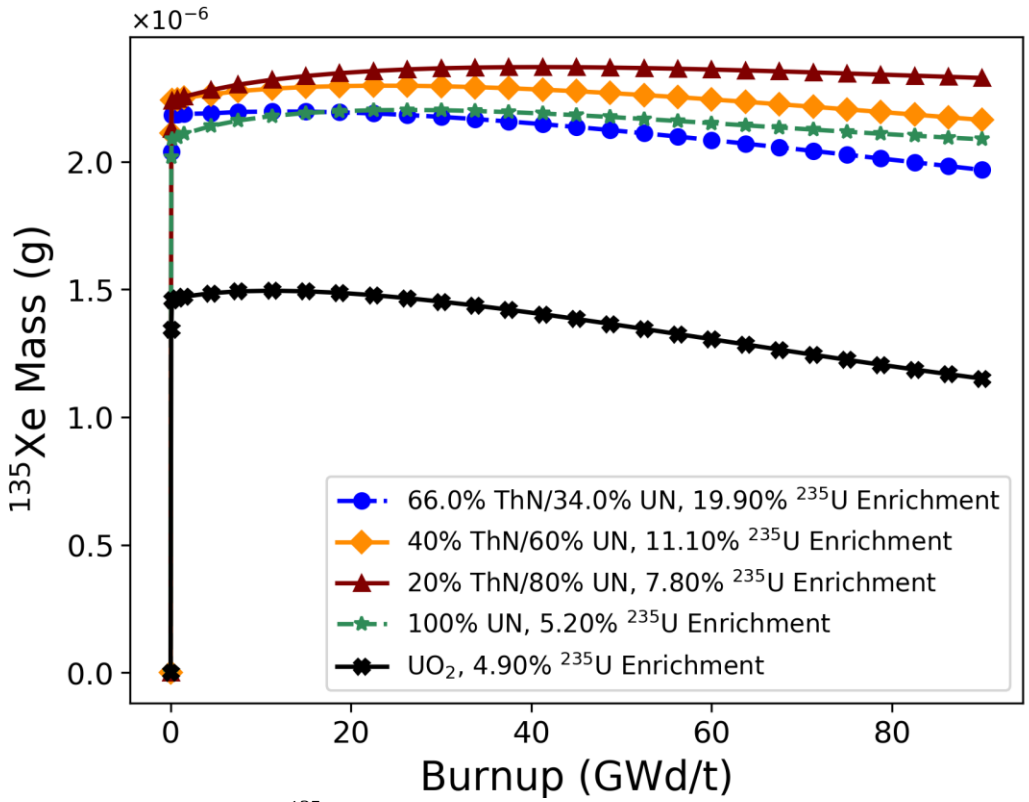

Figure 52: ^{135}Xe mass as a function of burnup for each fuel form

Table 14: Comparison of reactivity coefficients to AP1000 DCD limits

Case	FTC (pcm/°C)	MTC (pcm/°C)	SBC (pcm/ppm)
AP1000 DCD	-6.3 to -1.8	-72 to 0	-13.5 to -5.0
UO_2	-3.3 to -2.5	-62.8 to -42.1	-6.5 to -5.6
UN	-3.4 to -2.8	-71.1 to -51.9	-4.1 to -3.0
20% ThN – 80% UN	-4.3 to -3.7	-68.5 to -57.5	-3.9 to -2.9
40% ThN – 60% UN	-4.7 to -4.1	-67.1 to -58.4	-3.8 to -3.1
66% ThN – 34% UN	-5.0 to -4.5	-63.3 to -57.3	-4.0 to -3.5

All FTC and MTC values calculated in this study fall within the AP1000 DCD limits, but the boron coefficients for UN and the ThN-UN mixtures are less negative than the specified limits. The larger absolute values of the UN and ThN-UN MTCs, along with the significantly lower control rod worth for these fuels shown in Figure 51, may pose an issue with shutdown margin. Typically, a shutdown margin of 1.0–1.3% is required under all reactor conditions, the most limiting of which occur at cold moderator temperatures such as cold zero power or during a main steam line break in a PWR. In their analysis of a Th-MOX-fueled PWR core, Fridman and Kliem [172] also predicted a reduced boron worth and control rod worth in the Th-based fuels compared to a UO_2 baseline. They addressed this problem by suggesting that the soluble boron be enriched to 40% ^{10}B and by replacing control rods made of Ag-In-Cd, which is the more common control rod material in current PWRs, with control rods made of higher absorbing B_4C. The nitride-based fuels have less excess reactivity, as was shown in Figure 42, which may help compensate for the lower boron and control rod worth, but similar design changes may be required for a ThN-UN-fueled reactor.

5.3.2 Impact of 100% Enriched ^{15}N

All results presented thus far in the study used natural nitrogen, which is primarily ^{14}N, in UN and ThN phases. Previous studies have shown that ^{15}N enrichment boosts reactor and fuel performance over natural nitrogen since ^{14}N is a significant neutron absorber at thermal energies [163], [26], [171]. The differences in fuel performance from using 100% enriched ^{15}N in UN and ThN-UN fuels in terms of required ^{235}U enrichment and RTCs are quantified in this section.

The ^{235}U enrichments required to approximately match the 4.90%-enriched UO_2 cycle length of 472 EFPDs are listed in Table 15. With 100% ^{15}N, the relative decrease in required ^{235}U enrichment for 20% ThN-80% UN, 40% ThN-60% UN, and UN from the natural nitrogen cases are 24.4%, 23.4% and 25%, respectively. The maximum possible ThN weight fraction increased from 66 wt% to 73.5 wt%, a relative increase of 11.4%. To illustrate the impact of ^{15}N enrichment on RTCs, the 40% ThN-60% UN mixture and 100% UN is considered. Figure 53 shows the FTC as a function of burnup for 40% ThN-

Table 15: ThN-UN mixtures with enriched ^{15}N that approximately match the UO_2 cycle length

Thorium Content (wt%)	UN Content (wt%)	^{235}U Enrichment (wt% $^{235}U/U$)	Cycle Length (EFPD)
20.0	80.0	5.90	475
40.0	60.0	8.50	478
73.5	26.5	19.90	480
0	100	3.90	478

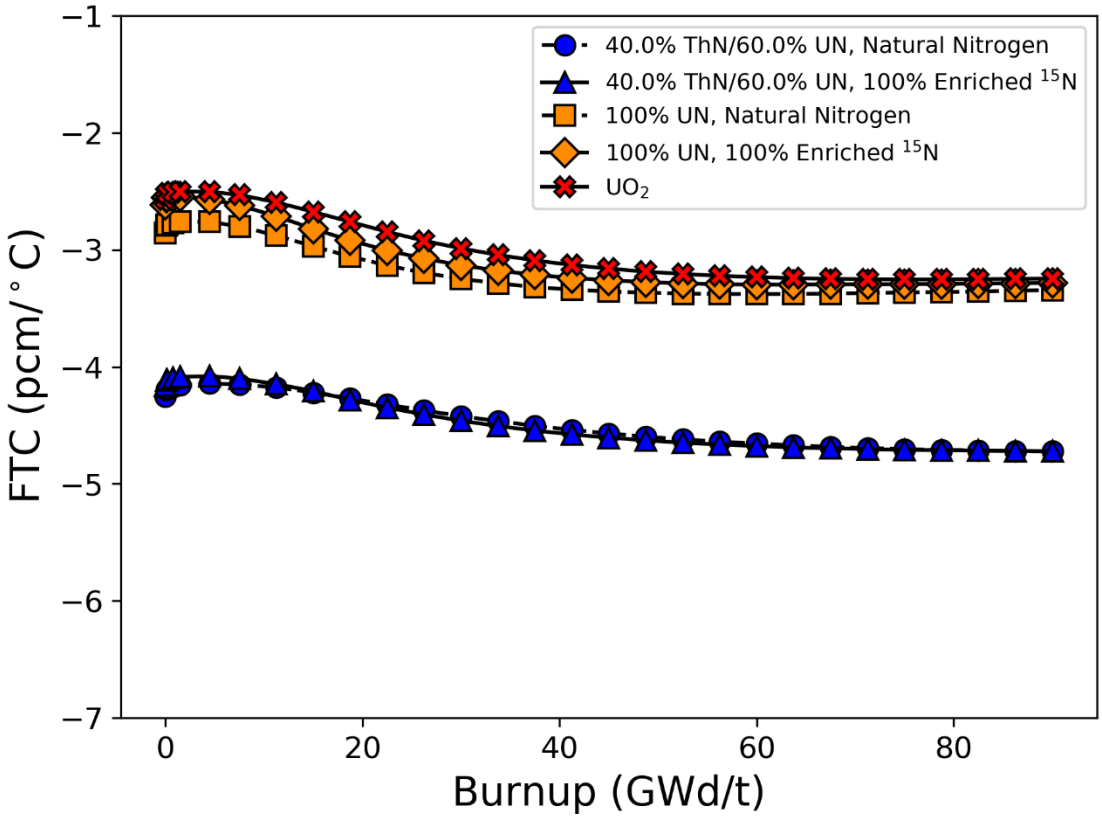

Figure 53: FTC for UO_2, 40ThN-60UN with natural nitrogen and 40ThN-60UN with 100% ^{15}N enrichment

-60% UN and 100% UN with natural nitrogen and 100% enriched ^{15}N, as well as the UO_2 reference case. Similar comparisons are shown in Figure 54–Figure 56 for MTC, SBC, and control rod worth, respectively. There is little difference in FTC between the natural nitrogen and enriched ^{15}N cases since this phenomenon is caused by the resonance broadening of the fertile and fissile material (primarily ^{238}U and ^{232}Th). The MTC is similar in magnitude between the natural nitrogen and enriched ^{15}N cases since they both have approximately the same heavy metal loading and therefore the same moderator-to-fuel ratio. The small increase in the MTC for the enriched ^{15}N cases is due to a lower equilibrium ^{135}Xe concentration. By enriching the fuel with ^{15}N, the neutron flux spectrum softens, which increases the worth of soluble boron and the control rods for the ThN-UN and UN cases. The control worth increases less for UN because it is the denser fuel, and the absorption from ^{238}U is greater than the combined absorption from ^{238}U and ^{232}Th in the ThN-UN fuel. While the control worth is still not equivalent to that in a UO_2 system and is still outside of the AP1000 DCD limits, the shutdown margin issue is somewhat mitigated by ^{15}N enrichment.

5.3.3 Thermal Performance

A 3-D fuel pin model was developed to evaluate the thermal performance of ThN-UN fuels relative to UO_2. The model utilizes VERA's thermal–hydraulics–to–neutronics coupling capability between CTF and MPACT. The fuel pin design is based on the AP1000 design, with the power and coolant mass flow rate scaled for a single pin and four surrounding subchannels. The same power density in W/cm^3 was used for all fuel forms. CTF's dynamic gap conductance model was employed. Built-in thermal properties for Zircaloy-4 cladding were used for all cases, and built-in properties for UO_2 were used for that case. Crossflow between the four CTF sub-channels was modeled using the CTF-default single-phase mixing factor of 0.037. The thermal conductivity and heat capacity for ThN and UN found in the forthcoming paper by Parker et al. [13] were used, and the thermal properties for the ThN-UN mixtures were estimated for calculation purposes using the respective volume fractions of each phase. The thermal conductivity and specific heat capacity of UN, ThN, and the ThN-UN mixtures used in the CTF

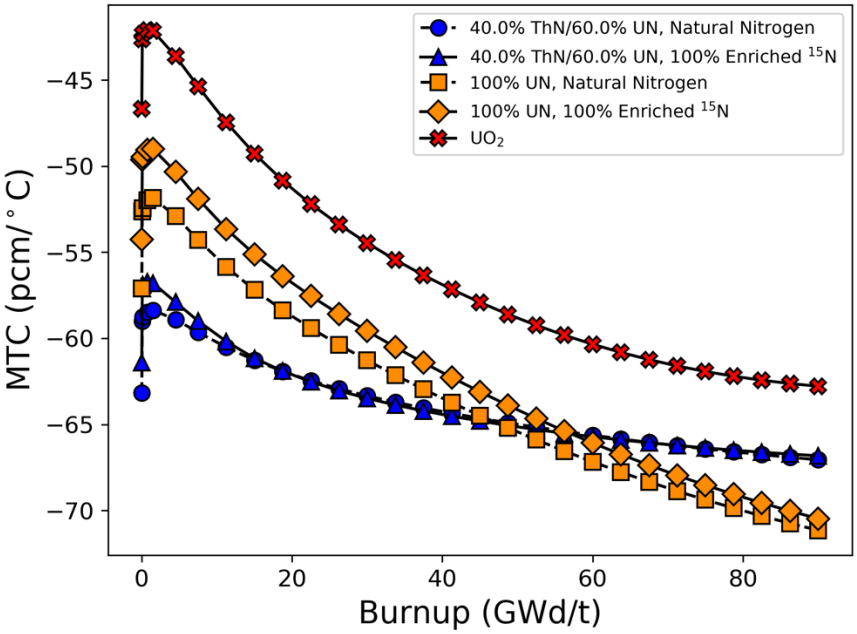

Figure 54: MTC for UO_2, 40ThN-60UN with natural nitrogen, and 40ThN-60UN with 100% ^{15}N enrichment

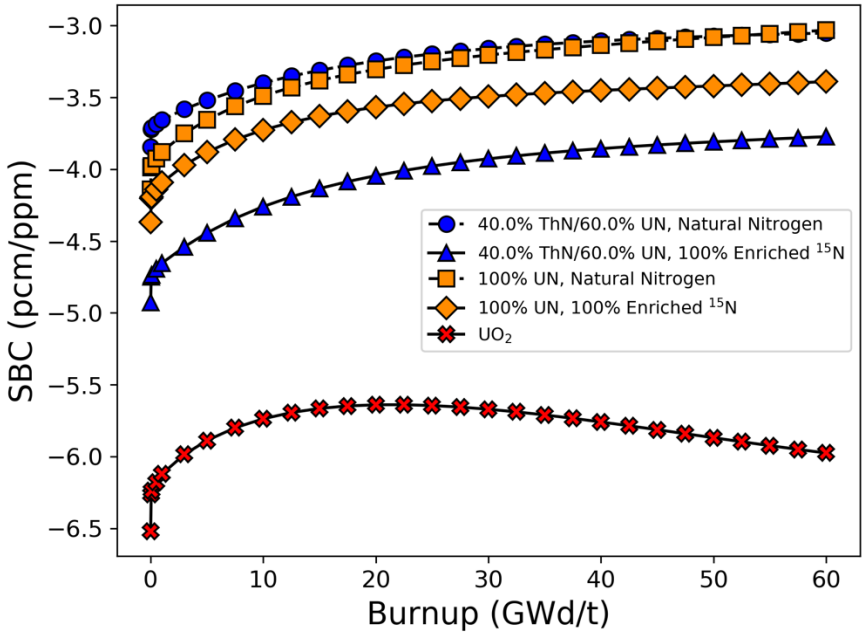

Figure 55: SBC for UO_2, 40ThN-60UN with natural nitrogen, and 40ThN-60UN with 100% ^{15}N enrichment

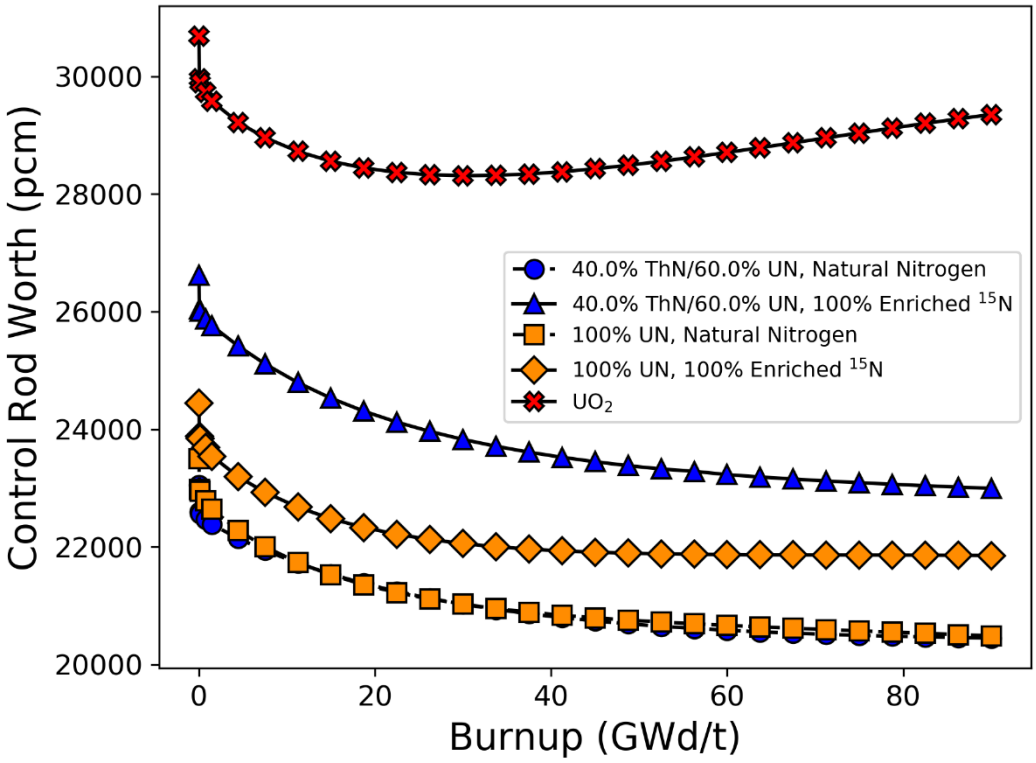

Figure 56: Control rod worth for UO_2, 40ThN-60UN with natural nitrogen, and 40ThN-60UN with 100% ^{15}N enrichment

models are shown in Figure 57 and Figure 58, respectively.

Figure 59 presents the calculated axial dependence of homologous temperature in the fuel pin for the different fuel forms at BOC, and the maximum homologous temperature as a function of burnup for each fuel form is shown in Figure 60. The homologous temperature is the ratio of the maximum fuel temperature (fuel centerline temperature) to the melting (or disassociation) temperature of the fuel. For UO_2 and 100% UN, a melting temperature of 3,123.2 K (2,850°C) was used, and for the ThN mixtures, a melting temperature of 3,063.2 K (2,790°C) was used.

The maximum homologous temperature reached at BOC was 0.34 for UO_2, and it was between 0.18 and 0.20 for all UN and ThN-UN cases. As a function of burnup, the homologous temperature for UO_2 peaks at approximately 0.42, but never gets above 0.21 for UN or any ThN-UN mixture. The change in homologous temperature as a function of burnup is caused by the shifting relative power profile in the rod. Note that the same thermal properties for fuel were used at all burnup steps. The significantly lower homologous temperature obtained using UN and ThN-UN fuels illustrates the enhanced thermal safety margin and accident tolerance of nitride-based fuels over oxide fuels. Although this calculation was performed under normal operating conditions, the nitride-based fuels may also have an improved safety margin during an accident scenario, thus reducing the likelihood of fuel melting and fission product release. An additional benefit from the greater thermal conductivity and smaller axial temperature gradient shown in Figure 59 is that there will be smaller thermal stresses induced in the fuel pellets and cladding, which may reduce the likelihood of pellet cracking and fission product release.

5.4 Discussion

A preliminary evaluation of composite ThN-UN fuel forms under normal PWR operating conditions was performed using CASL's neutronics and thermal hydraulics tools MPACT and CTF within the VERA modeling suite. There are two primary drivers for pursuing this fuel form. First, ThN and UN both have high thermal conductivity compared to conventional UO_2, which would provide performance and safety benefits in an LWR. Second, each phase may mitigate the main challenges associated with the other

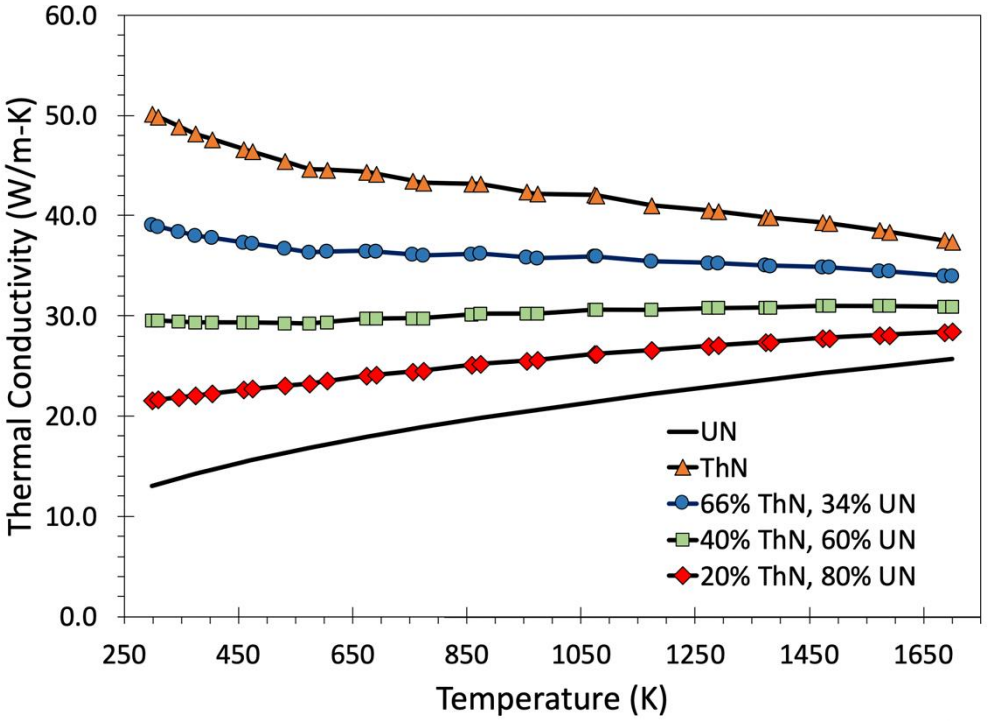

Figure 57: Thermal conductivity of UN, ThN, and ThN-UN mixtures

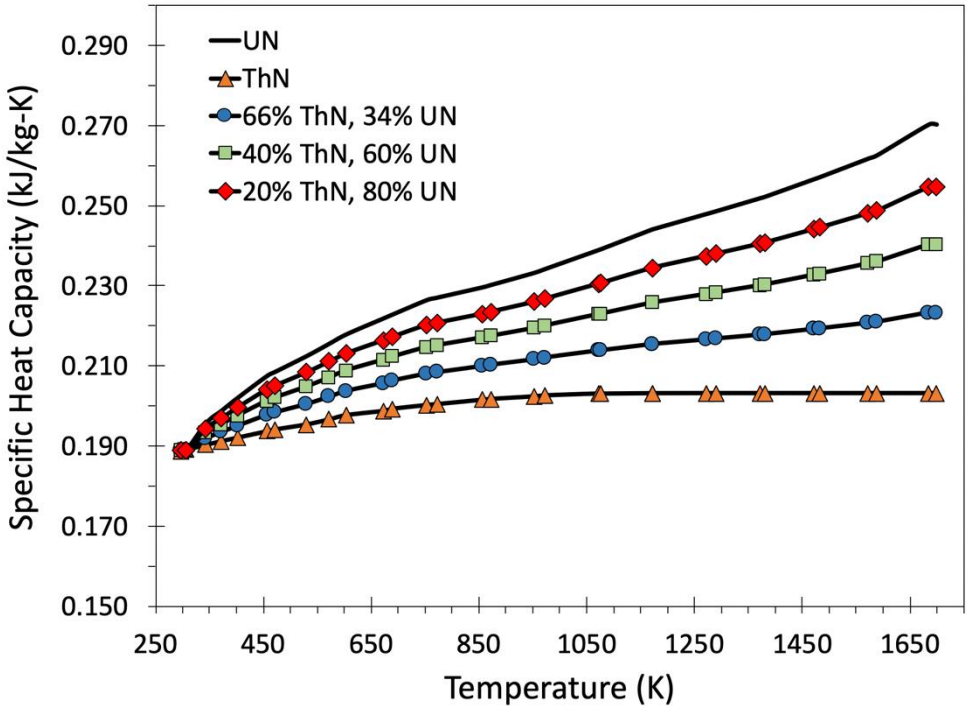

Figure 58: Specific heat capacity of UN, ThN, and ThN-UN mixtures

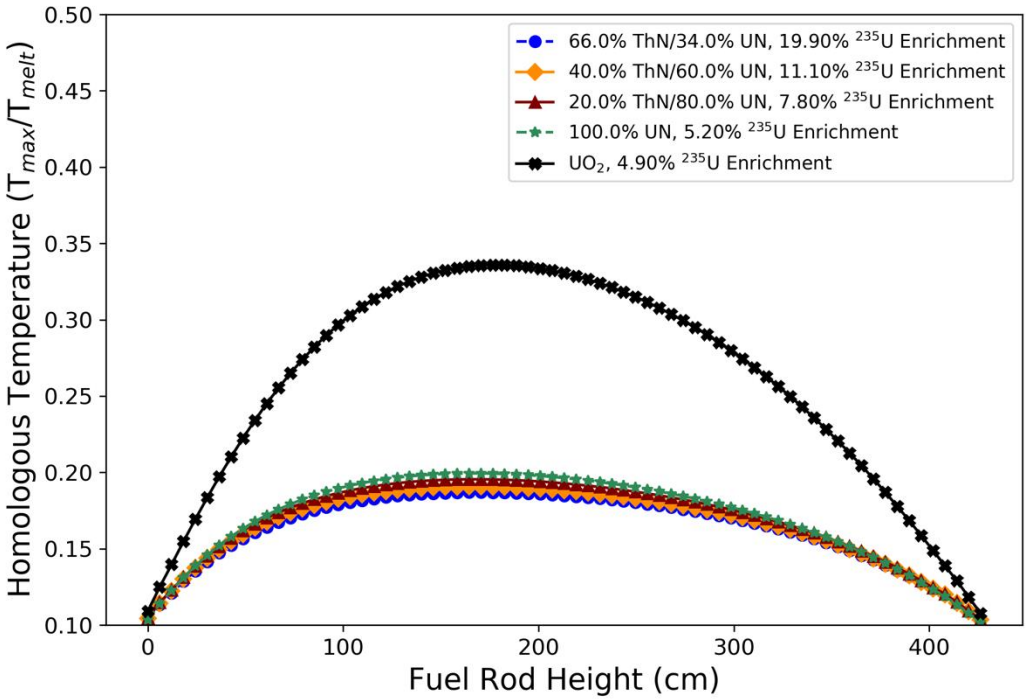

Figure 59: Homologous temperature as a function of fuel rod height at BOC

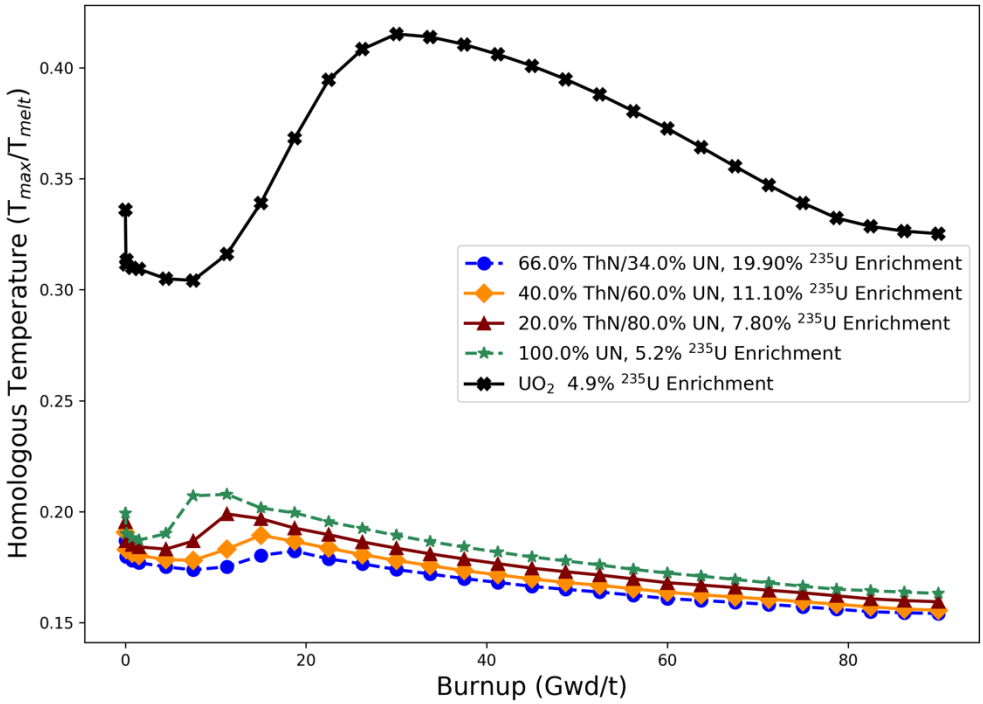

Figure 60: Homologous temperature as a function of burnup

phase, i.e. UN provides the external fissile material needed to transmute ^{232}Th into ^{233}U, while ThN may shield UN from chemically reacting with water. Further investigation is needed to understand these characteristics.

For any ATF candidate fuel to be considered for real-world application, it must perform equally as well as UO_2 in terms of fuel performance. Because of this requirement, ThN-UN mixtures and ^{235}U enrichments were determined that matched the cycle length of UO_2. Since it is not known what amount of ThN, if any, will prevent a ThN-UN composite fuel from degrading in water, several possible mixtures of ThN, UN, and ^{235}U enrichment were determined. When natural nitrogen is used, the maximum ThN weight fraction obtainable while remaining under the proliferation limit of 20 wt% ^{235}U enrichment was 66%, with the balance being UN. For a mixture consisting of 40% ThN and 60% UN, the required ^{235}U enrichment was 11.10 wt%, and for a 20% ThN, 80% UN mixture, the required enrichment was 7.80 wt%. Pure UN required a 5.20 wt% enrichment to match the UO_2 cycle length. N-15 enrichment was also considered, and the required ^{235}U enrichments for 20% ThN-80% UN, 40% ThN-60% UN, and UN were 5.90wt%, 8.50wt%, and 3.90wt%, respectively. Each of these enrichments is approximately 25% less than the enrichments needed for natural nitrogen, and the maximum possible weight fraction of ThN at 19.90 wt% enrichment increased from 66.0 to 73.5%.

Comparisons of reactivity coefficients between the nitride-based fuels and UO_2 showed that each of the RTCs and SBC were negative. However, the more negative MTC and smaller magnitude of the SBC and control worth for the nitride-based fuels prompt the need for a full-core shutdown margin calculation at a variety of reactor states and burnups. From an accident tolerance standpoint, the ThN-UN fuels exhibited a significantly lower homologous temperature compared with UO_2 in PWR fuel rod and fuel assembly models. This suggests that ThN-UN may display better fission product retention, reduced energy storage, and less thermal stress and expansion. It is noteworthy, however, that this is a preliminary screening study focused on neutronic and thermal hydraulic performance. The progression of this concept relies on a number of additional computational studies, such as full-core shutdown margin, accident analysis, and fuel

performance. Further, experimental work is needed to characterize the degradation of ThN-UN fuel forms in a relevant PWR coolant chemistry environment. The results from the current study warrant future investigation of ThN-UN, but is intended to be an early-stage screening study of neutronic and thermal hydraulic performance.

CHAPTER 6
REACTOR PERFORMANCE AND SAFETY CHARACTERISTICS OF UO_2 WITH MO INSERTS

6.1 Motivation

The incorporation of non-fissile inserts into UO_2 is being considered as a potential advanced low-enriched uranium (LEU) fuel form to increase heat transfer capabilities of LWRs [173]. The motivation for improving heat transfer capabilities with high thermal conductivity inserts is to improve short-term accident tolerance, improve fission product retention, and reduce the probability of PCIs, which can cause cladding burst and release fission products into the coolant. These benefits stem from the reduced fuel temperature, energy storage, and thermal stresses in the fuel caused by high thermal conductivity. Previous work on UO_2-Mo fuel forms has focused primarily on the measured thermal conductivity of fabricated samples and the heat transfer performance of small-scale, single-physics models. Much less attention has been given to the neutronic impact of using Mo inserts, especially on the fuel assembly scale with multiphysics methods. Additionally, advanced additive manufacturing techniques allow for a wide array of possible insert geometries. There is a direct need for a method that can be used to systematically optimize the insert geometry in a way that maximizes heat transfer and neutronic performance.

This work investigates nuclear reactor performance and safety characteristics of UO_2 with high thermal conductivity Mo insert structures using multiphysics modeling techniques. The purpose of this study is to use scoping analyses to quantify the impact of using Mo inserts from neutronic and heat transfer standpoints. Attention is given to reactor performance and safety parameters, such as cycle length, self-shielding, RTCs, maximum fuel temperature, temperature gradients in the fuel, and stored energy in the fuel. The finite-element code BISON and the Monte Carlo particle transport code Serpent were used to perform sensitivity analyses on the Mo insert geometry to optimize the insert design and inform larger scale modeling that required the homogenization of the

UO_2 and Mo. Although BISON is often used as a fuel performance analysis tool, it is used in this context for heat transfer analysis only. This work addresses a knowledge gap in the literature by quantifying the impact of Mo inserts on reactor physics and heat transfer parameters. The scope of this work remains focused on the areas of neutronics and heat transfer performance for this novel fuel concept and is not intended to optimize the UO_2-Mo design from a fuel performance standpoint.

6.2 Methodology

Sections 6.2.1–6.2.3 describe the methods used to evaluate Mo inserts in UO_2. In Section 6.2.1, two combinations of Mo content and ^{235}U enrichment were chosen based on their achievable cycle length compared with regular UO_2. One combination remains below the United States commercial LWR enrichment limit of 5% ^{235}U. The other case exceeds this enrichment limit and is studied to address the increasing interest in using HALEU in LWRs that are equipped with ATF materials and can safely operate at higher burnups [174].

Once the Mo content and ^{235}U enrichment combinations were chosen, two sensitivity studies were performed: one to determine the effect of insert geometry on initial neutron multiplication factors and one to determine the effect of insert geometry on the maximum fuel temperature. Section 6.2.2 describes the sensitivity analysis method, and Section 6.2.3 details the analyses performed to determine the reactor performance and safety of the UO_2 with Mo inserts. Lastly, Section 6.2.4 summarizes the overarching process of the study and all of the computational tools used.

6.2.1 Selection of Mo Content and ^{235}U Enrichment

To obtain a rough estimate of the maximum attainable Mo content in the fuel that can still match the cycle length of regular UO_2, an infinite 2-D pin-cell model was used to calculate cycle length for homogeneously mixed UO_2-Mo fuel ranging in Mo content from 0 to 30% by weight and 3 to 10% ^{235}U enrichment. MPACT and a 252-group ENDF/B-VII.1 nuclear cross section library [120] [156] were used to perform these calculations. The pin-cell geometry was based on the Westinghouse AP1000 design [168], the dimensions of which were previously provided in Table 11 in CHAPTER 5.

The linear reactivity model [169] was used to calculate the cycle length in which the infinite neutron multiplication factor k_∞ was adjusted for 4% reactivity leakage and the cycle length was adjusted for a typical three-batch loading scheme. The results are shown in the contour plot in Figure 61. Each contour line shows the relative difference in cycle length for a given Mo content and ^{235}U enrichment combination against a reference value, which—in this case—was chosen to be the cycle length of UO_2 that is 4.9% enriched. Any combination of Mo content and ^{235}U enrichment along a given contour line has the same cycle length, and two combinations of Mo content and ^{235}U enrichment were chosen as the focus of the remainder of the study.

The first combination is 6.25wt% Mo and 4.9% ^{235}U enrichment, which, from Figure 61, gives a cycle length that is equivalent to regular UO_2 that is 4.0% enriched, or approximately 360 EFPD. The second combination is 15.0wt% Mo and 7.52% ^{235}U enrichment, which gives the same cycle length as regular UO_2 that is 4.9% enriched (approximately 451 EFPD). These combinations were chosen because the primary objective of this paper is to make a relevant comparison between the performance of UO_2-Mo and typical PWR fuel.

To verify the accuracy of the cycle length predictions made using MPACT, comparisons of neutron multiplication factor as a function of burnup were made for the two identified homogeneously mixed fuel forms using the Monte Carlo particle transport code, Serpent [18]. The difference in neutron multiplication factors for both fuel forms is shown in Figure 62. Some differences are expected because the MPACT cross section libraries are based on ENDF/B-VII.1 data [156], whereas Serpent uses ENDF/B-VII.0 data [157]. The uncertainty in the Serpent results at each burnup step is approximately 20 pcm. Figure 62 shows that Serpent predicted a greater neutron multiplication factor at the beginning of cycle (BOC) for both fuel designs. Serpent also predicted a faster depletion rate, so MPACT predicted a higher neutron multiplication factor later in the cycle. Agreement within several hundred pcm is considered acceptable for this scoping study, and Figure 62 shows that Serpent and MPACT agreed within this range for relevant burnup levels.

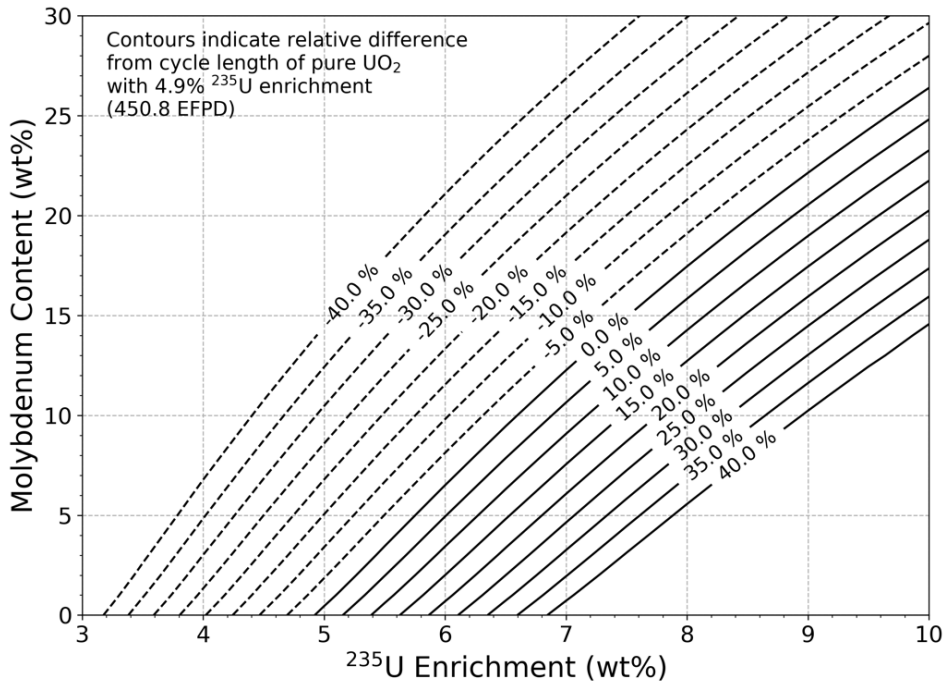

Figure 61: Difference in cycle length of various combinations of Mo content and ^{235}U enrichment relative to 4.9% enriched UO_2

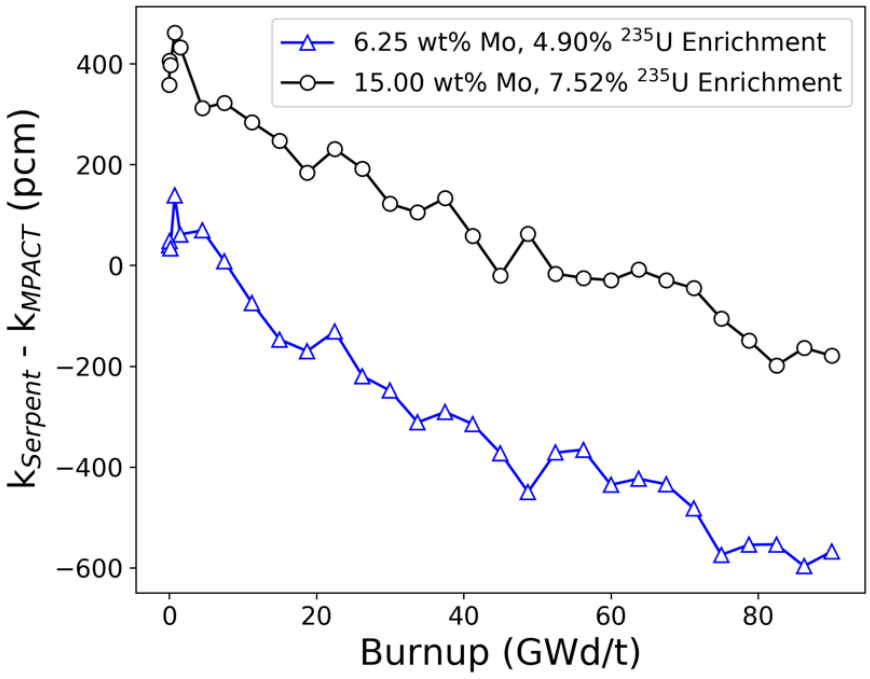

Figure 62: Difference in neutron multiplication factors between Serpent and MPACT

6.2.2 Sensitivity Analysis Methods

Sensitivity studies were performed using Monte Carlo and finite element models of a single AP1000 fuel pellet to determine the effect of the Mo insert geometry and the importance of geometric features on initial neutron multiplication factors and maximum fuel temperature. Serpent was used to perform the neutronics sensitivity study where the initial neutron multiplication factor was the FoM. The finite element code BISON was used to perform a heat transfer sensitivity study for which the maximum fuel temperature was the FoM. A greater initial neutron multiplication factor was assumed to correspond to a greater cycle length. This is a reasonable assumption for this study since all the fuel pellets tested have the same Mo content, ^{235}U enrichment, and U density. These sensitivity studies also provide insight into the effect of the insert geometry on other phenomena—such as self-shielding, temperature gradients across the fuel, and energy storage in the fuel—which all have performance and safety implications. Additionally, results from the sensitivity studies reflect upon the validity of assuming homogeneously mixed UO_2-Mo fuel pellets for purposes of scoping analysis and can be used to inform reactor analysis models for which homogenization may be required.

Relatively simple geometries were considered for these studies in which disks extend radially from a central, vertically-oriented rod. Heat transfer in nuclear fuel rods is predominantly in the radial direction, and the work of Medvedev and Mariani [10] already focused on thin, radial disks stacked alternately with UO_2 disks. Although this concept is simple from a manufacturing standpoint, a modification to the fuel rod loading process would be needed to alternate the UO_2 and Mo disks within the cladding. The rod-and-disk geometry considered in this study was selected because the axial structure may improve manufacturability using additive manufacturing and sintering techniques [175] and would not require any changes to how the fuel rods are loaded. Further, the axial structure eliminates the UO_2 centerline region, which is the hottest region in a typical UO_2 fuel pellet, and the disks provide a radial pathway for heat to move from the pellet to the coolant. Figure 63 shows how the rod-and-disk insert design alters the thermal resistance network in the fuel rod compared to a traditional UO_2 fuel pellet, where $\dot{q}$ indicates where heat is added to the system. Four geometric variables were considered in

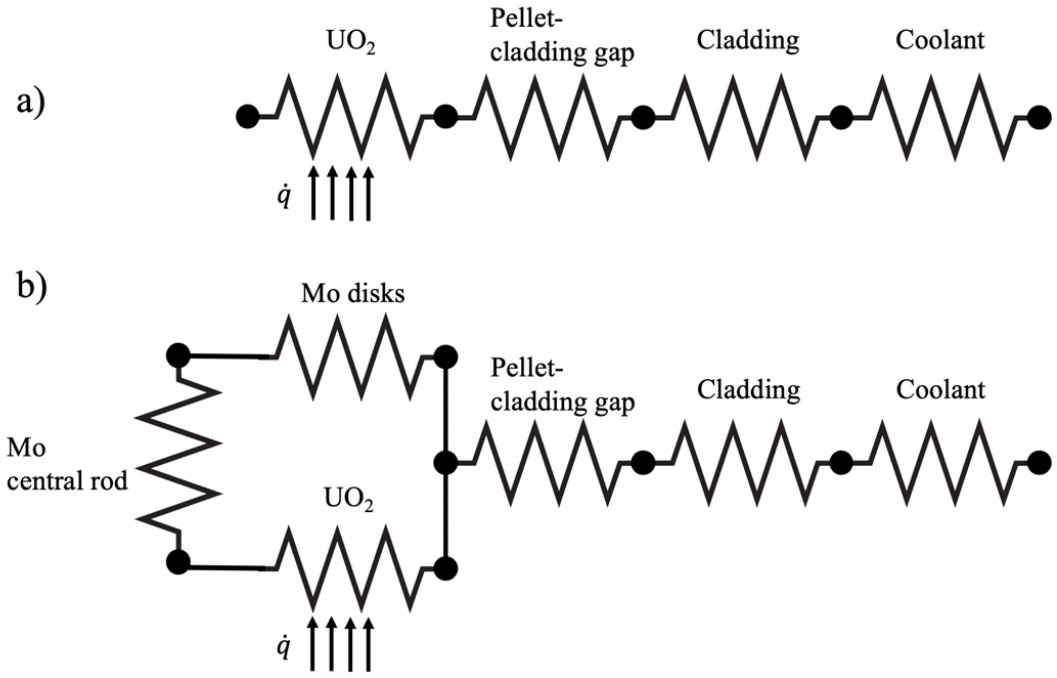

Figure 63: Thermal resistance network in a) a typical UO_2 fuel pellet and b) a UO_2 fuel pellet with a rod-and-disk Mo insert

the sensitivity studies: the radius of the central rod, r_c; the number of radial disks, n_d; the radius of each disk, r_d; and the thickness of each disk, t_d. An example of this insert geometry with two disks is shown in Figure 64. Only the 15.0wt% Mo and 7.52% ^{235}U enrichment design was considered for the sensitivity studies, and the geometric variables were sampled so that the weight fraction of Mo was constant.

A cumulative density function (CDF)-based sensitivity analysis method developed by Liu and Homma [176] was used for this study. The algorithm for this method for a generic model $Y = f(x_1, x_2,.., x_n)$ is as follows.

1. For N runs, use random or pseudorandom (i.e., Latin hypercube [177]) sampling to choose all input variables and run the model.
2. Calculate the unconditional CDF and the expected value of the output (i.e., $E[Y]$).
3. While holding one of the input variables, x_i, constant, randomly sample the other inputs and rerun the model to generate a new CDF.
4. Repeat Step 3 for a randomly selected or pseudorandomly selected discrete set of possible values of x_i until N model runs are performed.
5. Calculate the area between each new CDF, called the *conditional CDFs*, and the unconditional CDF, $A(x_i)$.
6. Calculate the expected value of $A(x_i)$ and calculate the sensitivity index, S_i^{CDF}, using Equation (11):

$$S_i^{CDF} = \frac{E\big(A(x_i)\big)}{E(Y)} \tag{11}$$

7. Repeat Steps 3—6 for all input variables $x_1, x_2,.., x_n$. A greater value of S_i^{CDF} indicates a higher importance for that variable.

For both sensitivity studies, n_d was an integer varied from one to four disks, r_c and t_d were both varied from 0.02 to 0.2 cm, and r_d was varied from 20 to 100% of the fuel radius but was required to be greater than r_c for a given geometry. The Mo fraction was also required to be constant at 15.0wt% for all cases, meaning three of the variables of interest could be randomly selected but the fourth variable had to be calculated from the other three. This interdependency of input variables negates the use of typical variance-based sensitivity analysis methods, such as Sobol indexing [178]. Although some

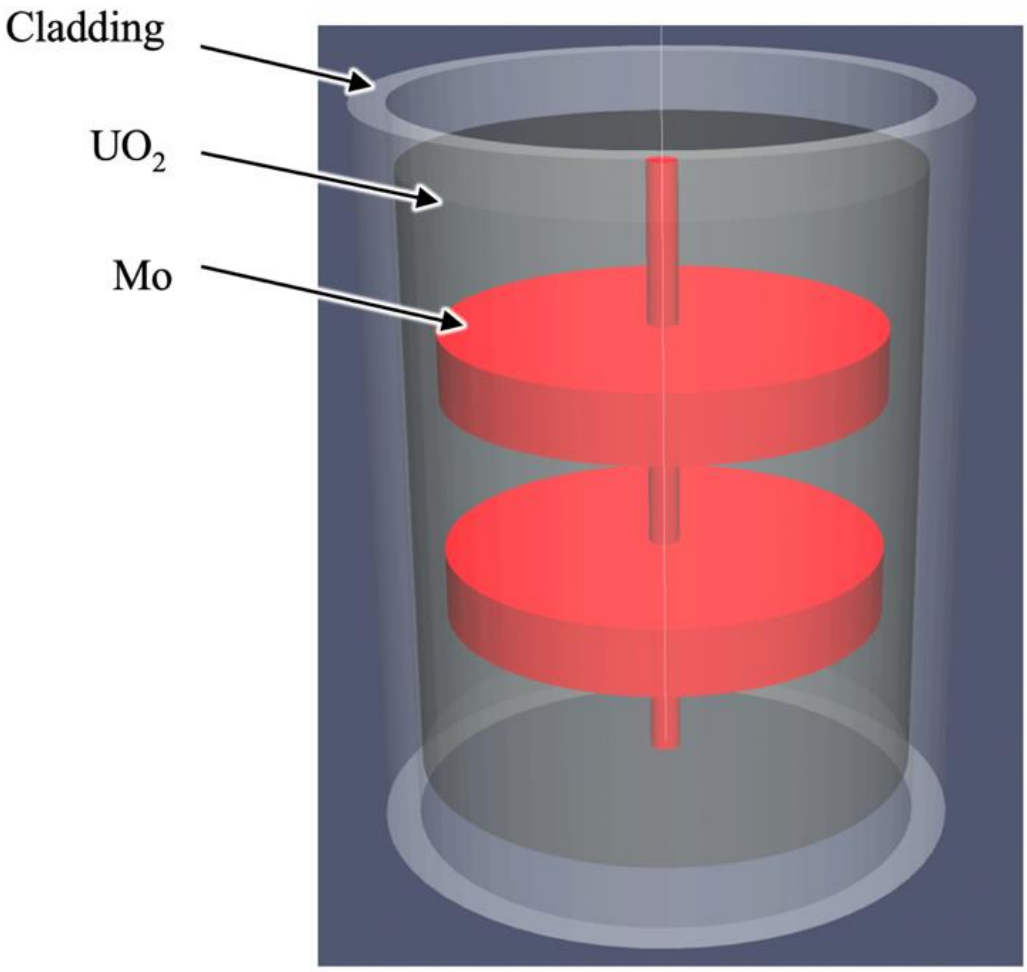

Figure 64: Example of Mo insert geometry with two radial disks

techniques have been developed to handle models with dependent inputs [179] [180], variance-based sensitivity methods are still inapplicable due to the uniqueness of inputs that make one-at-a-time sampling impossible for this case. For example, if values of n_d, r_c, and r_d are randomly selected, then there is the unique value of t_d that gives a geometry that meets the Mo fraction constraint; thus, it is impossible to hold three of the variables constant while only varying the fourth. However, the CDF-based method uses a complimentary strategy in which one variable is held constant and the other three are varied, which is possible for this case.

Latin hypercube sampling (LHS) [177] was used for all variables to generate the unconditional CDF to improve the statistical accuracy. This stratified sampling strategy was also used to select the discrete set of inputs for each conditional case, but regular Monte Carlo sampling was used to pick the other variables in the conditional cases. LHS is used because it ensures the entire range of possible values is sampled and reduces the required number of runs for these high-fidelity computationally expensive models to obtain statistical accuracy. The variables that are not being held constant in each conditional case (Step 3 in the algorithm) are sampled using regular random sampling because the emphasis of the CDF-based sensitivity method is on the change in the CDF caused by the conditional variable, x_i, not the other variables. Each sensitivity study was performed until the relative change in each sensitivity index per model run converged to less than 5×10^{-4} and a stability of importance ranking had been clearly demonstrated [181].

The Pearson correlation coefficient [182] was also determined for each input variable to quantify the association between the initial neutron multiplication factor and maximum fuel temperature on insert geometry, as well as to add confidence to the importance rankings of the variables obtained using the CDF-based method. The Pearson correlation coefficient varies between -1 and 1 and quantifies the linear association between a model output Y and an input x_i, as given by Equation (12).

$$\rho(x_i, Y) = \frac{Cov(x_i, Y)}{\sqrt{Var(x_i)Var(Y)}} \tag{12}$$

The closer the magnitude of $\rho(x_i, Y)$ is to 1, the stronger the linear association between x_i and Y. The value of the Pearson correlation coefficient does not necessarily indicate the importance of a variable and is used in this study only as a secondary measure of the relationship between each input variable and the FoMs.

The insert geometries that performed the best and worst in the sensitivity studies (i.e., the geometries that gave the highest and lowest initial neutron multiplication factor and the lowest and highest maximum fuel temperature, respectively) were identified for more in-depth analyses. From a neutronics perspective, the additional analyses include a burnup calculation to determine cycle length and a study to determine the impact that insert geometry has on self-shielding effects. The homogeneously mixed UO_2-Mo fuel is included in the self-shielding analysis, which—in conjunction with the cycle length calculations—informs on the validity of assuming the mixed fuel type for the other scoping analyses that are discussed in Section 6.2.3. From a heat transfer perspective, the maximum temperature gradient and energy storage were determined for the insert geometries that gave the lowest and highest maximum fuel temperature in the sensitivity study and were compared with what can be expected in monolithic UO_2.

6.2.3 Determination of Reactivity Coefficients and Reactor Performance

The importance and definition of RTCs and control rod worth were given in Section 2.3.1. To calculate the RTCs and control worth, several branch cases are modeled in which the fuel or moderator temperature, boron concentration, or control rod configuration is varied from a reference value and the reactivity at each state is calculated. The values used to calculate the RTCs were 800 and 900 K for fuel temperature, 550 and 585 K for moderator temperature (770 kg/m^3 and 701 kg/m^3 for liquid water density, respectively), and 0 and 1,000 ppm for SBC. These limits cover typical values for average fuel temperature, coolant temperature, and soluble boron content in PWRs. An infinite pin-cell model was used to calculate FTC, MTC, and SBC, and an infinite one-quarter symmetry model of a typical 17 × 17 PWR fuel assembly with Ag-In-Cd control rods was used to calculate control rod worth. This procedure is similar to the one used in CHAPTER 5 to calculate RTCs and control worth for the ThN-UN

fuels. All coefficients were calculated for regular UO_2 and the homogeneous UO_2-Mo fuels with 6.25 and 15wt% Mo as a function of burnup using MPACT and a 252-group cross section library.

A 3-D 17 × 17 PWR fuel assembly model was developed in VERA to determine the heat transfer performance of the homogenously mixed UO_2-Mo fuels. The impact of Mo inserts on heat transfer performance was quantified using the homologous temperature, which is the ratio of the maximum fuel temperature to its melting temperature, as a function of burnup. The same method that was used in CHAPTER 5 for calculating homologous temperature for ThN-UN fuels using the feedback loop between MPACT and CTF within VERA was used in the current study to calculate homologous temperature for UO_2-Mo. The PWR model used boundary conditions representative of those in the Westinghouse AP1000 design [168]. Before performing the multiphysics calculation, a thermal conductivity calibration scheme was developed so that uncoupled CTF results closely matched those from BISON in terms of maximum fuel temperature, average fuel temperature, and the relative RMSE in temperature across radial nodes in UO_2 fuel pellets with Mo inserts. The calibration procedure was performed using several data points from a single PWR fuel rod and is discussed in more detail in Section 6.5.2. Both the calibration procedure in the PWR fuel rod and the determination of homologous temperature in the PWR fuel assembly were performed for the best and worst performing geometries from the heat transfer sensitivity study.

6.2.4 Summary of Methods and Computational Tools

The analyses performed in this study span a range of scales and physical phenomena that required the use of multiple computational tools. A flowchart summarizing the general process followed in this study is given in Figure 65. Figure 66 further elucidates the role of each modeling tool in this study and the function of each portion of the study by providing a wholistic evaluation of the effect of Mo inserts in UO_2. In this study, all references to VERA imply the use of MPACT coupled to CTF to provide a neutronics-to-thermal-hydraulics feedback loop. Although a version of BISON has been integrated into VERA, BISON is only used in standalone mode in the current

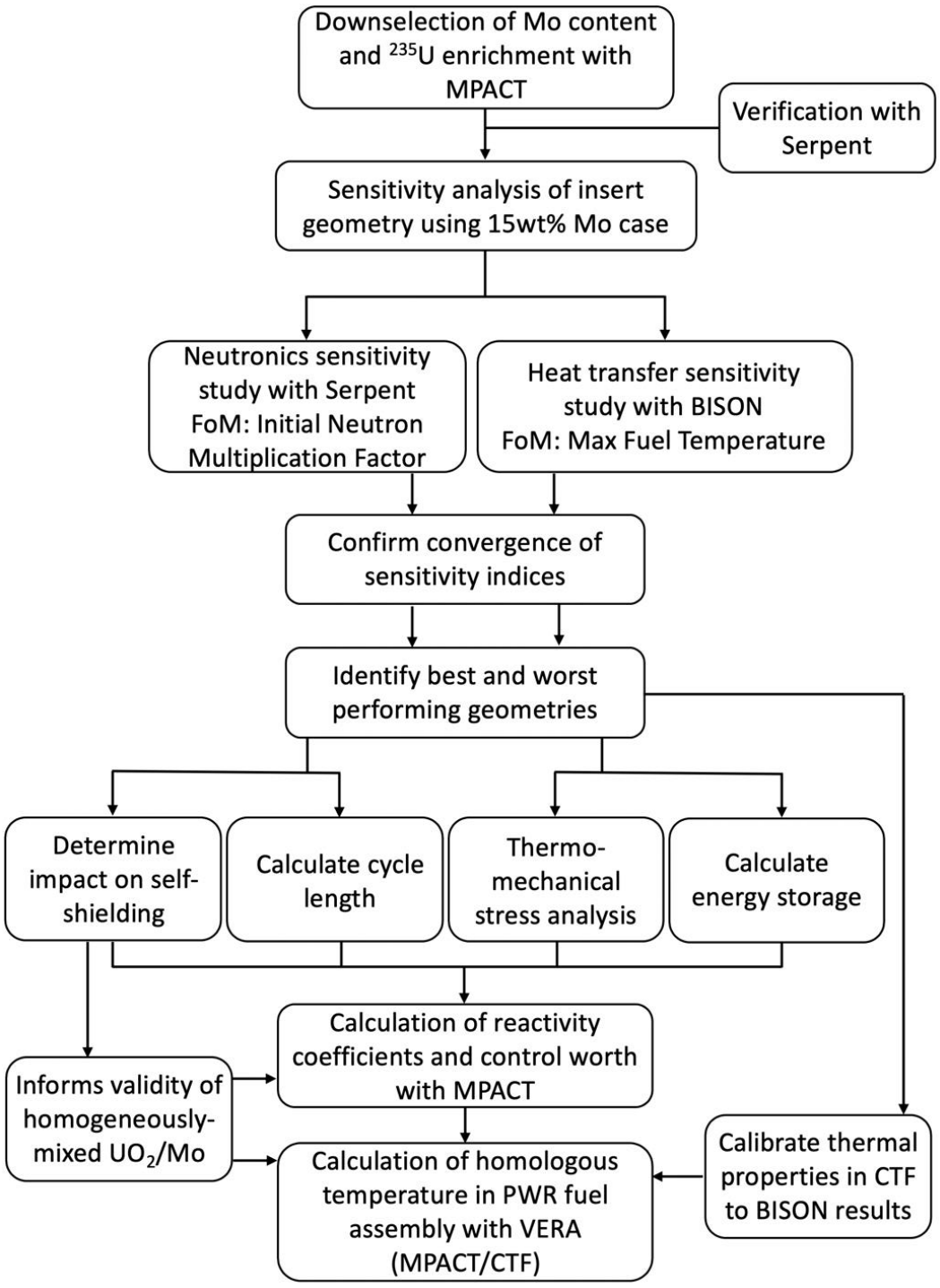

Figure 65: Process flowchart used for this study.

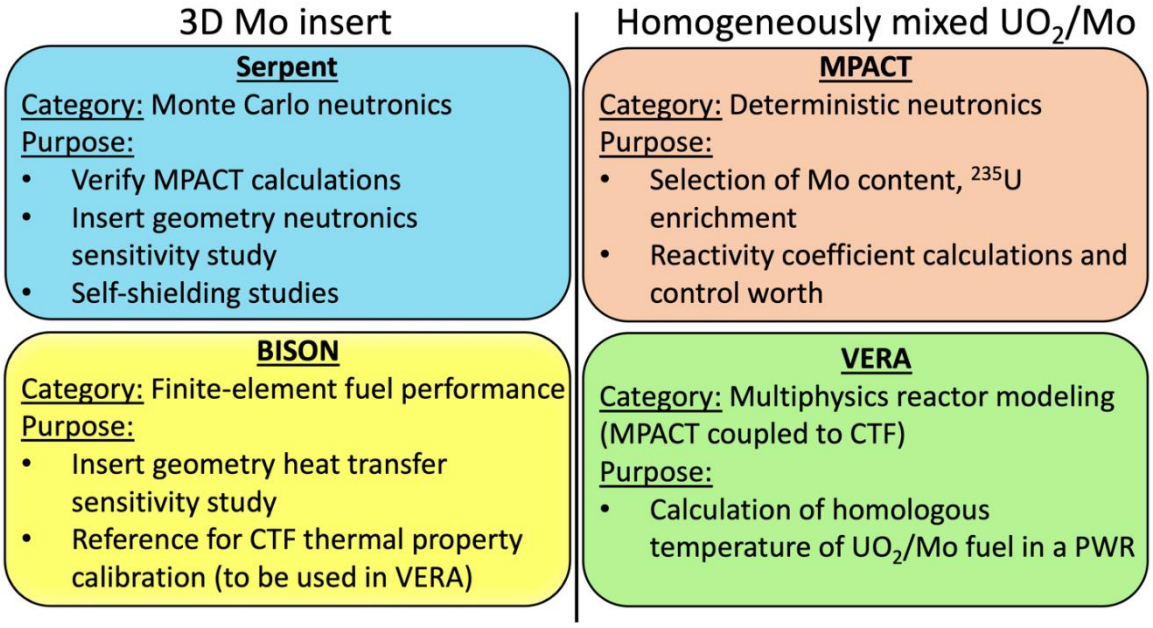

Figure 66: Summary of computational tools and their roles in this study.

study. Direct references to MPACT and CTF imply that they are being used in standalone mode.

6.3 Neutronics Results: Sensitivity Studies and In-Depth Analysis

6.3.1 Neutronics Sensitivity Analysis Results

Overall, 3,000 Serpent model runs were performed for the neutronic sensitivity analysis: 600 for each of the four geometric variables and an additional 600 model runs to generate the unconditional CDF. Figure 67 shows the infinite neutron multiplication factor as a function of each geometric variable for the 600 model runs that compose the unconditional CDF. Because Serpent is a Monte Carlo code, error bars are included on the figure to show the uncertainty in the neutron multiplication factor predictions, all of which were 20–25 pcm.

The algorithm described in Section 6.2.2 was used to determine S_i^{CDF} for each of the four input variables, and an example of $A(x_i)$ from this study is shown in Figure 68. A plot of the sensitivity indices as a function of the number of model runs per variable is shown in Figure 69. The indices were converged to a relative change per model run between 5×10^{-5} and 3×10^{-4}, and Figure 69 shows that the importance ranking had not changed since 200 runs per variable. Equation (12) was used to also determine the Pearson correlation coefficient for each variable, and the resulting values of S_i^{CDF}, $\rho(x_i, Y)$, and their associated rankings are given in Table 16. The results from Table 16 show that the CDF-based sensitivity method and the Pearson correlation coefficients both predicted the same ranking of the four variables and indicated that the radius/radii of the disks are the most important feature in terms of impact on the initial neutron multiplication factor.

6.3.2 Cycle Length and Self-Shielding

The highest and lowest neutron multiplication factor from all runs in the sensitivity study were 1.38182 and 1.37020, respectively—a difference of 1,152 pcm. Cross sections of the pin-cell model for these two cases, hereafter referred to as the *high-reactivity case (HRC)* and *low-reactivity case (LRC)*, are shown in Figure 70. The Mo

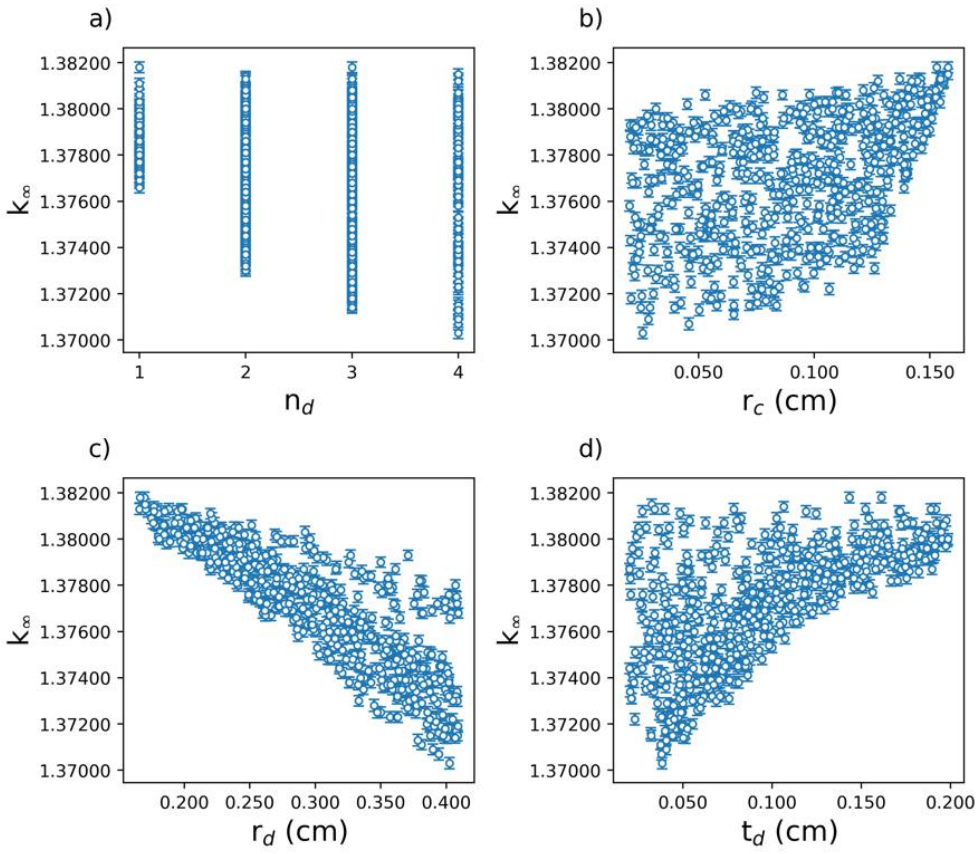

Figure 67: Unconditional neutronic results as a function of each input variable

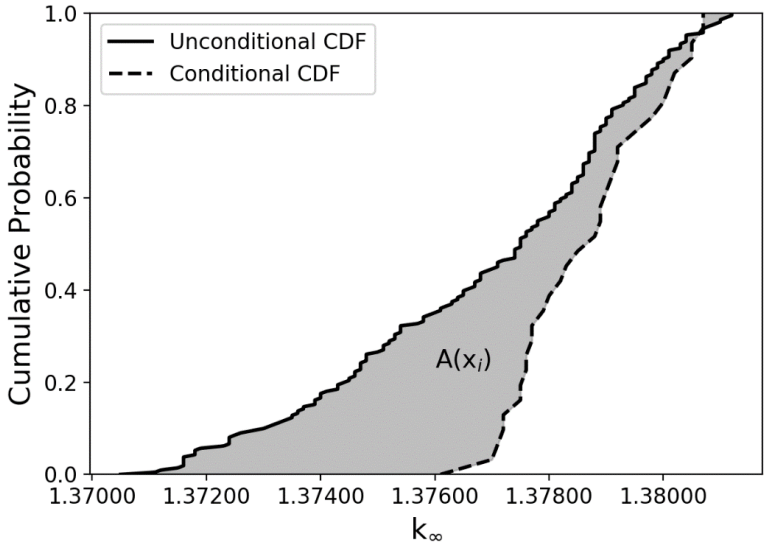

Figure 68: Example of $A(x_i)$ between the unconditional CDF and a conditional CDF

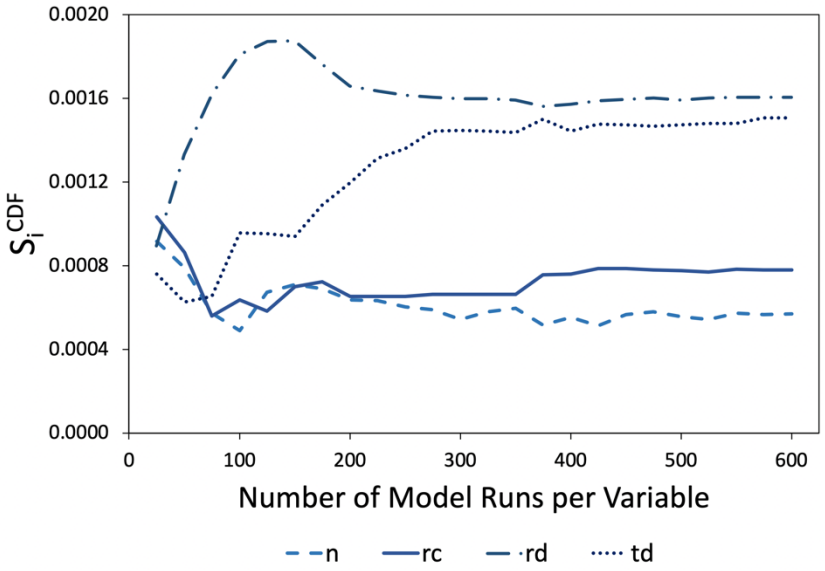

Figure 69: Neutronic sensitivity indices as a function of model runs per variable

Table 16: Neutronic sensitivity study results and variable rankings

Variable	S_i^{CDF}	Rank	$\rho(x_i, Y)$	Rank
n_d	0.0006	4	-0.1856	4
r_c	0.0008	3	0.3825	3
r_d	0.0016	1	-0.8620	1
t_d	0.0015	2	0.6270	2

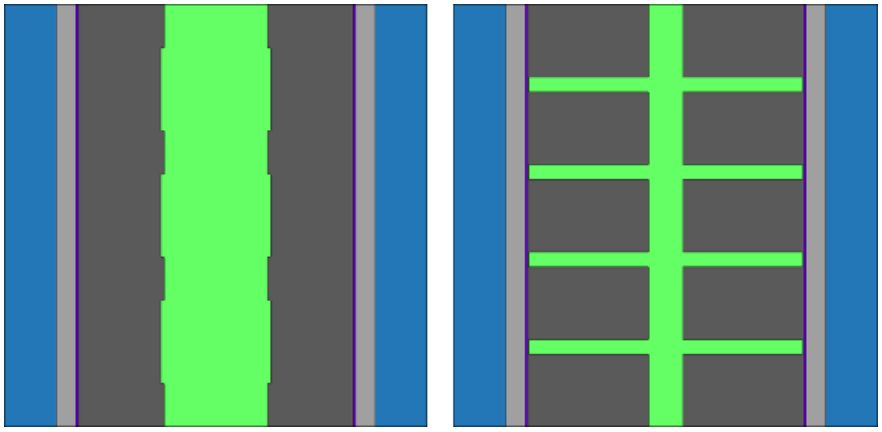
Figure 70: Cross sections of the HRC (left) and LRC (right) pin-cell models

inserts are bright green in the figure. Figure 70 shows that the HRC has a relatively large central rod with very small disk radii, whereas the LRC has four radial disks that extend nearly the full width of the fuel pellet.

Serpent was used to perform burnup calculations to determine the cycle length of each of these two cases for which 4% reactivity leakage and a three-batch loading scheme were assumed. The resulting cycle length of the HRC was 470.5 EFPD, and the cycle length of the LRC was about 3% lower at 456.7 EFPD. Previously shown in Figure 61, the cycle length of a homogeneously mixed UO_2-Mo fuel pellet with the same Mo content and ^{235}U enrichment as these two geometries was calculated using MPACT to be 450.8 EFPD, which is 1.3 and 4.2% lower than the cycle length of the LRC and HRC, respectively. These cycle length predictions suggest that the assumption that higher initial reactivity corresponds to longer cycle lengths for these fuels and the use of homogenized UO_2-Mo models is acceptable for this scoping study.

Serpent was used to study the effect of insert geometry on self-shielding within the fuel pellet. Self-shielding in the fuel is directly related to the rim effect in which the outer rim of the fuel pellet experiences greater fission rate. Self-shielding was studied by tallying the relative absorption rate in 10 concentric rings in the fuel pellet. Each of the 10 rings have equivalent volumes to each other. Only BOC was considered, and only absorption in the fuel was tallied because the purpose of studying self-shielding in this context is to determine whether the Mo inserts impact the rim effect. Figure 71 shows the tallies of the absorption rate in each of the 10 volumes relative to the total absorption rate in the fuel for the HRC, LRC, a homogeneously mixed UO_2-Mo fuel pellet, and a reference UO_2 fuel pellet that is 4.9% enriched. All fuel types had the same total power. The *x*-axis in the figure is the ratio of each of the 10 equal-volume radii to the total fuel pellet radius.

Because the radius of the central rod in the HRC is greater than the radius of the innermost equal-volume ring, there is no absorption in the fuel in this ring. The relative absorption rate in each of the eight outermost rings is greatest in the HRC since there is no Mo in these regions and also because the concentration of Mo near the center of the pellet reduces the relative absorption in this region. Compared with the reference UO_2

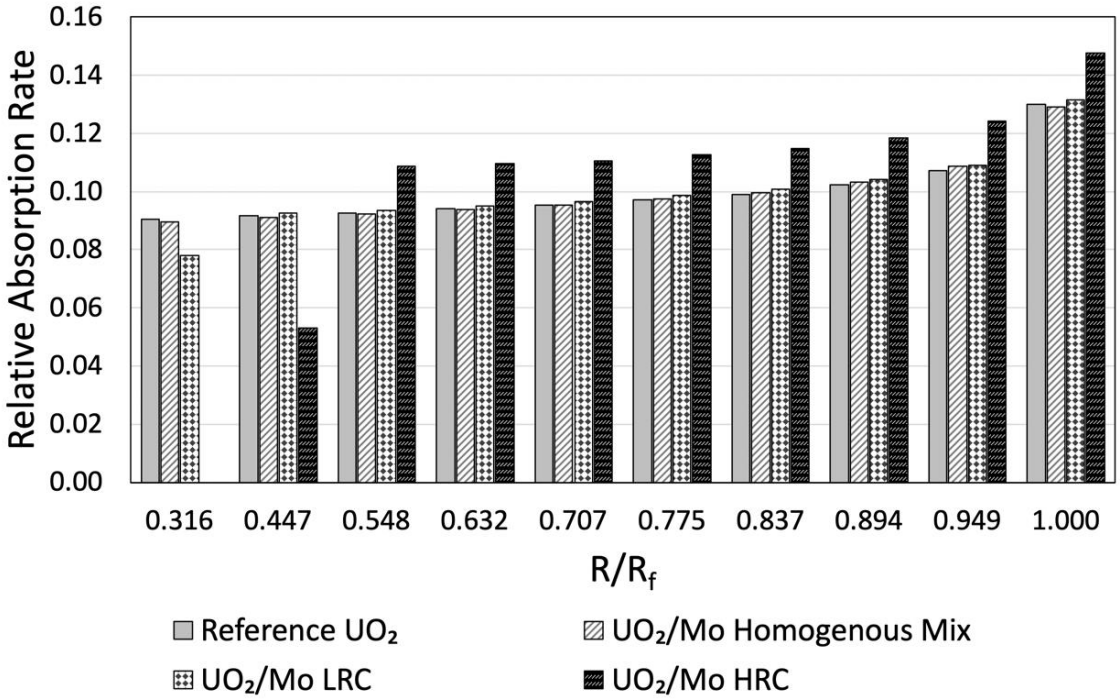

Figure 71: Impact of Mo inserts on self-shielding in the fuel pellet

case, the homogenously mixed UO_2-Mo has little impact on self-shielding, and the LRC has a lower absorption rate near the center of the pellet—again, because of the central Mo rod—but is relatively similar to the reference case in the other pellet regions.

6.4 Heat Transfer Results: Sensitivity Studies and In-Depth Analysis

6.4.1 BISON Setup

Due to the complexity of the UO_2-Mo configuration, it was necessary to employ a multidimensional tool to calculate the heat transfer and temperature profiles. For this purpose, BISON was selected for the simulations, and Cubit was selected to perform the meshing of the 3-D geometries. BISON was used in this study to optimize the heat transfer performance of the UO_2-Mo fuel form using the systematic regression techniques outlined in Section 6.2.2. This optimization using BISON focuses only on heat transfer and does not attempt to optimize the Mo insert for fuel performance. The thermal conductivity of the Mo was set to a curve fit to data presented by Rasor and McClelland [82], with resulting values of about 100 to 125 W/m-K in the temperature range of interest.

There is also a 50 μm thick boarder with a low thermal conductivity around the Mo inserts to provide a conservative estimate of the thermal resistance due to interface shearing or separation between the UO_2 and Mo. The thermal conductivity for this region was set to 0.25 W/m-K using the assumption that any free volume between the UO_2 and Mo would become filled with He. The heat generation was set to a radial power factor determined by the neutronics simulations and the heat was modeled as being generated into the UO_2. Gamma heating in the Mo was not included in the simulations, which is expected to have a negligible impact on results since the gamma heating in Mo would be small compared to the overall power and also because the Mo thermal conductivity is high.

A coolant pressure of 15.5 MPa was applied to outer cladding surface, and an initial He fill gas pressure of 2 MPa was applied to the fuel-cladding gap. However, fission gas was not added to the gap. The wide range of geometry produced a significant range of temperature gradients across the pellet. This resulted in significant differences in

the fission gas released and the cladding gap pressures. A pellet-cladding gap optimization would have been necessary for a fair comparison of the various geometries, which is beyond the scope of this work given the number of geometries considered and the emphasis on heat transfer performance rather than fuel performance. While the stresses are not reported, the thermal expansion of the UO_2 and Mo, and swelling of the UO_2 remains included in the following simulations to better assess the pellet-cladding gap thermal resistivity. The UO_2 and Mo were modeled as mechanically bonded to each other in the following simulations.

6.4.2 Heat Transfer Sensitivity Analysis Results

The heat transfer sensitivity analysis required 4,750 model runs for all sensitivity indices to converge to a relative change-per-model run between 5×10^{-4} and 5×10^{-5}, which equated to 950 model runs per variable plus 950 runs to generate the unconditional CDF. Figure 72 shows the maximum temperatures recorded in the 950 unconditional model runs as a function of each of the geometric variables. Figure 73 shows the value of the sensitivity indices for each variable as a function of model runs per variable and demonstrates the stability of each index. The plot also shows that the same importance ranking of the indices had been maintained since approximately 175 model runs per variable. Table 17 shows the CDF-based sensitivity indices and Pearson correlation coefficients for each variable, as well as the ranking determined with each method.

In terms of maximum fuel temperature, the radius of the central rod was the most important factor. Unlike the neutronics sensitivity study, the CDF-based method and the Pearson correlation gave different rankings since the rank of r_d and n_d are swapped. However, these two variables are of approximately equal importance, so this result is considered a qualitive verification.

6.4.3 Fuel Temperature Gradient and Energy Storage

A constant power of 270 W was used in each of the BISON models in the sensitivity studies, and it was found that the highest and lowest fuel temperature predicted at BOC in the study were 1,495.0 K and 1,133.9 K. Cross sections of the geometries that gave these maximum temperature values are shown in Figure 74 and are henceforth

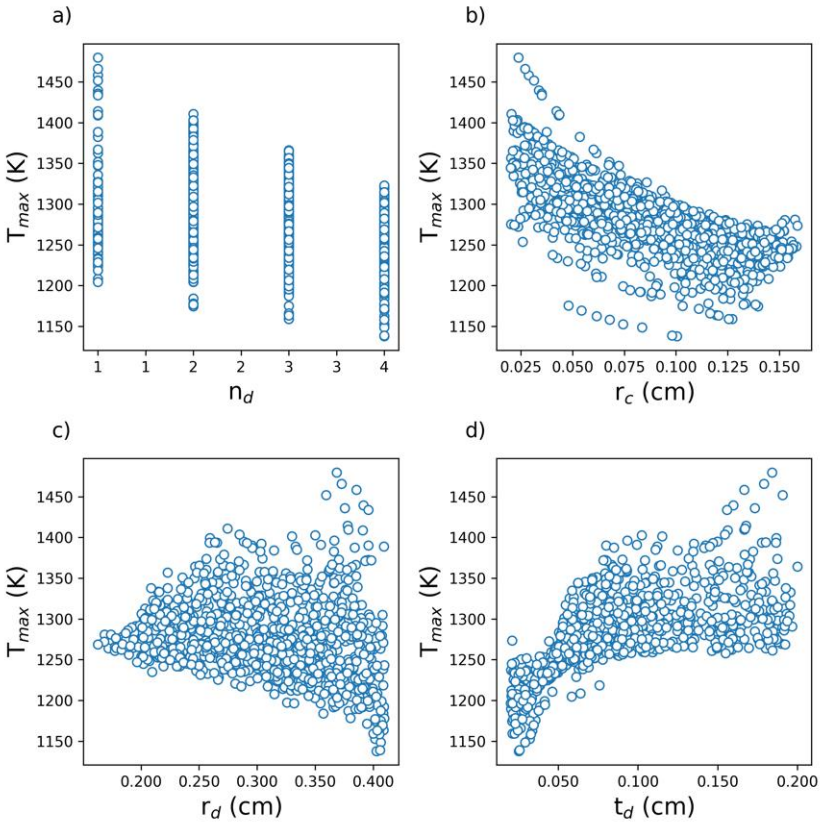

Figure 72: Unconditional predictions of maximum fuel temperature as a function of each input variable

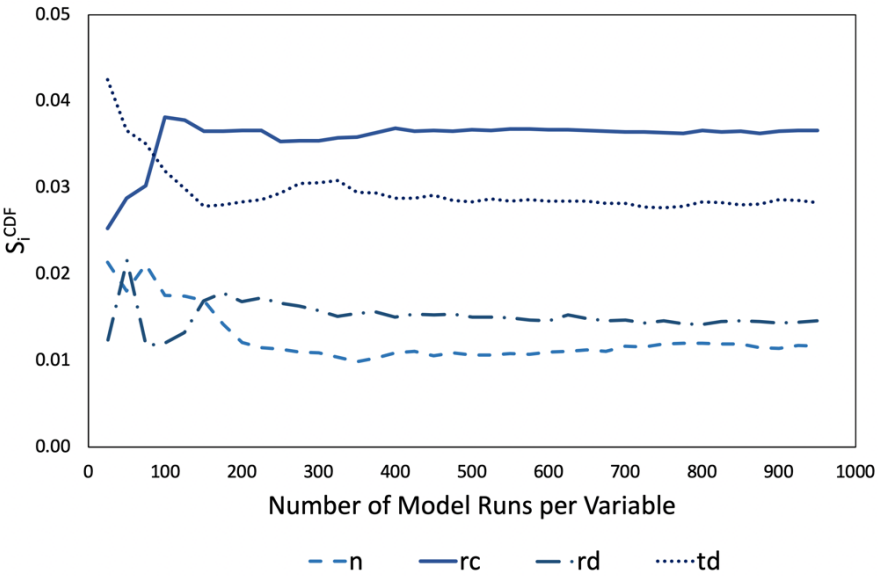

Figure 73: Heat transfer sensitivity indices as a function of model runs per variable

Table 17: Heat transfer sensitivity indices and variable rankings

Variable	S_i^{CDF}	Rank	$\rho(x_i, Y)$	Rank
Number of disks, n_d	0.0117	4	-0.1161	3
Central rod radius, r_c	0.0366	1	-0.7980	1
Disk radius/radii, r_d	0.0146	3	-0.1033	4
Disk thickness, t_d	0.0282	2	0.5728	2

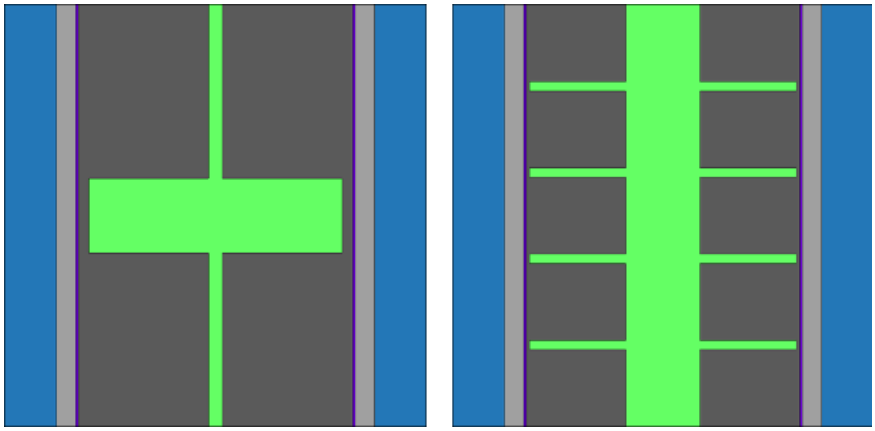

Figure 74: Cross sections of the HTC geometry (left) and the LTC geometry (right)

referred to as the *highest temperature case* (HTC) and *lowest temperature case* (LTC), respectively.

Further analyses of the HTC and LTC were performed to determine the radial temperature profile, maximum temperature gradient, and energy storage in the fuel pellet. A power of 250 W was used for these in-depth analyses. Energy storage was calculated by integrating the volumetric heat capacity of the fuel pellet over temperature and volume, as shown in Equation (13) [66].

$$\int_0^{V_{fuel}} dV \int_{T_x}^{T_{fuel}} \rho Cp(T)\, dT \tag{13}$$

In Equation (13), V_{fuel} is the volume of the fuel, T_{fuel} is the instantaneous temperature of the fuel, T_x is a reference temperature (set to room temperature in this case), and $\rho Cp(T)$ is the volumetric heat capacity of the fuel as a function of temperature. For comparison purposes, a reference UO_2 fuel pellet was also modeled at 250 W, and burnup calculations were performed with BISON to show BOC and EOC predictions for maximum fuel temperature, maximum temperature gradient, and energy storage. The burnup of the fuel at EOC was assumed to be 60 GWd/t in these scoping calculations. These results are summarized in Table 18. Note that the maximum temperature gradients reported in Table 18 refer to the maximum values anywhere in the pellet and occur at the interface between the fuel and the Mo insert in the UO_2-Mo designs. The results in Table 18 show that at BOC, the maximum fuel temperature of the HTC and LTC are 5.3 and 19.2% lower than in the monolithic UO_2, respectively. At EOC, these differences increase to 10.0 and 26.3%, respectively, since the temperature of UO_2 increases and the UO_2-Mo fuel temperature decreases. Energy storage in the fuel pellets is also lower in the UO_2-Mo fuels, which is partly due to the lower temperature but also due to the lower volumetric heat capacity of Mo, as shown in Figure 75.

Fuel temperature changes throughout the cycle can be explained by UO_2 thermal conductivity degradation due to irradiation, which increases temperature, and the closure of the pellet-cladding gap, which improves heat transfer and lowers the fuel temperature. Adding the high thermal conductivity Mo structure renders the UO_2 thermal conductivity

Table 18: Comparison of maximum fuel temperature, maximum temperature gradient, and energy storage in UO_2, the HTC, and the LTC.

Fuel design	T_{max} (K)		Maximum temperature gradient (K/mm)		Energy storage (J)	
	BOC	EOC	BOC	EOC	BOC	EOC
UO_2	1,422.1	1,448.6	237	309	1,371	1,280
HTC	1,346.6	1,303.4	334	361	1,334	1,144
LTC	1,149.3	1,068.1	297	341	1,226	1,028

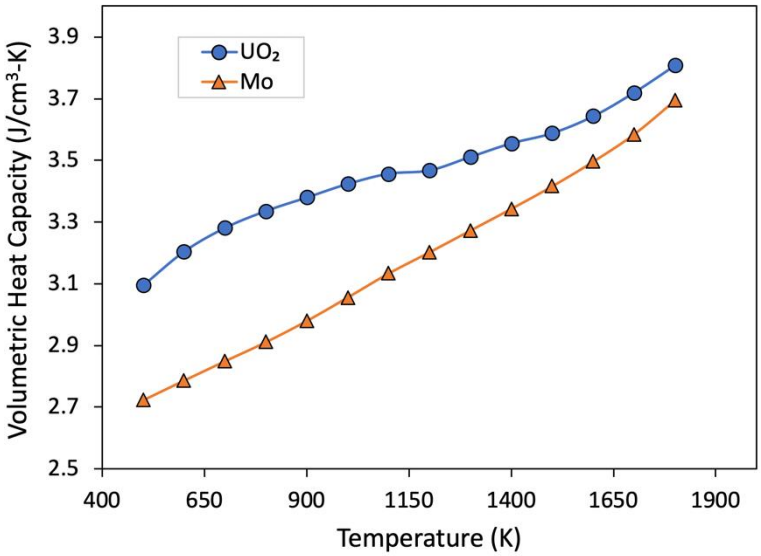

Figure 75: Volumetric heat capacity of UO_2 [34] and Mo [82]

degradation negligible compared with the heat transfer increase caused by the gap closure. It also causes the EOC temperature to be lower than the BOC value.

The maximum burnup reached in the simulations was 8.5% fissions per initial heavy metal atom (FIMA), while the pellet average burnup was about 6.8% FIMA. The pellet-cladding gap remains open longer in the UO_2-Mo designs compared with UO_2 due to the lower temperatures in the pellet, which also releases less gaseous fission product swelling compared to a UO_2 pellet. The released fission gas was minimal in the simulations resulting in lower temperatures but was more significant in the geometries resulting in hotter temperatures. However, the actual impact of the Mo-inserts on fission gas release would require experiments to determine. These scoping calculations may not capture all of the relevant physics.

Figure 76 shows the maximum temperature in the LTC, as well as the minimum and maximum pellet-cladding gap widths in the LTC design as a function of burnup. The maximum temperature decreases with time as the pellet-cladding gap width decreases, which does not close for the LTC or for most of the simulated geometries. The slow closure of the pellet-cladding gap improves heat transfer while the fuel is burned, and competes with the degradation of UO_2 thermal conductivity that typically causes a rise in fuel temperature as a function of burnup.

In Figure 76b, the maximum pellet-cladding gap occurs at the radial Mo disk locations, while the narrowest gap width occurs in between the disks. The maximum temperature gradient reported in Table 18 was the maximum value recorded anywhere in the fuel pellets, and is greater in the HTC and LTC than in UO_2. The large temperature gradients reported in Table 18 occur at the interface between the fuel and the central Mo rod, and another significant temperature gradient occurs at the interface between the fuel and the edge of the radial Mo disks.

Figure 77 compares the radial temperature profiles in UO_2, the HTC, and the LTC at both BOC and EOC. The figure shows that the temperature profiles in the fuels with Mo inserts are generally flatter than that of UO_2, with the exceptions occurring at the UO_2-Mo interface regions. This suggests that the UO_2-Mo fuels may have better overall fission gas retention, although an in-depth analysis and accompanying irradiation

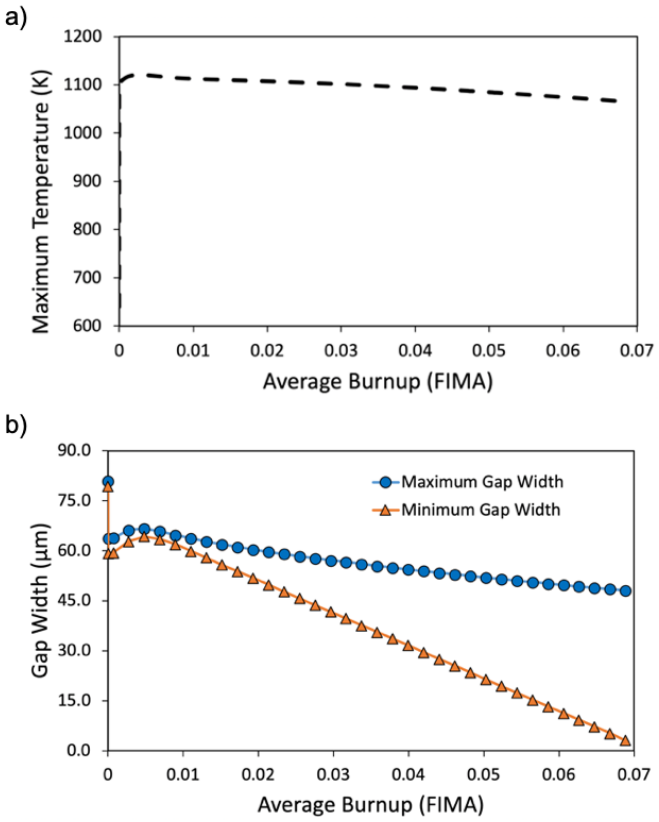

Figure 76. a) Plot of the maximum temperature in the pellet b) Maximum and minimum fuel-clad gap widths vs burnup for the LTC

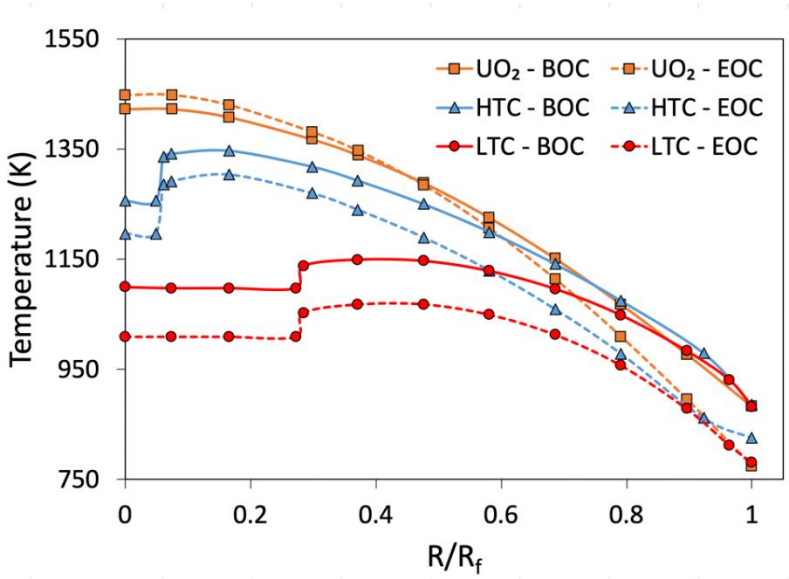

Figure 77: Radial temperature profiles in UO_2, the HTC, and the LTC

experiments on the impact of the large temperature gradient at the UO_2 and Mo interface would be required. Although fission gas release to the pellet-cladding gap was excluded from the BISON models, this assumption is not expected to significantly alter the results shown in Table 18.

A notable observation from the BISON sensitivity study was that the UO_2 with Mo insert design fuel centerline temperature is not the maximum temperature as it is in monolithic UO_2. In the LTC, the centerline temperature is approximately 50 K lower than the maximum temperature, and in the HTC, the centerline temperature is about 90 K lower than the maximum. To better explain this observation, Figure 78 compares the thermal conductivity and temperature profiles for the LTC and regular UO_2 at BOC. As can be seen from the figure, the Mo center rod reduces the maximum distance between the UO_2 and the pellet surface, and the radial Mo disks provide some heat transport capability from the interior towards the perimeter. This combination can result in a centerline temperature that is less than the maximum temperature of the pellet. The heat is then transported from the pellet surface to the cladding using the gap conduction model provided in BISON, where it is then rejected from the cladding using the convective boundary condition.

6.5 Reactor Performance and Safety

6.5.1 Reactivity Coefficients and Control Worth

Using 252-group cross section libraries, the FTC, MTC, SBC, and control rod worth were determined as a function of burnup for UO_2 and both UO_2-Mo cases selected in Section 6.2.1 using MPACT. FTC, MTC, and SBC were calculated using an infinite pin-cell model, and control rod worth was calculated in a one-eighth symmetry model of a typical 17 × 17 PWR fuel assembly. A homogenous UO_2-Mo mixture was modeled in all cases. Figure 79–Figure 82 show the FTC, MTC, SBC, and control rod worth, respectively, for both UO_2-Mo mixtures and regular UO_2 that is 4.9% enriched.

The FTCs for UO_2 and the two UO_2-Mo fuels are all relatively similar. FTC is dominated by the Doppler broadening in ^{238}U resonance absorption peaks, so differences in FTC that are present between the three fuels are primarily caused by differences in

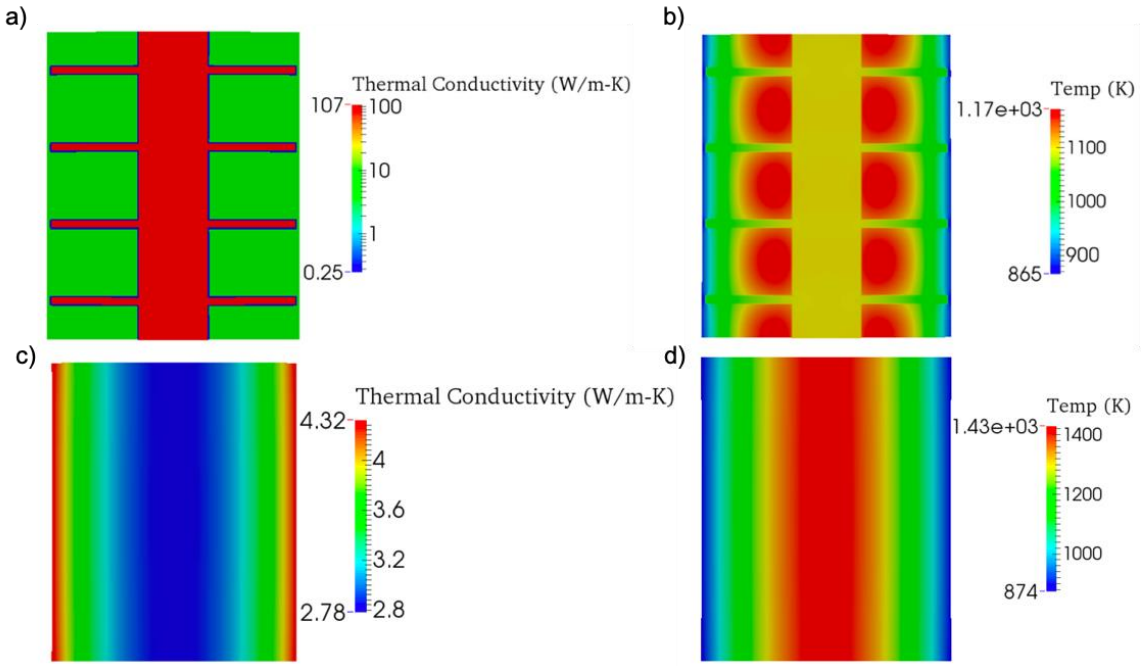

Figure 78: a) UO_2-Mo thermal conductivity profile. b) temperature profile for the UO_2-Mo pellet. c) UO_2 thermal conductivity profile. d) temperature profile for the UO_2 pellet.

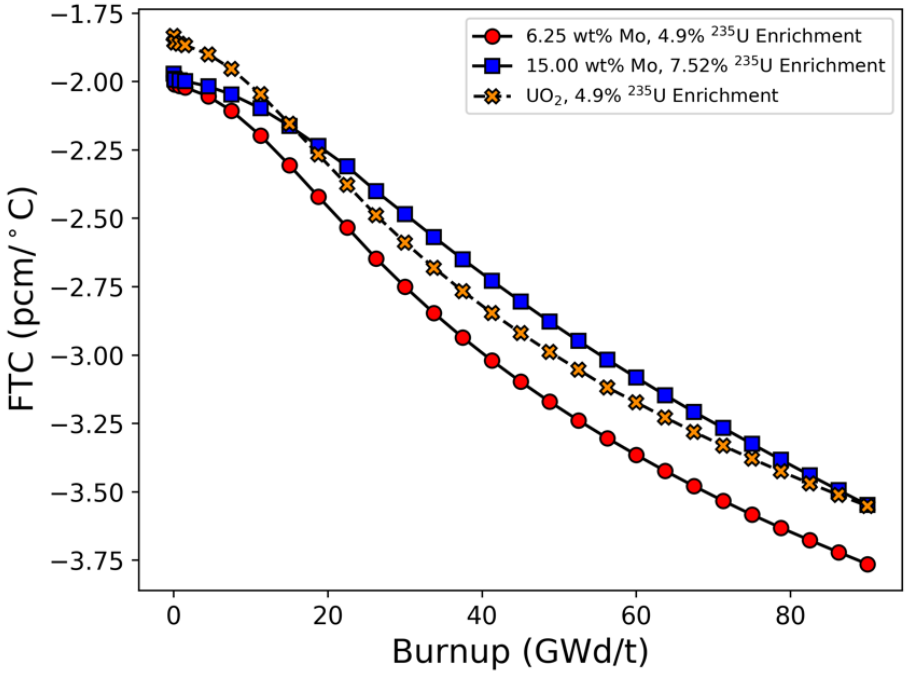

Figure 79: FTC for UO_2 and UO_2-Mo mixtures as a function of burnup.

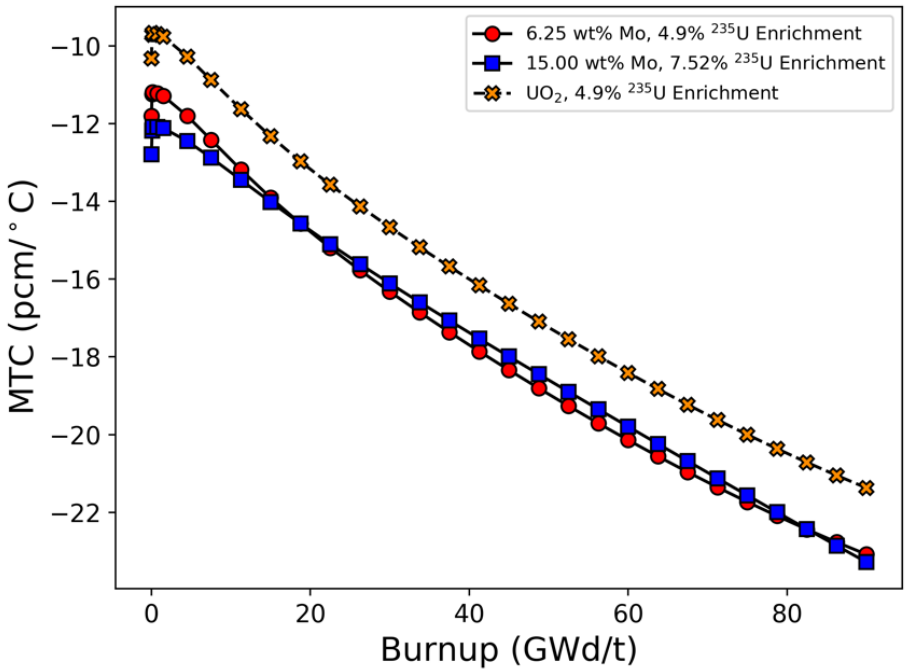

Figure 80: MTC for UO_2 and UO_2-Mo mixtures as a function of burnup.

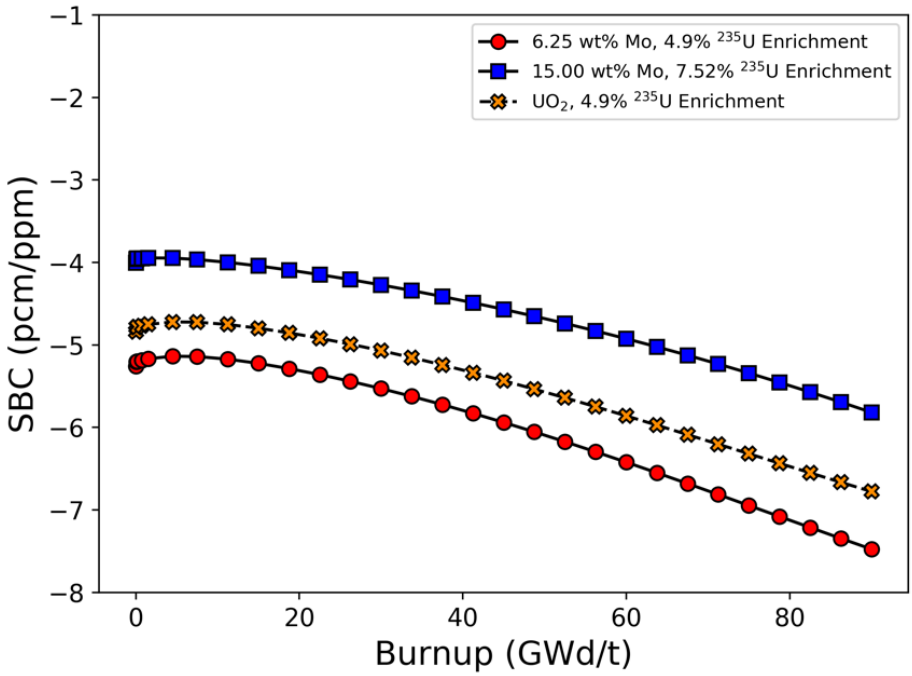

Figure 81: SBC for UO_2 and UO_2-Mo mixtures as a function of burnup.

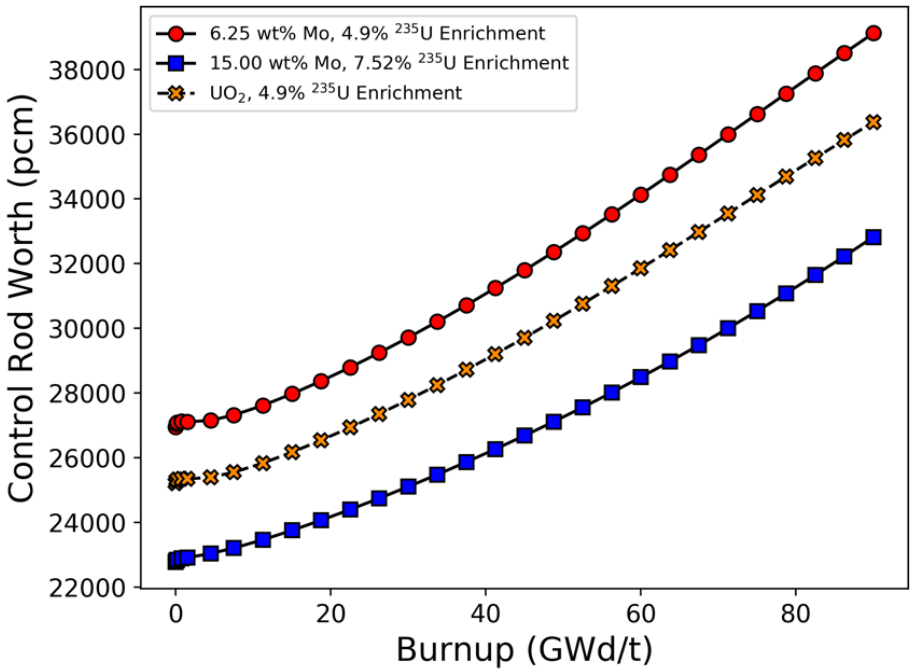

Figure 82: Control rod worth for UO_2 and UO_2-Mo mixtures as a function of burnup

^{238}U content. However, most Mo isotopes are also strong resonance absorbers, as highlighted by Brown et al. [26], so replacing fuel meat with Mo has little effect on FTC. Figure 80 shows that the MTC for the UO_2-Mo fuels is more negative compared with regular UO_2 by approximately 2–3 pcm/°C across all burnup steps. Differences in ^{238}U content and the insertion of a non-fissile resonance absorber again explain this difference from monolithic UO_2.

Figure 81 and Figure 82 show that the SBC and control rod worth of UO_2 are in between those of the two UO_2-Mo cases. This effect can be explained by the production of neutron poisons, e.g. ^{135}Xe, from fission in each fuel type. The accumulated mass of ^{135}Xe in each fuel type is presented in Figure 83, and the figure shows that the UO_2 case is also between the two UO_2-Mo cases. Because the 15wt% Mo case has the greatest amount of ^{135}Xe, the worth of soluble boron and control rods is reduced the most for this case. Equilibrium ^{135}Xe concentration in a reactor is a function of the macroscopic fission cross section and neutron flux, among other factors that should be relatively constant between all three fuel designs considered here, such as the fission product yield, decay constant, and absorption cross section of ^{135}Xe.

Two-group collapsed macroscopic absorption, fission, and capture cross sections and two-group neutron flux calculated using MPACT for the three fuels at BOC are listed in Table 19 to further explain the differences in reactivity coefficients and control worth for which Group 1 corresponds to fast neutron energies and Group 2 corresponds to thermal neutron energies. The data in Table 19 reinforce the given explanations for the differences in reactivity coefficients between UO_2 and the UO_2-Mo mixtures. The more negative FTC and MTC for the UO_2-Mo fuels at BOC are caused by the replacement of fuel meat with Mo and the higher neutron capture cross section in these fuels compared with UO_2. Differences in SBC and control rod worth stem from differences in^{135}Xe production, which are caused by differences in the macroscopic fission cross section and thermal neutron flux.

6.5.2 Calibration of CTF to BISON for Multiphysics Reactor Analysis

Multiphysics analyses to determine the performance of UO_2-Mo fuel in a PWR

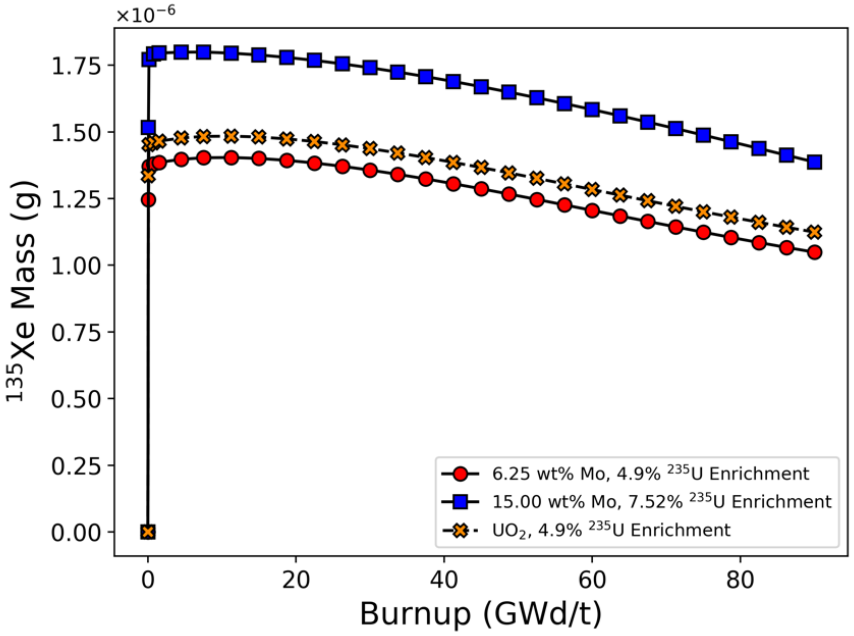

Figure 83: Concentration of ^{135}Xe for UO_2 and UO_2-Mo mixtures as a function of burnup.

Table 19: Two-group neutron flux and absorption, fission, and capture cross sections at BOC.

	6.25wt% Mo case		15wt% Mo case		Reference UO_2	
	Group 1	Group 2	Group 1	Group 2	Group 1	Group 2
ϕ (#/cm^2-s)	2.37×10^{14}	4.73×10^{13}	2.33×10^{14}	3.72×10^{13}	2.29×10^{14}	4.47×10^{13}
Σ_a (cm^{-1})	0.045	0.349	0.050	0.412	0.0443	0.359
Σ_f (cm^{-1})	0.0126	0.253	0.0152	0.306	0.0136	0.264
Σ_c (cm^{-1})	0.0324	0.0964	0.0348	0.106	0.0306	0.0949

fuel assembly were performed in VERA (i.e. MPACT coupled to CTF), but they first required the calibration of thermal conductivity values to be used in VERA's thermal hydraulic solver, CTF. This calibration is necessary because CTF homogenizes the fuel pellet into a single material, and a simple volume-weighted thermal conductivity for UO_2-Mo cannot accurately capture the heterogeneous effect on the radial temperature distribution caused by the Mo insert. The heterogeneous effect of the Mo insert on the temperature distribution in the fuel pellet is captured by finite element analysis in BISON, but not by CTF. Calibration of specific heat was not necessary since this parameter has no impact on steady state temperature calculations in the radial conduction equation used by CTF. The thermal conductivity calibration procedure comprised four primary steps.

1. An AP1000 fuel rod [168] was modeled in MPACT to obtain an axial relative power profile. The AP1000 design was chosen since it represents a state-of-the-art PWR design.
2. The relative power profile was used in a CTF model of the fuel rod to calculate cladding outer surface temperatures and heat transfer coefficients between the rod and coolant that could be used as boundary conditions in BISON models.
3. Six axial locations from the fuel rod model were selected to be modeled as a 1-cm tall fuel pellet in BISON. The BISON models used the corresponding relative powers, cladding outer surface temperatures, and heat transfer coefficients of those six axial locations as boundary conditions.
4. An iterative procedure was developed to run the CTF fuel rod model, pull fuel temperatures from the six specified axial locations, and compare them with the BISON-predicted results. The table in CTF that gives thermal conductivity as a function of temperature was adjusted based on the CTF-to-BISON comparisons, and the model was rerun. This iterative process was repeated until convergence criteria were met.

The relative power profile calculated by MPACT is shown in Figure 84 in which the markers indicate the six axial locations that were used for the CTF calibration. The six selected axial locations are at 15, 63, 147, 219, 315, and 411 cm and have respective

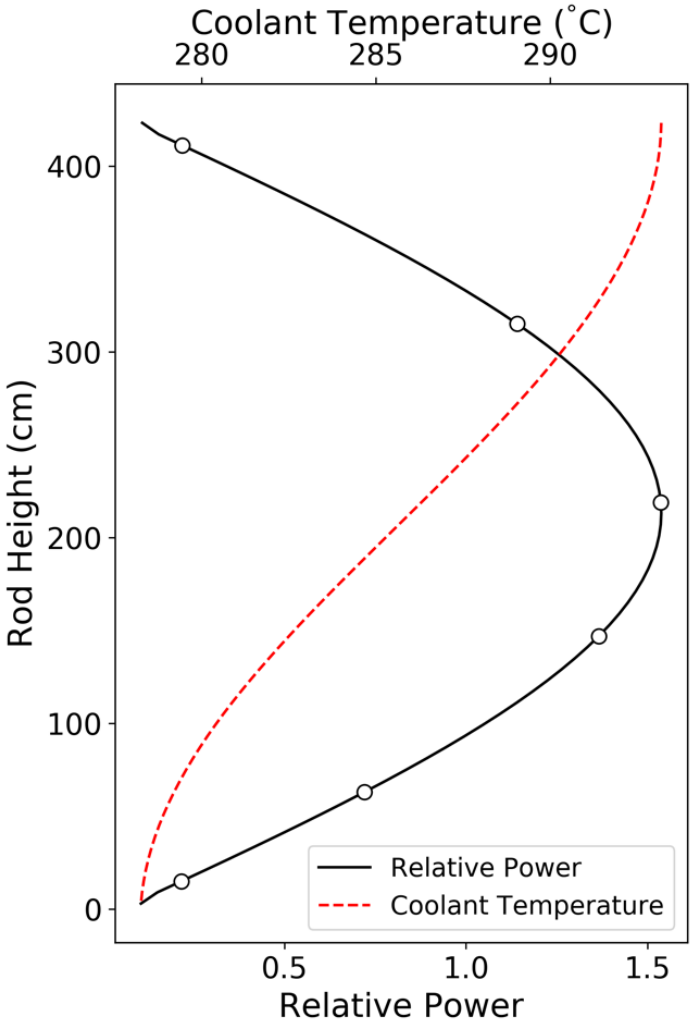

Figure 84: Relative power profile used for PWR fuel rod model in CTF; markers indicate locations used for calibration

relative powers of 0.22, 0.72, 1.37, 1.54, 1.14, and 0.22. Although the same relative power was selected twice, the other boundary conditions differ at the two points, as shown by the inclusion of coolant temperature in Figure 84.

Of the six selected calibration points, the BISON-predicted radial fuel temperatures for the LTC and HTC at three of the points are shown in Figure 85 for clarity. In the figure, the highest temperatures correspond to the 219 cm point, the middle temperatures correspond to the 63 cm point, and the lowest temperatures correspond to the 15 cm point. Calibration was performed by adjusting the temperature-dependent thermal conductivity in CTF to give reasonable agreement to the average fuel temperature and the maximum fuel temperature. Accurately predicting average fuel temperature is important since MPACT uses this value to update cross sections in a coupled calculation, and accurately predicting the maximum fuel temperature is important for safety implications. Additionally, fuel temperatures at 11 radial nodes in the fuel pellet were compared, and the calibration procedure also aimed to minimize the relative RMSE between CTF and BISON at these 11 nodes.

Figure 86 and Figure 87 show the calibrated CTF temperature predictions compared with the BISON predictions for the LTC and HTC, respectively, at the same three axial locations shown in Figure 85. Table 20 lists the relative agreement that the calibrated CTF predictions have with the BISON predictions in terms of average fuel temperature, maximum fuel temperature, and the RMSE across all 11 radial nodes in the fuel pellet. Table 20 shows that the average and maximum fuel temperatures predicted by CTF using the calibrated thermal conductivity relationships agreed with the BISON values within 3% for the LTC and within 1% for the HTC, whereas the relative RMSE across the 11 radial nodes was less than 5% for both cases. These values indicate acceptable agreement, especially since CTF is unable to capture the decrease in temperature that occurs at the central Mo rod interface with the fuel.

6.5.3 Scoping Analysis of PWR Thermal Performance

Models of a 17 × 17 PWR fuel assembly and a single PWR fuel rod were developed in VERA to compare the thermal performance of UO_2-Mo fuel in a reactor

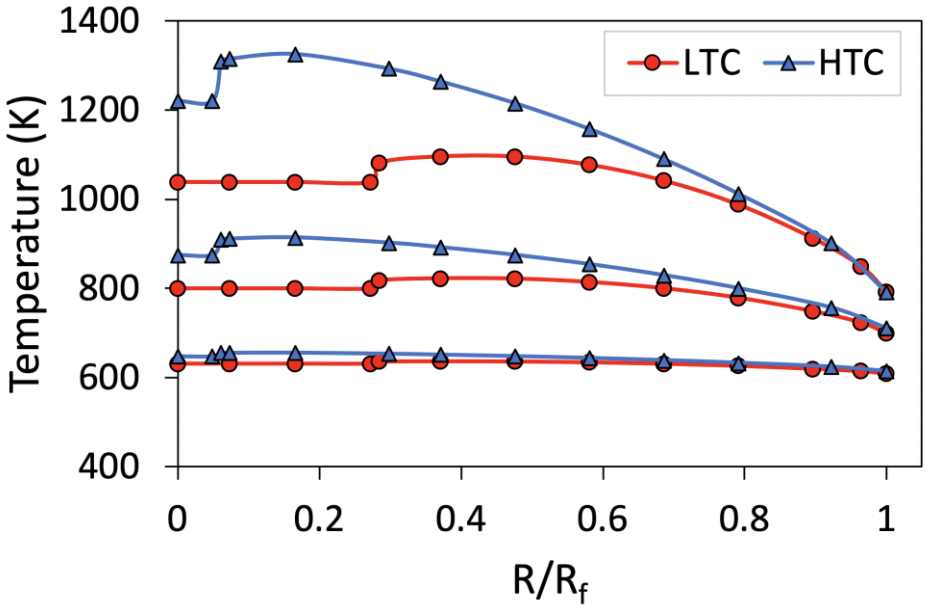

Figure 85: Radial fuel temperature profiles predicted by BISON at 219, 63, and 15 cm

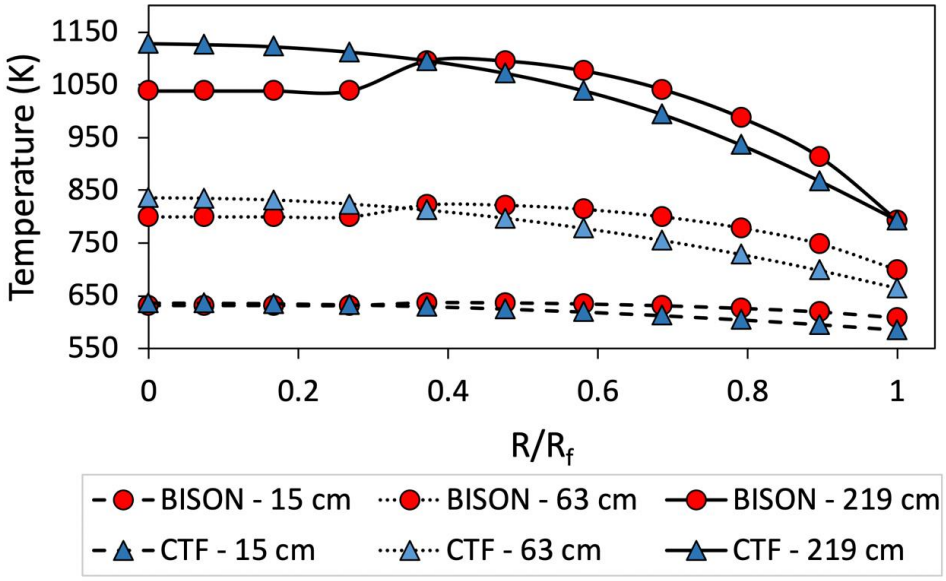

Figure 86: Comparison of calibrated CTF and BISON radial fuel temperature profiles for the LTC at 219, 63, and 15 cm

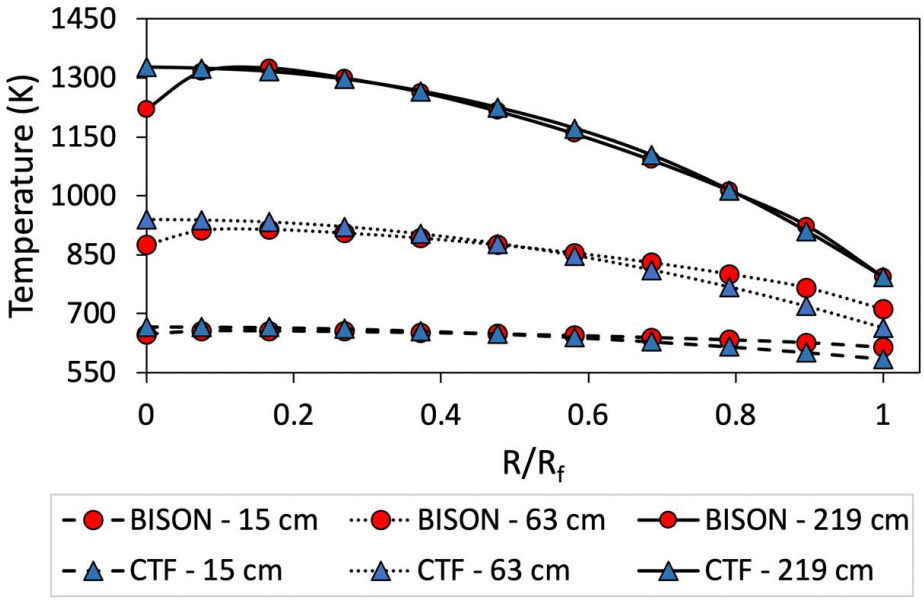

Figure 87: Comparison of calibrated CTF and BISON radial fuel temperature profiles for the HTC at 219, 63, and 15 cm

Table 20: Agreement of calibrated CTF results relative to BISON predictions

Case	T_{avg} agreement (%)	T_{max} agreement (%)	RMSE (%)
LTC	-2.81	3.00	4.98
HTC	0.96	0.15	3.20

environment with that of UO_2 using multiphysics methods. Thermal performance was quantified in this context using the homologous temperature, or the ratio of the fuel temperature to its melting point. The melting temperature of UO_2 is 2,850°C [69], and the melting temperature of Mo used to determine the homologous temperature of the UO_2-Mo fuels is 2,623°C [11]. The melting temperature of UO_2 decreases slightly as a function of burnup, although it is on the order of 0.5°C/GWd/t [183], so this effect is assumed negligible in the current study. In the 17 × 17 fuel assembly, homologous temperature was calculated in the hottest fuel rod at BOC only but was calculated as a function of burnup in the single fuel rod model. CTF's built-in properties for UO_2 were used for the reference calculation, and the calibrated thermal conductivity relationships derived for the LTC and HTC were used for the UO_2-Mo calculations.

Figure 88 shows the hottest rod's homologous temperature in the PWR fuel assembly at BOC as a function of the fuel rod's height for UO_2, the LTC, and the HTC. Figure 89 shows the homologous temperature at the hottest location in the single fuel rod model as a function of burnup for the three fuel designs. All thermal conductivity relationships were assumed to be constant as a function of burnup because the version of VERA used for this analysis does not account for UO_2 thermal conductivity degradation as a function of burnup. The impact of this assumption is that the predictions of homologous temperature will be conservative since the BISON analysis showed that the monolithic UO_2 temperature will increase as a function of burnup, but the temperature of the UO_2-Mo fuel goes down as a function of temperature.

The changes in homologous temperature that occur as a function of burnup are due to axial power shifts during the cycle and the use of CTF's dynamic gap conductance model. Figure 90 shows the relative power in the single fuel rod model for monolithic UO_2 and the LTC at 0, 30, and 60 GWd/t as examples of how the power shape evolves for these fuels. In the fuel assembly, the LTC lowers the peak homologous temperature by 23.5% and the HTC lowers the homologous temperature by 4.2% compared with UO_2. As a function of burnup, the LTC reduced the peak homologous temperature by 13–32%. The HTC showed a maximum reduction of homologous temperature of 21%, but there were several points near BOC in which the HTC caused an increase in homologous

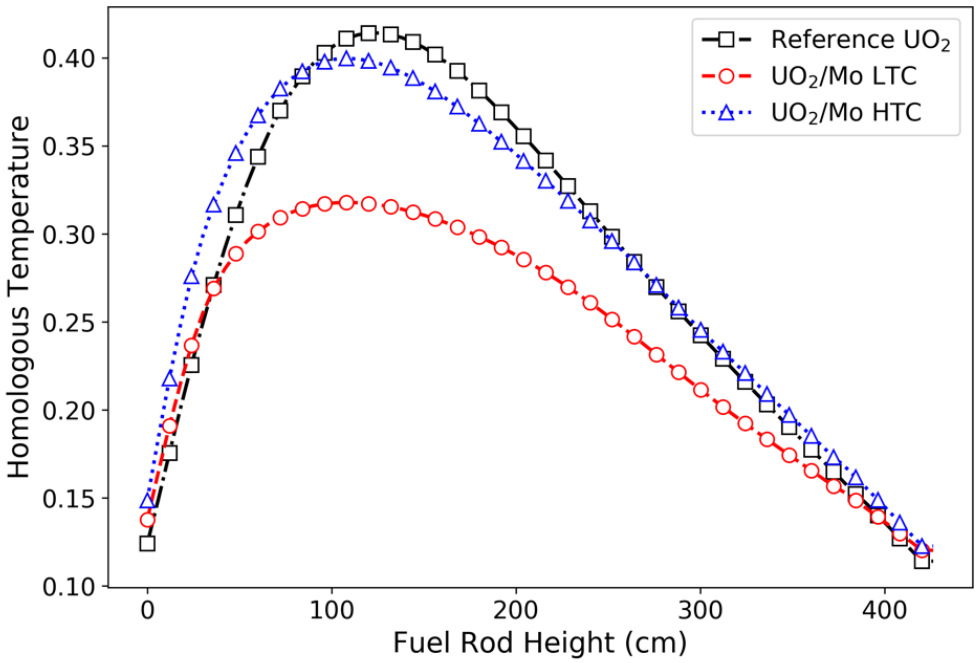

Figure 88: Homologous temperature in the hottest rod in a PWR fuel assembly at BOC

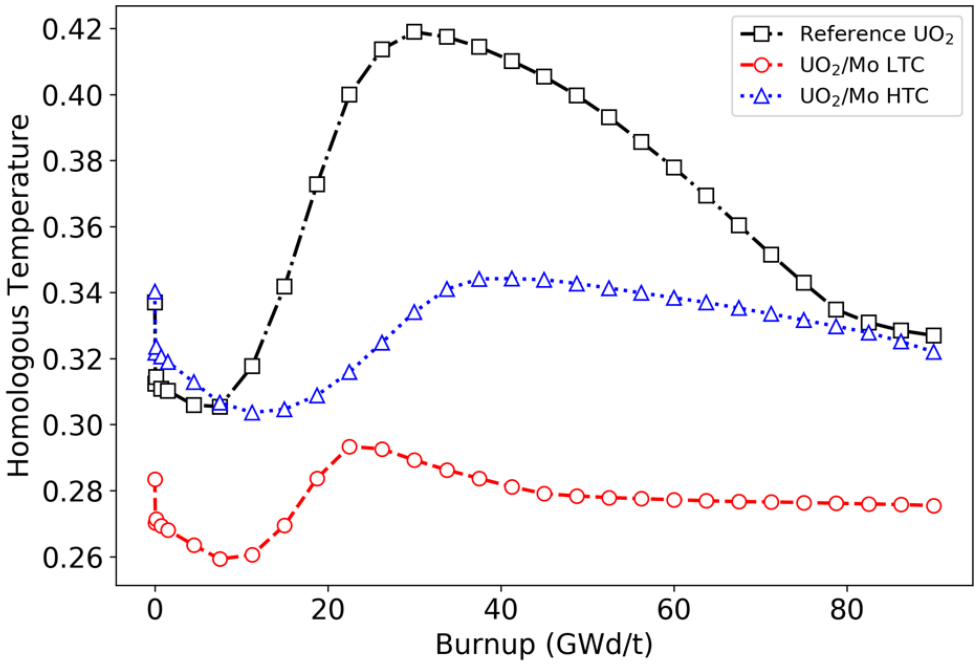

Figure 89: Peak homologous temperature in a PWR fuel rod as a function of burnup

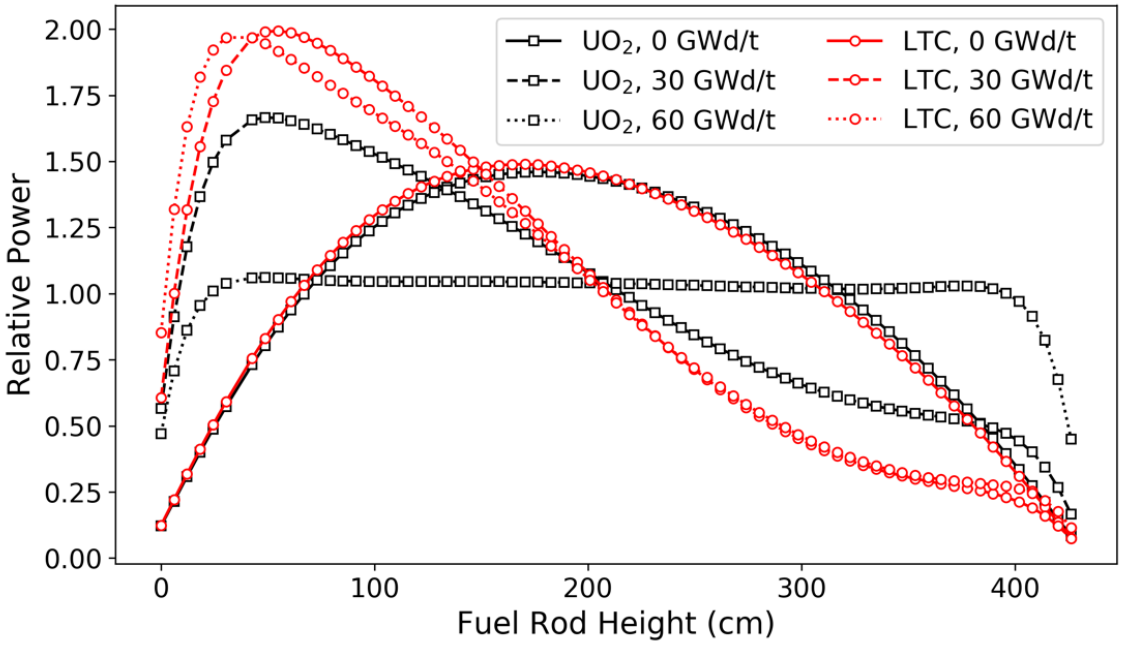

Figure 90: Relative power shapes for UO_2 and the LTC at different burnup values.

temperature by several percent. Although the operating temperature of the HTC is lower than that of UO_2, this result is caused by the melting temperature of Mo being more than 200°C lower than that of UO_2.

6.6 Discussion of Results

The sensitivity study results presented in Section 6.3 indicate that the Mo insert geometry does impact neutronic and heat transfer performance. However, the effect of geometry on initial neutron multiplication factors and cycle length was small since the best performing geometry had a cycle length that was about 14 days, or 3%, longer than the worst performing geometry. Furthermore, the geometry that gave the highest initial reactivity augmented spatial self-shielding effects. The self-shielding in the geometry that gave the lowest initial reactivity and the self-shielding in the homogeneously mixed UO_2-Mo design was more similar to what is experienced in UO_2. In terms of heat transfer, the insert geometry had a much larger impact. Compared with UO_2 at a power of 270 W, the worst performing UO_2-Mo design in the heat transfer sensitivity study lowered the maximum temperature by approximately 80 K at BOC, whereas the best performing geometry lowered the maximum temperature by approximately 280 K. BISON calculations at EOC showed even more significant temperature reductions from the Mo structures. Temperature differences between the bounding insert geometries were approximately 15–20%.

Generally, the geometric features that were best for cycle length were not the best for heat transfer. The only exception was the radius of the central rod, r_c, since an increase in this value tended to give an increase in cycle length and a decrease in fuel temperature. A cycle length calculation was performed for the LTC from the heat transfer sensitivity study, and it was determined to be 459 EFPD. Despite the LTC having a relatively large value for r_c, this cycle length is just 2 days longer than the cycle length of the worst performing geometry from the neutronics sensitivity study. This occurs because the LTC also had large disk radii, which was the most impactful parameter on neutronics that brings down the achievable cycle length. Although the geometric features of the insert that are best for heat transfer typically do not optimize the cycle length, the results

of this study suggest that emphasis could be placed on optimizing the heat transfer performance since the geometric impact on temperatures is on the order of 20%, whereas the impact on cycle length is just a few percent. However, a formal cost-benefit analysis would need to be performed to determine if the reduction in fuel temperature and related safety and operational benefits outweigh the monetary costs associated with a several percent reduction in cycle length. It may be found that some combination of Mo content, ^{235}U enrichment, and insert geometry minimizes the cost of the design while still realizing most of the potential heat transfer benefits.

The results from the heat transfer sensitivity study showed that r_c was the most impactful geometric feature on the maximum fuel temperature. Annular fuel pellets, in which the central region of the fuel pellet is hollow, have been previously studied and it was found that the benefits of annular fuel are greater than those from the UO_2-Mo fuel form in terms of reducing fuel temperatures [184]. At 150% nominal power density, the dual-cooled annular fuel pellet concept showed a peak temperature decrease of 1300°C compared to UO_2 at 100% nominal power density. However, for these benefits to be realized, the annular fuel requires internal cooling and changes to the typical PWR fuel rod geometry. An in-depth cost-benefit analysis would need to be performed for the UO_2-Mo fuel to determine which fuel form is more economically feasible.

Because the impact of insert geometry on cycle length and neutron multiplication factor calculations was small, it was justified to homogeneously mix the UO_2 and Mo in neutronics models used for RTCs and multiphysics calculations. Although homogenously mixing UO_2 and Mo was deemed appropriate for neutronics calculations, the relatively large impact of the Mo insert geometry on fuel temperature and heat transfer performance required thermal conductivity calibration in CTF. BISON results showed that the maximum fuel temperature did not occur at the centerline in the UO_2-Mo designs, and there were large temperature gradients at the insert-to-fuel interface. Neither phenomena can be mimicked in CTF, although thermal conductivity calibration was performed that allowed CTF to closely match the temperatures predicted by BISON in terms of pellet average, maximum, and RMSE across a set of radial nodes. This calibration enabled scoping analysis which include thermal hydraulic effects.

Multiphysics PWR fuel rod and assembly calculations performed using calibrated fuel thermal conductivity and MPACT coupled to CTF within VERA showed that an optimized Mo insert could increase the margin to fuel melt by as much as 32% during the fuel cycle compared with UO_2. This prediction was made under the assumption that the thermal conductivity relationships were constant with burnup and might differ with the use of burnup-dependent thermal conductivity and gap closure models. Regardless, this evaluation of the UO_2-Mo fuel form with multiphysics modeling tools consistently suggests that an optimal insert geometry can reduce fuel temperatures by up to about 30% and provide an associated decrease in stored energy in the fuel on the order of 10–20% compared with UO_2. These reductions in temperature and stored energy may improve fuel performance during normal reactor operation, reduce fission gas release, and possibly provide enhanced accident tolerance. A transient analysis of large-break LOCAs in LWRs by Terrani et al. [35] showed that an increase in fuel thermal conductivity and the associated decrease in stored energy at nominal power can have a modest impact on the peak fuel and cladding temperature in a PWR during the transient. In that study, the reduction in peak cladding temperature during the large-break LOCA in a PWR due to increases of fuel thermal conductivity of 200% and 500% were 56°C and 92°C, respectively. Similar benefits may be realized with the UO_2-Mo fuel form, as indicated by the lower stored energy in the fuel pellet compared with UO_2 indicated in Table 18. It is important to note that the benefits of incorporating Mo inserts requires an increase in ^{235}U enrichment to match the cycle length of monolithic UO_2. A ^{235}U enrichment of over 7.5% was required to approximately match the cycle length of UO_2 that is 4.9% enriched. However, based on the contour plot in Figure 61, the detriment to cycle length in a 4.9% enriched UO_2 fuel pellet with 15wt% Mo would be over 40%.

A secondary outcome of this work can be used to guide ongoing and future investigations of UO_2-Mo fuel forms. The present study does not take into account the challenges or methods that would be required to produce UO_2 fuel pellets containing Mo inserts of the geometries investigated. While a number of experimental efforts have produced UO_2-Mo composite microstructures of varying complexity, none disclosed have to date achieved the complexity represented in Figure 64. Advances in fuel fabrication

methods are required to achieve this level of complexity [185]. The systematic approach used in this study could be applied to other UO_2-Mo fuel forms, such as the concepts developed by Medvedev and Mariani [10]. However, a concept that uses additive manufacturing techniques may allow for a more complex insert structure that is optimized for performance and safety, improves manufacturability, and does not impact the fuel rod assembly process since the UO_2 and Mo would not need to be alternately stacked. The results of this work agree with previous investigations that insert geometry will have a modest impact on maximum fuel temperature, but minimal impact on neutronic characteristics. Research programs seeking to further develop UO_2-Mo fuel forms can therefore prioritize fabrication trials and experimental work with an understanding that reactor performance and safety should be minimally impacted by the specific geometry of the Mo inserts used.

CHAPTER 7
CONCLUSION

7.1 Summary and Conclusions

The development of accident tolerant fuel, cladding, and core structural materials is motivated by the need to extend the coping time during a severe accident, such as the one that occurred at the Fukushima-Daiichi nuclear power plant in 2011. Computational evaluations of four ATF technologies spanning from early-stage to near-term deployment concepts were performed in this dissertation. Additionally, an initial assessment of VERA's ability to perform BWR analysis and demonstration of the modeling suite's advanced features and application to ATF research was performed. These types of simulation-based evaluations are vital to enhancing the efficiency of new materials research and make the licensing process for new materials more economical. Although a variety of ATF concepts were studied using a breadth of methods, the single underlying theme of this work is the support of ATF development through advanced, multiphysics modeling methods. Results from each of these evaluations highlighted key advantages and potential challenges associated with each concept.

7.1.1 FeCrAl Cladding Thermal Hydraulic Evaluation

CHAPTER 3 presented a computational thermal hydraulic analysis of FeCrAl cladding subjected to an RIA-like power transient. When predictions of CHF and cladding temperature calculated by RELAP5-3D and CTF were compared to experimental data, it was found that the computer models errored on the side of conservatism by underpredicting CHF and overpredicting the cladding temperature when the power transient was applied. To understand the discrepancy between the computer simulation results and the experimental data, two sensitivity studies were conducted to determine if the differences between the experimentally measured CHF and the CHF predicted using the look-up method may be explained by differences in heat transfer coefficients, material thermal properties, or the enhancement of CHF that occurs during a heating transient.

Both sensitivity studies used RAVEN coupled to the RELAP5-3D model of the experiment. The first sensitivity study varied multipliers on heat transfer coefficients and also included variation of the CHF multiplier, which may reflect the enhancement of CHF caused by a transient heating process. It was found that CHF was not dependent upon most of the heat transfer coefficients and was only impacted somewhat by the variation in the transition boiling heat transfer coefficient and much more so by the CHF multiplier. The PCT was sensitive to the transition and film boiling heat transfer coefficients and the CHF multiplier because transition and film boiling are the flow regimes that occur in the post-CHF regime. The second sensitivity study varied the thermal conductivity and volumetric heat capacity of the FeCrAl cladding based on measurement uncertainties. The CHF multiplier was also included in the second sensitivity study. Variations in thermal effusivity and thermal diffusivity were able to be calculated from the thermal conductivity and volumetric heat capacity. The resulting trends showed that CHF increases with the CHF multiplier, thermal conductivity, thermal effusivity, and thermal diffusivity, but somewhat decreased as volumetric heat capacity increased. PCT decreased as the CHF multiplier, volumetric heat capacity, and thermal diffusivity increased, but decreased as thermal effusivity increased. There was no apparent sensitivity of PCT to thermal conductivity.

The discrepancies between experimental data and simulated results indicate the areas of research that require the most attention. The relative insensitivity of CHF and PCT to heat transfer coefficients suggest that improving upon the numerous empirical heat transfer correlations is less of a priority than understanding the material property evolution of FeCrAl and the need for a correlation that predicts the CHF enhancement caused by a power transient. The results in CHAPTER 3 show that this is an important quantity to understand to correctly predict CHF and PCT.

An important contribution from the FeCrAl study is the demonstrated difference between how CHF is being modeled and the real-world phenomenon. From the sensitivity studies, which included a total of 17,883 trial runs, the runs that best matched the experimental data could be determined in terms of three FoMs: MHF, PCT, and integral heat flux. A best match for each FoM was determined based on relative error to

the experiment. An overall best match was also determined, which was identified as the run with the minimum combined RMSE for each FoM. The overall best match from the first sensitivity study had relative errors for the MHF, PCT, and integral heat flux of 3.22%, 36.52%, and 2.52%, respectively, giving an RMSE of 36.74%. The overall best match from the second sensitivity study involving material thermal properties had relative errors for the MHF, PCT, and integral heat flux of 1.24%, 27.02%, and 1.70%, respectively, resulting in an RMSE of 27.10 %.

The relative errors from the best match cases show that even when a good match to the MHF and integral heat flux is made, RELAP5-3D is still conservative when predicting the post-CHF temperature excursion. This is due to the difference between the post-CHF behavior modeled by computer codes and the phenomenon that occurs in reality. In the UNM FeCrAl experiment, there was a 1-second transition period after DNB occurred where the heat flux continued to increase. This led to a difference between the CHF and the MHF, which broadened the heat flux pulse width and allowed more heat to be transferred to the coolant during the power transient. The distinction between CHF and MHF was only experienced in the experiment using FeCrAl, and may be due to uncertainty in the measurements. However, it was shown in the experimental for Inconel, stainless steel, and FeCrAl that the heat flux decreases at a much slower rate in reality than in the computer models after CHF is reached. The faster rate of heat flux reduction in the codes reduces the width of the heat flux pulse during the transient and caused a large overshoot in the post-CHF surface temperature prediction. These observations are key contributions from the study of FeCrAl cladding that highlight conservatism in computer models and area of needed research.

7.1.2 Assessment of VERA BWR Modeling and Analysis of SiC/SiC Channel Box

An initial assessment of the BWR modeling capability in CASL VERA and its application to predicting temperature and fast neutron flux distributions in SiC/SiC channel boxes was made in CHAPTER 4. Two types of code-to-code comparisons were made for this assessment, both of which used historical Peach Bottom BWR fuel assembly geometries. First, two-group cross sections generated by VERA's deterministic

neutron transport code MPACT and the Monte Carlo code Serpent were compared. The cross sections generated for the 2-D fuel lattices were typically in good agreement, especially when the statistical uncertainties in the Monte Carlo estimates from Serpent were taken into account. The greatest discrepancies between the two modeling tools occurred in the scattering cross sections produced from the lattices that contained gadolinia, but it was found that using the P_2 approximation for scattering significantly reduced the differences.

Predictions of several key reactor parameters made by VERA and PARCS/PATHS were compared for six fuel assembly designs from the Peach Bottom Unit 2 reactor. To perform the comparisons, the high-fidelity results from VERA were radially averaged to match the output resolution produced by PARCS/PATHS. In terms of k_{eff}, the two modeling tools agreed within approximately 150-410 pcm, and the differences in relative power, exit void fraction, pressure drop, and fuel temperature were mostly on the order of 1-10%. While the exit void fractions predicted by the two codes were similar, VERA always predicted noticeably greater voids at lower regions in the assemblies. Standalone comparisons between CTF and PATHS showed that these void fraction discrepancies are a primary cause of other discrepancies in the coupled calculations. Differences between the two modeling codes may also be explained through differences in methodology and design philosophy since VERA was specifically designed to utilize multiphysics capabilities, a high-fidelity output structure, and higher-order solution methods compared to PARCS/PATHS.

Following the assessment of VERA's BWR modeling capability, the modeling suite was used to generate temperature and fast neutron flux boundary conditions in SiC/SiC channel boxes in single fuel assembly and mini-core models. Calculations of temperature and fast neutron flux distributions in SiC/SiC channel boxes showed that the fast neutron flux varies significantly in both the radial and axial directions, especially in the presence of an inserted control blade. These distributions are important because fast flux gradients are the primary cause of potential SiC/SiC channel box deformation due to nonuniform irradiation swelling rates.

In the single fuel assembly models, two energy cutoffs were used for predicting the fast flux. In previous SiC/SiC characterization studies, 0.1 MeV was considered as the energy cutoff for neutrons that could cause displacement damage and lead to irradiation swelling. The cutoffs of 0.067 MeV and 0.183 MeV were the nearest available cutoffs to 0.1 MeV in the VERA cross section library. Calculating the fast flux distribution at these two energy cutoffs showed the sensitivity of the fast flux and the channel box deformation to the fast neutron energy. The difference in fast flux between the two cutoffs was between 4% and 17% depending on the axial location considered and the control blade configuration. Regardless of the fast flux energy cutoff used, the radial fast neutron flux gradient is approximately 35-40% when the control blade is fully inserted, and the peak fast flux is approximately 5 to 7 times greater than the minimum peak flux in the axial direction. The axial temperature gradient is about 10°C and the radial temperature gradient is about 2-3°C depending on the control blade configuration.

Results from the mini-core model showed similar distributions to the single fuel assembly models. The fast neutron flux gradient across all four channel boxes in the control cell ranged from a relative difference of approximately -99–130% from the average flux value. Both the temperature and fast neutron flux gradient were most pronounced in the channel box nearest to the control blade and would be expected to undergo the most deformation.

This study suggests that VERA is capable of predicting steady-state BWR performance at least as well as current regulatory tools, while also offering numerous advanced modeling features that allow it to solve complex and novel problems. To further improve confidence in the application of VERA to BWRs, uncertainty quantification studies, code-to-code comparisons of full-core and depletion analyses, additional cross section comparisons in fuel lattices at different states and burnup, and validation against measured BWR data should be performed. Benchmarking of VERA's ability to model grid spacers in BWRs also needs addressed. Overprediction of void fraction in bubbly and slug flow regimes by CTF compared to experimental data has been highlighted in previous studies and is an area of continued development within CASL. From an ATF standpoint, analyses of SiC/SiC channel boxes can also be expanded upon

to account for operational procedures such as varying control blade configurations and core shuffling maneuvers, and additional deformation studies could be performed using the boundary conditions generated in this study.

7.1.3 Reactor Performance and Safety Characteristics of ThN-UN

The ATF evaluation presented in CHAPTER 5 involved finding mixtures of ThN and UN that could match the UO_2 cycle length, and then determining the reactor performance safety characteristics of those mixtures. The motivation for this study is that both UN and ThN have a higher thermal conductivity than UO_2, so better thermal performance was expected. However, on their own, UN is known to readily deteriorate in water, and thorium has no fissile isotopes and is unable to be used as a standalone fuel type. The consideration of composite ThN-UN fuel forms was driven by the hypothesis that ThN may mitigate the degradation of UN in water, while UN provides the external neutron source to transmute ^{232}Th to the fissile ^{233}U. Compositions were determined for both natural nitrogen and 100% enriched ^{15}N cases.

RTCs were calculated for the determined UN and ThN-UN fuel compositions and compared to the UO_2 reactivity coefficients. The FTC and MTC were more negative for the UN and ThN-UN fuels but were still within the acceptable limits provided by the AP1000 DCD. Both the SBC and control rod worth for the nitride fuels were found to be less negative than the UO_2 case and were outside the AP1000 limits. The reduced control worth and more negative MTC suggest that shutdown margin may be an issue for this fuel form. When 100% enriched ^{15}N was used, the FTC and MTC for UN and 40%ThN-60%UN were similar to the natural nitrogen cases. The worth of the soluble boron and control rods increased by using enriched ^{15}N, but they were still less than the control worth in a UO_2 system and still outside the AP1000 DCD limits. Although the reduced control rod worth may partially be compensated for by less excess reactivity and ^{15}N enrichment, full-core analysis should be performed to confirm if shutdown margin is truly an issue for UN or ThN-UN-fueled PWRs. If shutdown margin is insufficient for these fuel types, then design changes such as soluble boron with enriched ^{10}B or B_4C control rods may need to be considered.

The thermal performance of ThN-UN fuel in an AP1000 fuel pin was determined using the coupled neutronics and thermal hydraulics capabilities of MPACT and CTF within VERA. Axial distribution of homologous temperature was found at BOC for each fuel form, and results showed that the maximum homologous temperature for the nitride fuels was approximately 50% of the UO_2 homologous temperature. When burnup was considered, the maximum UO_2 homologous temperature was found to be 0.42, whereas the maximum homologous temperature for UN was approximately 0.20. The homologous temperature never surpassed 0.195 for any of the ThN-UN mixtures. This significant reduction in homologous temperature highlights the benefits of nitride fuels from an ATF perspective: these fuels have a larger thermal safety margin and therefore a smaller chance of melting and releasing fission products.

Overall, the preliminary results from this study point to ThN-UN mixtures being a feasible fuel form in a PWR under normal operating conditions, and they may have advantages from an accident tolerance viewpoint. For ThN-UN to be implemented, further evaluation is required to address key remaining challenges, such as shutdown margin, ThN-UN chemical reactivity with water, fuel behavior during irradiation, and fuel safety during accident scenarios. An analysis could be performed to determine if moving to a thorium-based fuel is viable from an economic viewpoint. Future work could expand upon the work on this study by performing assembly-level and full-core analyses in which additional factors would need to be considered such as varying fuel loading patterns, the impact of fuel assembly location within the core, fuel management schemes, and the axial and radial dependence of burnup within the fuel. The comparison of ThN-UN fuels to a UO_2 fuel pin-cell of a single enrichment value provides a first look at the feasibility of this novel fuel type, but further investigation would be required to optimize the core design in terms of fuel management and loading patterns.

7.1.4 Reactor Performance and Safety Characteristics of UO_2 with Mo Inserts

The impact of UO_2 with Mo inserts and insert geometry on reactor performance and safety characteristics was investigated in CHAPTER 6 using sensitivity analysis techniques and multiphysics methods. Sensitivity analyses on the insert geometry impact

on neutronic and heat transfer performance were performed using Serpent and BISON. Results from the sensitivity studies that used single fuel pellet models informed reactor analysis models in coupled MPACT and CTF within the VERA multiphysics modeling environment. This included justifying the use of homogenized UO_2-Mo in neutronics models and calibrating UO_2-Mo thermal conductivity to allow CTF to approximate the finite element results produced by BISON.

The sensitivity analyses showed that the most impactful geometric features differed between the neutronics and heat transfer studies, and that optimal features in one study hurt performance in the other study. For example, large radial disks caused the greatest decrease in cycle length but improved the thermal performance of the insert. However, the overall impact of insert geometry on cycle length was much smaller than the impact on fuel temperature and energy storage. Although the impact of the insert geometry on cycle length was small for the Mo content and ^{235}U enrichment considered in this study, the inclusion of Mo in UO_2 significantly affects cycle length in a way that will likely require compensation via HALEU.

RTC calculations showed that the investigated geometries had a relatively small effect on FTC and MTC, likely due to the similarity in absorption cross sections between Mo and ^{238}U. However, Mo content did impact SBC and control worth since replacing fuel with Mo and the varying ^{235}U enrichments affected flux levels and fission product poisoning. Homologous temperatures predicted at BOC in a PWR fuel assembly and as a function of burnup in a single fuel rod showed that the optimal Mo insert geometry increased the margin to fuel melt from 13 to 32%. Also, an unoptimized geometry can exhibit little to no benefit compared with UO_2 in terms of homologous temperature since the melting point of Mo is lower than that of UO_2.

The key takeaway from this study is that using Mo inserts in UO_2 can potentially provide significant safety and fuel performance benefits in a reactor environment if the insert geometry is optimized, but these benefits come with a significant decrease in cycle length that requires more than 5% ^{235}U enrichment as compensation. Features of an optimal geometry were identified in this study using sensitivity analysis methods, and a central axial rod with a large radius was the most important geometric feature for

reducing maximum fuel temperature. Inserts with many thin, radial disks that extend to the edge of the fuel pellet further reduce temperature by providing a radial pathway for heat to transfer out of the fuel. Incorporating Mo inserts into nuclear fuel appears feasible based on the RTC calculations made in this study since the impact to FTC and MTC was small. However, full-core shutdown margin calculations are suggested to confirm this since reduced control worth and a somewhat more negative MTC were observed in the fuel design with 15wt% Mo and 7.52% ^{235}U enrichment. A stress analysis of UO_2 with Mo inserts is also suggested to determine whether stress-induced failure could occur during fabrication or reactor operation, and comparisons with other UO_2-Mo concepts should be carried out that focus on the feasibility of manufacturing and assembling these designs. Lastly, an optimization study and accompanying irradiation experiments that focus on fuel performance of this novel fuel form is also suggested for future work since the optimization performed in this study focused on neutronics and heat transfer only.

7.2 Contributions and Evaluation of Hypotheses

7.2.1 Contributions

In general, the work presented in this dissertation contributes new knowledge of the operational and safety performance of potential ATF candidates using advanced computational methods. This work demonstrates a key step in the licensing process of new materials that is made more efficient and economical through the application of novel multiphysics methods and tools. The significant and specific contributions of this dissertation include:

1. Comparison of experimental and simulated results for a flow boiling CHF apparatus.
2. Quantification of the sensitivity of CHF and post-CHF phenomena to heat transfer coefficients, material properties, and the CHF enhancement caused by a heating transient.
3. Examination of key differences between CHF modeling and the observed phenomenon, most notably the transition period from nucleate boiling to post-CHF boiling regimes in which heat transfer is yet to decline.

4. An initial assessment of CASL's multiphysics modeling suite, VERA, for BWR fuel assembly cross section generation and performance modeling using current state-of-the-art simulation tools.
5. Calculation of 3-D temperature and fast neutron flux distributions in SiC/SiC channel boxes for a variety of control blade configurations using VERA.
6. Identification of multiple ThN-UN mixtures that are capable of meeting the fuel cycle length of UO_2 in a PWR for both natural nitrogen and 100% enriched ^{15}N.
7. Determination of reactor performance and safety characteristics, specifically RTCs and homologous temperature, of ThN-UN fuel forms using both natural nitrogen and enriched ^{15}N in a PWR.
8. Development of an optimization scheme that uses sensitivity analysis methods to maximize the neutronic and heat transfer performance of Mo inserts in UO_2.
9. Programming of a calibration scheme to obtain close matches between UO_2-Mo fuel temperature profiles in CTF in which the Mo is smeared in the UO_2 to finite element profiles from BISON in which Mo inserts are explicitly modeled.
10. Determination of RTCs and homologous temperature of UO_2 with Mo inserts in a PWR using multiphysics methods.

7.2.2 Review of Hypotheses

The hypotheses presented in Section 1.3 are reviewed based on the findings presented in this dissertation.

1. The CHF and PCT of FeCrAl cladding are sensitive to heat transfer coefficients, material properties, and the transient-induced CHF enhancement.

This statement is largely true because it was shown that CHF and PCT of FeCrAl were most sensitive to material properties and the CHF multiplier. CHF and PCT showed some sensitivity to the heat transfer coefficients in the post-CHF boiling regimes (transition and film boiling), but their effect was minor compared to that of material properties and the CHF multiplier.

2. VERA is capable of accurately predicting BWR performance and is valid to use for novel, complex problems, such as ATF evaluations.

An assessment was made of VERA's ability to generate nuclear cross sections and predict reactor performance parameters. Comparisons of two-group cross sections were made between VERA's deterministic neutron transport solver, MPACT, and the Monte Carlo code Serpent using 2-D BWR fuel lattice models. These comparisons showed that the cross sections predicted by MPACT matched or nearly matched those predicted by Serpent within uncertainty bounds. Peach Bottom BWR fuel assembly models were developed in VERA and PARCS/PATHS to compare reactor performance parameters. Predictions from each tool showed agreement of neutron multiplication factors within approximately 409 pcm or less, relative agreement of peak fuel temperature between 4.4 and 17.8%, and agreement in pressure drop of 4.4% or less. Outlet equilibrium quality predictions were the same between VERA and PARCS/PATHS for all six assembly types, and both modeling tools predicted similar exit void fractions, although CTF typically predicted a faster vapor generation rate. This level of agreement is typically considered acceptable, and confirms the hypothesis.

3. Temperature and fast neutron flux gradients in a SiC/SiC channel box will lead to deformation and control blade interference.

VERA was used to calculate 3-D distributions of temperature and fast neutron flux in SiC/SiC channel boxes. Both single fuel assembly and mini-core models were utilized, and several control blade configurations were considered. The resulting distributions showed significant fast neutron flux gradients in both the axial and radial directions. These distributions were used as boundary conditions in finite-element deformation and stress analysis models [17], which showed that significant deformation will occur and control blade interference is likely, at least until swelling in the channel box saturates. The residual deformation from thermal gradients is not enough to cause control blade interference.

4. ThN-UN fuels provide an enhanced thermal safety margin due to the high thermal conductivity of nitride-based fuel.

The results presented in CHAPTER 5 confirm this statement. Each of the nitride-based fuels considered had a homologous temperature in PWR conditions that was approximately half that of UO_2 across all burnups considered. Additionally, the ThN-UN

fuels considered were able to match the cycle length of conventional UO_2 when HALEU was used and RTCs for these fuels were relatively similar to those for UO_2. The preliminary screening study in this dissertation highlights the feasibility of composite ThN-UN fuel concepts in LWRs.

5. A Mo insert design for UO_2 fuel pellets can be optimized to improve thermal safety margin of LWRs while having minimal impact on neutronic performance.

An optimization and sensitivity analysis procedure was developed to optimize the neutronic and heat transfer performance of Mo inserts in UO_2. The study showed that the geometry of the insert had a minimal impact on cycle length, although the inclusion of a non-fissile insert in-and-of itself reduces cycle length in a way that will require compensation via HALEU. Geometry of the Mo insert does have an impact on heat transfer capabilities, however, and the difference in maximum fuel temperature between the bounding insert geometries was about 15–20%. Further analyses are needed to determine if the safety and operational benefits from the reduction in fuel temperature outweigh the costs associated with the reduction in cycle length. It was also shown that the Mo insert had a minimal impact on RTCs, preliminarily implying that this is a feasible fuel concept for LWRs.

7.3 Recommended Future Work

Owing to the computational nature of the studies in this dissertation, much of the suggested work for these potential ATF concepts is based on experiments and additional computational analyses. One of the key takeaways from the FeCrAl analysis is that there is no current model for the transition period that occurs when CHF is reached before the heat transfer declines. Investigation of this phenomena and subsequent development of a correlation is necessary to increased accuracy of accident modeling in which CHF is a factor. Additionally, no model exists for predicting the enhancement in CHF caused by a power transient. Without correlations for these phenomena, current modeling tools make overly conservative predictions of when CHF is reached and the resulting PCT, which may be acceptable from a safety standpoint but is uneconomical.

The assessment of VERA presented in this dissertation was performed for a limited set of 2-D BWR fuel lattices and 3-D fuel assembly models at steady state and normal operating conditions. A broader array of progression problems is required for the V&V process and should build up to comparisons of plant operation data, similar to the Watts Bar 20-year operational history that was simulated to validate VERA for PWR applications [138]. In regards to the SiC/SiC channel box study, it would be beneficial to determine the effect of fuel assembly location within the core, control blade history, and burnup on the fluence a particular channel box is subjected to. Inclusion of these effects will give a more realistic set of fast flux boundary conditions to be used in channel box deformation studies. Additionally, fuel loading schemes and other operational maneuvers, such as core shuffling and fuel assembly rotations, could be optimized to limit channel box deformation and control blade interference.

The evaluation of ThN-UN fuels indicate that it is capable of enhancing accident tolerance and is a feasible fuel form for LWRs if HALEU is able to be used. However, the purpose of introducing ThN in the first place is to reduce the chemical reactivity of UN in water. Further experimentation is needed to characterize the degradation of mixed ThN-UN fuels in water and the performance of these fuels under irradiation. It was shown that control rods and soluble boron have reduced reactivity worth for nitride-based fuels relative to UO_2, which suggests that shutdown margin may be an issue with this fuel concept. This concern is exacerbated by the more negative MTC of these fuels compared with UO_2. Further analysis on a full-core scale is recommended to determine if this is the case, and if so, design changes may be required. If shutdown margin is confirmed to be an issue for ThN-UN fuels with typical AIC control rods, it is possible that B_4C control rods with enriched ^{10}B may mitigate the issue.

Similarly to the ThN-UN fuels, UO_2 with optimized Mo inserts is a fuel concept that was shown to improve the margin to fuel melt during normal operation and be feasible for LWRs when HALEU is used. Because the study in CHAPTER 6 focused on neutronics and heat transfer, the primary future work suggested for this concept is the characterization of fuel performance and accompanying irradiation experiments. Additionally, stress analyses should be performed to design an insert geometry that will

not fail during fabrication or reactor operation. Since it has been shown that the insert geometry has a minimal impact on neutronic performance, future studies may focus primarily on developing a geometry that optimizes heat transfer performance while also attempting to maximize fuel performance and minimize mechanical and thermal stress. Cost-benefit analyses should be performed in parallel with future optimization studies to ensure the performance and safety benefits make up for any additional costs incurred from cycle length reduction. The results from the UO_2-Mo study indicate that changes in Mo content and ^{235}U enrichment have a stronger impact on cycle length than the insert geometry. The approach developed for insert geometry optimization could be utilized in these future studies.

Each ATF concept analyzed in this dissertation shows potential for eventual application, but each one also requires additional evaluations and testing before being licensed. Both ThN-UN and UO_2 with Mo inserts are in the early stages of screening, and many more material characterization experiments and testing will be needed for these concepts to progress. SiC/SiC as a channel box material is considered a long-term concept by the NRC, and must also undergo a number of additional tests and computational evaluations. Bowing of the channel box and potential control blade interference is currently the most pressing challenge for the concept, and additional work is needed to determine methods for alleviating this issue. FeCrAl cladding is the concept closest to being deployed, but several years of analysis and testing are still required for this concept as well. At the time of this writing, lead test assemblies containing IronClad, the name given to Global Nuclear Fuel's FeCrAl cladding design, are loaded into Southern Nuclear's Edwin I. Hatch Plant in Georgia and Exelon's Clinton Power Station in Illinois.

REFERENCES

[1] S. J. Zinkle, K. A. Terrani, J. C. Gehin, L. J. Ott and L. L. Snead, "Accident Tolerant Fuels for LWRs: A Perspective," *Journal of Nuclear Materials,* vol. 448, pp. 374-379, 2014.

[2] U.S. Nuclear Regulatory Commission, "Project Plan to Prepare the U.S. Nuclear Regulatory Commission for Efficient and Effective Licensing of Accident Tolerant Fuels," U.S. Nuclear Regulatory Commission, 2018.

[3] S. M. Bragg-Sitton, M. Todosow, R. Montgomery, C. R. Stanek, R. Montgomery and W. J. Carmack, "Metrics for the Technical Performance Evaluation of Light Water Reactor Accident-Tolerant Fuel," *Nuclear Technology,* vol. 195, no. 2, pp. 111-123, 2016.

[4] Y. Yamamoto, B. A. Pint, K. A. Terrani, K. G. Field, Y. Yang and L. L. Snead, "Development and property evaluation of nuclear grade wrought FeCrAl fuel cladding for light water reactors," *Journal of Nuclear Materials,* vol. 467, pp. 703-716, 2015.

[5] K. G. Field, M. A. Snead, Y. Yamamoto and K. A. Terrani, "Handbook on the Material Properties of FeCrAl Alloys for Nuclear Power Production Applications," ORNL/TM-2017/186, 2017.

[6] S. K. Lee, M. Liu, N. R. Brown, K. A. Terrani, E. D. Blandford, H. Ban, C. B. Jensen and Y. Lee, "Comparison of steady and transient flow boiling critical heat flux for FeCrAl accident tolerant fuel cladding alloy, Zircaloy, and Inconel," *International Journal of Heat and Mass Transfer,* vol. 132, pp. 643-654, 2019.

[7] T. Cheng, J. R. Keiser, M. P. Brady, K. A. Terrani and B. A. Pint, "Oxidation of fuel cladding candidate materials in steam environments at high temperature and pressure," *Journal of Nuclear Materials,* vol. 427, pp. 396-400, 2012.

[8] N. H. Larsen, "Core Design and Operating Data for Cycles 1 and 2 of Peach Bottom 2," No. EPRI-NP-563, General Electric Company, 1978.

[9] W. Zhou and W. Zhou, "Enhanced thermal conductivity accident tolerant fuels for improved reactor safety - A comprehensive review," *Annals of Nuclear Energy,* vol. 119, pp. 66-86, 2018.

[10] P. G. Medvedev and R. D. Mariani, "Conductive inserts to reduce nuclear fuel temperature," *Journal of Nuclear Materials,* vol. 531, p. 151966, 2020.

[11] D.-J. Kim, Y. W. Rhee, J. H. Kim, K. S. Kim, J. S. Oh, J. H. Yang, Y.-H. Koo and K.-W. Song, "Fabrication of micro-cell UO2-Mo pellet with enhanced thermal conductivity," *Journal of Nuclear Materials,* vol. 462, pp. 289-295, 2015.

[12] S. C. Finkeldei, J. O. Kiggans, R. D. Hunt, A. T. Nelson and K. A. Terrani, "Fabrication of UO2-Mo composite fuel with enhanced thermal conductivity from sol-gel feedstock," *Journal of Nuclear Materials,* vol. 520, pp. 56-64, 2019.

[13] J. P. Gorton, S. K. Lee, Y. Lee and N. R. Brown, "Comparison of experimental and simulated critical heat flux tests with various cladding alloys: Sensitivity of iron-chromium-aluminum (FeCrAl) to heat transfer coefficients and material properties," *Nuclear Engineering and Design,* vol. 353, p. 110295, 2019.

[14] J. P. Gorton, B. S. Collins, A. J. Wysocki and N. R. Brown, "Assessment of CASL VERA for BWR analysis and application to accident tolerant SiC/SiC channel box," *Nuclear Engineering and Design,* vol. 365, p. 110732, 2020.

[15] J. P. Gorton, B. S. Collins, A. T. Nelson and N. R. Brown, "Reactor performance and safety characteristics of ThN-UN fuel concepts in a PWR," *Nuclear Engineering and Design,* vol. 355, p. 110317, 2019.

[16] J. P. Gorton, D. Schappel, A. T. Nelson and N. R. Brown, "Impact of uranium oxide (UO2) fuel with molybdenum (Mo) inserts on pressurized water reactor performance and safety," *Journal of Nuclear Materials,* vol. 542, p. 152492, 2020.

[17] G. Singh, J. P. Gorton, D. Schappel, B. S. Collins, Y. Katoh, N. R. Brown and B. D. Wirth, "Impact of control blade insertion on the deformation behavior of SiC-SiC channel boxes in BWRs," *Nuclear Engineering and Design,* vol. 363, p. 110621, 2020.

[18] J. Leppänen, "Serpent - a Continuous-energy Monte Carlo Reactor Physics Burnup Calculation Code," VTT Technical Research Centre of Finland, 2013.

[19] R. L. Williamson, J. D. Hales, S. R. Novascone, M. R. Tonks, D. R. Gaston, C. J. Permann, D. Andrs and R. C. Martineau, "Multidimensional multiphysics simulation of nuclear fuel behavior," *Journal of Nuclear Materials,* vol. 423, pp. 149-163, 2012.

[20] H. G. Rickover, L. D. Geiger and B. Lustman, "History of the Development of Zirconium Alloys for Use in Nuclear Reactors," United States Energy Research and Development Administration Division of Naval Reactors, Denver, CO, 1975.

[21] S. J. Zinkle, K. A. Terrani and L. L. Snead, "Motivation for utilizing new high-performance advanced materials in nuclear energy systems," *Current Opinion in Solid State and Materials Science,* vol. 20, pp. 401-410, 2016.

[22] A. Labib and M. J. Harris, "Learning how to learn from failures: The Fukushima nuclear disaster," *Engineering Failure Analysis,* vol. 47, pp. 117-128, 2015.

[23] Y.-H. Koo, Y.-S. Yang and K.-W. Song, "Radioactivity release from the Fukushima accident and its consequences: A review," *Progress in Nuclear Energy,* vol. 74, pp. 61-70, 2014.

[24] Nuclear Regulatory Commission, "Nuclear Reactor Risk," July 2018. [Online]. Available: https://www.nrc.gov/docs/ML0318/ML031830809.pdf.

[25] J. Carmack, F. Goldner, S. M. Bragg-Sitton and L. L. Snead, "Overview of the U.S. DOE Accident Tolerant Fuel Development Program," Idaho National Laboratory, INL/CON-13-29288, 2013.

[26] N. R. Brown, M. Todosow and A. Cuadra, "Screening of advanced cladding materials and UN-U3Si5 fuel," *Journal of Nuclear Materials,* vol. 462, pp. 26-42, 2015.

[27] L. J. Ott, K. R. Robb and D. Wang, "Preliminary assessment of accident-tolerant fuels on LWR performance during normal operation and under DB and BDB accident conditions," *Journal of Nuclear Materials,* vol. 448, pp. 520-533, 2014.

[28] B. A. Pint, K. A. Terrani, Y. Yamamoto and L. L. Snead, "Material Selection for Accident Tolerant Fuel Cladding," *Metallurgical and Materials Transactions E,* vol. 2E, pp. 190-196, 2015.

[29] K. A. Terrani, "Accident tolerant fuel cladding development: Promise, status, and challenges," *Journal of Nuclear Materials,* vol. 501, pp. 13-30, 2018.

[30] K. A. Terrani, S. J. Zinkle and L. L. Snead, "Advanced oxidation-resistant iron-based alloys for LWR fuel cladding," *Journal of Nuclear Materials,* vol. 448, pp. 420-435, 2014.

[31] C. Gillen, A. Garner, A. Plowman, C. P. Race, T. Lowe, C. Jones, K. L. Moore and P. Frankel, "Advanced 3D characterisation of iodine induced stress corrosion cracks in zirconium alloys," *Materials Characterization,* vol. 141, pp. 348-361, 2018.

[32] N. Capps, R. Montgomery, D. Sunderland, M. Pytel and B. D. Wirth, "Evaluation of missing pellet surface geometry on cladding stress distribution and magnitude," *Nuclear Engineering and Design,* vol. 305, pp. 51-63, 2016.

[33] E. Epremian, "Uranium Compounds for New High-Temperature Fuels," in *Fuel Elements Conference: Paris, November 18-23, 1957. Sessions IV, V, VI,* Atomic Energy Commission, 1957, p. 549.

[34] J. K. Fink, "Thermophysical properties of uranium dioxide," *Journal of Nuclear Materials,* vol. 279, pp. 1-18, 2000.

[35] K. A. Terrani, D. Wang, L. J. Ott and R. O. Montgomery, "The effect of fuel thermal conductivity on the behavior of LWR cores during loss-of-coolant accidents," *Journal of Nuclear Materials,* vol. 448, pp. 512-519, 2014.

[36] G. Singh, J. Gorton, D. Schappel, N. R. Brown, Y. Katoh, B. D. Wirth and K. A. Terrani, "Deformation analysis of SiC-SiC channel box for BWR applications," *Journal of Nuclear Materials,* vol. 513, pp. 71-85, 2019.

[37] L. H. Ortega, B. J. Blamer, J. A. Evans and S. M. McDeavitt, "Development of an accident-tolerant fuel composite from uranium mononitride (UN) and uranium sesquisilicide (U3Si2) with increased uranium loading," *Journal of Nuclear Materials,* vol. 471, pp. 116-121, 2016.

[38] K. A. Terrani, T. M. Karlsen and Y. Yamamoto, "Input Correlations for Irradiation Creep of FeCrAl and SiC Based on In-Pile Halden Test Results," Oak Ridge National Laboratory, ORNL/TM-2016/191, 2016.

[39] N. M. George, K. Terrani, J. Powers, A. Worrall and I. Maldonado, "Neutronic analysis of candidate accident-tolerant cladding concepts in pressurized water reactors," *Annals of Nuclear Energy,* vol. 75, pp. 703-712, 2015.

[40] X. Wu, T. Kozlowski and J. D. Hales, "Neutronics and fuel performance evaluations of accident tolerant FeCrAl cladding under normal operation conditions," *Annals of Nuclear Energy,* vol. 85, pp. 763-775, 2015.

[41] B. A. Pint, K. A. Terrani, M. P. Brady, T. Cheng and J. R. Keiser, "High temperature oxidation of fuel cladding candidate materials in steam-hydrogen environments," *Journal of Nuclear Materials,* vol. 440, pp. 420-427, 2013.

[42] K. A. Unocic, Y. Yamamoto and B. A. Pint, "Effect of Al and Cr Content on Air and Steam Oxidation of FeCrAl Alloys and Commercial APMT Alloy," *Oxidation of Metals,* vol. 87, no. 3-4, pp. 431-441, 2017.

[43] K. G. Field, S. A. Briggs, K. Sridharan, R. H. Howard and Y. Yamamoto, "Mechanical properties of neutron-irradiated model and commercial FeCrAl alloys," *Journal of Nuclear Materials,* vol. 489, pp. 118-128, 2017.

[44] R. B. Rebak, "Iron-chrome-aluminum alloy cladding for increasing safety in nuclear power plants," *EPJ Nuclear Science Technology,* vol. 3, no. 34, 2017.

[45] C. P. Massey, K. A. Terrani, S. N. Dryepondt and B. A. Pint, "Cladding burst behavior of Fe-based alloys under LOCA," *Journal of Nuclear Materials,* vol. 470, pp. 128-138, 2016.

[46] N. R. Brown, A. J. Wysocki, K. A. Terrani, K. G. Xu and D. M. Wachs, "The potential impact of accident tolerant cladding materials on reactivity initiated accidents in light water reactors," *Annals of Nuclear Energy,* vol. 99, pp. 353-365, 2017.

[47] A. F. Ali, J. P. Gorton, N. R. Brown, K. A. Terrani, C. B. Jensen, Y. Lee and E. D. Blandford, "Surface wettability and pool boiling Critical Heat Flux of Accident Tolerant Fuel cladding-FeCrAl alloys," *Nuclear Engineering and Design,* vol. 338, pp. 218-231, 2018.

[48] K. Yueh and K. A. Terrani, "Silicon carbide composite for light water reactor fuel assembly applications," *Journal of Nuclear Materials,* vol. 448, pp. 380-388, 2014.

[49] Y. Katoh, K. Ozawa, C. Shih, T. Nozawa, R. J. Shinavski, A. Hasegawa and L. L. Snead, "Continuous SiC fiber, CVI SiC matrix composites for nuclear applications: Properties and irradiation effects," *Journal of Nuclear Materials,* vol. 448, pp. 448-476, 2014.

[50] G. Singh, R. Sweet, N. R. Brown, B. D. Wirth, Y. Katoh and K. Terrani, "Parametric Evaluation of SiC/SiC Composite Cladding with UO2 Fuel for LWR Applications: Fuel Rod Interactions and Impact of Nonuniform Power Profile in Fuel Rod," *Journal of Nuclear Materials,* vol. 499, pp. 155-167, 2018.

[51] C. H. Henager, Jr., Y. Shin, Y. Blum, L. A. Giannuzzi, B. W. Kempshall and S. M. Schwarz, "Coatings and joining for SiC and SiC-composites for nuclear energy systems," *Journal of Nuclear Materials,* Vols. 367-370, pp. 1139-1143, 2007.

[52] S. J. Zinkle and G. S. Was, "Materials challenges in nuclear energy," *Acta Materialia,* vol. 61, pp. 735-758, 2013.

[53] P. Grimm, F. Jatuff, M. Murphy, R. Seiler, T. Williams, R. Jacot-Guillarmod and R. Chawla, "Experimental Validation of Channel Bowing Effects on Pin Power Distributions in a Westinghouse SVEA-96+ Assembly," *Nuclear Science and Technology,* vol. 43, no. 3, pp. 223-230, 2006.

[54] D. G. Franklin and R. B. Adamson, "Implications of Zircaloy Creep and Growth to Light Water Reactor Performance," *Journal of Nuclear Materials,* vol. 159, pp. 12-21, 1988.

[55] F. Garzarolli, R. Adamson, P. Rudling and A. Strasser, "BWR Fuel Channel Distortion," Advanced Nuclear Technology International, Mölnlycke, Sweden, 2011.

[56] P. Cantonwine, D. Crawford, M. Downs, B. Joe, T. Bahensky, J. Reimer, C. del la Hoz, K. Petersen, M. Reitmeyer, J. Morris and A. Zbib, "Channel Control-Blade Interference Management at LaSalle 1 and 2 during 2007 and 2008," in *Topical Meeting on Advances in Nuclear Fuel Management III*, Hilton Head Island, South Carolina, 2003.

[57] P. Rodriguez and C. V. Sundaram, "Nuclear and materials aspects of the thorium fuel cycle," *Journal of Nuclear Materials,* vol. 100, pp. 227-249, 1981.

[58] International Atomic Energy Agency, "Thorium fuel cycle - Potential benefits and challenges," IAEA-TECDOC-1450, 2005.

[59] M. Lung and O. Gremm, "Perspectives of the thorium fuel cycle," *Nuclear Engineering and Design,* vol. 180, pp. 133-146, 1998.

[60] M. Todosow, A. Galperin, S. Herring, M. Kazimi, T. Downar and A. Morozov, "Use of Thorium in Light Water Reactors," *Nuclear Technology,* vol. 151, no. 2, pp. 168-176, 2005.

[61] C. S. Pillai and P. Raj, "Thermal conductivity of ThO2 and Th0.98U0.02O2," *Journal of Nuclear Materials,* vol. 277, pp. 116-119, 200.

[62] K. Bakker, E. Cordfunke, R. Konings and R. Schram, "Critical evaluation of the thermal properties of ThO2 and Th1-yUyO2 and a survey of the literature data on Th1-yPuyO2," *Journal of Nuclear Materials,* vol. 250, pp. 1-12, 1997.

[63] S. S. Parker, J. T. White, P. Hosemann and A. T. Nelson, "Thermophysical properties of thorium mononitride from 298-1700 K," *Accepted to Journal of Nuclear Materials,* 2019.

[64] J. H. Yang, K. W. Kang, K. W. Song, C. B. Lee and Y. H. Jung, "Fabrication and Thermal Conductivity of (Th,U)O2 Pellets," *Nuclear Technology,* vol. 147, no. 1, pp. 113-119, 2004.

[65] T. R. G. Kutty, K. B. Khan, P. S. Somayajulu, A. K. Sengupta, J. P. Panakkal, A. Kumar and H. S. Kamath, "Development of CAP process for fabrication of ThO2-UO2 fuels Part I: Fabrication and densification behaviour," *Journal of Nuclear Materials,* vol. 373, pp. 299-308, 2008.

[66] S. L. Hayes, J. K. Thomas and K. L. Peddicord, "Material property correlations for uranium mononitride: III. Transport properties," *Journal of Nuclear Materials,* vol. 171, no. 2-3, pp. 289-299, 1990.

[67] M. Uno, T. Nishi and M. Takano, "Thermodynamic and Thermophysical Properties of the Actinide Nitrides," *Comprehensive Nuclear Materials,* pp. 61-85, 2012.

[68] R. Benz, C. G. Hoffman and G. N. Rupert, "Some Phase Equilibria in the Thorium-Nitrogen System," *Journal of the American Chemical Society,* vol. 89, no. 2, pp. 191-197, 1967.

[69] D. Manara, C. Ronchi, M. Sheindlin, M. Lewis and M. Brykin, "Melting of stoichiometric and hyperstoichiometric uranium dioxide," *Journal of Nuclear Materials,* vol. 342, pp. 148-163, 2005.

[70] L. van Brutzel, R. Dingreville and T. J. Bartel, "Nuclear fuel and deformation phenomena," NEA/NSC/R(2015)5, 2015.

[71] H. Nickel, H. Nabielek, G. Pott and A. W. Mehner, "Long time experience with the development of HTR fuel elements in Germany," *Nuclear Engineering and Design,* vol. 217, pp. 141-151, 2002.

[72] L. Mathieu, D. Heuer, R. Brissot, C. Garzenne, C. Le Brun, D. Lecarpentier, E. Liatard, J.-M. Loiseaux, O. Méplan, E. Merle-Lucotte, A. Nuttin, E. Walle and J. Wilson, "The thorium molten salt reactor: Moving on from the MSBR," *Progress in Nuclear Energy,* vol. 48, pp. 664-679, 2006.

[73] D. Heuer, E. Merle-Lucotte, M. Allibert, M. Brovchenko, V. Ghetta and P. Rubiolo, "Towards the thorium fuel cycle with molten salt fast reactors," *Annals of Nuclear Energy,* vol. 64, pp. 421-429, 2014.

[74] L. B. Freeman, B. R. Beaudoin, R. A. Frederickson, G. L. Hartfield, H. C. Hecker, S. Milani, W. K. Sarber and W. C. Schick, "Physics experiments and lifetime performance of the light water breeder reactor," *Nuclear Science and Engineering,* vol. 102, no. 4, pp. 341-364, 1989.

[75] A. Radkowsky and A. Galperin, "The nonproliferative light water thorium reactor: A new approach to light water core technology," *Nuclear Technology,* vol. 124, no. 3, pp. 215-222, 1998.

[76] K. Balakrishnan, S. Majumdar, A. Ramanujam and A. Kakodkar, "The Indian perspective on thorium fuel cycles," *Thorium fuel utilization: Options and trends,* p. 257, 2002.

[77] R. K. Sinha and A. Kakodkar, "Design and development of the AHWR - the Indian thorium fuelled innovative nuclear reactor," *Nuclear Engineering and Design,* vol. 236, pp. 683-700, 2006.

[78] S. Şahin, H. M. Şahin, M. Alkan and K. Yildiz, "An assessment of thorium and spent LWR-fuel utilization potential in CANDU reactors," *Energy Conversion and Management,* vol. 45, pp. 1067-1085, 2004.

[79] B. P. Bromley, "High-utilization lattices for thorium-based fuels in heavy water reactors," *Nuclear Technology,* vol. 186, no. 1, pp. 17-32, 2014.

[80] S. Permana, N. Takaki and H. Sekimoto, "Breeding Capability and Void Reactivity Analysis of Heavy-Water-Cooled Thorium Reactor," *Journal of Nuclear Science and Technology,* vol. 45, no. 7, pp. 589-600, 2008.

[81] N. R. Brown, J. J. Powers, B. Feng, F. Heidet, N. E. Stauff, G. Zhang, M. Todosow, A. Worrall, J. C. Gehin, T. K. Kim and T. A. Taiwo, "Sustainable

thorium nuclear fuel cycles: A comparison of intermediate and fast neutron spectrum systems," *Nuclear Engineering and Design,* vol. 289, pp. 252-265, 2015.

[82] N. S. Rasor and J. D. McClelland, "Thermal properties of graphite, molybdenum and tantalum to their destruction temperatures," *Journal of Physics and Chemistry of Solids,* vol. 15, pp. 17-26, 1960.

[83] J. Buckley, J. D. Turner and T. J. Abram, "Uranium dioxide - Molybdenum composite fuel pellets with enhanced thermal conductivity manufactured via spark plasma sintering," *Journal of Nuclear Materials,* vol. 523, pp. 360-368, 2019.

[84] B. V. Cockeram, R. W. Smith, N. Hashimoto and L. L. Snead, "The swelling, microstructure, and hardening of wrought LCAC, TZM, and ODS molybdenum following neutron irradiation," *Journal of Nuclear Materials,* vol. 418, pp. 121-136, 2011.

[85] J. R. Lamarsh and A. J. Baratta, Introduction to Nuclear Engineering, Third Edition, Upper Saddle River, New Jersey: Prentice-Hall, Inc., 2001.

[86] J. J. Duderstadt and L. J. Hamilton, Nuclear Reactor Analysis, Ann Arbor, Michigan: John Wiley & Sons, Inc., 1976.

[87] J. Desquines, D. A. Koss, A. T. Motta, B. Cazalis and M. Petit, "The issue of stress state during mechanical tests to asses cladding performance during a reactivity-initiated accident (RIA)," *Journal of Nuclear Materials,* vol. 412, pp. 250-267, 2011.

[88] Japan Atomic Energy Agency, "Fuel Safety Research Group: Research on Fuel Behavior during RIA," [Online]. Available: https://www.jaea.go.jp/04/anzen/en/group/fsrg/index2.html. [Accessed 1 September 2020].

[89] M. Liu, N. R. Brown, K. A. Terrani, A. F. Ali, E. D. Blandford and D. M. Wachs, "Potential impact of accident tolerant fuel cladding critical heat flux characteristics on the high temperature phase of reactivity initiated accidents," *Annals of Nuclear Energy,* vol. 110, pp. 48-62, 2017.

[90] N. E. Todreas and M. S. Kazimi, Nuclear Systems, Vol. 1: Thermal Hydraulic Fundamentals, Boca Raton, FL: CRC Press, 2nd Edition, 2012.

[91] D. C. Groeneveld, J. Q. Shan, A. Z. Vasic, L. K. H. Leung, A. Durmayaz, J. Yang, S. C. Cheng and A. Tanase, "The 2006 CHF look-up table," *Nuclear Engineering and Design,* vol. 237, pp. 1909-1922, 2007.

[92] R. Hohl, M. Buchholz, T. Lüttich, H. Auracher and W. Marquardt, "Model-based experimental analysis of pool boiling heat transfer with controlled wall temperature transients," *International Journal of Heat and Mass Transfer,* vol. 44, pp. 2225-2238, 2001.

[93] H. Auracher and W. Marquardt, "Heat transfer characteristics and mechanisms along entire boiling curves under steady-state and transient conditions," *International Journal of Heat and Fluid Flow,* vol. 24, pp. 223-242, 2004.

[94] L. C. Witte and J. H. Lienhard, "On the existence of two 'transition' boiling curves," *International Journal of Heat and Mass Transfer*, vol. 25, no. 6, pp. 771-779, 1982.

[95] V. Bessiron, "Modelling of Clad-to-Coolant Heat Transfer for RIA Applications," *Journal of Nuclear Science and Technology*, vol. 44, no. 2, pp. 211-221, 2007.

[96] OECD NEA, "Nuclear Fuel Behavior Under Reactivity-initiated Accident (RIA) Conditions, State-of-the-art Report," ISBN 978-92-64-99113-2, NEA/CSNI/R(2010)1, Paris, France, 2010.

[97] F. Lemoine and M. Balourdet, "RIA related analytical studies and separate effects tests," in *International Topical Meeting on Light Water Reactor Fuel Performance*, Portland, OR, 1997.

[98] M. Le Saux, J. Besson, S. Carassou, C. Poussard and X. Averty, "A model to describe the anisotropic viscoplastic mechanical behavior of fresh and irradiated Zircaloy-4 fuel claddings under RIA loading conditions," *Journal of Nuclear Materials*, vol. 378, pp. 60-69, 2008.

[99] W. R. Martin, "Challenges and prospects for whole-core Monte Carlo analysis," *Nuclear Engineering and Technology*, vol. 44, pp. 151-160, 2012.

[100] B. Collins, S. Stimpson, B. W. Kelley, M. T. H. Young, B. Kochunas, A. Graham, E. W. Larsen, T. Downar and A. Godfrey, "Stability and accuracy of 3D neutron transport simulations using the 2D/1D method in MPACT," *Journal of Computational Physics*, vol. 326, pp. 612-628, 2016.

[101] B. T. Rearden, M. A. Jessee and Eds., "SCALE Code System," ORNL/TM-2005/39, Version 6.2, Oak Ridge National Laboratory, Oak Ridge, Tennessee, 2016.

[102] T. J. Downar, D. A. Barber, R. M. Miller, C. H. Lee, T. Kozlowski, D. Lee, Y. Xu, J. Gan, H. G. Joo, J. Y. Cho and K. Lee, "PARCS: Purdue advanced reactor core simulator," 2002.

[103] B. J. Ade, "SCALE/TRITON Primer: A Primer for Light Water Reactor Lattice Physics Calculations," NUREG/CR-7041, U.S. Nuclear Regulatory Commission, 2012.

[104] M. Bernard, C. Gingrich, C. L. Hoxie, A. Ireland, J. Kelly, J. Mahaffy, J. Murray, C. Murray, J. Spore, J. Staudenmeier, M. Thurgood, K. Tien and J. Whitman, "Development, Validation and Assessment of the TRACE Thermal-Hydraulics Systems Code," in *16th International Meeting on Nuclear Reactor Thermal Hydraulics (NURETH-16)*, Chicago, Illinois, 2015.

[105] B. Collins, L. Li, D. Wang, S. Stimpson, D. Jabaay, A. Ward, Y. Xu and T. Downar, "PATHS: A Steady State Two-Phase Thermal-Hydraulics Solver for PARCS Depletion," Toronto, Ontario, 2011.

[106] A. Wysocki, A. Ward, A. Manera, T. Downar, Y. Xu, J. March-Leuba, C. Thurston, N. Hudson and A. Ireland, "The modeling of advanced BWR fuel designs with the NRC fuel depletion codes PARCS/PATHS," *Nuclear Technology*, vol. 190, no. 3, pp. 323-335, 2015.

[107] P. Yarsky, Y. Xu, A. Ward, N. Hudson and T. Downar, "BWR Control Rod Drift Analysis Capability in the U.S. NRC Core Simulator PATHS/PARCS," *Nuclear Technology,* vol. 197, no. 3, pp. 265-283, 2017.

[108] K. Ivanov and M. Avramova, "Challenges in coupled thermal-hydraulics and neutronics simulations for LWR safety analysis," *Annals of Nuclear Energy,* vol. 34, pp. 501-513, 2007.

[109] A. G. Mylonakis, M. Varvayanni, N. Catsaros, P. Savva and D. G. Grigoriadis, "Multi-physics and multi-scale methods used in reactor analysis," *Annals of Nuclear Energy,* vol. 72, pp. 104-119, 2014.

[110] D. Gaston, C. Newman, G. Hansen and D. Lebrun-Grandié, "MOOSE: A parallel computational framework for coupled systems of nonlinear equations," *Nuclear Engineering and Design,* vol. 239, pp. 1768-1778, 2009.

[111] B. T. Rearden and R. A. Lefebvre, "Objectives of the NEAMS Workbench," Oak Ridge National Laboratory, Oak Ridge, Tennessee, 2018.

[112] M. R. Tonks, D. Gaston, P. C. Millet, D. Andrs and P. Talbot, "An object-oriented finite element framework for multiphysics phase field simulations," *Computational Materials Science,* vol. 51, pp. 20-29, 2012.

[113] D. R. Gaston, C. J. Permann, J. W. Peterson, A. E. Slaughter, D. Andrs, Y. Wang, M. P. Short, D. M. Perez, M. R. Tonks, J. Ortensi, L. Zou and R. C. Martineau, "Physics-based multiscale coupling for full core nuclear reactor simulation," *Annals of Nuclear Energy,* vol. 84, pp. 45-54, 2015.

[114] Y. Wang, S. Schunert, M. DeHart, R. Martineau and W. Zheng, "Hybrid PN - SN with Lagrange multiplier and upwinding for the multiscale transport capability in Rattlesnake," *Progress in Nuclear Energy,* vol. 101, pp. 381-393, 2017.

[115] R. A. Berry, L. Zou, H. Zhao, H. Zhang, J. W. Peterson, R. C. Martineau, S. Y. Kadioglu, D. Andrs and J. E. Hansel, "RELAP-7 Theory Manual, Revision 3," INL/EXT-14-31366, Idaho National Laboratory , 2018.

[116] F. Gleicher, J. Ortensi, M. DeHart, Y. Wang, S. Schunert, S. Novascone, J. Hales, R. Williamson, A. Slaughter, C. Permann, D. Andrs and R. Martineau, "The Application of MAMMOTH for a Detailed Tightly Coupled Fuel Pin Simulation with a Station Blackout," in *Top Fuel 2016*, Boise, Idaho, 2016.

[117] R. Schmidt, K. Belcourt, R. Hooper, R. Pawlowski, K. Clarno, S. Simunovic, S. Slattery, J. Turner and S. Palmtag, "An approach for coupled-code multiphysics core simulations from a common input," *Annals of Nuclear Energy,* vol. 84, pp. 140-152, 2015.

[118] J. A. Turner, K. Clarno, M. Sieger, R. Bartlett, B. Collins, R. Pawlowski, R. Schmidt and R. Summers, "The Virtual Environment for Reactor Applications (VERA): Design and architecture," *Journal of Computational Physics,* vol. 326, pp. 544-568, 2016.

[119] B. W. Kelley and E. W. Larsen, "A consistent 2D/1D approximation to the 3D neutron transport equation," *Nuclear Engineering and Design,* vol. 295, pp. 598-614, 2015.

[120] K. S. Kim, M. L. Williams, D. Wiarda and K. T. Clarno, "Development of the multigroup cross section library for the CASL neutronics simulator MPACT: Method and procedure," *Annals of Nuclear Energy*, vol. 133, pp. 46-58, 2019.

[121] R. K. Salko and M. N. Avramova, "CTF Theory Manual," Consortium for Advanced Simulation of LWRs, CASL-U-2016-1110-000, 2016.

[122] B. Kendrick, V. Petrov, D. Walter, A. Manera, B. Collins, T. Downar, J. Secker and K. Belcourt, "CALS multiphysics modeling of crud deposition in PWRs," in *Proceedings of the 2013 LWR Fuel Performance Meeting/Top Fuel*, Charlotte, North Carolina, 2013.

[123] A. Godfrey, B. Collins, K. S. Kim, J. Powers, R. Salko, S. Stimpson, W. Wieselquist, R. Montgomery, B. Kochunas, D. Jabaay, N. Capps and J. Secker, "VERA Benchmarking Results for Watts Bar Nuclear Plant Unit 1 Cycles 1-12," Oak Ridge National Laboratory, CASL-U-2015-0206-000, 2015.

[124] B. Collins and A. Godfrey, "Analysis of the BEAVRS Benchmark Using VERA-CS," Nashville, Tennessee, 2015.

[125] J. P. Gorton, B. S. Collins and N. R. Brown, "A Demonstration of BWR Coupled Analysis and Potential ATF Applications Using CASL's MPACT/CTF," Minneapolis, MN, 2019a.

[126] Idaho National Laboratory, "RELAP5-3D Code Manuals, Volumes I, II, III, IV, V, and Appendix A, Revision 4.3," Idaho National Laboratory, Idaho Falls, ID, INEEL-EXT 98-00834, 2015.

[127] D. Maljovec, B. Wang, P. Rosen, A. Alfonsi, G. Pastore, C. Rabiti and V. Pascucci, "Rethinking Sensitivity Analysis of Nuclear Simulations with Topology," in *IEEE Pacific Visualization Symposium*, Taipei, Taiwan, 2016.

[128] H. S. Abdel-Khalik, Y. Bang and C. Wang, "Overview of hybrid subspace methods for uncertainty quantification, sensitivity analysis," *Annals of Nuclear Energy*, vol. 52, pp. 28-46, 2013.

[129] Z. Chen, J. Cai, R. Liu and Y. Wang, "Preliminary thermal hydraulic analysis of various accident tolerant fuels and claddings for control rod ejection accidents in LWRs," *Nuclear Engineering and Design*, vol. 331, pp. 282-294, 2018.

[130] C. Rabiti, A. Alfonsi, J. Cogliati, D. Mandelli, R. Kinoshita, S. Sen and C. Wang, "RAVEN User Manual," Idaho National Laboratory, Idaho Falls, ID, 2016.

[131] J. W. McMurray, R. Hu, S. V. Ushakov, D. Shin, B. A. Pint, K. A. Terrani and A. Navrotsky, "Solid-liquid phase equilibria of Fe-Cr-Al alloys and spinels," *Journal of Nuclear Materials*, vol. 492, pp. 128-133, 2017.

[132] Nuclear Energy Agency, "RIA Fuel Codes Benchmark Volume 1," NEA/CSNI/R(2013)7, 2013.

[133] J. C. Chen, R. K. Sundaram and F. T. Ozkaynak, "A Phenomenological Correlation for Post-CHF Heat Transfer," Lehigh University Department of Mechanical Engineering and Mechanics, Bethlehem, PA, NUREG-0237, 1977.

[134] G. Pastore, L. P. Swiler, J. D. Hales, S. R. Novascone, D. M. Perez, B. W. Spencer, L. Luzzi, P. Van Uffelen and R. L. Williamson, "Uncertainty and sensitivity analysis of fission gas behavior in engineering-scale fuel modeling," *Journal of Nuclear Materials,* vol. 456, pp. 398-408, 2015.

[135] Kanthal, "Material Datasheets," Sandvik Group, [Online]. Available: https://www.kanthal.com/en/products/material-datasheets/?query=fecral&sort=&page=1. [Accessed 25 October 2018].

[136] P. J. Turinsky and D. B. Kothe, "Modeling and simulation challenges pursued by the Consortium for Advanced Simulation of Light Water Reactors (CASL)," *Journal of Computational Physics,* vol. 313, pp. 367-376, 2016.

[137] M. N. Avramova and K. N. Ivanov, "Verification, validation and uncertainty quantification in multi-physics modeling for nuclear reactor design and safety analysis," *Progress in Nuclear Energy,* vol. 52, pp. 601-614, 2010.

[138] A. Godfrey, B. Collins, K. S. Kim, J. Powers, R. Salko, S. Stimpson, W. Wieselquist, K. Clarno and J. Gehin, "VERA benchmarking results for Watts Bar Nuclear Plant Unit 1 Cycles 1-12," Sun Valley, ID, 2016.

[139] B. Kochunas, D. Jabaay, A. Fitzgerald, T. J. Downar and S. Palmtag, "Initial BWR Modeling Capacility for MPACT," in *M&C 2017*, Jeju, Korea, 2017.

[140] S. M. Bowman, "SCALE 6: Comprehensive Nuclear Safety Analysis Code System," *Nuclear Technology,* vol. 174, no. 2, pp. 126-148, 2011.

[141] N. W. Porter and M. N. Avramova, "Validation of CTF pressure drop and void predictions for the NUPEC BWR database," *Nuclear Engineering and Design,* vol. 337, pp. 291-299, 2018.

[142] M. Avramova, K. Ivanov, B. Krzykacz-Hausmann, K. Velkov, A. Pautz and Y. Perin, "Uncertainty analysis of COBRA-TF void distribution predictions for the OECD/NRC BFBT Benchmark," Saratoga Springs, NY, 2009.

[143] J. P. Gorton, B. S. Collins and N. R. Brown, "Effect of crossflow modeling on vapor void fraction and criticality in a BWR fuel assembly using MPACT/CTF," Seattle, WA, 2019b.

[144] A. L. Costa, C. Pereira, W. Ambrosini and F. D'Auria, "Simulation of an hypothetical out-of-phase instability case in boiling water reactor by RELAP5/PARCS coupled codes," *Annals of Nuclear Energy,* vol. 35, pp. 947-957, 2008.

[145] Y. Xu, T. Downar, R. Walls, K. Ivanov, J. Staudenmeier and J. March-Lueba, "Application of TRACE/PARCS to BWR stability analysis," *Annals of Nuclear Energy,* vol. 36, pp. 317-323, 2009.

[146] Studsvik Scandpower, "SIMULATE-3 Advanced Three-Dimensional Two-Group Reactor Analysis Code," SSP-95/15 Rev. 3, 2005.

[147] E. Fridman and J. Leppänen, "On the use of the Serpent Monte Carlo code for few-group cross section generation," *Annals of Nuclear Energy,* vol. 38, pp. 1399-1405, 2011.

[148] M. Hursin, L. Rossinelli, H. Ferroukhi and A. Pautz, "BWR full core analysis with Seprent/SIMULATE-3 hybrid stochastic/deterministic code sequence," Nashville, TN, 2015.

[149] A. Bennett and N. Martin, "Validation of APOLLO2-A Against Serpent 2 on BWR Lattices," Portland, OR, 2019.

[150] S. W. Churchill, "Friction-factor equation spans all fluid-flow regimes," *Chemical Engineering,* vol. 84, no. 24, pp. 91-92, 1977.

[151] G. Lellouche and B. Zolotar, "Mechanistic Model for Predicting the Two-Phase Void Fraction in Vertical Tubes, Channels, and Rod Bundles," EPRI NP-2246-SR, Electric Power Research Institute, 1982.

[152] J. C. Chen, "Correlation for boiling heat transfer to saturated fluids in convective flow," *Industrial & Engineering Chemistry Process Design and Development,* vol. 5, no. 3, pp. 322-329, 1966.

[153] P. Ferroni, "Steady State Thermal Hydraulic Analysis of Hydride Fueled BWRs," Master's Thesis, Massachusetts Institute of Technology, Cambridge, MA, 2006.

[154] I. C. Gauld, "Scale-4 Analysis of LaSalle Unit 1 BWR Commercial Reactor Critical Configurations," ORNL/TM-1999/247, Oak Ridge National Laboratory, 2000.

[155] M. L. Fensin, "Optimum Boiling Water Reactor Fuel Design Strategies to Enhance Reactor Shutdown by the Standby Liquid Control System," Master's Thesis, University of Florida, 2004.

[156] M. B. Chadwick, M. Herman, P. Oblozinsky, M. E. Dunn, Y. Danon, A. C. Kahler, D. L. Smith, B. Pritychenko, G. Arbanas, R. Arcilla, R. Brewer, D. A. Brown, R. Capote, A. D. Carlson, Y. S. Cho, H. Derrien, K. Guber, G. M. Hale and S. Hoblit, "ENDF/B-VII.1 Nuclear Data for Science and Technology: Cross Sections, covariances, Fission Product Yields and Decay Data," *Nuclear Data Sheets,* vol. 112, pp. 2887-2996, 2011.

[157] M. B. Chadwick, P. Oblozinsky, M. Herman, N. M. Greene, R. D. McKnight, D. L. Smith, P. G. Young, R. E. MacFarlane, G. M. Hale, S. C. Frankle, A. C. Kahler, T. Kawano, R. C. Little, D. G. Madland, P. Moller, R. D. Mosteller, P. R. Page and T, "ENDF/B-VII.0: Next Generation Evaluated Nuclear Data Library for Nuclear Science and Technology," *Nuclear Data Sheets,* vol. 107, pp. 2931-3060, 2006.

[158] D. Wang, B. J. Ade and A. Ward, "Cross Section Generation Guidelines for TRACE-PARCS," No. ORNL/TM-2012/518, Oak Ridge National Laboratory, 2013.

[159] K. Tada, A. Yamamoto, Y. Yamane and Y. Kitamuray, "Applicability of the Diffusion and Simplified P3 Theories for Pin-by-Pin Geometry of BWR," *Journal of Nuclear Science and Technology,* vol. 45, no. 10, pp. 997-1008, 2008.

[160] T. Fujita, T. Endo and A. Yamamoto, "Application of correction technique using leakage index combined with SPH or discontinuity factors for energy collapsing

on pin-by-pin BWR core analysis," *Journal of Nuclear Science and Technology,* vol. 52, no. 3, pp. 355-370, 2015.

[161] X. Zhao, A. J. Wysocki, K. Shirvan and R. K. Salko, "Assessment of the Subchannel code CTF for Single- and Two-Phase Flows," *Nuclear Technology,* vol. 205, no. 1-2, pp. 338-351, 2019.

[162] A. T. Nelson, A. Migdisov, E. S. Wood and C. J. Grote, "U3Si2 behavior in H2O environments: Part II, pressurized water with controlled redox chemistry," *Journal of Nuclear Materials,* vol. 500, pp. 81-91, 2018.

[163] N. R. Brown, A. Aronson, M. Todosow, R. Brito and K. J. McClellan, "Neutronics performance of uranium nitride composite fuels in a PWR," *Nuclear Engineering and Design ,* vol. 275, pp. 393-407, 2014.

[164] B. J. Jaques, J. Watkins, J. R. Croteau, G. A. Alanko, B. Tyburska-Püschel, M. Meyer, P. Xu, E. J. Lahoda and D. P. Butt, "Synthesis and sintering of UN-UO2 fuel composites," *Journal of Nuclear Materials,* vol. 466, pp. 745-754, 2015.

[165] J. H. Yang, D.-J. Kim, K. S. Kim and Y.-H. Koo, "UO2-UN composites with enhanced uranium density and thermal conductivity," *Journal of Nuclear Materials,* vol. 465, pp. 509-515, 2015.

[166] J. T. White, A. W. Travis, J. T. Dunwoody and A. T. Nelson, "Fabrication and thermophysical property characterization of UN/U3Si2 composite fuel forms," *Journal of Nuclear Materials,* vol. 495, pp. 463-474, 2017.

[167] E. S. Wood, J. T. White, C. J. Grote and A. T. Nelson, "U3Si2 behavior in H2O: Part I, flowing steam and the effect of hydrogen," *Journal of Nuclear Materials,* vol. 501, pp. 404-412, 2018.

[168] Westinghouse Electric Company, "AP1000 Design Control Document Rev. 19," 2011.

[169] M. J. Driscoll, T. J. Downar and E. E. Pilat, The Linear Reactivity Model for Nuclear Fuel Management, La Grange Park, Illinois: American Nuclear Society, 1990.

[170] Z. Xu, M. J. Driscoll and M. S. Kazimi, "Neutron Spectrum Effects on Burnup, Reactivity, and Isotopics in UO2/H2O Lattices," *Nuclear Science and Engineering,* vol. 141, pp. 175-189, 2002.

[171] J. Zakova and J. Wallenius, "Fuel residence time in BWRs with nitride fuels," *Annals of Nuclear Energy,* vol. 47, pp. 182-191, 2012.

[172] E. Fridman and S. Kliem, "Pu recycling in a full Th-MOX PWR core. Part I: Steady state analysis," *Nuclear Engineering and Design,* vol. 241, pp. 193-202, 2011.

[173] R. Mariani, A. Nelson, R. Blomquist, D. Keiser, G. Hofman, G. Youinou and G. Griffith, "Initial Evaluation of Fuel-Reactor Concepts for Advanced LEU Fuel Development," Idaho National Laboratory, INL/EXT-20-54641, 2020.

[174] J. R. Burns, R. Hernandez, K. A. Terrani, A. T. Nelson and N. R. Brown, "Reactor and fuel performance of light water reactor fuel with 235U enrichments above 5%," *Annals of Nuclear Energy,* vol. 142, p. 107423, 2020.

[175] K. A. Terrani and A. T. Nelson, "3D Printing of Additive Structures for Nuclear Fuels". United States of America Patent 138974.186629-US, 2019.

[176] Q. Liu and T. Homma, "A new importance measure for sensitivity analysis," *Journal of Nuclear Science and Technology,* vol. 47, no. 1, pp. 53-61, 2010.

[177] M. D. Mckay, R. J. Beckman and W. J. Conover, "A comparison of three methods for selecting values of input variables in the analysis of output from a computer code," *Technometrics,* vol. 21, no. 2, pp. 239-245, 1979.

[178] I. M. Sobol, "Sensitivity estimates for nonlinear mathematical models," *Mathematical Modeling and Computational Experiments,* vol. 1, no. 4, pp. 407-414, 1993.

[179] C. Gaëlle, F. Gamboa and C. Prieur, "Generalized Hoeffding-Sobol decomposition for dependent variables - application to sensitivity analysis," *Electronic Journal of Statistics,* vol. 6, pp. 2420-2448, 2012.

[180] A. Saltelli and S. Tarantola, "On the relative importance of input factors in mathematical models: Safety assessment for nuclear waste disposal," *Journal of the American Statistical Association,* vol. 97, no. 459, pp. 702-709, 2002.

[181] F. Sarrazin, F. Pianosi and T. Wagener, "Global Sensitivity Analysis of environmental models: Convergence and validation," *Environmental Modelling & Software,* vol. 79, pp. 135-152, 2016.

[182] R. J. Larsen and M. L. Marx, An Introduction to Mathematical Statistics and its Applications, 6th ed., Upper Saddle River, New Jersey: Prentice-Hall, 2017.

[183] J. J. Carbajo, G. L. Yoder, S. G. Popov and V. K. Ivanov, "A review of the thermophysical properties of MOX and UO2 fuels," *Journal of Nuclear Materials,* vol. 299, pp. 181-198, 2001.

[184] P. Hejzlar and M. S. Kazimi, "Annular fuel for high-power-density pressurized water reactors: Motivation and overview," *Nuclear Technology,* vol. 160, no. 1, pp. 2-15, 2007.

[185] A. T. Nelson, "Features that further the Performance Limits of Nuclear Fuel Fabrication: Opportunities for Additive Manufacturing of Nuclear Fuels," Oak Ridge National Laboratory, ORNL/SPR-2019/1183, 2019.

VITA

Jacob P. Gorton was born in Warren, Pennsylvania in 1995. He graduated Summa Cum Laude from Gannon University in Erie, PA in 2017, where he received his Bachelor of Science degree in Mechanical Engineering. He then went on to earn his Master of Science degree in Nuclear Engineering from the Pennsylvania State University in December of 2018. While earning his master's degree, Jacob was inducted into and elected president of the local Alpha Nu Sigma Nuclear Engineering Honor Society and held a summer internship at Oak Ridge National Laboratory in Oak Ridge, Tennessee. Jacob began attending the University of Tennessee, Knoxville in January, 2019, where he has received the UTK Top 100 Graduate Student Fellowship and an Innovations in Nuclear Technology R&D award for his work on ThN-UN fuels. He has accepted a staff scientist position at Oak Ridge National Laboratory, which he intends to begin after earning his PhD in Nuclear Engineering in December, 2020.